# Development of an Ultra-High Performance Concrete H-Pile and It's Connections for Alabama Bridge Foundations

Final Report

October 2024

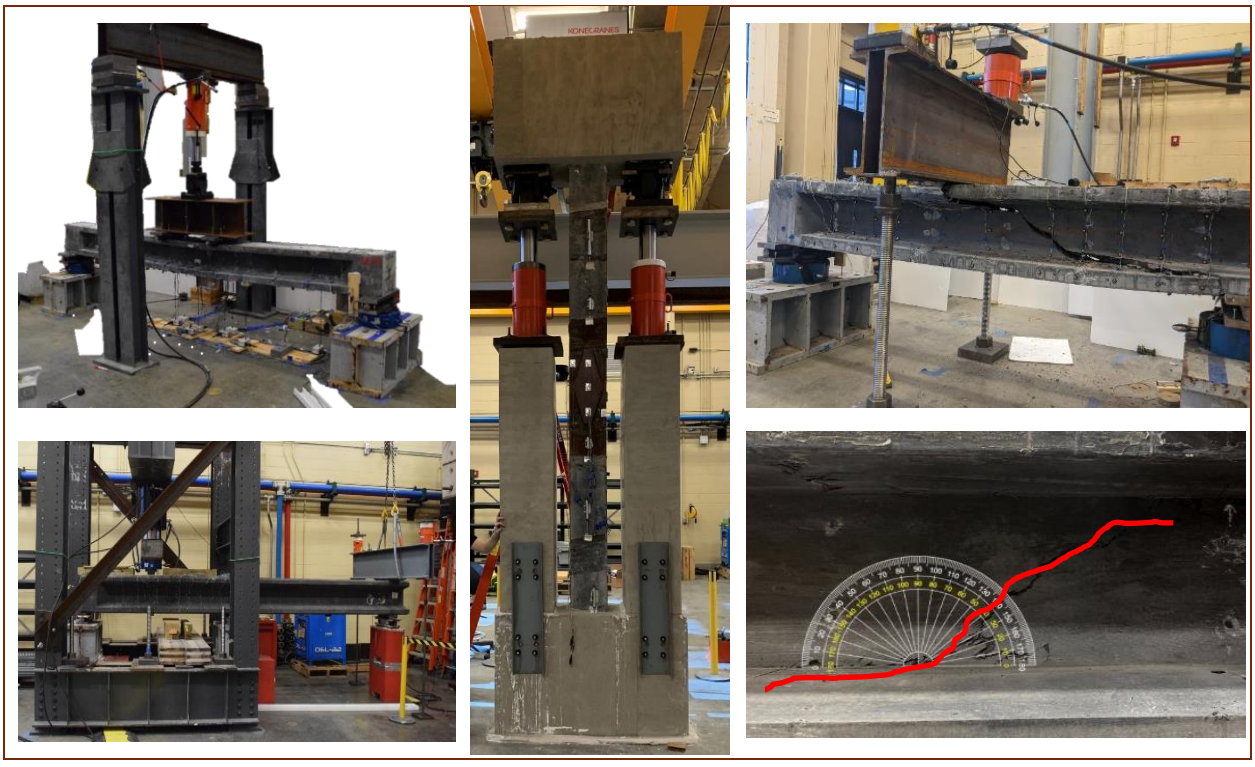

**Sponsored by**

Alabama Department of Transportation

Project No. 931-019

# Development of an Ultra-High-Performance Concrete H-Pile and It's Connections for Alabama Bridge Foundations

Final Report


**Principal Investigator**
Sriram Aaleti, Ph.D.
Department of Civil, Construction, and Environmental Engineering
The University of Alabama

**Graduate Assistant**
Gabrielle Willis, Ph.D. (former research assistant)
Eunice Mendes Mello, research assistant

**Authors**
Gabrielle Willis, Eunice Mendes Mello, and Sriram Aaleti



Sponsored by
Alabama Department of Transportation
(Project No. 931-019)

Preparation of this report was supported by
Alabama Department of Transportation



A Report from
**Department of Civil, Construction, and Environmental Engineering**
**The University of Alabama**
3043 H.M. Comer
245 7th Avenue
Tuscaloosa, AL 35487
https://cce.eng.ua.edu

# LIST OF ABBREVIATIONS AND SYMBOLS

| Symbol | | Definition |
|---|---|---|
| $A_{cv}$ | = | interface shear area (in.$^2$) |
| $A_g$ | = | gross-section section area (in.$^2$) |
| $A_{ps}$ | = | area of prestressing steel (in.$^2$) |
| $A_t$ | = | transformed section area (in.$^2$) |
| $A_{vf}$ | = | area of interface shear reinforcement (in.$^2$) |
| $b_v$ | = | shear width of section (in.) |
| $c$ | = | cohesion coefficient |
| $d_b$ | = | nominal strand diameter (in.) |
| $d_v$ | = | shear depth of section (in.) |
| $e_{pg}$ | = | prestressing force eccentricity with respect to section centroid (in.) |
| $E_c$ | = | modulus of elasticity of UHPC at full strength (ksi) |
| $E_{ci}$ | = | modulus of elasticity of UHPC at the time of detensioning (ksi) |
| $E_{ps}$ | = | modulus of elasticity of prestressing strand (ksi) |
| $f_c$ | = | compressive stress in UHPC (ksi) |
| $f_c'$ | = | ultimate compressive strength of UHPC at full strength (ksi) |
| $f_{cgp}$ | = | concrete stress at transfer due to prestressing (ksi) |
| $f_{ci}'$ | = | ultimate compressive strength UHPC at the time of detensioning (ksi) |
| $f_{pe}$ | = | effective prestressing stress, after losses (ksi) |
| $f_{pi}$ | = | initial prestressing strand stress (ksi) |
| $f_{rr}$ | = | residual tensile strength of UHPC (ksi) |
| $f_{t,cr}$ | = | tensile cracking stress of UHPC (ksi) |
| $f_y$ | = | yield strength of reinforcing steel (ksi) |
| $G$ | = | shear modulus |
| $I_g$ | = | gross-section moment of inertia (in.$^4$) |
| $k_f$ | = | compressive strength factor, for calculating prestressing losses |
| $k_{hc}$ | = | humidity factor for creep, for calculating prestressing losses |
| $k_{hs}$ | = | humidity factor for shrinkage, for calculating prestressing losses |
| $k_l$ | = | loading age factor, for calculating prestressing losses |
| $k_s$ | = | volume-to-surface factor, for calculating prestressing losses |
| $k_{td}$ | = | time development factor, for calculating prestressing losses |
| $K$ | = | limiting factor for interface shear capacity |
| $K_{(id)}$ | = | transform section coefficient between transfer and deck placement |
| $K_3$ | = | creep correction factor, for calculating prestressing losses |
| $K_4$ | = | shrinkage correction factor, for calculating prestressing losses |
| $M_u$ | = | moment at a section (kips) |
| $P_c$ | = | net compressive force normal to shear place (kips) |
| $P_e$ | = | effective for in prestressing steel after losses (ksi) |
| $t_d$ | = | time at deck placement, for calculating prestressing losses (days) |
| $t_f$ | = | final age, for calculating prestressing losses (days) |
| $t_i$ | = | time at transfer, for calculating prestressing losses (days) |

| | | |
|---|---|---|
| $V_{cf}$ | = | concrete and fiber contribution to UHPC shear capacity per PCI (kips) |
| $V_n$ | = | total section shear capacity (kips) |
| $V_p$ | = | shear capacity component in the direction of the applied shear of the effective prestressing force (kips) |
| $V_s$ | = | steel stirrup contribution to shear capacity (kips) |
| $V_u$ | = | shear force at a section (kip) |
| $V_{UHPC}$ | = | shear capacity of UHPC (kips) |
| $\Delta f_{ES}$ | = | prestressing loss due to elastic shortening (ksi) |
| $\Delta f_{pCR}$ | = | prestressing loss due to creep (ksi) |
| $\Delta f_{pLT}$ | = | long-term prestressing loss (ksi) |
| $\Delta f_{pR}$ | = | prestressing loss due to strand relaxation (ksi) |
| $\Delta f_{pshi}$ | = | prestressing loss due to autogenous shrinkage prior to detensioning (ksi) |
| $\Delta f_{pSR}$ | = | prestressing loss due to shrinkage of concrete (ksi) |
| $\Delta f_{pT}$ | = | total prestressing losses in pretensioned members (ksi) |
| $\Delta_v$ | = | shear displacement (in.) |
| $\epsilon_{b,exp}$ | = | total strain at the extreme tension fiber at midspan (in./in.) |
| $\epsilon_{b(id)}$ | = | concrete shrinkage strain between transfer and deck placement (in./in.), for calculating prestressing losses |
| $\epsilon_{DT}$ | = | strain loss due to strand detensioning (in./in.) |
| $\epsilon_{pe}$ | = | strain associated with effective prestressing stress (in./in.) |
| $\epsilon_{shi}$ | = | autogenous shrinkage strain (in./in.) |
| $\epsilon_{t,cr}$ | = | tensile cracking strain of UHPC (in./in.) |
| $\gamma_v$ | = | shear strain (in./in.) |
| $\mu$ | = | friction coefficient for interface shear capacity |
| $\nu$ | = | Poisson's ratio |
| $\psi_b$ | = | creep coefficient, for calculating prestressing losses |
| $\theta_v$ | = | shear cracking angle (degrees) |

# TABLE OF CONTENTS

# LIST OF FIGURES

# LIST OF TABLES

# 1 INTRODUCTION

## 1.1 Background

Cast-in-place Bridges play a crucial role in our infrastructure, serving as the primary means of transporting raw materials, goods, and people across various obstacles worldwide. Consequently, ensuring the safety and structural integrity of bridges is of utmost importance. However, in the United States, many transportation infrastructure elements were constructed in the 1960s with a design lifespan of 50 years, and several of these bridges are still in use but have deteriorated over time. The American Road and Transportation Builder's Association (ARTBA) reported in 2023 that an alarming 36% of US bridges required replacement or rehabilitation, with an estimated repair cost exceeding $54 billion, based on data from the Federal Highway Administration (FHWA) in 2022 (ARTBA, 2023).

Recognizing the need for improvement, recent research efforts have focused on the development of more efficient construction materials and processes. These advancements aim to increase the lifespan of new bridges and reduce the need for repairs. Moreover, these technologies can also be utilized to repair or retrofit existing bridge elements that have become structurally deficient. One of the key strategies employed by several state departments of transportation for the construction of new bridges is the utilization of Accelerated Bridge Construction (ABC) techniques with prefabricated structural elements. ABC techniques aim to lessen on-site construction time, resulting in faster build times, reduced project costs, minimized road closures, and diminished environmental impacts. One approach is the use of precast concrete elements that are produced off-site and transported to the jobsite. The advantage of precast elements lies in their uniformity and the ability to conduct quality checks before shipping them to the jobsite. Bridges constructed using ABC techniques exhibit improved durability and longevity, reducing the need for frequent repairs or replacements. Nonetheless, there are still challenges that need to be overcome, in areas such as connections and installation damage for certain elements.

Despite the emphasis on prefabricated elements, the connections between these elements must still be made on-site. These connections include deck panel-to-deck panel, deck panel-to-girder, girder-to-girder, column-to-cap and foundation elements-to-abutment connections. Precast concrete element joints are often heavily reinforced and susceptible to stress concentrations that can lead to damage. Therefore, special consideration must be given to the connections between bridge elements. Additionally, another aspect that needs to be considered is unforeseen repairs due to impact damage resulting from accidents during a bridge's service life. While such damage primarily affects decks and girders, maritime crashes can also cause harm to bridge columns. In these instances, the ideal approach to repairs is to reopen the bridge as quickly as possible while effectively addressing the damage, without compromising the repair's strength or timeliness.

Bridge foundation elements face their own challenges that warrant careful consideration in bridge construction projects. Foundations serve as the critical support system for bridges, and their integrity is crucial for ensuring the long-term stability and safety of the structure. Several issues arise when assessing bridge foundations, which can be classified into short-term and long-term concerns. Current practices in foundation design involve the selection of either shallow or deep foundations, depending on the site conditions and load requirements. Shallow foundations, such as spread footings and mat foundations, are commonly used when the soil near the surface possesses sufficient bearing capacity or for lower loads. On the other hand, deep foundations, including driven piles and drilled shafts, are employed when the underlying soil lacks the necessary load-bearing

capacity at shallow depths. Bridge foundations are entirely comprised of deep foundations, anchoring the bridge superstructure (deck and girders) and substructure (pier caps, piers, and pile caps), as shown in Figure 1-1.

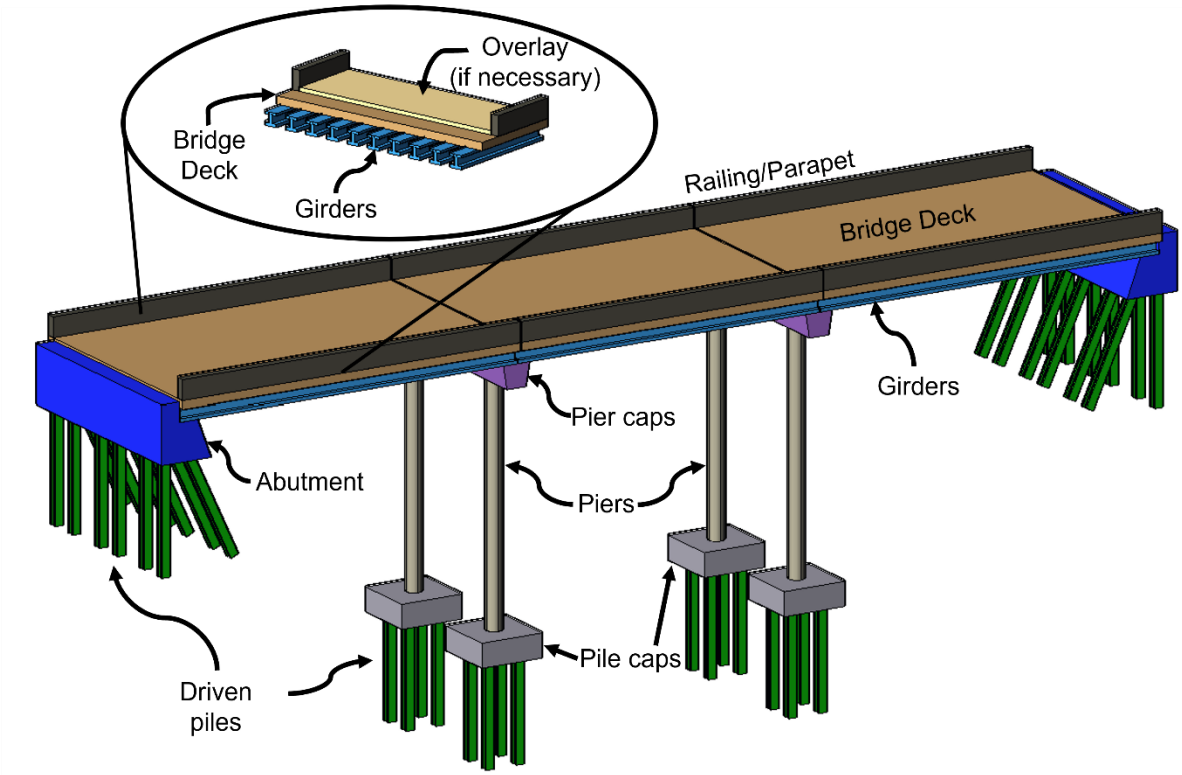


**Figure 1-1 Typical bridge structure components**

Steel and concrete are the most common materials used for construction of foundation elements as they are adaptable to a variety of soil conditions and can achieve high bearing capacities. Timber foundations have also been used, but they are less common in current construction, mainly found in older construction, temporary shoring, or low-load applications such as footbridges. One of the short-term concerns in the case of driven piles, is the damage during driving (Figure 1-2). The forces generated by hammer blows during driving can cause high compressive and tensile stresses in the pile. This can cause cracking in normal or prestressed concrete piles, while it can cause local buckling in steel piles. Mitigating this issue typically involves cutting off or removing piles with excessive damage. In the long term, bridge foundations face challenges associated with deterioration over time (Figure 1-2). Regardless of the chosen foundation type, no perfect option exists that guarantees immunity against deterioration. Factors such as exposure to environmental conditions, chemical reactions, and soil movement can gradually compromise the structural integrity of foundations, especially in marine environments, which most bridges are. For steel piles, the result is often corrosion, and with concrete piles, gradual cracking and spalling will occur, which will lead to corrosion of the reinforcement. Repairing deteriorated pile foundations poses significant challenges due to the complexity and criticality of these elements. In many cases, these damaged systems are in hard-to-reach places, so ensuring effective repair while maintaining the stability and safety of the bridge requires intricate solutions and are generally expensive.

Ultra-High-Performance Concrete (UHPC) has emerged as a potential solution for addressing the shortcomings of traditional steel and concrete deep foundations, as well as for other bridge construction and repair applications. UHPC is an advanced form of concrete that exhibits exceptional strength and durability compared to normal concrete. The constituents of UHPC typically include cementitious materials, fine aggregates, fibers, water, and chemical admixtures. Cementitious materials in UHPC usually consist of Portland cement combined with supplementary cementitious materials (SCMs) such as silica fume, fly ash, or ground granulated blast furnace slag. These SCMs enhance the cementitious matrix by filling in the gaps between cement particles, resulting in improved strength, density, and durability. Fine aggregates, such as silica sand or quartz powder, are added to UHPC to provide optimal gradation and improve the packing density of the mixture. Fibers, typically made of steel, are used to increase the ductility and tensile strength of the matrix. Water, as in normal concrete, is essential for the hydration process in UHPC. However, the water content in UHPC is significantly lower than in conventional concrete. The limited water-to-cementitious materials ratio helps achieve the desired high strength and dense microstructure. Chemical admixtures play a crucial role in UHPC by enhancing its properties. These admixtures can include high-range water reducers, viscosity-modifying agents, and dispersants. They improve workability, reduce water content, increase flowability, and enhance the overall performance of the UHPC mixture.

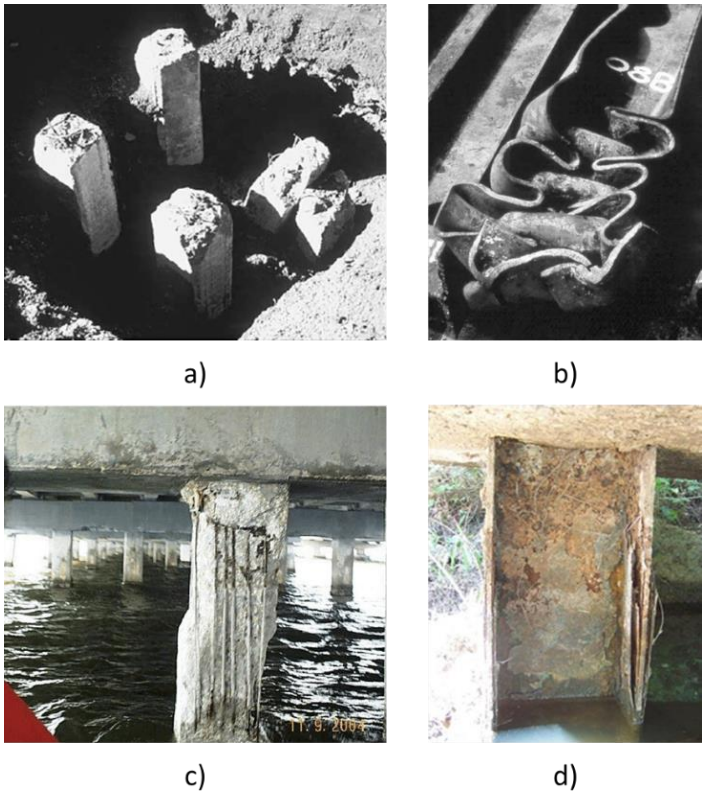


**Figure 1-2 Problems with pile foundations: a) Concrete piles damaged during driving (Salgado 2006) b) Steel pile buckling after driving (Salgado 2006) c) Environmental damage of concrete piles (Sen, 2007) and d) Corrosion of steel piles (Hyzak, et al., 2014)**

After significant amounts of research, some of which will be discussed in detail in the following chapter, UHPC has been found to be a useful material for application in various structural elements, including girders and deck panels. UHPC girders can effectively support heavy loads while reducing

overall structural weight, leading to more efficient and cost-effective designs. Deck panels constructed with UHPC exhibit enhanced resistance to cracking, chemical attack, and environmental degradation, resulting in a longer service life and reduced maintenance requirements.

As for pile foundations, UHPC provides viable solutions to the challenges faced by traditional steel and concrete piles. UHPC piles offer improved corrosion resistance, increased load-bearing capacity, and reduced susceptibility to cracking. These exceptional mechanical properties allow for longer and more slender pile designs compared to traditional concrete or steel piles, thereby can potentially reduce the number of piles required for a given load and simplify construction logistics. UHPC shows promise as a material of choice for bridge construction's repair and replacement work. UHPC overlays can efficiently restore deteriorated concrete surfaces, ensure structural integrity, and lengthen the service life of existing bridges by enhancing conventional repair techniques like overlays and cold joints. Nevertheless, factors like substrate strength, compatibility with existing materials, and surface roughness must be carefully considered.

Thorough research has been conducted to evaluate the performance of normal concrete-to-UHPC bond, but as UHPC bridge elements become more prevalent, the likelihood of encountering UHPC-to-UHPC interfaces increases. As an example, the connection between piles and pile caps plays a critical role in bridge construction and repair, particularly with ABC techniques. If a pile is cast using UHPC, and the connection between the pile cap and pile is filled with UHPC, there exist two interfaces: a normal concrete-to-UHPC interface between the pile cap and filler; and a UHPC-to-UHPC interface between the filler and pile. In these cases, it is crucial to ensure efficient, durable, and robust linkages. Moreover, UHPC offers potential for repairing existing bridge elements in use, ensuring their structural integrity and extended service life. Furthermore, if UHPC piles become a standard in deep foundation design, the development of reliable and efficient repair methods for these elements will be crucial in maintaining the long-term stability and safety of bridges.

Overall, the aim of this dissertation is to tackle three tasks. First, characterize the bond behavior and applicability of current code equations for UHPC-to-UHPC interfaces. The second goal is to create several driven pile foundation sections made of UHPC and evaluate their construction feasibility and structural performance in shear and flexure. Finally, create a comprehensive plan for filed implementation of these piles, including a planned splice design.

## 1.2 Scope of Research

The research scope of this proposal focuses on the development and testing of an innovative Ultra-High Performance Concrete (UHPC) H-pile system for use in bridge foundations in Alabama. The main goal is to design a cost-effective, durable H-shaped prestressed pile that matches the physical dimensions and weight characteristics of traditional steel H-piles. By leveraging the superior strength, durability, and drivability properties of UHPC, the study aims to produce a pile that not only offers higher bearing capacity but also reduces maintenance costs over time compared to conventional steel or concrete piles. This will be achieved through detailed design, optimization, and testing of several H-shaped UHPC cross-sections, followed by full-scale field testing to evaluate their performance under axial and lateral loads in various soil conditions.

The scope also extends to investigating the splicing techniques and connection details for UHPC piles, ensuring they can be efficiently extended in the field without compromising on strength or durability. The research will utilize both analytical and experimental approaches to characterize the behavior of these UHPC piles under real-world conditions, including their drivability and structural

performance. Collaborations with industry stakeholders such as ALDOT, precast producers, and material suppliers will support the research efforts, with the ultimate objective of developing practical recommendations for the use of UHPC piles in Alabama's infrastructure projects.

## 1.3 Report Layout

This report is divided into six chapters, including this introduction. Each chapter details an aspect of research, separated by major purpose. A general literature review is presented in a separate chapter, though some relevant background information is given in the individual chapters as needed to improve reading flow.

Chapter 2 presents a comprehensive literature review, providing background on the typical constituents and properties of Ultra-High-Performance Concrete (UHPC), as well as the behavior of UHPC interfaces under shear forces. It also highlights previous research on the flexural and shear performance of UHPC structural members and explores the development of splices for piles, offering context for the experimental studies conducted in the subsequent chapters. In Chapter 3, the development, design, and experimental testing of 12-in. and 14-in. UHPC H-piles are detailed. These UHPC piles were designed as alternatives to steel HP piles commonly used by departments of transportation in the U.S. Ten large-scale tests were conducted to evaluate the flexural and shear performance of these new pile sections. Chapter 4 addresses the development of a 16-in. UHPC H-pile section, which was designed as a lightweight, high-strength alternative to traditional prestressed concrete piles. Four large-scale tests were conducted to assess the pile's flexural and shear performance, further advancing the understanding of UHPC applications in pile foundations. Chapter 5 introduces the development and testing of a pile splice compatible with the UHPC pile sections discussed in Chapter 3. This chapter reports on eight full-scale tests that evaluated the splice's performance in flexure, shear, and tension, comparing its behavior to that of unspliced piles, and verifying its suitability for practical applications. Finally, Chapter 6 presents the major conclusions of the research, summarizing the key findings and contributions. It also offers recommendations for future studies, aiming to expand the knowledge base on UHPC piles and their potential applications in deep foundation systems.

# 2 LITERATURE REVIEW

This chapter discusses the background and previous research on several topics relevant to this dissertation. Following an outline of what UHPC is, from constituent materials to typical material properties, there will be a discussion of the various structural uses of UHPC that have been tested in a lab setting and implemented in real-world projects. Following that, driven piles will be discussed, including pile types, sizes, driving methods, and splicing methods available in industry. Finally, background information on concrete interface shear behavior and previous studies on UHPC interfaces will be provided.

## 2.1 UHPC as a Material

First developed in the 1990s, UHPC can be defined as a reactive powder concrete tailored for high compressive strength, high ductility, and sustainability. This is achieved through low water-cementitious material ratios, tight particle packing of fine and ultrafine aggregates, and reinforcement with high-strength steel fibers (Bajaber & Hakeem, 2021). The typical material constituents of normal concrete consist of coarse aggregate, fine aggregate, cement, and water. Admixtures are often added to encourage more desirable properties, such as water reducers to improve workability or air entrainers to improve environmental resilience but are not strictly necessary. Supplementary cementitious materials (SCMs) are sometimes mixed with Portland cement to make concrete more environmentally friendly with industrial waste byproducts like fly ash or slag, but once again, these are not necessary for basic concrete. Typical water-cementitious material (w/cm) ratios range from 0.4 to 0.6. Higher w/cm ratios increase the workability of a concrete mix but decrease the strength. This is combatted through the use of admixtures such as superplasticizers and water reducers.

The liquids in a concrete mix design combine with the cementitious materials to form a paste, like a glue between the different solid aggregates. The interface between the paste and aggregates, or the interfacial transition zone, are the weakest point in the material matrix of concrete. Good gradation of aggregates in concrete minimizes the impact of the interfacial transition zone and reduces the amount of paste required. Figure 2-1 shows a poorly graded concrete matrix compared to one which is well-graded. In the poorly graded matrix, there is a considerable amount of area not occupied by particles of any size, whereas the well-graded mix fills much of this area with tight particle packing.

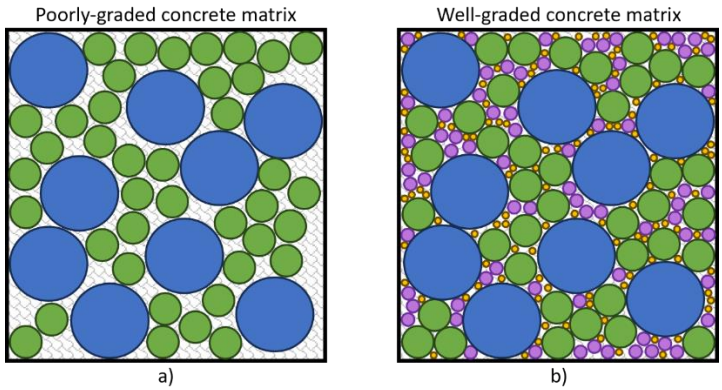


**Figure 2-1 Particle packing of a concrete matrix with a) poorly graded particles and b) well-graded particles.**

The constituents of UHPC include fine aggregates (typically fine sand), Portland cement, silica fume, steel fibers, water, and admixtures. Different admixtures are used depending on the specific mix design, but there is always at least one high-range water reducer (HRWR) or superplasticizer. Accelerators are often implemented as well to encourage faster chemical reactions. Through the heavy usage of admixtures, the w/cm of UHPC ranges from 0.14 to 0.22 (Bajaber & Hakeem, 2021). At this level of w/cm ratio, much higher strengths can be achieved compared to normal concrete.

UHPC mixes are also optimized to capitalize on the principle of particle packing. Sand particles range from 150 to 600-μm, and Portland cement particles average 15-μm. Silica fume is a SCM which increases the compressive strength of UHPC but reduces the workability. Silica fume also has a very fine particle size, less than 1-μm (Bajaber & Hakeem, 2021). This range of sizes produces a very dense particle matrix, promoting higher strengths and better durability. The final element of UHPC is steel fibers. Normal concrete is brittle and possesses very little tensile strength. Once a crack begins in concrete, it will continue to propagate until encountering a material which can transfer the tensile stresses. This is one reason normal concrete is reinforced with rebar. The addition of steel fibers to UHPC fulfills that purpose, but distributes the tensile capacity throughout the mix, instead of at discrete locations like rebar. Fibers are typically added at either 2% or 2.5% by UHPC mix volume.

There are several UHPC mix designs available, separated into proprietary and non-proprietary mixes. In the United States, there are currently seven major proprietary mixes in use: Ductal, Steelike, Aalborg, Dura, SmartUP (Vicat), Cor-TUF, and CeEntek. The University of Alabama researchers have casting and testing experience with five of the seven indicated in Table 2-1, which displays the proportions for a one cubic feet volume yield. The quantities for each proprietary mix vary. In comparison to the other mixes, Aalborg has a lower fiber content, and the dry mix contains larger fines. Both Dura and Vicat use two admixtures, one of which is a high-range water reduced (HRWR) admixture and the other of which is either an accelerator or a workability-retaining admixture. Because some additional admixtures are baked into the dry mix, Steelike requires less admixture to be added to the mix.

**Table 2-1 Example proportions for 1-ft$^3$ volume of proprietary UHPCs mixed at The University of Alabama**

| Material | Ductal | Steelike | Dura | Aalborg | Vicat |
|---|---|---|---|---|---|
| Dry Mix | 137 lbs | 137 lbs | 154 lbs | 138 lbs | 130 lbs |
| Water | 8.11 lbs | 12.36 lbs | 13.46 lbs | 12.38 lbs | 11.24 lbs |
| Fiber | 9.74 lbs | 10.09 lbs | 11.60 lbs | 6.88 lbs | 12.33 lbs |
| HRWR | 1.87 lbs | 0.628 lbs | 2.13 lbs | 1.72 lbs | 1.44 lbs |
| Other admixtures | -- | -- | 0.72 lbs | -- | 0.50 lbs |

Non-proprietary mixes are becoming increasingly common as several companies and departments of transportation (DOTs) attempt to use locally-sourced materials to reduce the cost of UHPC (Abokifa & Moustafa, 2021) (Berry, Snidarich, & Wood, 2017) (Shahrokhinasab & Garber, 2021) (Federal Highway Administration (FHWA), 2013). The properties and mix designs for these mixes can vary greatly but should at least meet the minimum criteria set forth by standard codes for UHPC, which will be discussed shortly.

UHPC behavior is characterized by its compressive and tensile behavior. Figure 2-2 shows the typical stress-strain responses of UHPC compared to normal concrete in compression and uniaxial tension. Both of these properties and curves can vary based on the specific mix design, constituent materials, and curing. AASHTO LRFD (2017) defines the minimum compressive capacity of UHPC as 17.5 ksi, with an ultimate strain of 0.0035 in./in. The compressive strength of UHPC is typically measured through testing of 3-in. by 6-in. cylinders using the same ASTM standard as normal concrete, ASTM C39 (2021), modified by ASTM C1856 (2017) a companion standard for UHPC. For analysis, the compressive stress-strain is idealized as a bilinear curve, elastic until the ultimate compressive stress, then the ultimate stress is sustained until ultimate strain, as shown Figure 2-3a. This model is currently adopted by AASHTO's (2017) recommendations for UHPC.

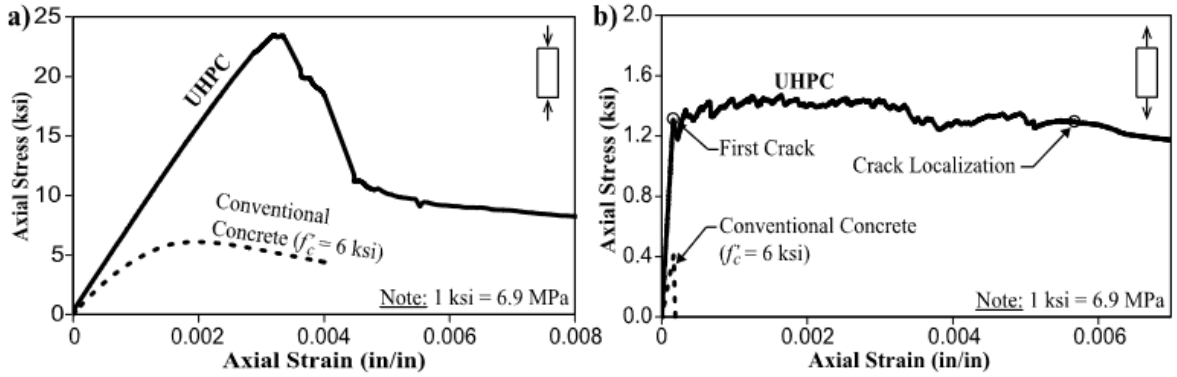


**Figure 2-2 Typical stress-strain response for UHPC in a) compression and b) uniaxial tension (El Helou & Graybeal, 2019)**

The tensile behavior of UHPC is critical to achieving the full potential of UHPC. The quantity and orientation of fibers plays a large role in the capacity and has been a frequent topic of research. Increasing percentages of fibers and fiber orientation in the direction of tensile stresses improve the flexural and tensile properties of UHPC (Graybeal & Baby, 2013; Huang, Gao, Li, & Wang, 2018; Bridi Valentim, 2023). UHPC behaves elastically until first cracking occurs, after which the multi-cracking phase begins, where many tightly spaced microcracks form. During testing, these microcracks cracks are not visible to the naked eye. Some additional load is gained during the multi-cracking phase, until peak stress and localization occurs. Localization is determined as the point where a microcrack visibly opens, which on a stress-strain diagram, appears as the point after which the stress continuously decreases. This behavior can be idealized in different ways, with one method shown in Figure 2-3b.

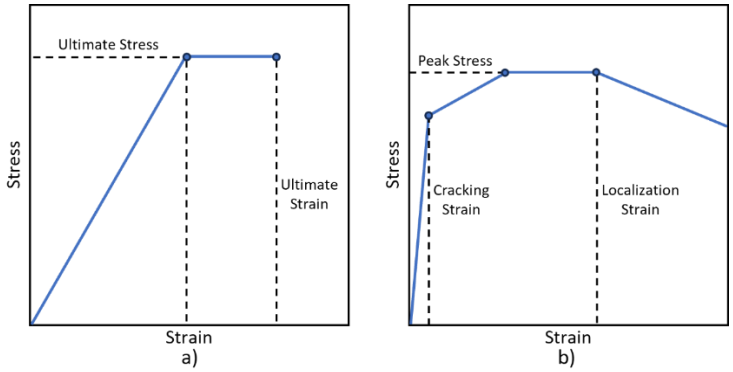


**Figure 2-3 Idealized stress-strain response of UHPC in a) compression and b) tension**

For design purposes, the behavior past localization is typically discounted, though in the full response is used in analysis. The typical design curves either use a bilinear approach similar to the compressive curve, where stress increases linearly until the cracking stress and strain, then this stress is sustained until localization. AASHTO does permit another design curve when the localization stress is at least 20% greater than cracking strain, where after cracking, the stress increases to localization stress and strain. AASHTO recommends minimum tensile properties of 0.75 ksi cracking and localization stresses, with a localization strain of 0.005 in./in. Depending on the specific mix and fiber content, localization stresses can reach 2.0 ksi.

There are numerous methods to find the tensile capacity of UHPC. Bridi Valentim (2023) conducted a study comparing three methods: direct tension (DT), four-point bending (4PB), and double-edge wedge splitting (DEWS) tests. Although each method measures the tensile capacity, this is achieved in different ways, shown in Figure 2-4. Direct tension is the more commonly accepted method and as the name suggests, it directly measures the tensile response of UHPC through uniaxial tension of a prism. There is an AASHTO testing method for this test, T-397 (AASHTO, 2022). However, it requires specialized tension testing equipment which is not typically found on jobsites or in testing labs. The other two methods are able to utilize a compression testing machine, which is more universal. Four-point bending and DEWS both measure the tensile strength indirectly through flexure and splitting, respectively. Four-point bending has an ASTM standard, C78 (2022), but the stress achieved in flexure is higher than the true tensile capacity. DEWS does not have an associated standard but boasts the advantage of being able to be cut from concrete coring disks, so could be a potential diagnostic tool for finding the capacity of existing structures.

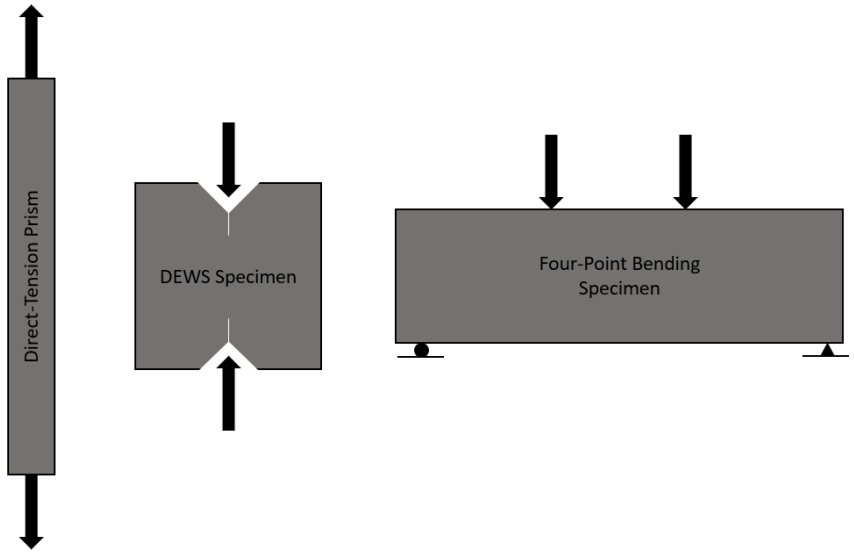


**Figure 2-4 Different test methods for determining UHPC tensile behavior.**

Several different standards currently exist for UHPC, although several have only recently been approved or implemented. In the United States, AASHTO has recently approved a specification for UHPC as a companion to the AASHTO LRFD Bridge Design Guide (2017). The Prestressed Concrete Institute (PCI) has also published a report with recommendations for the use of UHPC in precast, prestressed structures (2021). Several of the equations and recommendations are similar to those recommended by AASHTO, but with modifications for prestressed members. Internationally, standards have been published in France, Germany, Switzerland, Korea, Japan, Australia, and Canada.

## 2.2 Structural Uses of UHPC

UHPC has been examined as a candidate for a variety of structural applications, for both horizontal and vertical construction. Research has been conducted evaluating the suitability of UHPC as a supplementary material to other structural members in a hybrid fashion or as a connector material. The material cost of UHPC is higher than more conventional structural materials, and although the cost has become more economical with time, focus was initially placed on finding applications of UHPC that could take advantage of the superior mechanical properties without sacrificing project budgets. One major hybrid application of UHPC is as a bridge deck overlay. Bridge decks often experience long-term degradation, especially in areas with fluctuating temperatures and frequent freeze-thaw cycles. The most common repair for this is to repave or place an overlay on the surface. UHPC, with its superior environmental performance, was identified as a suitable overlay material that would not suffer from the same level of freeze-thaw damage. A UHPC overlay could also be thinner than one cast from normal concrete due to its advanced mechanical properties. Several studies have been conducted to determine the interface shear behavior of the UHPC-normal concrete interface present in an overlay, which will be discussed in further depth in Section 2.3. Several UHPC bridge deck overlays have been used in real-world projects, with 17 bridges in the United States using UHPC bridge deck overlays as of 2021, mostly in the northeastern United States (FHWA, 2021).

UHPC is also commonly used as a joint material in bridge applications. Research has been conducted to evaluate the performance of UHPC as a material in field-cast joints between separate bridge decks (Graybeal, 2010), separate girders (Semendary, Walsh, & Steinberg, 2017), as well as joints between decks and girders (Aaleti, Petersen, & Sritharan, 2013). UHPC has also been examined as an option for the connection between a UHPC posttensioned bridge column and a footing (Mohebbi, Saiidi, & Itani, 2018). According to the FHWA, there are 270 applications of UHPC as a connection in bridge projects in the United States as of 2021 (FHWA, 2021).

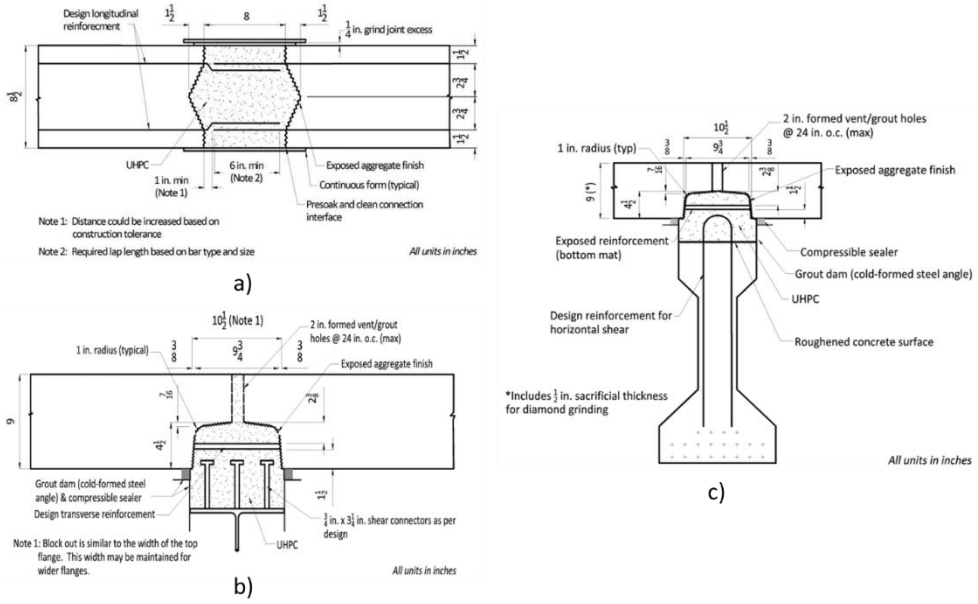


**Figure 2-5 Examples of field-cast UHPC connections in bridge systems between a) two bridge decks, b) bridge decks and steel girder, and c) bridge decks and concrete girder (Graybeal, 2014)**

In addition to its development as a connection material, UHPC can be used as the primary material for different structural elements. UHPC has been investigated as deck panels (Aaleti, Petersen, & Sritharan, 2013), bridge columns (Mohebbi, Saiidi, & Itani, 2018), and as girders of different shapes, including Bulb-T, I-shaped, Pi-shaped, and U-shaped girders (Wang, et al., 2021). The instances of UHPC use as bridge elements is less common, with only one UHPC bridge deck and five cases of UHPC girders being implemented in US bridge projects, as of 2021 (FHWA, 2021). A 10-in. UHPC driven pile section was also developed at Iowa State University (T. Vande Voort, 2008) along with a complimentary splice design and abutment connection detail (Garder, Aaleti, Zhong, & Sritharan, 2019). This pile was developed as an alternative to the HP 10x57 steel driven pile section. During phase I of the project, H-shaped precast, prestressed UHPC piles were designed and fabricated, with comparable dimensions and self-weight to a steel HP 10 x 57 pile (Figure 2-6). The tapered H-shaped section of 10 in. x 10 in. cross-section was reinforced with ten 13-mm (0.5 in.) diameter prestressing strands and no mild steel, with 0.75 in. of cover. A proprietary Ductal® mix was used for all piles. At the end of all H-shapes, the tapered part was flared over 9 in. and modified to a solid 10 in. square section that extended 9 in. on top of the pile (Figure 2-7). This was done to increase the area in which the driving tension force was distributed, especially since the prestressing is not fully effective at the ends of the piles. By modifying the ends, the allowable tensile force at the pile top was increased by 78 percent.

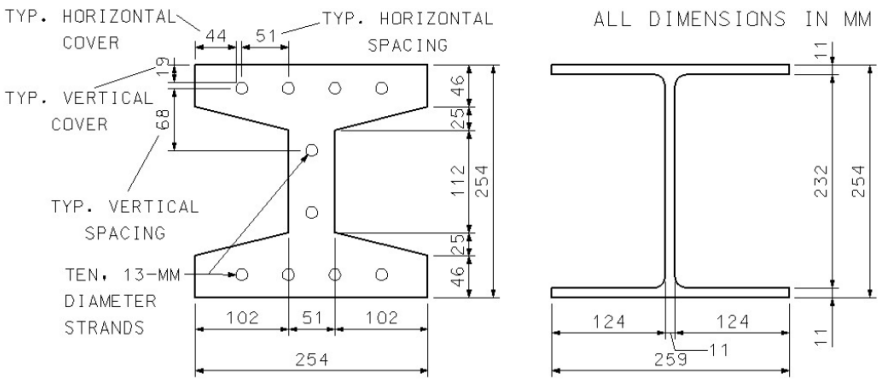


**Figure 2-6: Comparison of UHPC pile designed and Steel HP 10 x 57 pile (T. Vande Voort, 2008)**

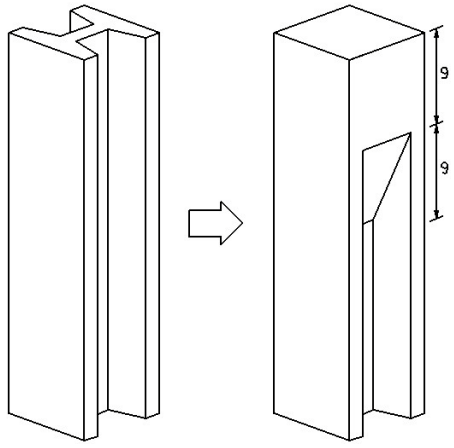


**Figure 2-7: Expanded region on the top of UHPC piles[2]**

Additionally, in this study, the drivability of UHPC piles was examined using various driving parameters and GRLWEAP, using driving soils profiles and driving hammers. The high compressive strength and high prestressing that can be used in UHPC allows for high driving stress limits. Therefore, the results showed that the UHPC piles have an increased drivability compared to normal concrete (NC) and precast high-performance concrete (HPC), and comparable to steel piles. Two piles were tested on the laboratory under combined axial and lateral loads to verify the moment-curvature behavior of the pile section.

**Table 2-2: Ratios of calculated stresses to stress limits for NC, HPC, UHPC, and Steel piles**

| Pile | (1) Calc. Tens. Str. (MPa) | (2) Tens. Str. Limit (MPa) | (1)/(2) | (3) Calc. Comp. Str. (MPa) | (4) Comp. Str. Limit (MPa) | (3)/(4) |
|---|---|---|---|---|---|---|
| NC | 9.1 | 6.2 | 1.47 | 18.3 | 24.5 | 0.74 |
| HPC | 3.6 | 8.3 | 0.44 | 32.1 | 64.3 | 0.50 |
| UHPC | 1.8 | 37.3 | 0.05 | 53.0 | 122.0 | 0.43 |
| Steel | 20.2 | 310.0 | 0.07 | 238.6 | 310.0 | 0.77 |

Additionally, during phase-II of this project, researchers conducted a field investigation to evaluate the application of UHPC on two test piles[3]. One pile being 13.7 m (45 ft) long and the other pile consisting of two 4.6 m (15 ft) sections welded end to end at a structural steel splice. For this, the pile responses were monitored using a Pile Driving Analyzer (PDA) during installation and driving. Both the drivability analysis obtained using GRLWEAP and the PDA confirmed that the pile stresses observed were well below the allowable stress limits, with no visible structure damage to either pile or on or near the splice. Additionally, four HP 14x79 steel piles were driven on the same site, and the results showed that the UHPC piles had approximately 50 percent higher total axial capacity. Vertical load tests were also performed once on the steel pile and twice for one of the UHPC piles. Additionally, lateral load tests were performed on both UHPC piles simultaneously, which resulted in the shear failure of the UHPC pile that was subjected to all tests. This was believed to have happened due to the pile being weakened at the critical section for shear due to the ineffective area taken by the presence of six bar wires and strain gauges.

On another case, in Canada, UHPC H-piles were used to complete an entire foundation for one abutment for a detour replacement bridge in Ontario (Loh et al., 2021). For this, the prestressed UHPC pile used was based on a 12 in. UHPC pile designed (Figure 2-8). In total, 8 piles were fabricated using Dura UHPC and with different shapes at one of the ends. For the drivability analysis, GRLWEAP was used, and before constructing the bridge, one pile was driven on a Facca plant site to ensure constructability. The test pile was monitored with the Pile Drive Analyzer (PDA) and driven in the same conditions as it would be on the real bridge site. The results showed that the UHPC piles would provide suitable support, with the condition of being driven to bedrock or a penetration depth of 7.5 m or 0.3 in. per blow or less, and as long as the resulting ultimate geotechnical axial resistance was greater than two times the design load. For comparisons, the UHPC piles were set at a depth of approximately 26.2 to 30.7 ft above the anticipated bedrock, while the steel piles in the east abutment had to be driven to bedrock, at approximately 50 ft below ground level. With this, it was possible to conclude that the UHPC piles can be driven with similar driving equipment, and, although slightly heavier, it can be also handled by conventional transportation and hoisting equipment. Furthermore, UHPC piles can be tested using the same techniques as steel piles and, in this project, UHPC piles were approximately 50 to 60% shorter than steel piles to attain similar resistance.

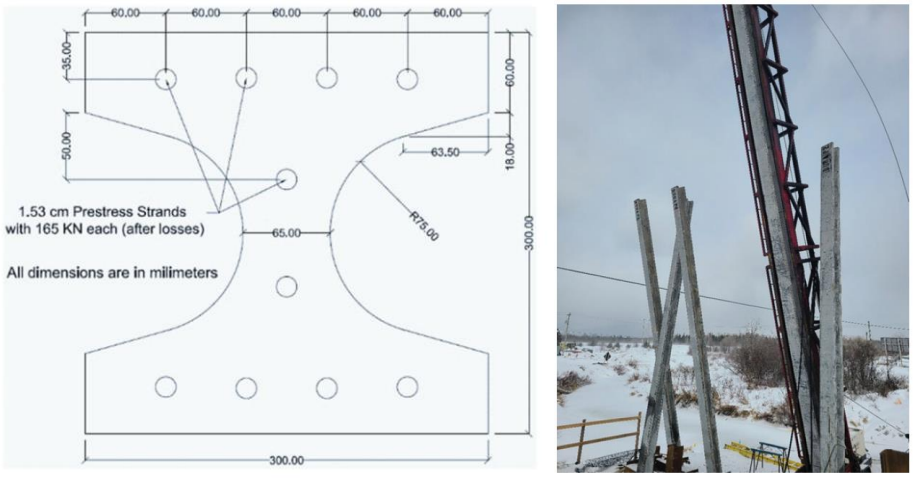


**Figure 2-8: UHPC H-pile section details used in detour bridge in Canada and piles driven[4]**

The Florida Department of Transportation (FDOT) ( FDOT, included a 30-inch UHPC H-pile in the CR 339 over Waccasassa River Bridge. The 30-inch UHPC H-pile was used as a substitute for a 20-inch square prestressed concrete pile that was used for the rest of the piles in the structure. The Pile was constructed using Cor-Tuf UHPC by a local precaster and was driven at a project site to demonstrate the pile drivability and driving capacity. The driving process are shown in Figure 2-9

*Pile driving photos coutesy of Cor-Tuf UHPC*

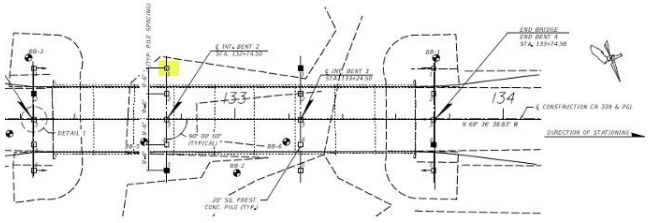

*Plan View of Foundation Layout (Highlighted pile is substituted with UHPC H-pile).*

**Figure 2-9: 30 in. UHPC H-pile Driven in Florida by FDOT**

## 2.3 Interface Behavior

### 2.3.1 Shear-Friction Theory

Shear-friction theory has been the prevailing interface shear behavior theory since its conception in the 1960s. The initial theory proposed a “saw-tooth model” utilizing Equation 2-1 to calculate interface shear capacity (Birkeland & Birkeland, 1966). In this model, a connection subjected to shear will resist motion based on the amount of friction due to aggregate interlock at the interface. Once a crack forms, the roughened surface slips, increasing dilation between the layers and adding tension to the interface reinforcement. The maximum interface shear capacity is reached when the

reinforcement reaches yield stress, with a factor applied based on the tangent of the contact angle along the interface surface. This initial theory is still implemented to some degree in current code standards to characterize interface shear strength due to interface reinforcement but lacks consideration for chemical concrete bond or capacity due to an external normal force.

$$V_u = A_s f_y * \tan(\phi) \quad \textbf{2-1}$$

where:

$$\tan(\phi) = 1.7 \; for \; monolithic \; joints$$

$$\tan(\phi) = 1.4 \; for \; artifically \; roughened \; joints$$

$$\tan(\phi) = 0.8 \; to \; 1.0 \; for \; nonroughened \; joints$$

The research by Birkeland and Birkeland was further expounded upon throughout the 1960s (Mast, 1968) (Hofbeck, Ibrahim, & Mattock, 1969), but the next major changes to interface shear theory came in 1972. Another term was proposed to incorporate the cohesive bond of concrete and the friction term was separated into two parts, one for interface reinforcement, and another for external normal forces (Mattock & Hawkins, 1972), resulting in Equation 2-2.

$$v_u = 200 \; psi + 0.8(\rho f_y + \sigma_{Nx}) \quad \textbf{2-2}$$

Currently, four parameters are considered to contribute to interface shear transfer: concrete compressive strength of the weaker interface concrete, external normal force, interface shear reinforcement, and surface roughness (Santos & Júlio, 2014). For an uncracked interface, cohesion dominates the earliest parts of loading, any slip occurs, adhesion and mechanical interlock of an interface prevent slip. Friction engages once the interface begins to slip due to the interface roughness, and as slip increases, interface shear reinforcement will begin to engage. Once a significant amount of slip has occurred, any interface reinforcement will also be subjected to shear, and this mechanism is referred to as dowel action. The contribution of these three mechanisms to shear stress as slip increases can be seen in Figure 2-10.

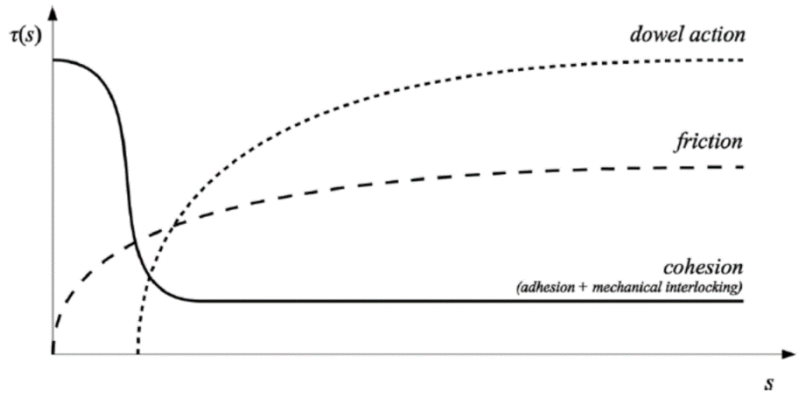


**Figure 2-10 Interface shear mechanisms (Santos & Júlio, 2014)**

### 2.3.2 Design Code Equations for Interface Shear

Current AASHTO (2017) and Eurocode 2 (2004) provisions include terms for cohesion and friction, with the friction terms accounting for both interface reinforcement and external normal forces. Dowel action is not considered in either case. In both cases, cohesion terms are multiplied

by a cohesion coefficient, c, and friction terms are multiplied by a friction coefficient, μ. These coefficient values vary based on the interface preparation, with smoother surfaces permitting smaller interface strengths and rougher surfaces allowing larger capacities.

AASHTO (2017) finds the interface strength in terms of force, with cohesion strength based on the area of the interface and the friction strength based on the tension in interface reinforcement and normal force. The cohesion and friction coefficients change if the interface is monolithically cast, concrete-concrete with depths of at least 6.4-mm (0.25-in), concrete-concrete with depths less than 6.4-mm, and concrete-steel interfaces. In this equation, the cohesion coefficient is the strength of the chemical bond of concrete in terms of stress, which is then multiplied by the interface area to find the cohesion capacity. Concrete strength is not considered in this equation. The coefficient of friction is unitless. The AASHTO equation and interface conditions can be found in Table 2-3. It is worth noting in the AASHTO standard, there is a 60% decrease in cohesion capacity and a 40% decrease in friction capacity for interfaces with depths less than 6.4-mm (0.25-in), and that interface texture depth is the only defining characteristic for concrete-concrete interfaces.

The recent addendum to the AASHTO code adds new specification specific to UHPC. This includes several new interface shear capacity cases. Most of these cases use the same overall equation as the general AASHTO code, which combines the cohesion capacity of the interface area with the friction capacity due to shear reinforcement and normal forces. The case for monolithic UHPC adds an additional friction term for the tensile capacity of UHPC. Several other cases are also included, for UHPC cast on UHPC (UHPC-UHPC), UHPC cast on normal concrete (UHPC-NC), and normal concrete cast on UHPC (NC-UHPC) interfaces. Notably, the capacity for UHPC-UHPC interfaces that are not intentionally roughened, classified as any interfaces with less than 6.4-mm (0.25-in.) square flutes, is even less than the equivalent interface in the broader AASHTO code. The coefficients for each case are shown in Table 2-3.

Eurocode 2 (2004) calculates interface capacity in terms of stress. Both the cohesion and friction coefficients are unitless, and similar to AASHTO, the values change based on the surface roughness. The surface preparation categories for Eurocode 2 are indented, in which the interface has depths of at least 5-mm (0.20-in); rough, where depths are at least 3-mm (0.12-in), smooth, without specific preparation, and very smooth, for concrete-steel or concrete-plastic interfaces. This equation utilizes the tensile strength of concrete to calculate the cohesive bond of concrete. The angle of interface reinforcement is used to find the friction capacity. The equations and values for both cohesion and friction coefficients can be found in Table 2-4. Unlike the AASHTO provisions, Eurocode 2 puts some limits on texture groove spacing.

**Table 2-3 AASHTO interface shear capacity cases**

| | | | |
|---|---|---|---|
| AASHTO (2017), Interface Shear Capacity | | | |
| Overall Equation: $V_{ni} = cA_{cv} + \mu\left(A_{vf}f_y + P_c\right) \leq KA_{cv}$ | | | |
| Interface Preparation Case | Cohesion Coefficient (c) | Friction Coefficient (μ) | Limiting interface shear resistance (K) |
| 1. Concrete placed monolithically | 400 psi | 1.4 | 1500 psi |
| 2. Concrete interfaces with at least 6.4-mm (0.25-in) depth | 240 psi | 1.0 | 1500 psi |
| 3. Concrete interfaces with less than 6.4-mm (0.25-in) depth | 75 psi | 0.6 | 800 psi |
| 4. Concrete-steel interfaces | 25 psi | 0.7 | 800 psi |
| AASHTO UHPC Specifications, Interface Shear Capacity | | | |
| Overall Equation: $V_{ni} = cA_{cv} + \mu(A_{vf}f_y + P_c) \leq KA_{cv}$ | | | |
| For Case 1: $V_{ni} = cA_{cv} + \mu(A_{vf}f_s + A_{cv}f_{t,loc} + P_c) \leq KA_{cv}$ | | | |
| 1. UHPC placed monolithically | 1400 psi | 1.0 | 4500 psi |
| 2. UHPC-UHPC interfaces with 12.7-mm (0.5-in.) depth shear keys | 500 psi | 1.0 | 1800 psi |
| 3. UHPC-UHPC interfaces with 6.4-mm by 6.4-mm (0.25-in.) flutes | 240 psi | 1.0 | 1200 psi |
| 4. UHPC-UHPC interfaces not intentionally roughened | 25 psi | 0.6 | 800 psi |
| 5. UHPC-NC interfaces with at least 6.4-mm (0.25-in) depth | 240 psi | 1.0 | 1800 psi |
| 6. UHPC-NC interfaces with less than 6.4-mm (0.25-in) depth | 75 psi | 0.6 | 800 psi |
| 7. NC-UHPC interfaces with 6.4-mm by 6.4-mm (0.25-in.) flutes | 240 psi | 1.0 | 1800 psi |
| 8. NC-UHPC interfaces not intentionally roughened | 25 psi | 0.6 | 800 psi |

*1 MPa = 145.05 psi

**Table 2-4 Eurocode 2 interface shear capacity cases**

| Eurocode 2 (2004), Interface Shear Capacity | | |
|---|---|---|
| Overall equation: | $v = cf_{ctd} + \mu\sigma_n + \rho f_{yd}(\mu \sin\alpha + \cos\alpha)$ | |
| Interface Preparation Case | Cohesion Coefficient (c) | Friction Coefficient (μ) |
| 1. Indented: a surface with depths of at least 5-mm (0.20-in) and groove spacing less than 10 times the depth | 0.50 | 0.90 |
| 2. Rough: a surface with at least 3-mm (0.12-in) depths at about 40-mm (1.57-in) groove spacing | 0.40 | 0.70 |
| 3. Smooth: free surfaces left without further treatment/roughening | 0.20 | 0.60 |
| 4. Very smooth: a surface cast against steel, plastic, or prepared wooden molds | 0.025-0.10 | 0.50 |

*1 MPa = 145.05 psi

### 2.3.3 Previous Studies

Numerous studies have been conducted examining the effects of interface preparation and surface roughness on concrete interfaces, the primary bulk of which have focused on UHPC-normal strength concrete (NSC) interfaces, though some studies look at lightweight concrete (LWC) or high-strength concrete (HSC). Recently, more studies have been conducted for UHPC-UHPC interfaces.

Banta (2005) set out to evaluate the interface shear behavior of UHPC-LWC interfaces. In this experiment, the surface preparation/roughness, reinforcement ratio, and specimen aspect ratio were varied. There were four surface preparation conditions: 38.1-mm (1.5-inch) tall by 76.2-mm (3-inch) wide shear keys, 12.7-mm (0.5-inch) radius deformations at 50.8-mm (2-inch) spacing, a chipped surface created by a jackhammer, and a smooth surface without additional preparation. Two specimens of each type of interface roughness were tested. Reinforcement varied from 1-#3 to 6-#3 rebar going across the interface from the LWC to UHPC blocks. Aspect ratios of 12-inches, 18-inches, and 24-inches were used. 24-horizontal push off tests were conducted with dimensions as in Figure 3. Two L-shaped blocks of concrete were compressed directly along the interface line. Banta found that as the interface shear capacity increased with increasing roughness. Compared to the smooth-surface specimens, the deformed surface roughness saw 65% more strength, shear-keyed specimens saw 210% more strength, and chipped surfaces experienced 291% more shear strength. Despite not increasing the texture depth by much for the chipped specimens, Banta concluded that the fibers exposed from chipping contributed additional mechanical strength for the interface.

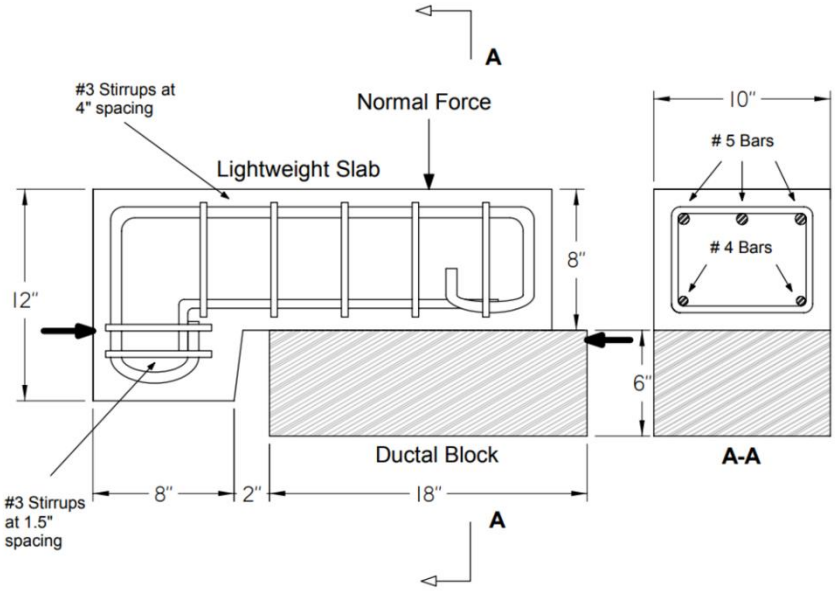


**Figure 2-11 Push-off test specimens used by Banta (2005)**

Sarkar (2010) performed slant shear tests of NSC-UHPC interfaces with different surface preparations to look at the application of UHPC as an overlay material. 27 slant shear tests were conducted, in which a cylinder with an angled interface is compressed to subject the interface to a combined shear and normal force. The specimen textures varied, with nine specimens possessing a smooth interface, five specimens chipped to an average 0.1-inch depth, eight specimens prepared with 0.2-inch-thick grooves cut horizontally along the interface, and five specimens with a trapezoidal shear key embedded. Examples of each texture are shown in Figure 2-12. In this case, the normal concrete side of the interface was chipped rather than the UHPC side, so no fibers were bridging across the interface. Testing showed that increasing texture depth yielded higher interface shear capacities, though in each case except for the smooth texture, failure occurred in the normal-concrete substrate and not along the interface itself.

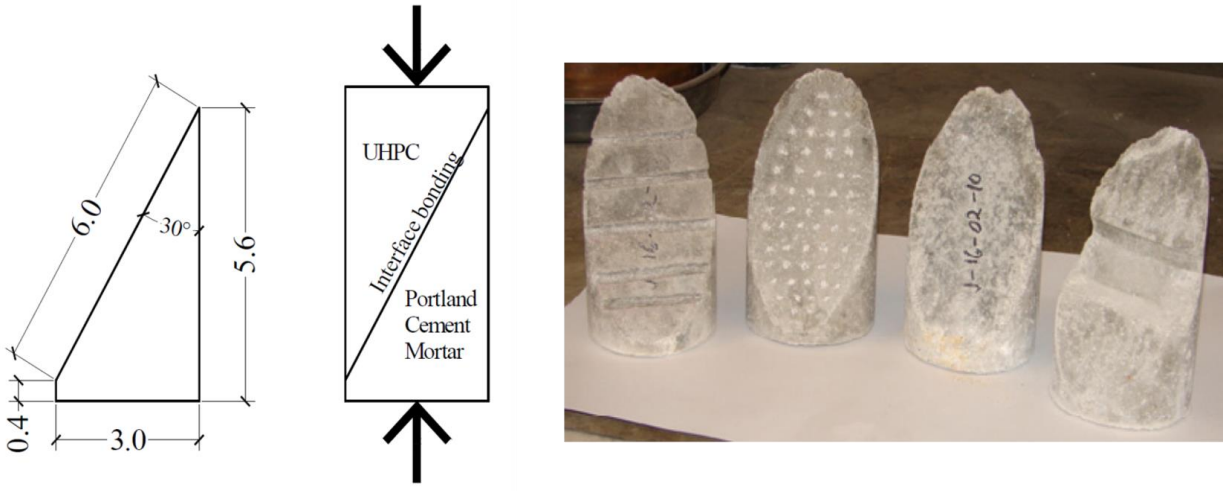


**Figure 2-12 Slant shear specimens and textures from (Sarkar, 2010)**

Munoz et al. (2014) looked at the bond strength provided by various low-depth field-roughening techniques, as well as the effects of changing slant shear interface angle and specimen age. Fifty-four slant shear test specimens were prepared with four preparation methods: wire-brushing, sandblasting, aggregate exposure, and saw-cutting. The average texture depth for each of these were 0.73-mm (0.03-inch), 0.96-mm (0.04-inch), and 2.18-mm (0.09-inch), respectively. No depth was provided for the saw-cut textures. Test results did not indicate much change in bond capacity for these texture depths, and most textures failed due to normal concrete substrate failure.

Another study using slant shear specimens was published by Julio and Santos. (2014) This study uses five interface roughness levels: left as cast (0.06-mm [0.002-inch] depth), wire-brushing (0.18-mm [0.007-inch] depth), sandblasting (0.77-mm [0.03-inch] depth), shot-blasting (0.81-mm [0.03-inch] depth), and hand-scrubbing (3.79-mm [0.15-inch] depth). Experimental results showed that textures with more roughness consistently obtained higher bond strength. Researchers used experimental results to calculate coefficients of cohesion and friction for each texture based on Eurocode 2 and suggested an amended equation for the cohesion coefficient that depended on mean texture depth.

Aaleti and Sritharan (2019) tested sixty slant shear specimens as well as four 9-foot long deck overlays to examine UHPC overlay bond on normal concrete bridge decks. Five texture formliners were used with average depths between 1.26-mm (0.05-inch) and 6.5-mm (0.26-inch). The use of formliners kept specimens of the same texture roughness consistent, compared to other studies that used manual surface preparation. Slant shear test results indicated that at depths above 2-mm (0.08-inch), the bond strength was governed by the weaker concrete strength, as these specimens experienced substrate failure. Below 2-mm (0.08-inch), the roughness was insufficient to develop adequate bond strength. Testing results of deck slabs with at least 3-mm (0.12-inch) roughness did not experience any bond failure or slip.

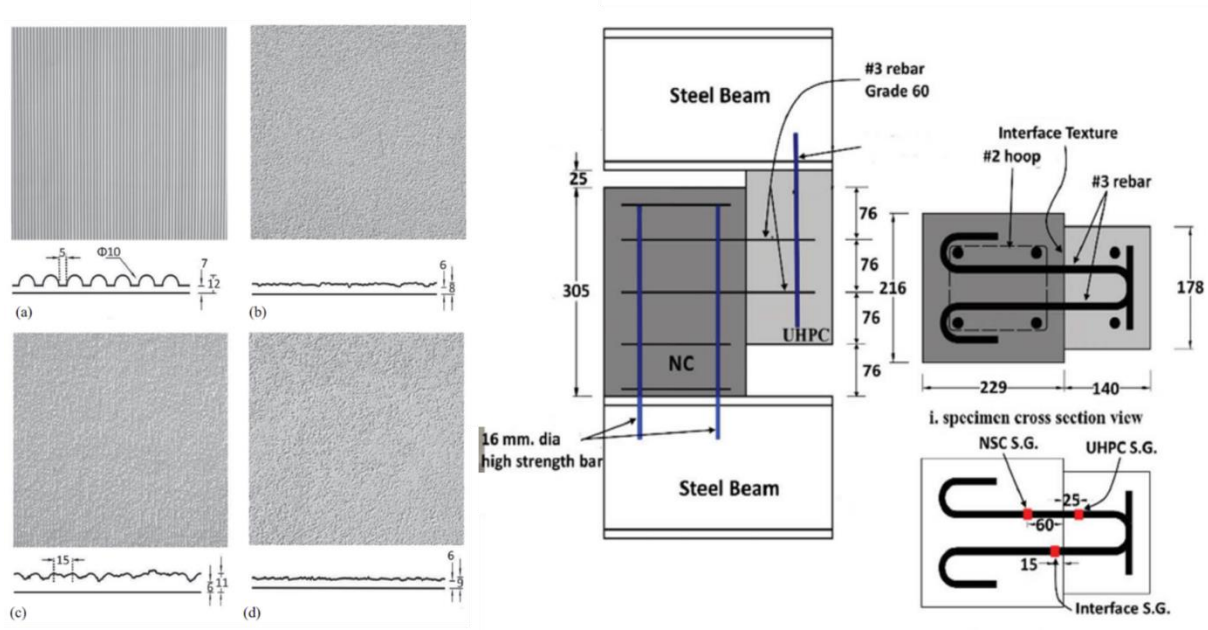


**Figure 2-13 Slant shear interface formliners and specimen dimensions used in (Sharma, Ronanki, Aaleti, & Okumus, 2021)**

Sharma et al. (2021) conducted a push-off test study of UHPC-NSC interface behavior, varying texture preparation and area of shear reinforcement crossing the interface. Form-liners were used to keep textures consistent from the nine total specimens, with depths of 5.08-mm (0.2-inch), 2.03-mm (0.08-inch), 4.83-mm (0.19-inch), and 2.80-mm (0.11-inch). Research showed that increasing texture depth and interface reinforcement ratio increased shear capacity, though this increase was not linear. Crane examined the bond behavior of monolithic UHPC and UHPC-HSC interfaces (Crane, 2010). Three interface conditions were used for the composite push-off test specimens: 6.35-mm (0.25-inch) texture made with a form-liner, a lightly roughened texture made from laying burlap on the interface, and a smooth left-as-cast interface. The shear strength for these specimens increased as depth increased. Additionally, Crane varied the amount of interface reinforcement and observed a linear increase in shear capacity when the reinforcement ratio was tripled.

A study focusing on UHPC-to-UHPC interface preparation and push-off specimen shear strength was conducted by Jang et al. (2017). This study was the first to explicitly examine UHPC-UHPC interface shear performance, with a focus on higher-depth textures. In addition to smooth interfaces, the study examined water-jetted interfaces, as well as 10-mm (0.39-inch), 20-mm (0.79-inch), and 30-mm (1.18-inch) square-grooved interfaces. Researchers discovered that the presence of fibers in the grooves greatly improved ductility at interfaces where the grooves were larger than the fiber length. Furthermore, as groove size increased, so did shear capacity.

Precast UHPC and cast-in-place (CIP) UHPC interfaces were studied by Semendary and Scevova (2021). Five textures using form-liners with mean depths ranging from 1.32-mm (0.05-inch) to 4.28-mm (0.17-inch) were tested in slant shear. Generally, the cohesion coefficient increased as texture depth increased, while the friction coefficient stayed constant. Muzenski et al. (2022) conducted an additional study of UHPC-UHPC interfaces. They proposed model for UHPC-UHPC interface shear behavior by combining experimental data from Crane (2010), with results from additional monolithic UHPC-UHPC interface specimens with interface reinforcement. The proposed modified coefficients for UHPC-UHPC interfaces, 9.8 MPa (1.4 ksi) for the cohesion and 1.0 for friction, with a shear capacity limit of 4.5 ksi for the overall interface (31 MPa).

# 3 DEVELOPMENT AND STRUCTURAL CHARACTERIZATION OF 12 in. and 14 in. UHPC ALTERNATIVE TO STEEL H-PILES

## 3.1 Introduction

In the ever-evolving landscape of construction materials, the emergence of Ultra-High-Performance Concrete (UHPC) has prompted a potential shift in foundation engineering. UHPC H-piles, in particular, have surfaced as an alternative to their steel HP-section counterparts, promising a fusion of new technology and sustainable design. This is fueled by several key attributes that position UHPC H-piles as a superior choice for modern structural foundations. One of the cornerstones of UHPC's appeal lies in its exceptional mechanical properties. With commendable compressive and tensile strength, UHPC can rival the load-bearing capabilities of steel sections, providing engineers with the freedom to design piles that match the strength of traditional steel piles with improved durability. Moreover, UHPC's mechanical properties enable cross-section optimization to keep pile weights within the range of steel sections, facilitating seamless integration into existing construction methodologies without compromising on performance.

The use of prestressing in UHPC H-piles can address a persistent issue faced by normal concrete piles—pile driving damage. The tensile driving stresses, coupled with the lack of tensile strength associated with conventional concrete often results in cracks and fractures at the pile head during installation. However, UHPC's exceptional tensile strength and flexibility, coupled with prestressing, mitigate these concerns, ensuring that UHPC H-piles maintain their structural integrity even under the rigors of pile driving. UHPC H-piles also possess better environmental resilience. Unlike steel piles, which are susceptible to corrosion and often require regular maintenance and protective coatings, UHPC's inherent durability and resistance to harsh environments lead to substantially reduced long-term upkeep requirements. UHPC requires a higher upfront material cost, but its resiliency can help keep the life-cycle costs of piles competitive with steel H-piles.

This chapter will discuss the development of two UHPC pile sections for use as an alternative to two of the more commonly used steel H-piles in current bridge foundation designs. First, the design process will be detailed, followed by descriptions of the pile fabrication at a local prestressing facility. Subsequently, materials and structural testing will be discussed, followed by the results and conclusions formed through this testing.

## 3.2 Section Design

This section focuses on UHPC H-pile design, specifically two sections: a 12-in. pile as a replacement for the HP12x53 steel pile and a 14-in. pile as a replacement for the HP14x89 steel pile. The HP12x53 and HP14x89 steel pile foundations were chosen as reference models while designing UHPC pile sections since they are two of the most regularly used steel pile foundations by DOTs today. The basic design objectives are to match the weight of steel piles, maintain similar dimensions for equipment compatibility, allow simple construction with current precast facility technologies, and provide equal load-bearing performance. Furthermore, the UHPC sections' shear strength should be sufficient to eliminate the necessity for transverse mild steel reinforcement. Despite the higher material cost, the absence of mild steel reinforcement will help keep long-term UHPC pile prices low. Aside from first principles analysis, the primary design process was performed similar to previous Iowa State University research (T. Vande Voort, 2008), where a 10-in. pile was developed to replace the HP10x57 steel pile.

### 3.2.1 Design Parameters

It was vital to establish the material properties of the proposed UHPC for the development of 12- and 14-in. prestressed UHPC piles before settling on cross-section details. A preliminary material study was carried out to attain the characteristic compressive strength, tensile stress-strain response, shrinkage properties, and development length of prestressing strand in UHPC, using methods that will be discussed in greater detail in Section 4.4. Based on these findings, the compressive strength and peak tensile strength of the UHPC for design purposes was determined to be 19.5 ksi and 1.25 ksi respectively. The overall stress-strain response of UHPC to be used for the design is shown in Figure 3-1.The standard stress-strain response for 270 ksi strands were used for the prestressing strand, which is a crucial component of these piles. Equations 3-1 and 3-2 depict these equations, and Figure 3-2 depicts the stress-strain curve for the prestressing strand.

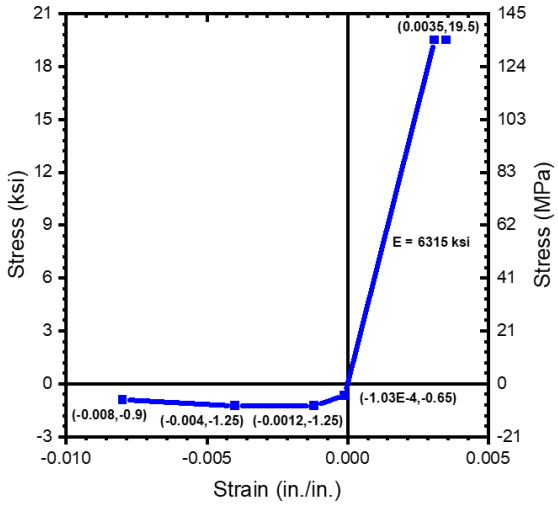


**Figure 3-1 UHPC stress-strain curves used in design.**

$$when\ \epsilon_{ps} \leq 0.0085, f_{ps} = 28500 * \epsilon_{ps} \quad \textbf{3-1}$$

$$otherwise, f_{ps} = 270 - \frac{0.04}{\epsilon_{ps} - 0.007} \quad \textbf{3-2}$$

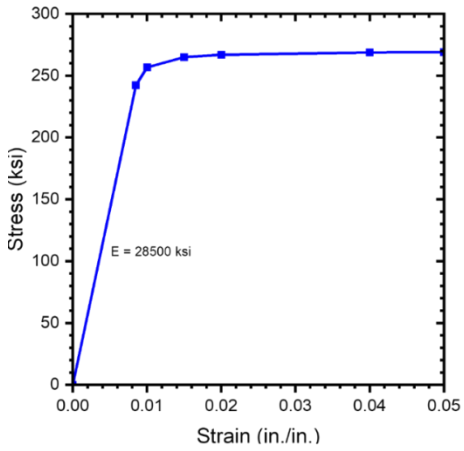


**Figure 3-2 Prestressing strand design stress-strain curve.**

After the determination of the material properties, the focus shifted to the cross-section shape. A solid square cross-section, similar to traditional precast/prestressed piles underutilizes UHPC's excellent compressive and tensile strength, as well as adds a significant weight to the pile section. Another UHPC pile type that was considered is one with a hollow circular or octagonal cross-section. Though this cross-section choice eliminates the underutilization of UHPC and addition of weight, the formworks are difficult to construct, and there may be issues with the core hollow formworks floating during mixing due to the UHPC head pressure, potentially resulting in the rejection of the pile at the precast plant. Demolding processes for hollow portions are also more labor-intensive compared to square cross-sections. Based on previous studies at Iowa State (T. Vande Voort, 2008), a tapered H-section was considered for the UHPC pile shape. An H-shape would aid in keeping the whole production process as simple as possible for precast/prestressed concrete producers.

One option for H-shape that was considered was a classic H-shape with straight flanges perpendicular to the web, as shown in Figure 3-3. However, this shape can cause a number of problems. Stress concentrations can build-up at web-to-flange intersections due to shrinkage. This shape makes demolding difficult and trapped air on the bottom flanges impossible to escape. However, the tapered H-shape alleviates these concerns. The inclination of the flanges reduces stress concentrations and provides a more natural channel for air to escape to the top of the forms. For all of these reasons, the tapered H-shape was selected for the 12 and 14-in. piles.

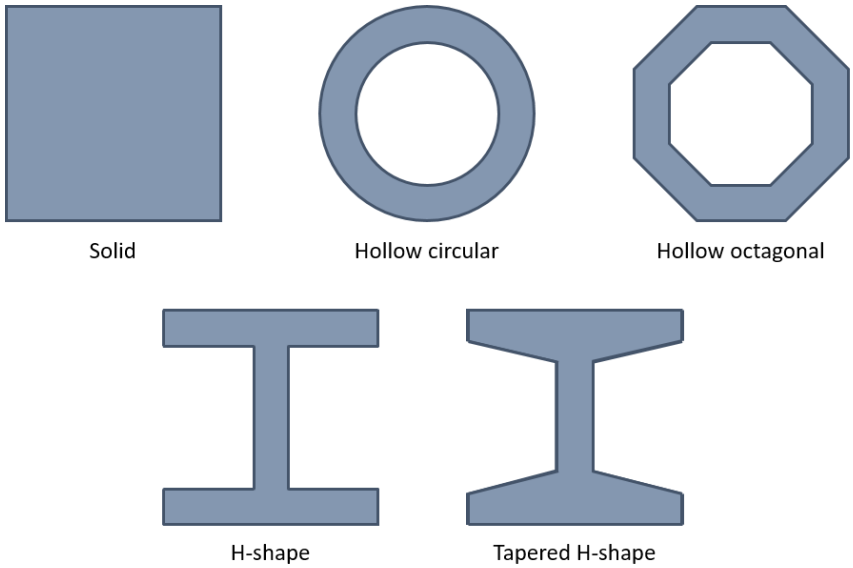


**Figure 3-3 UHPC pile shape options**

The nominal depth and width of the H-shapes were kept the same as their equivalent steel sections in the original design iteration of these piles, hence 12-in. by 12-in. and 14-in. by 14-in. As the designs were refined, it became clear that the flanges did not have to reach the whole width to attain adequate moment capacities. For this reason and to reduce the weight of the pile and volume of UHPC required, the flange widths were reduced to 10-in. and 13-in. for the 12-in. and 14-in. piles, respectively. The web widths have to be large enough for UHPC to flow around any web prestressing strands while simultaneously providing adequate cover. According to prior research on UHPC cover, 0.9-in. is the minimal amount of cover that has been demonstrated to be sufficient (T. Vande Voort, 2008). Prior casting experience suggested that 0.9-in. on either side of a prestressing strand would be adequate for UHPC flow, thus a 2.5-in. web was selected for the 12-in. pile. For the 14-in. pile, a

3-in. web was used since the 14-in. pile required more width for greater moment capacity. All strands received at least 0.9-in. cover in all directions on the flanges.

Standard 270 ksi, 0.6-in. diameter prestressing strands were used in the design to allow for greater prestressing of the section. The initial compressive stress on each pile increases with the increased prestressing. Tensile stresses during pile driving can often cause cracking in standard concrete piles, but with increased prestressing and tensile strength of UHPC, more driving energy can be introduced into the UHPC pile section prior to the onset of tensile stresses leading to cracking. To comply with standard precast and prestressed production process, a typical horizontal prestressing strand spacing of 2-in. was used. After interviewing a local precast producer, they agreed that guiding header plates could be utilized to construct any specific spacing as long as the strand spacing was not less than 2-in. The final cross-section details were thus finalized with all design criteria into consideration.

### 3.2.2 Final Section Details

Both pile sections were named with a similar convention as HP steel sections. The name of UHPC pile sections begins with UH, which stands for UHPC H-pile, and continues with the nominal section depth and weight in pounds per linear foot. Thus, the 12-in. pile, which weights 71 lb/ft, was named UH12x71, and the 14-in. pile was named UH14x105. Figure 3-4 shows the final cross-sectional details.

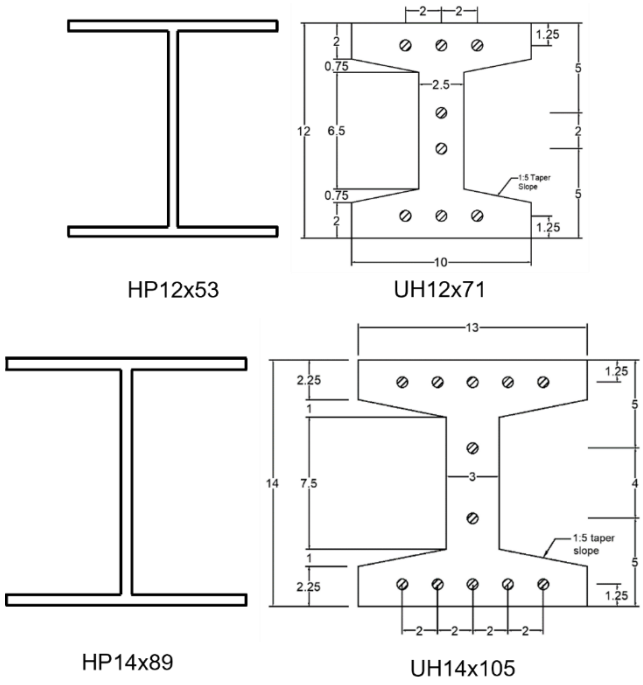


**Figure 3-4 UHPC pile sections compared to their steel pile counterparts.**

The overall dimensions of the UH12x71 are 12-in. by 10-in., with a 2.5-in. web. The UH14x89 measures 14 in. by 13 in. and has a 3-in. web. The sections use eight and twelve, 0.6-in. 270 ksi, respectively, stressed to 202.5 ksi, or 75% of the ultimate strand strength. Both pile sections were designed without any mild steel shear reinforcement, depending solely on UHPC. The initial prestressing on the concrete portion of the UH12x71 and UH14x89 is 5.36 ksi and 5.44 ksi, respectively, before any losses. Other important parameters for both UHPC piles and their HP

equivalent sections are shown in Table 3-1, including weight, cross-sectional area, and perimeter. The weight per linear foot of each UHPC pile is within 18 lb/ft, or 20% of the HP sections, with a significant increase in cross-sectional area, even if the perimeter is slightly less.

**Table 3-1: 12 and 14-in. UHPC pile and steel alternate properties**

| Property | HP12x53 | UH12x71 | HP14x89 | UH14x105 |
|---|---|---|---|---|
| Weight (lb/ft) | 53 | 71 | 89 | 105 |
| Cross-sectional Area (in$^2$) | 15.5 | 65.6 | 26.1 | 97 |
| Perimeter (in.) | 70.7 | 56.3 | 85.2 | 70.4 |

### 3.2.3 Section Analysis

To examine the moment-curvature and moment-axial interaction of the UHPC pile sections, a spreadsheet was created. The approach for each was based on first-principles concrete analysis, considering the tensile properties of UHPC. The stress-strain relationships in prestressed UHPC sections differ slightly from those in non-prestressed concrete sections. The variations are related to UHPC's tensile behavior and the influence of prestressing. Normal concrete has a very low tensile strength and is considered to have zero tensile capacity after cracking for analysis. Due to the sustained post-cracking tensile strength of UHPC is greater than zero, unlike traditional concrete sections, there will be contributions from UHPC in tension in the case of these piles, as shown in Figure 3-5. Prestressing alters the section analysis process by adding an initial compressive strain and stress to the system before application of any external loading. Because these strains cannot be discounted during loading, any strain profile will be a combination of the strain when just prestressing forces occur on the section and the strain owing to external load, as shown in Figure 3-5. Because there is no prestressing eccentricity in UHPC piles, the initial curvature is zero, and the system is subjected to uniform compressive strain and stress.

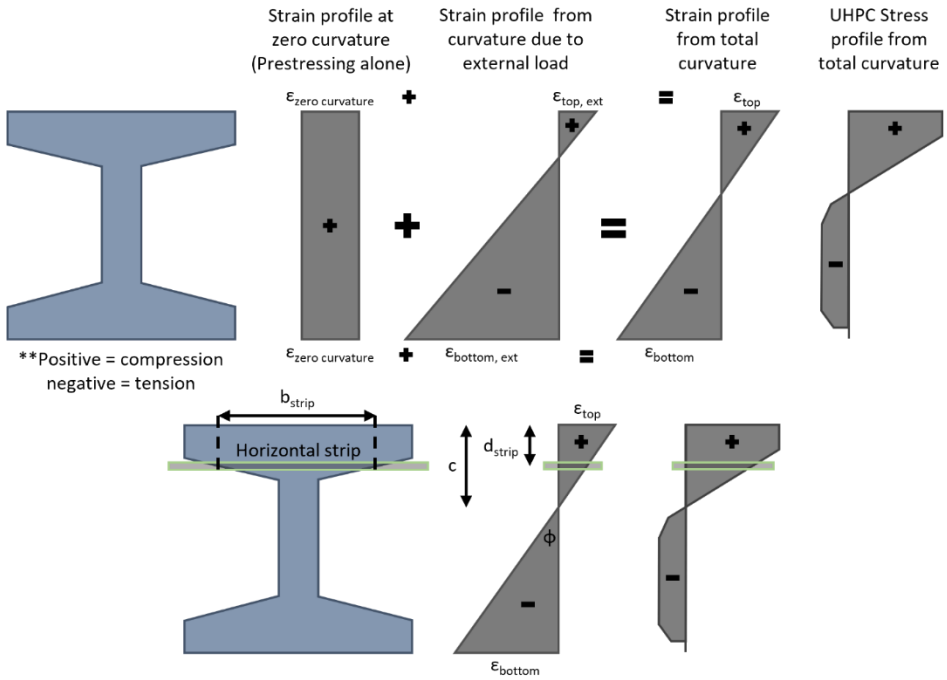


**Figure 3-5 Section analysis stress-strain profiles for concentrically prestressed members**

The flowchart in Figure 3-6 depicts the procedure used for estimating moment curvature, which begins by establishing the starting section state from prestressing alone, after deducting short-term losses. Early in the design process, before defined numbers could be used to account for short-term losses, 65 percent of the ultimate prestressing capacity, or 175 ksi, was used to represent the prestressing force after short-term losses. After pile fabrication was completed, as will be described in later portion of this chapter, the measured prestressing force after immediate elastic shortening losses was used for calculating the moment-curvature response. After the initial condition, a value for the top total compressive strain was chosen and a value for the corresponding neutral axis, c, was assumed. The curvature and strain profile along the member depth were calculated using the plane-sections remain plane assumption. A stress profile, similar to the one shown in Figure 3-5, could be generated based on this strain profile and the UHPC stress-strain behavior. The forces in the UHPC could then be computed using the stress-profile. The forces in the prestressing strands could be calculated by adding the stress corresponding to the strain caused by external loading and using the prestressing strands' stress-strain behavior. The assumed neutral axis depth could then be confirmed by using the equilibrium of system's internal and exterior forces. If the equilibrium was not achieved (i.e., total of forces did not equal zero), the neutral axis depth was adjusted, and the process was iterated until equilibrium was achieved. Once the equilibrium was achieved, the corresponding moment was calculated. The top strain was incremented to a next value and this process was repeated until the top strain reached the maximum compressive strain of UHPC. The section depth was separated into thin horizontal strips for analysis due to the non-uniform section shape, and the sum of the stresses and forces in these strips culminated in the overall forces in the section. Finally, as shown in Figure 3-7, the moment-curvatures for each pile in each bending direction were calculated. Based on the predicted moment-curvature response, each of these pile sections is expected to fail due to the crushing of UHPC in the compression region.

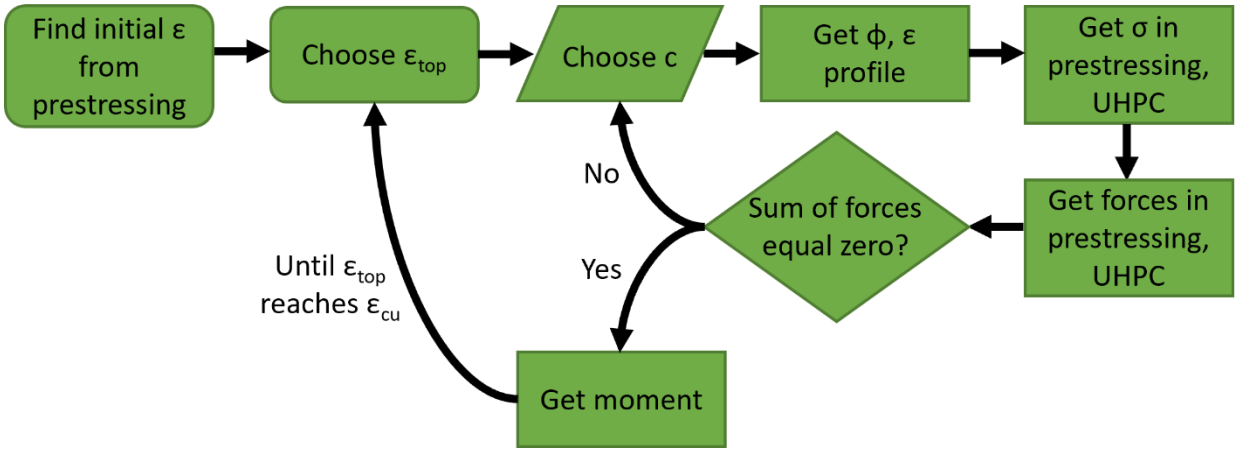


**Figure 3-6 Moment-curvature analysis flowchart**

Analyses for moment-axial interaction diagrams followed a similar approach. The top strain and neutral axis values are determined, but instead of iterating the neutral axis until the sum of the internal and external forces is zero, the external axial load was computed as the sum of the forces operating on the system. Other specific cases were investigated, such as pure flexure, in which the axial force is zero and the moment equals the maximum moment predicted for moment-curvature. The other particular situation was pure axial when the moment is zero and the pile is analyzed as a column.

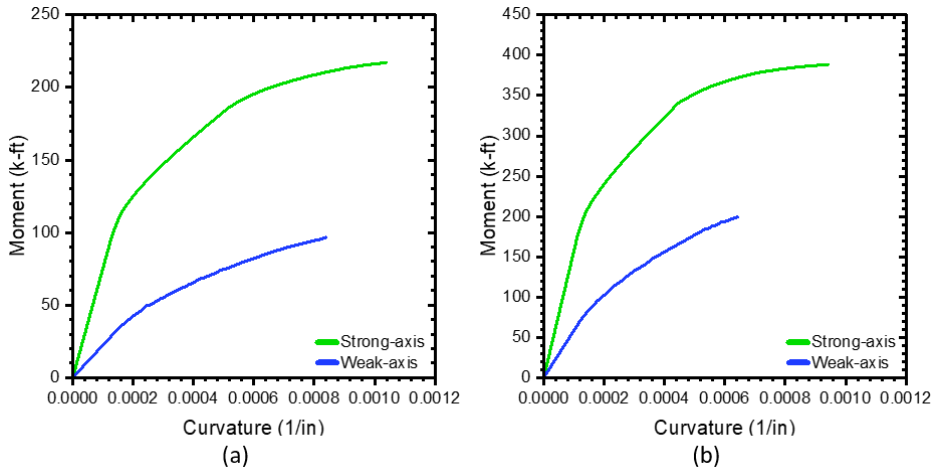


**Figure 3-7 Moment-curvature calculated in the design phase for a) UH12x71 and b) UH14x105.**

In both the strong-axis and weak-axis bending directions, the moment-axial interaction diagrams for each UHPC pile section were compared to their steel HP counterpart. Figure 3-8 depicts these interaction diagrams. In both cases, the HP sections have higher flexural capacity, but the UHPC sections have a larger axial capacity and overall envelope. This implies that a UHPC pile could be used in place of an HP pile if the axial and moment demands are inside the envelope using conventional methods.

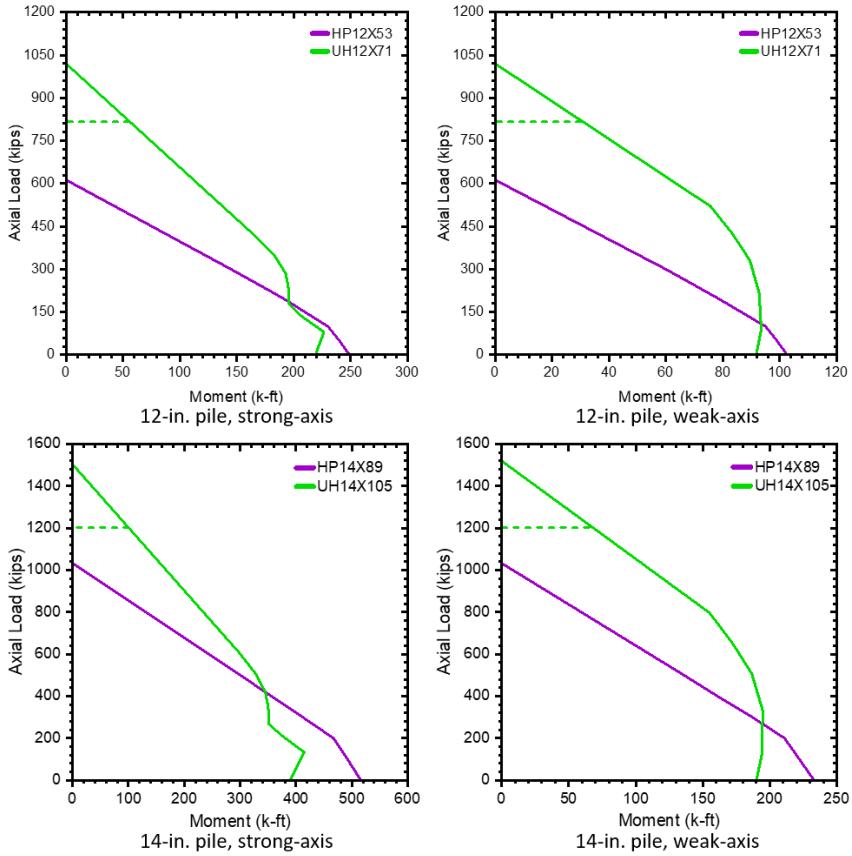


**Figure 3-8 Moment-axial interaction diagrams for UHPC UH and steel HP pile sections**

## 3.3 Pile Fabrication

A local precast producer in Pelham, Alabama, was selected to cast several UH12s and UH14s of varied lengths. The primary objective of the experimental program was to assess the flexural and shear behavior of each pile section along with their applicability in an abutment or pile bent. The secondary objective was to develop details for field splicing of these UHPC piles and assess the impact of the splice detail on the performance of the pile. To attain these objectives, two piles of each size were designated for each flexural and shear testing, one in strong-axis orientation and other in weak-axis orientation. Except for the 14-in. UHPC pile specimen for strong-axis orientation, all other pile specimens were 12-ft long. Preliminary structural analysis determined that a longer length of 20-ft was required for the 14-in. pile tested in strong-axis bending to ensure flexural failure before shear failure. The lengths chosen for the pile specimens also provided an opportunity to be reused for shear testing, if the damage during flexural testing was restricted to midspan. Two 14-in. piles and one 12-in. pile were chosen for abutment connections. The 12-in. pile was 12-ft long and the 14-in. piles were 12-ft and 14-ft long respectively. Six 6.5-ft long pile specimens with an embedded splice detail were chosen for evaluating the field-splicing and performance of spliced piles, which will be discussed in Chapter 6. These six piles with embedded spliced details would be welded together to form three 13-foot piles for testing.

Table 3-2 shows the nomenclature of the piles based on pile size, test type, and bending axis. The UH12x71 pile used for Flexural testing was designated as UH12FS for the Strong axis and UH12FW for the Weak axis. For the 14-in. piles, the strong-axis flexural pile was designated UH14FS, and the weak-axis flexural pile was designated UH14FW. The piles designated for abutment testing were designated with an A rather than a F for test-type, therefore they were designated as UH12AW, UH14AW, and UH14AS for 12 and 14-in. weak-axis abutment testing piles, and 14-in. strong-axis abutment testing heaps, respectively. Finally, the splice test piles were labeled with a S to indicate the test type. Strong-axis, weak-axis, and tensile piles were designated as UH12SS, UH12SW, and UH12ST, respectively. As the focus of this chapter pertains to the flexural and shear testing, only the instrumentation details for those four piles will be discussed, though the general casting of all 13 piles will be described here.

**Table 3-2 Pile testing names, sizes, and lengths cast.**

| Pile Testing Name | Section Size | Testing Type | Testing Axis | Length (ft) |
|---|---|---|---|---|
| UH12FS | UH12x71 | Flexural | Strong | 12 |
| UH12FW | UH12x71 | Flexural | Weak | 12 |
| UH14FS | UH14x105 | Flexural | Strong | 20 |
| UH14FW | UH14x105 | Flexural | Weak | 12 |
| UH12AW | UH12x71 | Abutment/Bent | Weak | 12 |
| UH14AS | UH14x105 | Abutment/Bent | Strong | 14 |
| UH14AW | UH14x105 | Abutment/Bent | Weak | 12 |
| UH12SS | UH12x71 | Splice | Strong | (2) 6.5 |
| UH12SW | UH12x71 | Splice | Weak | (2) 6.5 |
| UH12ST | UH12x71 | Splice | Tension | (2) 6.5 |

All piles were cast with a block-end as per the recommendations of the ALDOT project advisory committee and also to ensure no end-zone cracking during detensioning. Additionally, block-ends are not uncommon in driven piles on the end of the pile impacted by the hammer. Based on the expected prestressing transfer length of $24d_b$, or 15-in, the block-end was designed to be 9-in. long, with a 6-in. taper to the H-shaped portion. Three #3 stirrups were put in the block end every 3-in.

starting 2-in. from the end to prevent end-zone cracking, however later testing of these piles and other piles without this extra reinforcement revealed that the stirrups were unnecessary.

The instrumentation plan used for the flexural and shear test specimens was arrived at to achieve three primary objectives. First, verification of the transfer length of the prestressing strands. Second, quantifying the extent of prestressing losses experienced during detensioning and evaluating the applicability of standard first principles. Third, to capture the pile section responses (such as moment-curvature) during flexural and shear testing. A set of instruments that contained both foil gauges for measuring strains in prestressing strands and embedded gauges for measuring strains in concrete were used. A total of 13 internal strain gauges including 6 foil gauges, and 7 embedded gauges were installed in each flexural pile. Figure 3-9 depicts the schematic and nomenclature of each internal strain gauge.

Strain gauges were designated for the type of material strain measured, the strand depth at which the gauge was installed, and the order along pile length in which it was installed. C is for concrete embedded gauge, and S stands for foil strand gauge. T denoted the top strand level, M the middle strand level, and B the bottom strand level. As an example, the fourth concrete gauge on the pile, which is located on the top strand, would be designated as C4T. The majority of gauges were concentrated in the middle of the span.

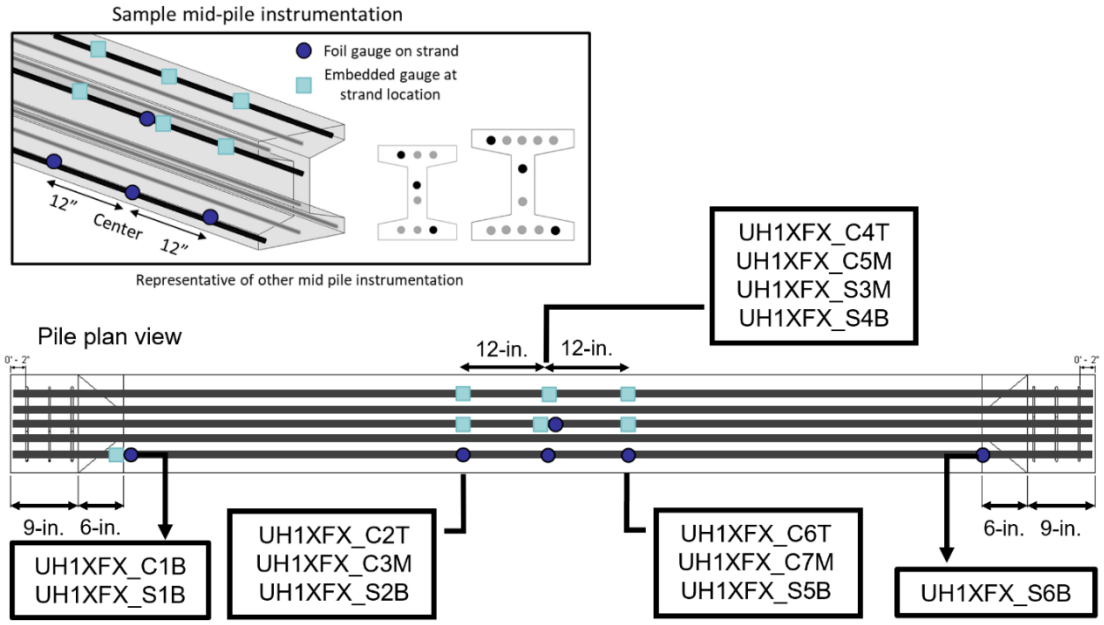


**Figure 3-9 Schematic of internal pile instrumentation**

Formwork construction at the precast plant began once the pile number, lengths, and instrumentation were determined. Figure 3-10a depicts formworks made entirely of plywood and assembled with nails and caulk to ensure any gaps were closed to avoid UHPC leakage. The UH12s and UH14s were cast side by side on the same prestressing bed. The inner side-forms were fastened to the prestressing bed, and each of the strands were pulled to an initial stress of 202.5 ksi, or 75% of their ultimate strand capacity. The internal strain gauges were affixed to the stressed strands before fitting the exterior side forms. The foil gauges used were 1-mm long, short enough to sit in the direction of the prestressing strand on a single wire without significant curvature.

Initial strain gauge readings were taken on the same day they were applied, three days before UHPC was cast. The concrete and strand gauges at midspan, as well as the gauges at transfer length, were the primary focus of the readings because they would provide the greatest information about elastic shortening losses. The next morning, wooden 2x4s were attached across the top of the forms at various positions along each pile's length. These 2x4s served two functions: one was to give bracing along the top of the piles, and the other was to hold pickup point threaded inserts for removing the piles after casting. In addition to the piles, formworks for ten direct tension, ten four-point bending, and twelve Double-Edge Wedge Specimens (DEWS) were built to characterize the tension behavior of UHPC. Three-by-six-inch (3x6) cylinders were also cast for compressive strength testing.

Prior to this project, the precast producer in Pelham had never worked with UHPC and did not have their own UHPC mix developed. As a result, a local UHPC supplier was consulted, and their UHPC was selected for the piles. The material was provided by the UHPC supplier, as was the high-shear mixer (Figure 3-10c). The UHPC used for these piles had a fiber content of 2.5 percent by volume. On pour day, October 21, 2021, 2.9 cubic yards were poured in three batches: two batches of two supersacks of dry mix (1.25 cubic yards each batch) and one batch of one supersack (0.63 c.y.). UHPC was mixed and tested by representatives from UHPC suppliers. The flow was tested in accordance with ASTM C1437 (2020). The mixed UHPC was discharged into a hopper bucket, which was forklifted to the prestressing bed's gantry crane. Figure 3-10b shows the hopper being mounted to the gantry crane and UHPC being poured into each of the formworks. This technique of pouring was chosen due to the uncertainty of whether the precast plant's standard buggy would fit beneath the discharge chute of the UHPC supplier's mixer.

Each formwork had UHPC placed at one end and allowed to flow to the other. The UHPC flowed through 2.5-in. webs with a 0.6-in. strand in the center with no evident difficulties. To assist any trapped air in rising to the UHPC surface, rubber mallets were used to strike the side forms. Pile surfaces were supposed to be finished using spiked rollers, however, voids on the finished pile surfaces suggest that proper surface rolling was not done by the construction crew during casting. A tarp was pulled over the prestressing bed once all piles were cast, some hours after pouring began. Material testing specimens were cast on-site in a small room, with half of each tension testing type coming from Batch 1 and the other half coming from Batch 2. There was no temperature control in this room, but the specimens were relatively protected from the outside temperatures. The first few nights following casting were unusually chilly, so propane heaters were mounted at each end of the prestressing bed and ran through the night until detensioning to try to keep temperatures around 75 F (24 C).

Readings for the same selected strain gauges taken prior to pouring of UHPC were taken one hour after casting of UHPC, in the evening. Several readings were also taken throughout the next day. Three cylinders for compressive strength were tested two days after casting. The average measured compressive strength was 13.9 ksi, which was adequate for detensioning. In preparation for demolding the formwork, air voids were discovered on the top surfaces of several piles, such as those depicted in Figure 3-10d. These air voids were most likely caused by insufficient rolling and failing to cover the piles with a tarp until all piles were cast, rather than covering each pile as it was completed. The voids were present on all pile surfaces, but were more severe on UH14FS, the 20-ft long pile used for the strong axis flexural pile.

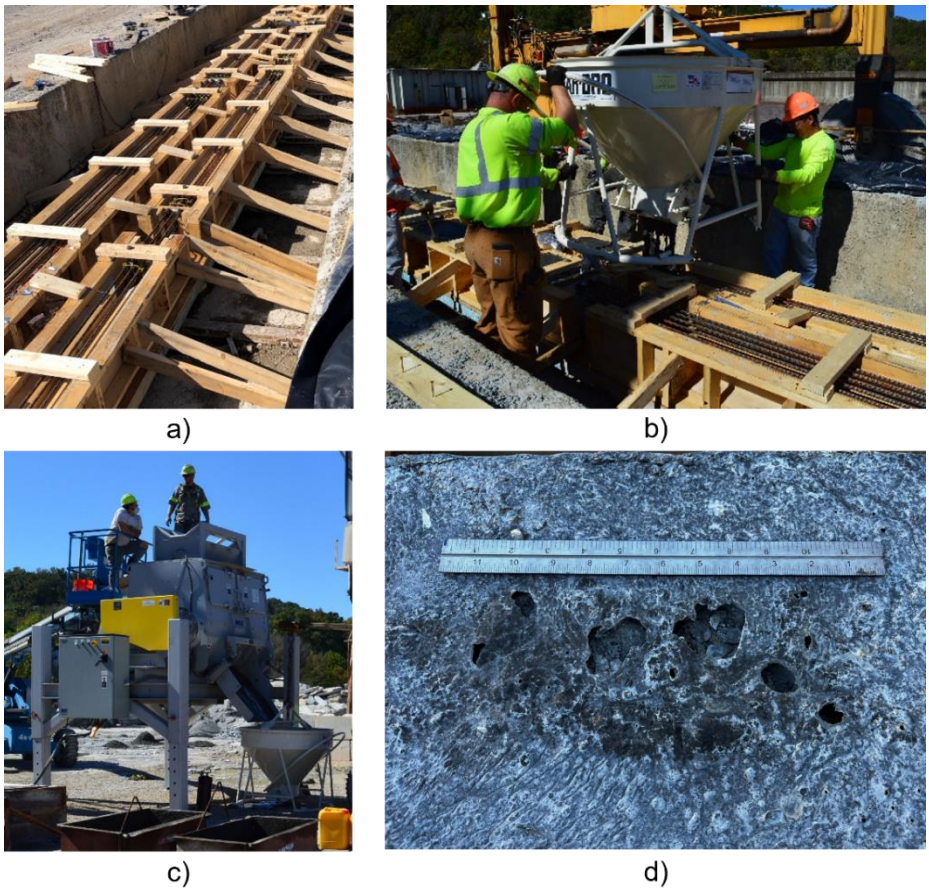


**Figure 3-10 Fabrication of UH12s and UH14s: a) wooden forms, b) UHPC poured with a hopper, c) high-shear mixer, d) voids on pile surface.**

The piles were detensioned at two days strength, with blowtorches used on each end of the prestressing bed to cut the strands at the bed ends, moving inward to the next set of strands until all strand connections between the piles were cut. The order of strands cut for each pile is shown in Figure 3-11. During this process, the select strain gauges continued to be monitored.

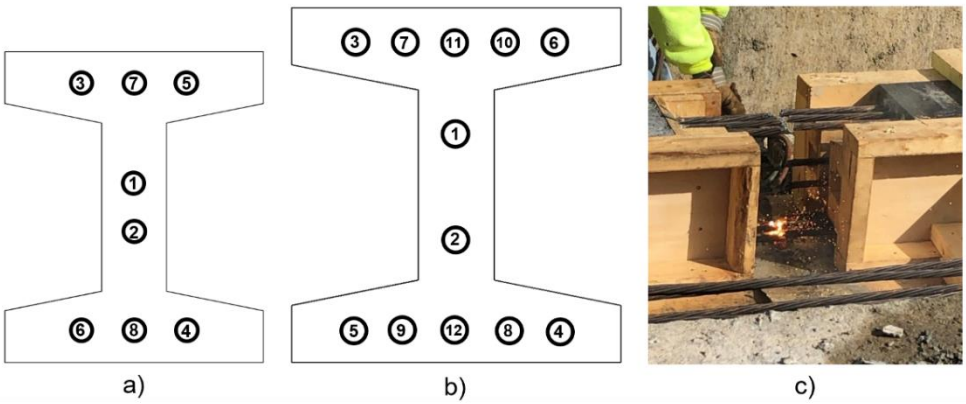


**Figure 3-11 Detensioning sequence for a) UH12x71, b) UH14x105, c) detensioning photo**

## 3.4 Material Properties

### 3.4.1 Compressive Testing

The compressive strength of UHPC was determined following standard procedures listed in ASTM C39 (2021) and modified ASTM C1856 (2017). Compressive testing was conducted for the first 28 days, and then on large-scale test days. Each time, three cylinders were tested, and the average compressive strength was recorded. The measured 28-day compressive strength was 21.5 ksi, with typical large-scale test day compressive strengths reaching 23 ksi, several months after casting. Figure 3-12 shows the variation of measured compressive strength with time.

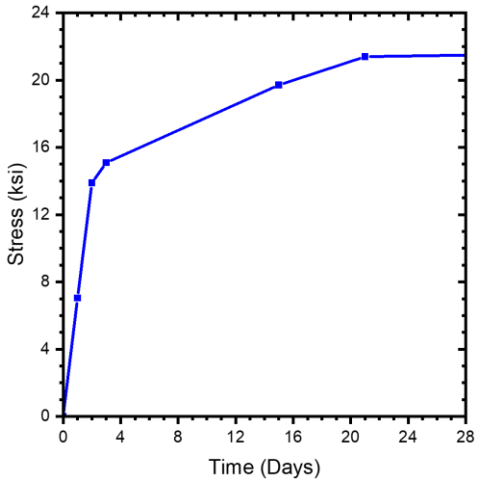


**Figure 3-12 Measured compressive strength over time.**

### 3.4.2 Modulus of Elasticity

For this UHPC, modulus of elasticity testing was performed at two different times. The first testing was done one day after strand detensioning, and the second testing was performed when large-scale testing was performed, several months after casting. The first testing value represents the elastic modulus at release. The modulus could not be tested until one day after detensioning due to time constraints. Both moduli of elasticity were tested in accordance with ASTM C469 (2022), which was modified for UHPC in accordance with C1856 (2017). Figure 3-13 depicts a photograph of the test setup. At three days, the modulus of elasticity was 6052 ksi. Later, the modulus of elasticity was determined to be 6974 ksi. These values are consistent with the current accepted AASHTO specifications equations for modulus of elasticity, which will be discussed in more details in Section 3.6.1.

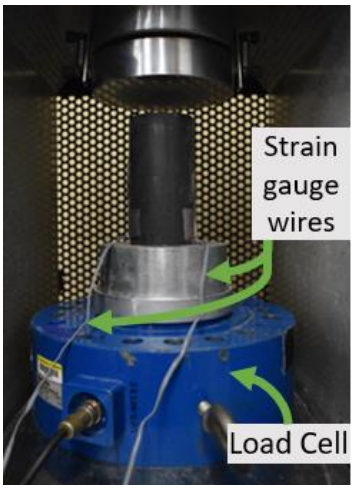


**Figure 3-13 Modulus of elasticity test setup**

### 3.4.3 Tensile Testing

Tensile strength of the UHPC was determined using three different types of tests: direct tension (DT), four-point bending (4PB), and double-edge wedge splitting (DEWS). AASHTO currently accepts direct tension as a standard for UHPC. This test directly measures tensile behavior by pulling each end of a standard rectangular prism with a 2-in. square cross-section. Four-point bending indirectly provides tensile behavior via strains induced in the bending of small prisms. DEWS also indirectly measures tensile behavior by compressing a notch in a square prism.

#### 3.4.3.1 Direct Tension Test

Direct Tension (DT) testing was carried out in accordance with AASHTO T397 (2022), using 2-in. by 2-in. by 17-in. prisms. Prior to testing, tapered aluminum plates were epoxied to the parallel faces of the specimen's ends. An MTS machine performed a fixed-end, uniaxial, displacement-controlled test, gripping each end of the specimen at a consistent pressure between 2.03 and 3.62 ksi. The MTS measures load and platen displacement, but specimen displacements were recorded using non-contact LED position trackers. Figure 3-14 shows the test setup and instrumentation. A special gripping technique was used because specimen gripping can generate tensile or compressive forces on the DT specimens before testing begins. The bottom end of a specimen was initially gripped tightly. The top end was then slowly gripped, and as the MTS force readings changed, the platen was moved in 0.01-mm increments to keep the force as close to zero as possible. Because UHPC's cross-section and elastic tensile limit are relatively low, this gripping procedure was critical to ensuring that no premature cracking occurred prior to testing.

LED displacement trackers were used to capture displacements on the specimen rather than the traditional system of extensometers. Prior testing at the University of Alabama (Bridi Valentim, 2023) indicated that LED and extensometer results were comparable. The specimen strains in the gauge length zone between the two tapered aluminum plates were calculated using the LED displacements. Displacement-controlled loading was performed at a rate of 0.0001 in./s until localization, when the displacement rate was increased to 0.001 in./s. The test was terminated when the isolated crack had expanded to at least 1/16-in., corresponding to a strain of about 0.015. On these specimens, localized cracks appeared at the gauge length between the two gripping plates or just above the gauge length at the extreme end of the gripping plates in the transition zone.

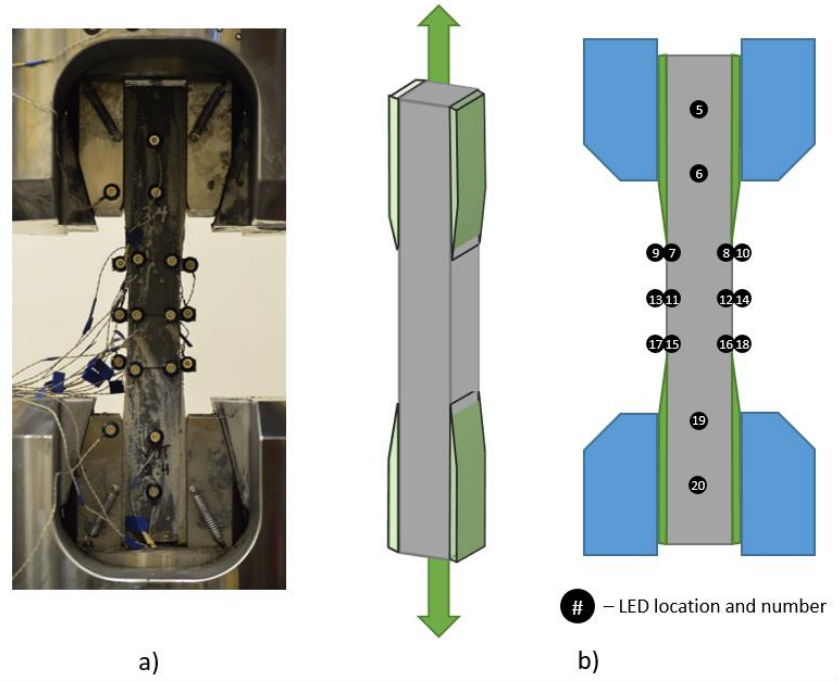


**Figure 3-14 Direct tension test setup and instrumentation**

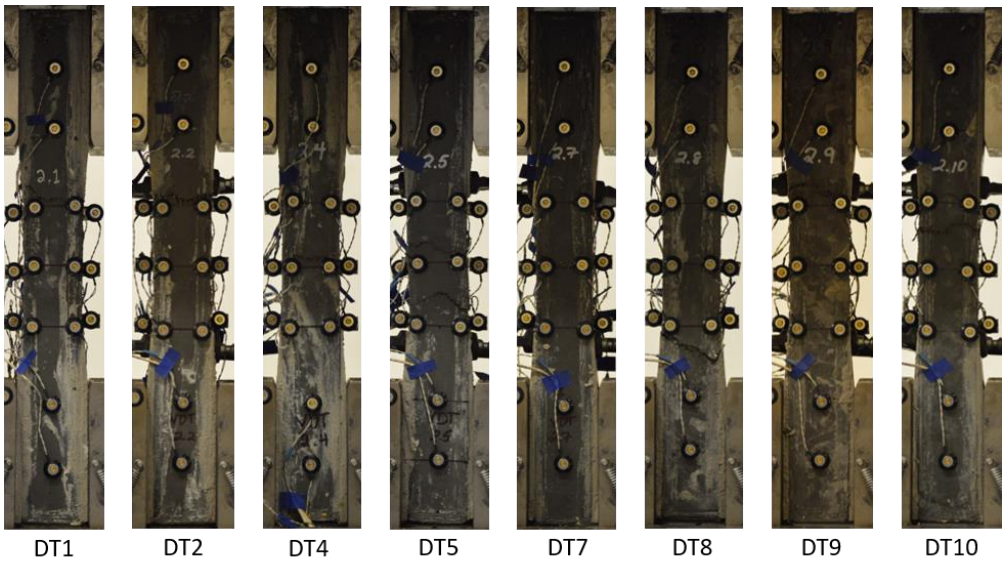


**Figure 3-15 Direct tension specimens after testing**

Two specimens, DT3 and DT6 were not tested. Due to a fabrication issue, DT3 was slightly too wide to fit in the MTS grips with plates in either direction. DT6 was not tested because the UHPC substrate beneath the plates cracked and failed during the gripping process. This manifested as a crack running the length of the gripping plate. Specimens DT 1 to 5 were from Batch 1, and DT 6 to 10 were from Batch 2. Because one specimen from each batch was disqualified, it was determined that the test integrity was still intact with 8 viable specimens. Figure 3-15 depicts each specimen after testing, and Figure 3-16 depicts a schematic of the crack locations for each tested specimen.

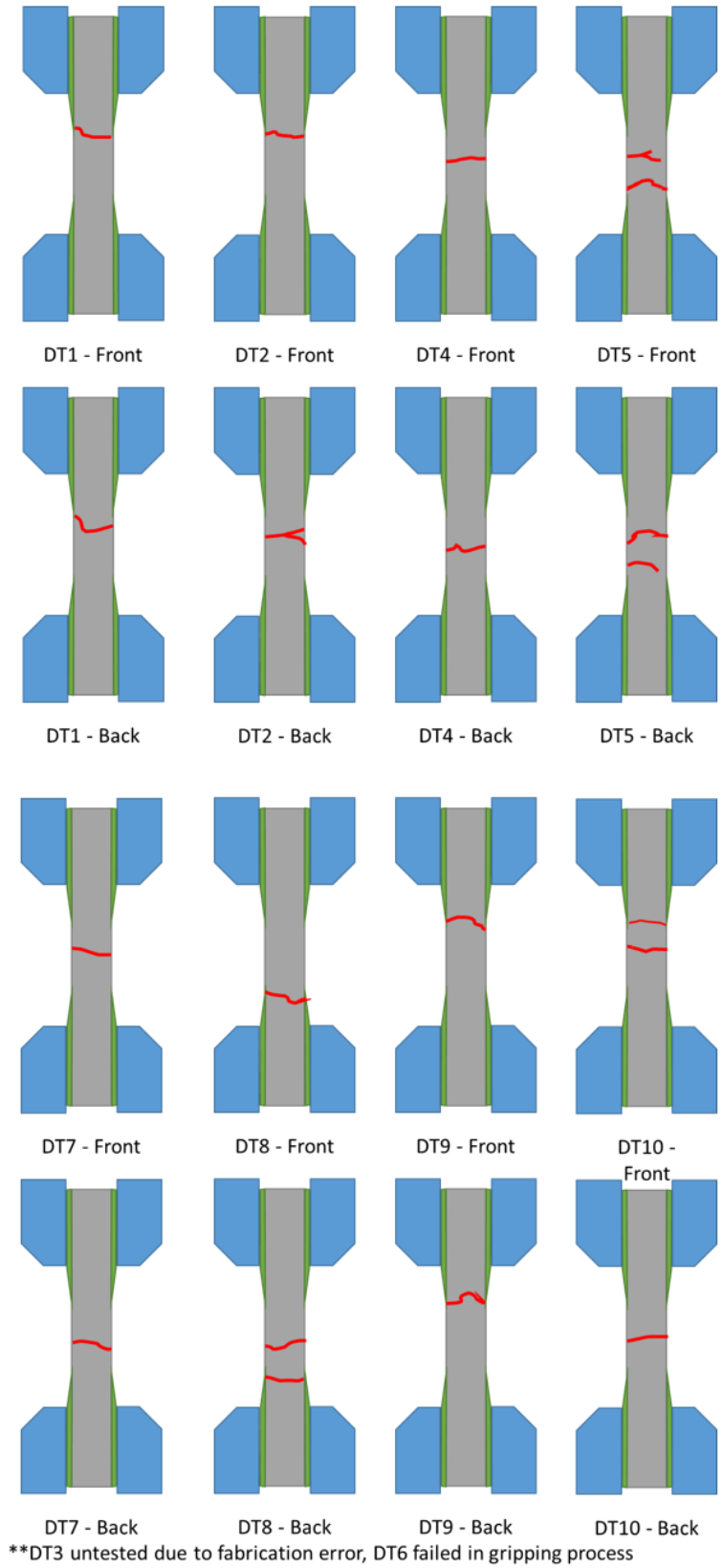


**Figure 3-16 Direct tension test crack schematics**

For each test, data was transformed into stress-strain curves. The stresses were calculated for each specimen using the force from the MTS machine and the average cross-sectional area along the gauge length as measured with a caliper. Tensile strain was calculated by averaging the strains of the LEDs paired at the gauge length ends on each corner, i.e., LEDs 7 and 15, 8 and 16, 9 and 17, and 10 and 18. The localization strain was identified for each curve as the point after which the stress consistently decreases. The strains used for localization ranged from 3900 to 8900 microstrains, with an average of 6200 microstrains. Peak stresses varied between 1.16 and 1.76 ksi, with an average of 1.40 ksi. Each batch has specimens on either side of the average curve, indicating that the fiber distribution and strength are similar.

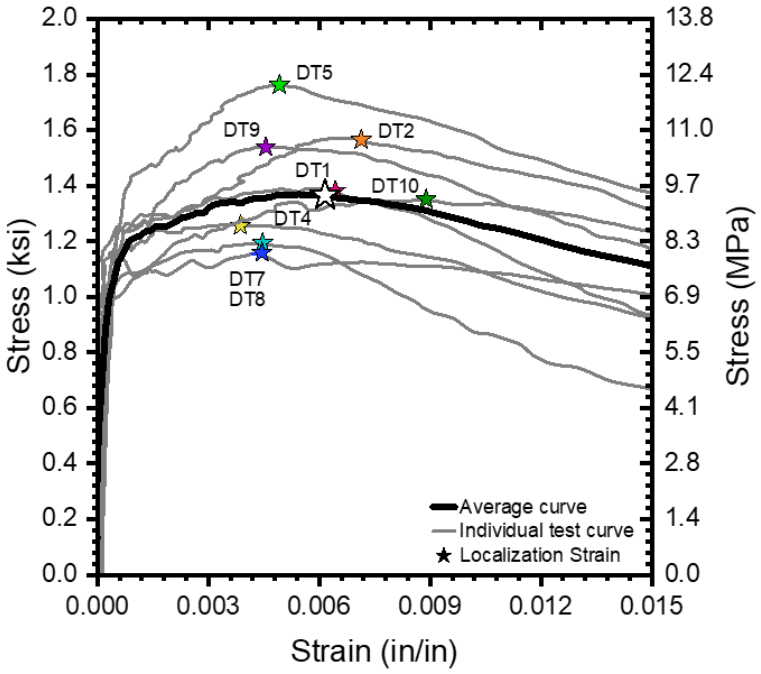


**Figure 3-17 Stress-strain curves for all direct tension specimens**

### 3.4.3.2 Four-Point Bending Test

Four-Point Bending (4PB) prisms measured 3 in. by 3 in. by 14 in. Each prism was simply supported on 12-in. rollers, and the compressive load was applied to two 4-in. rollers on top of the beams. The MTS machine measured the force and platen displacement. A system of LEDs tracked the displacements on the specimen. Figure 3-18 depicts this experimental setup, including LED numbers.

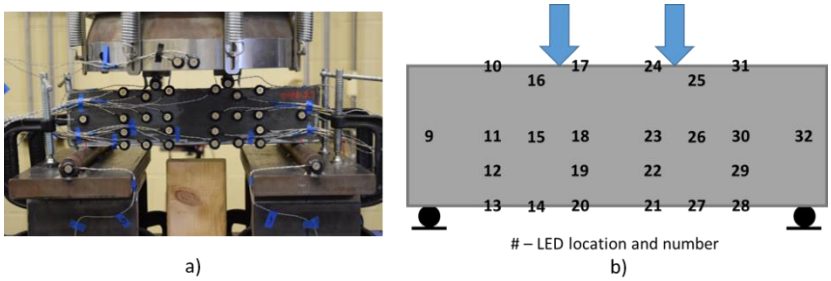


**Figure 3-18 Four-point bending a) test photo and b) instrumentation schematic.**

Ten tests were carried out, with five beams from the first batch of UHPC, 4PB-1 through 4PB-5, and the remaining five from the second batch of UHPC, 4PB-6 through 4PB-10. The main localized crack occurred within the constant moment region at midspan for most specimens, but for three specimens, 4PB-4, 5, and 6, the crack localized under the load-application roller, at the edge of the constant moment region. For 4PB-4 and 4PB-6, the crack extended beyond this region on the back side of the specimen, indicating shear failure. As a result, the results of these tests were not included in the final results and averages. Figure 3-19 depicts the tested specimens, while Figure 3-20 depicts schematics of each specimen with localized crack locations.

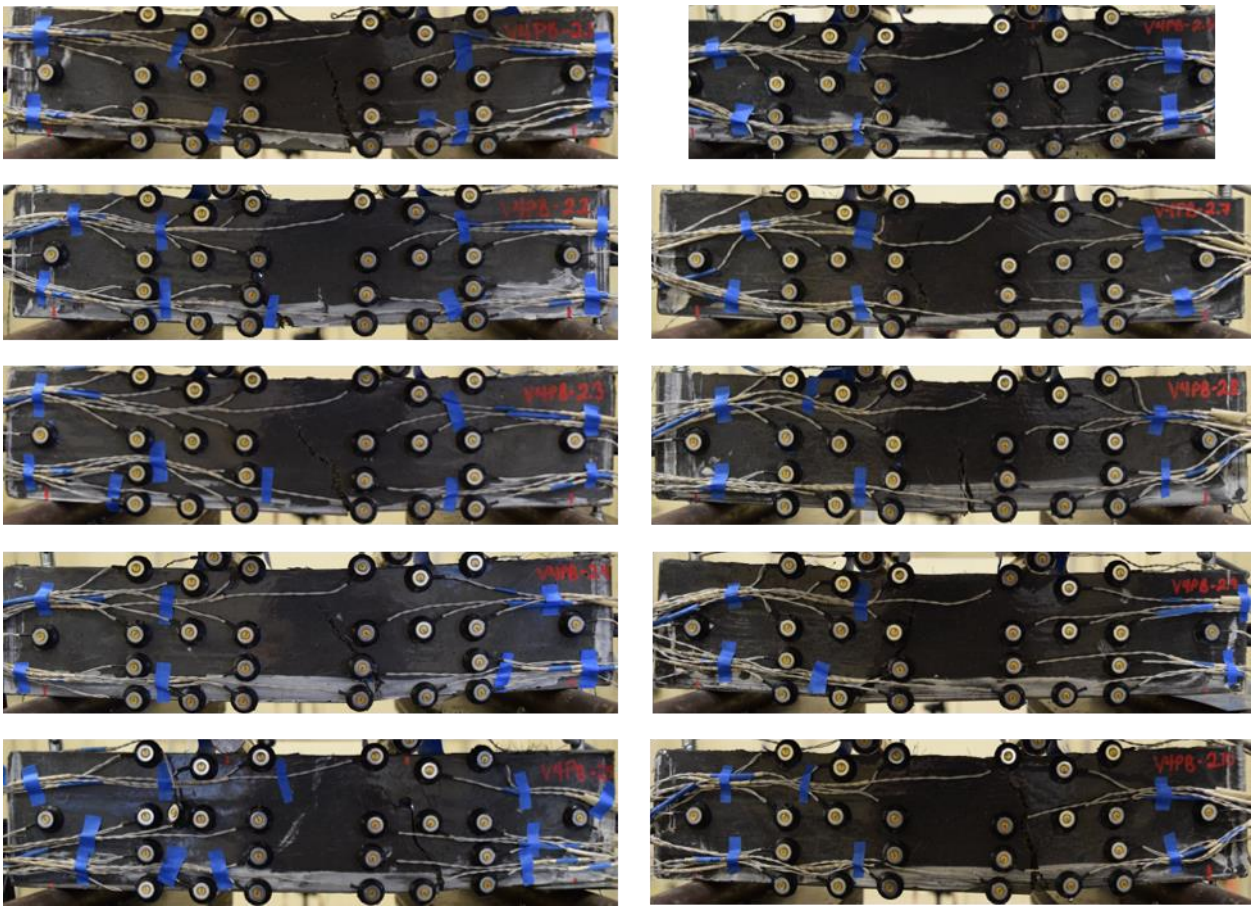

**Figure 3-19 Four-point bending specimens after testing**

Inverse analysis was used to generate tensile stress-strain curves from force and displacement data. The force and span length were used to calculate the amount of moment acting in the constant moment region. Horizontal pairs of LEDs were used to calculate strain at different heights along the specimen, culminating in strain profiles and curvature throughout the test. After that, the experimental moment-curvature curve was compared to one calculated using material properties. Tensile properties were calibrated until the two curves for each specimen matched. Figure 3-21 depicts these curves.

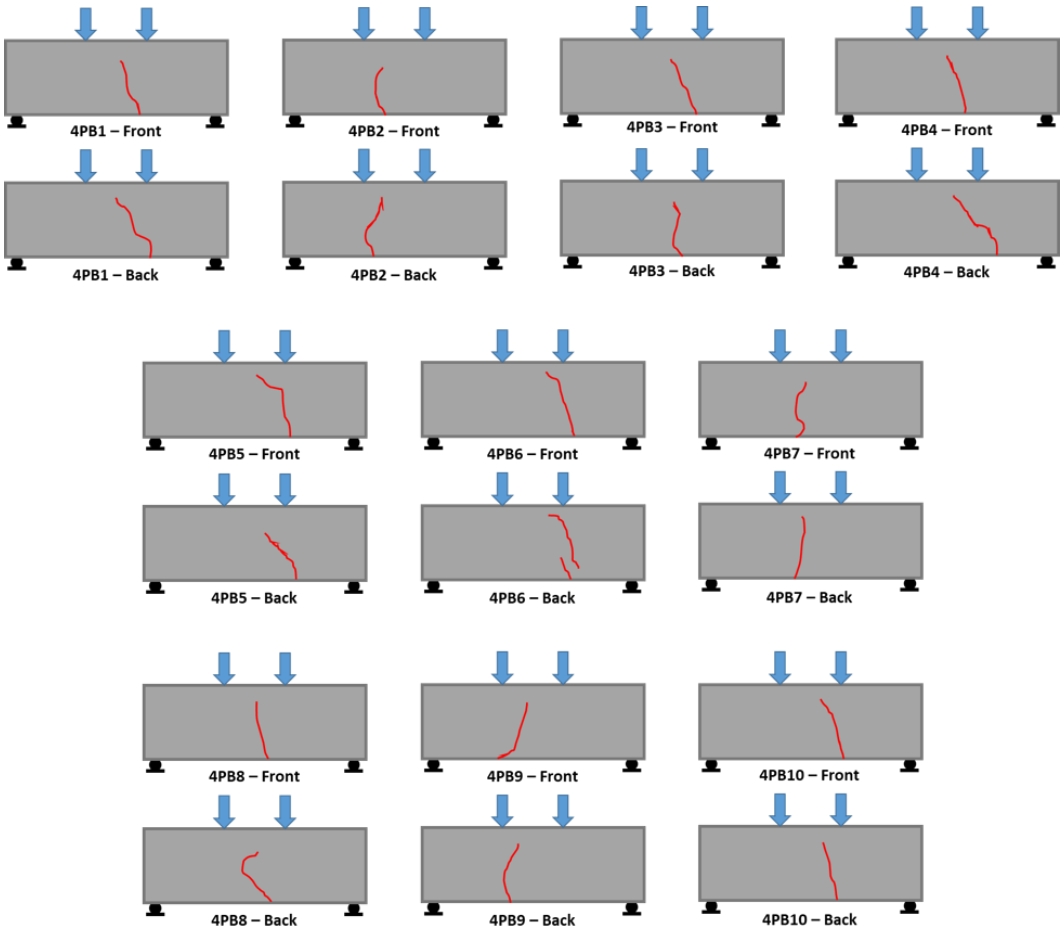


**Figure 3-20 Four-point bending specimen crack schematics.**

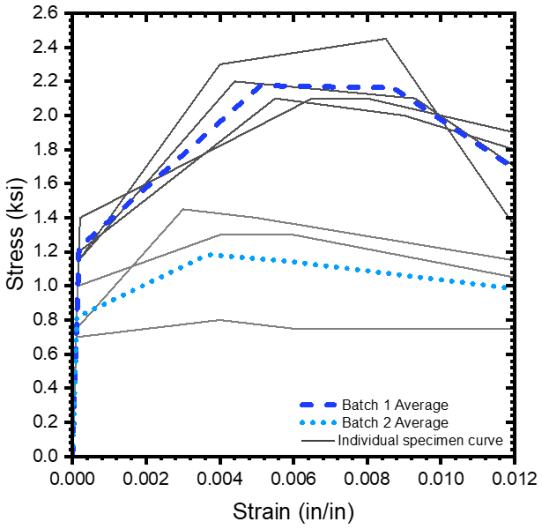


**Figure 3-21 Tensile stress-strain curves back-calculated from four-point bending tests.**

These stress-strain curves show a clear trend. The peak stress range for Batch 1 was 2.1 ksi to 2.45 ksi, while the range for Batch 2 was 0.8 to 1.45 ksi. There were no geometry irregularities or other explanations for this difference in testing, so the specimens were cut to get a sense of the fiber

distribution. Visual inspection, shown in Figure 3-22, found that there was fiber settlement as well as fewer fibers in Batch 2 compared to Batch 1. The fiber counts in Table 3-3 support the visual inspection findings. Batch 1 specimens had an average of 3512 fibers, while Batch 2 specimens had an average of 2780 fibers. A two-sample t-test was performed on the two batches to determine if their averages were statistically equivalent. The difference between the two batches is statistically significant at a significance level of 0.05, with a p-value of 0.00048.

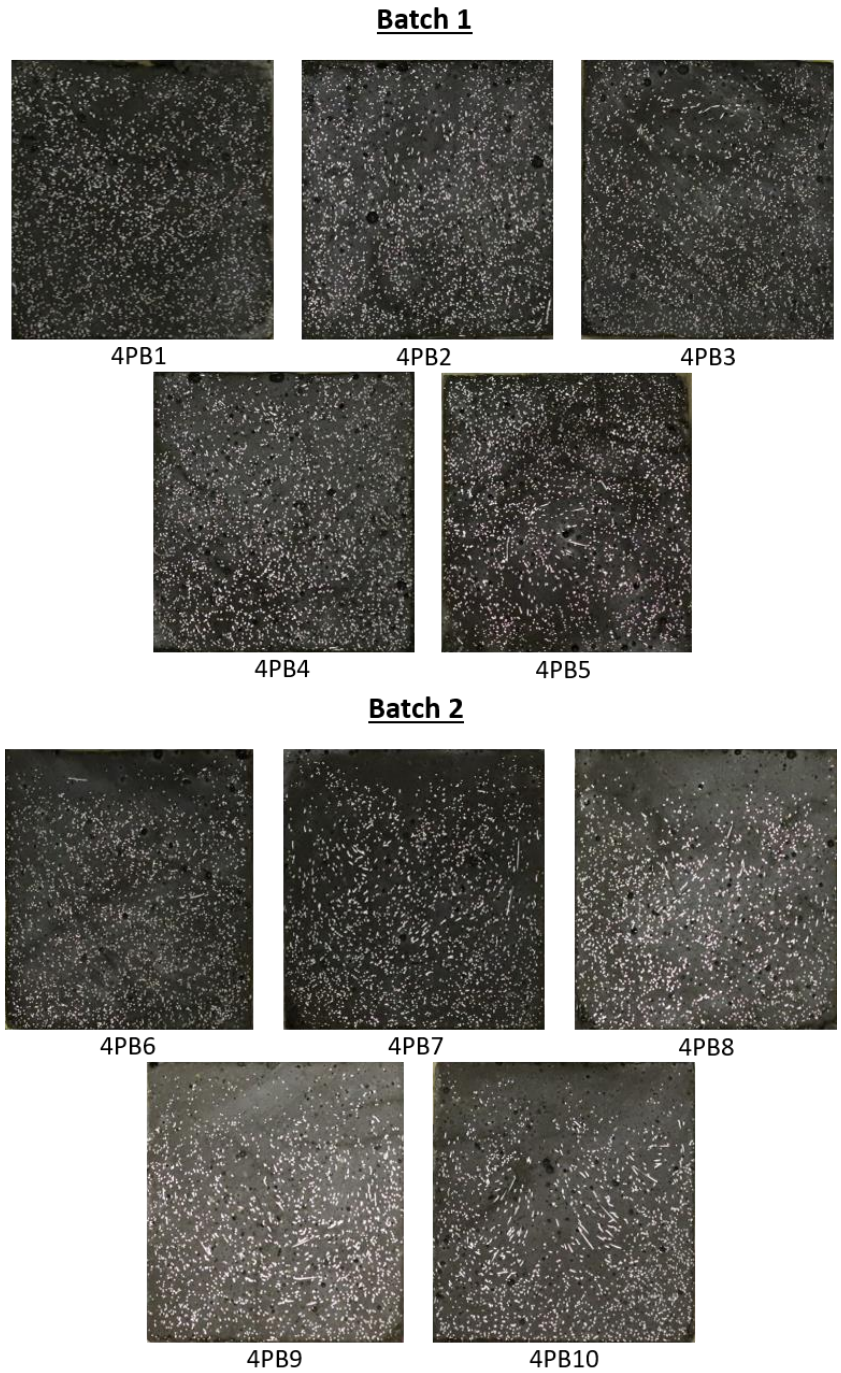


**Figure 3-22 Four-point bending cut cross-sections.**

**Table 3-3 Fiber counts for four-point bending specimens.**

| Batch 1 | | Batch 2 | |
|---|---|---|---|
| Specimen Name | Fiber Count | Specimen Name | Fiber Count |
| 4PB-1 | 3276 | 4PB-6 | 3049 |
| 4PB-2 | 3492 | 4PB-7 | 2753 |
| 4PB-3 | 3407 | 4PB-8 | 2485 |
| 4PB-4 | 3832 | 4PB-9 | 2842 |
| 4PB-5 | 3552 | 4PB-10 | 2769 |

### 3.4.3.3 Double-Edge Wedge Splitting (DEWS) Test

The Double-Edge Wedge Splitting (DEWS) test is a less common way of determining the tensile behavior of fiber-reinforced concrete. These specimens were cast in a long rectangular prism before being cut into individual specimens. The advantage of this test was that the prisms could be poured to mimic the dimensions and flow of the pile flange and webs. To that end, the Batch 1 prism measured 2-in. by 6.5-in. by 42-in., while the Batch 2 prism measured 2.5-in. by 6.5-in. by 42-in. The UH12s' flange depth and web width are represented by the 2-in. and 2.5-in. dimensions, respectively. Using a tile saw, each prism was cut into six 6.5-in. by 6.5-in. squares. The specimen was then prepared by cutting two V-notches and pre-cracks into each square prism, as shown in Figure 3-23. Because of notch-cutting issues on one specimen from each batch, DEWS-1 and DEWS-8, those specimens were not tested.

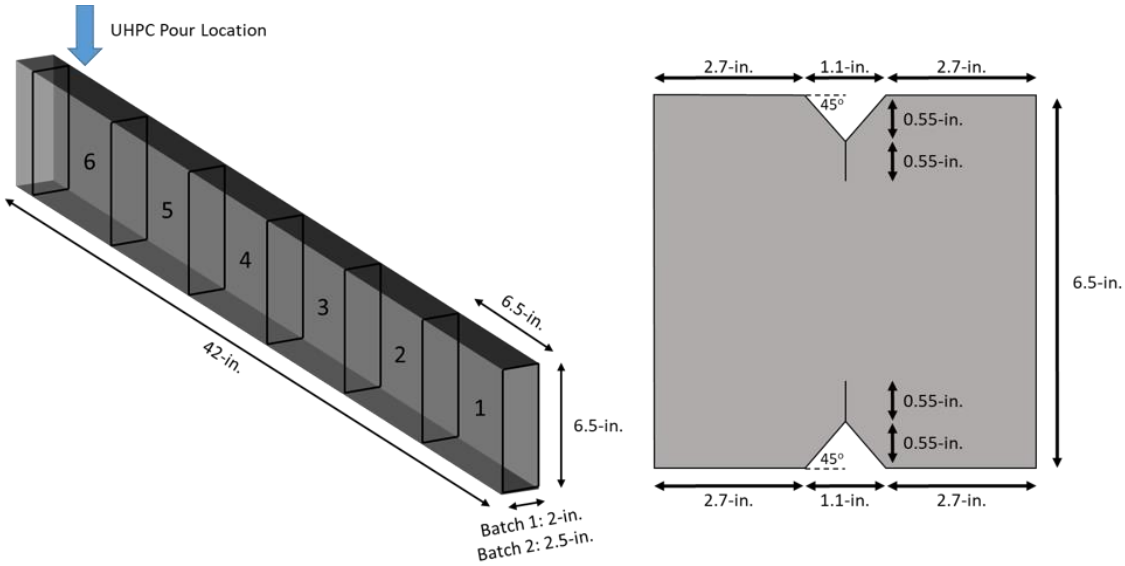


**Figure 3-23 DEWS specimen dimensions**

The two V-notches were compressed with steel rollers by an MTS machine. Figure 3-24 depicts the overall test setup. This compressive force generated tensile stress in the direction of the pre-cracks, which widened as testing progressed. To reduce friction between the specimen and the rollers, grease was applied to the V-notches and the rollers, and a laser level was used to ensure the force line of action between the two rollers was vertical. During testing, the crack always began at the top of the pre-crack V-notch. The crack propagated vertically as loading progressed, though it did sometimes deviate horizontally, taking the path of least resistance through the UHPC, as shown in Figure 3-25.

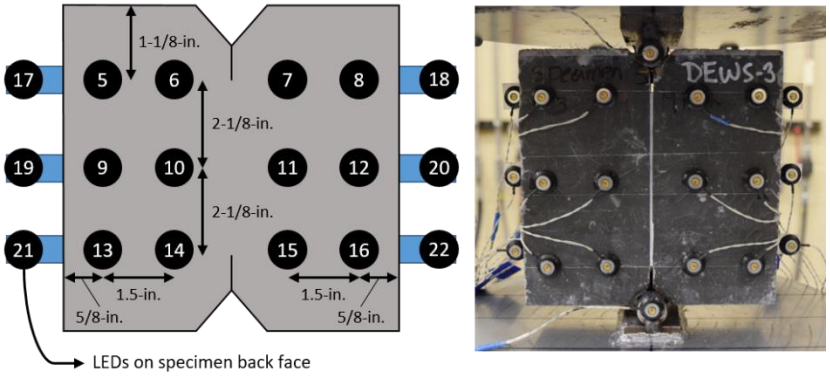


**Figure 3-24 DEWS test setup and instrumentation**

The MTS machine measured force and platen displacement, while the specimen displacement was measured using a system of LED displacement trackers, as shown in Figure 3-24. The average strain across the localized crack was calculated using the paired LEDs, and the stress was calculated using the force and specimen geometry, defined as the length between the two pre-cracks multiplied by the depth of the specimen. Figure 3-26 depicts the stress-strain curves for each specimen. As with the previous 4PB tests, there is a difference in the results from Batch 1 and Batch 2, with average peak stresses of 1.8 and 1.2-ksi, respectively.

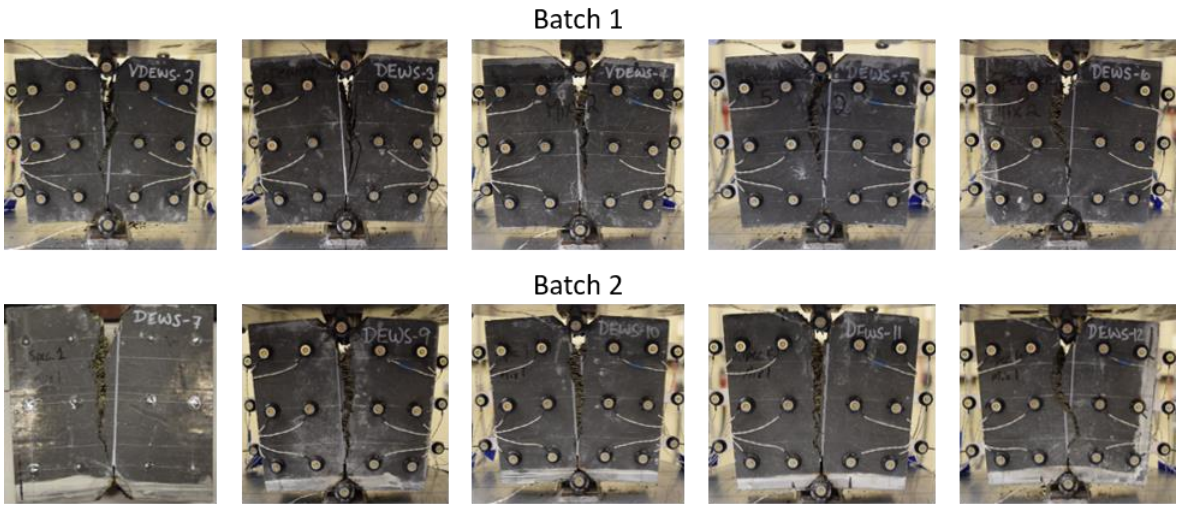


**Figure 3-25 DEWS specimens after testing**

Following the completion of testing, specimens were cut adjacent to the crack location and fiber counts were performed. Similar to the 4PB specimens, there was fiber settlement and fewer fibers in Batch 1 compared to Batch 2, though the difference was not as severe. Because the two batches contained specimens of varying sizes, the fiber percent by area was compared rather than the number of fibers. The fiber percentage for each specimen is shown in Table 3-4, and the cut cross-sections are shown in Figure 3-27. A two-sample t-test was run at a 0.05 significance level, and the two batches were found to be statistically different, with a p-value of 0.014.

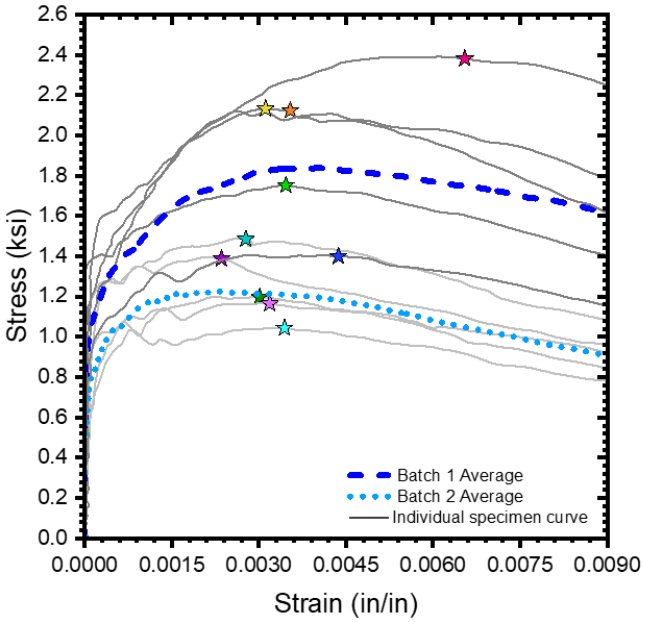


**Figure 3-26 DEWS stress-strain curves**

**Table 3-4 DEWS fiber percentage by area**

| Batch 1 | | Batch 2 | |
|---|---|---|---|
| Specimen Name | Fiber % by area | Specimen Name | Fiber % by area |
| DEWS-2 | 2.35 | DEWS-7 | 1.82 |
| DEWS-3 | 2.48 | DEWS-9 | 1.89 |
| DEWS-4 | 2.59 | DEWS-10 | 1.92 |
| DEWS-5 | 2.16 | DEWS-11 | 2.07 |
| DEWS-6 | 2.05 | DEWS-12 | 2.02 |

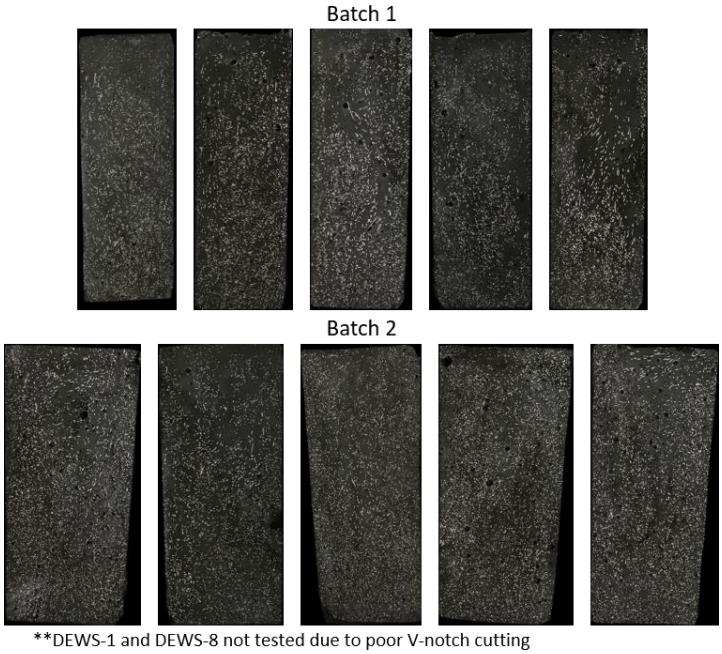


**Figure 3-27 DEWS cut cross-sections.**

#### 3.4.3.4 Idealized Tensile Behavior for Section Analysis

Following experimental material testing, idealized tensile stress-strain curves were developed for use in section analysis. Based on the previous sections, the results from the two batches for 4PB and DEWS differed in terms of fiber amount and fiber settlement. The results of the direct tension test did not have this issue. This could be because 4PB and DEWS find tensile behavior via flexural action, whereas direct tension applies tensile action directly. Flexural action causes a portion of the cross-section to be in tension while the rest is compressed. Tensile capacities found through flexural action then may be more greatly influenced by differences in fiber distribution.

The average curves for each tension test are shown in Figure 3-28. For 4PB and DEWS, an average curve was created for each batch. Direct tension falls between the other two test types, and because no fiber distribution issues were observed between the two batches, this test type was chosen to form the idealized tensile behavior curves. Furthermore, the direct tension test is the only AASTHO-accepted method for determining UHPC tensile strength.

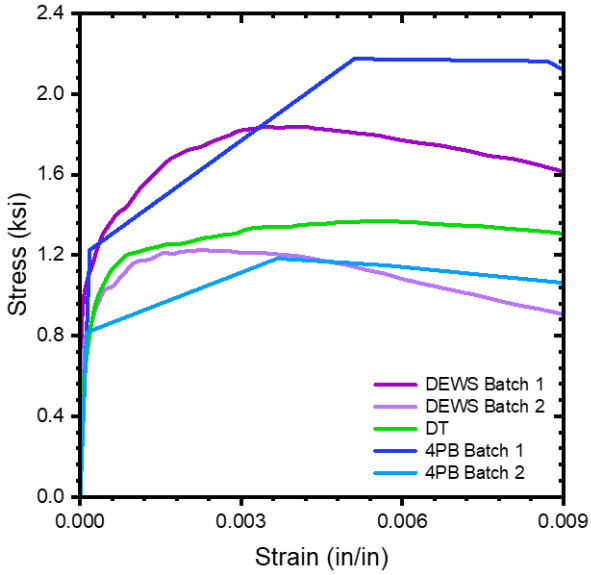


**Figure 3-28 Tension test comparisons**

Three direct tension curves were chosen to represent idealized tensile behavior. The average curve was calculated by averaging all of the direct tension curves. DT5 exhibited the strongest behavior, so it was chosen to represent the upper-bound, and DT7 exhibited the weakest behavior, so it was chosen to represent the lower-bound. Figure 3-29 and Table 3-5 show the graph and table of these curves, respectively.

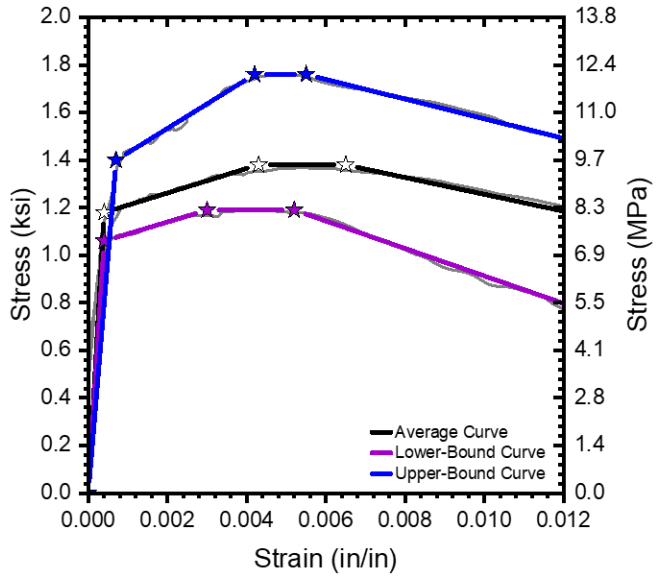


**Figure 3-29 Idealized tensile stress-strain curves for UH12s and UH14s**

**Table 3-5 Idealized tensile stress-strain curves used in analysis for UH12s and UH14s**

| | Average | | Upper Bound | | Lower Bound | |
|---|---|---|---|---|---|---|
| | Strain (με) | Stress (ksi) | Strain (με) | Stress (ksi) | Strain (με) | Stress (ksi) |
| Zero | 0 | 0 | 0 | 0 | 0 | 0 |
| Cracking | 400 | 1.18 | 700 | 1.40 | 400 | 1.06 |
| Peak | 4300 | 1.38 | 4200 | 1.76 | 3000 | 1.19 |
| Localization | 6500 | 1.38 | 5500 | 1.76 | 5200 | 1.19 |
| Ultimate | 13000 | 1.15 | 13000 | 1.45 | 13000 | 0.74 |

### 3.4.4 Prestressing Strand Bond Testing

The purpose of prestressing strand bond testing was to assess the development and transfer of unstressed 0.6-in. prestressing strands in UHPC used for UH12s and UH14s. In order to accomplish this, three specimens were cast based on previous testing at The University of Alabama (Bridi Valentim, 2023). The formworks were made of PVC and were cylindrical in shape, with wooden end pieces to allow the prestressing strands to pass through. The specimens were 14.5 in. long and 4 in. in diameter.

The PT bond specimens were tested in the pull-out configuration as shown in Figure 3-30. The bottom strand was gripped and held in place while the test frame was pulled upwards with UHPC in contact. To reduce friction and stress concentrations, oiled Teflon sheets were placed between the test frame steel plate and the UHPC specimen. The load was applied in a displacement-controlled manner at a rate of 0.1 in./min. An LVDT was placed at the top of the specimen to measure top slip, an LED system was used to measure specimen elongation and bottom PT slip, and two surface strain gauges were placed at 3.63-in. and 7.25-in. along the specimen height.

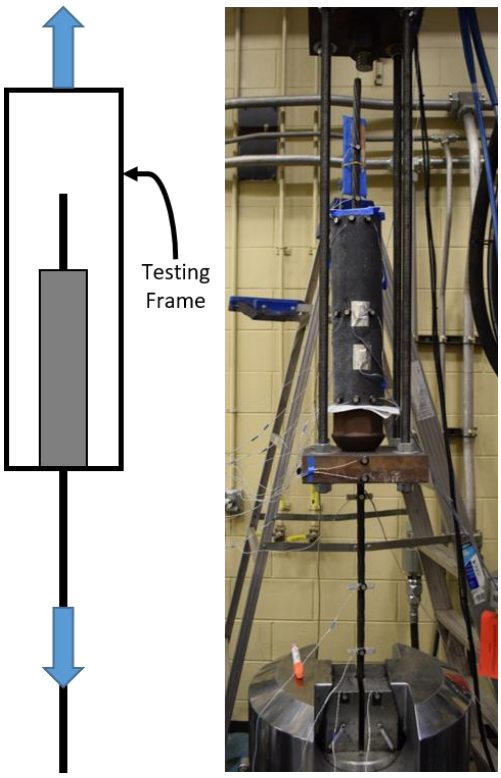


**Figure 3-30 Prestressing bond test setup**

All specimens failed as the prestressing strand slipped from the UHPC and at least one radial crack formed on the UHPC surface. Figure 3-31 shows the measured force-slip response for each specimen, as well as the yield force for the prestressing strand. In all cases, the test was able to progress until the strand began to yield. This indicates that the prestressing strand is able to fully develop over $24d_b$, or 15-in., and the chosen transfer length of $24d_b$ is appropriate.

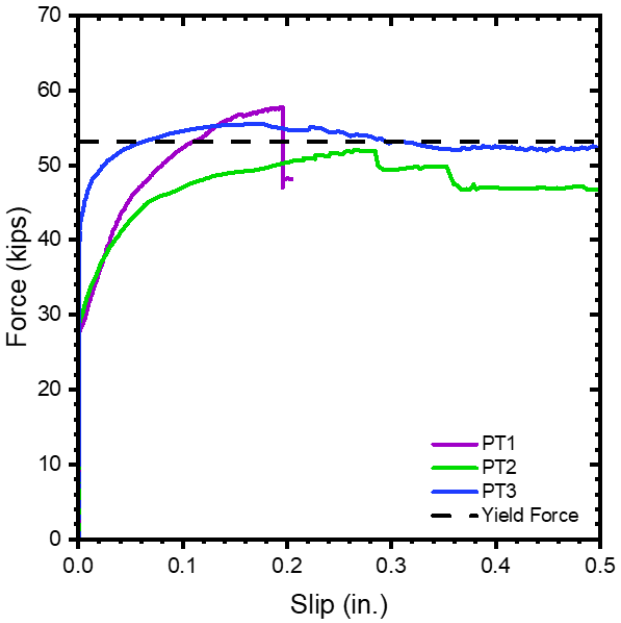


**Figure 3-31 Measured prestressing force vs. slip response.**

### 3.4.5 Shrinkage Testing

The autogenous shrinkage of UHPC was measured as the final component of preliminary testing. The test was carried out in accordance with ASTM C157 (2017), with modifications for UHPC in accordance with ASTM C1856 (2017). Prisms measuring 3-in. by 3-in. by 12-in. were cast and tested in the shrinkage measurement apparatus shown in Figure 3-32. Measurements began one day after casting and continued every day for the next 28 days. The shrinkage over time curve derived from these three specimens is depicted in Figure 3-33. At two days after casting, the early-age shrinkage strains were approximately 80 microstrains, which is relevant to the calculation of prestressing losses. This excludes strains from the first 24-hours because the prisms are still in their molds at this time and initial measurements cannot be taken. An average of 360 microstrains were observed after 28 days.

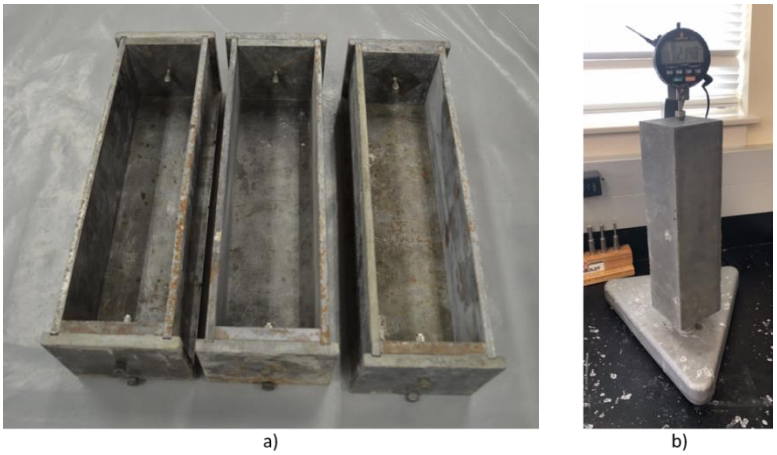


**Figure 3-32 Shrinkage beam a) formwork b) test measurements**

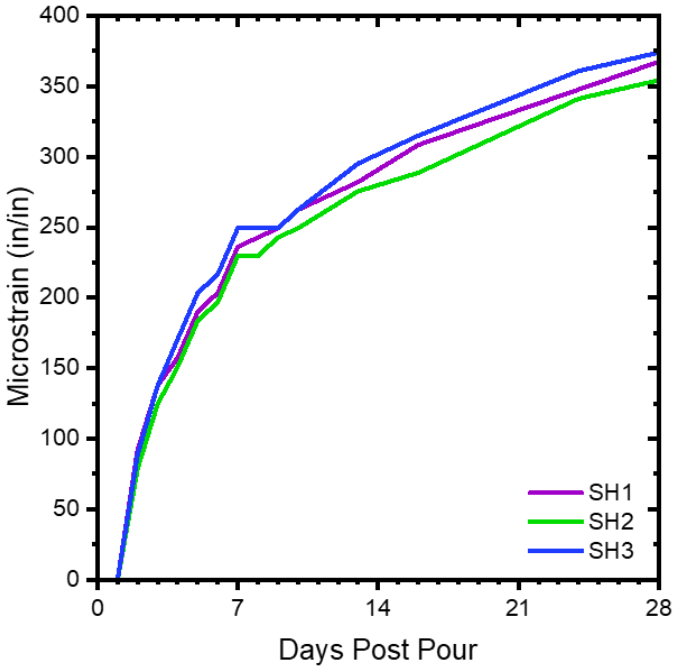


**Figure 3-33 Shrinkage over time graph**

## 3.5 Experimental Testing and Observations

As part of this project, a total of eleven large-scale tests were conducted on 12 in. and 14 in. pile specimens including four flexural tests and seven shear tests. Two of the four flexure tests were performed on UH12x71 piles and two on UH14x105 piles, with one performed in strong-axis bending and one in weak-axis bending. Table 3-2 lists the names of these piles. Because the damage was always localized to the midspan, the pile specimens from flexural tests were reused for shear testing up to two times, one for each end shear failure. The subsequent shear tests were named after the original purpose of the pile, followed by V1 or V2, depending on the pile's shear test number. The second shear test on the 12-in. weak-axis flexural pile, for example, was designated as UH12FW_V2. This section will go over the test setups, instrumentation, load protocol, and testing observations.

### 3.5.1 Flexural Testing

All flexural piles were simply supported at each end by a roller and pin and tested in a four-point bending configuration. The pile ends were 3-in. from the center of each support, which was 6-in. wide. A 200-kip capacity hydraulic load jack, with a manually operated pump was used to apply force to a spreader beam. The load was distributed to two rollers attached to the spreader beam and spaced 24-in. apart. To collect testing data, a variety of instruments were used, including pressure sensors, load cells, string potentiometers, 3D LED based non-contact displacement tracking sensors, and internal and external strain gauges.

Two 400-kip load cells were installed beneath the pile at the supports to capture support reactions, while the pressure sensor recorded the total force applied to the specimen. Ten string potentiometers distributed along the length of the pile were used to measure pile specimen displacement. Several LEDs also were used to measure displacement of the pile. Throughout the testing, internal and external strain gauges were used to monitor the strains in UHPC and prestressing strands.

#### 3.5.1.1 Strong-axis Flexure

One 12-in. pile and one 14-in. pile were tested in strong-axis bending. UH12FS was a 12-ft pile, while UH14FS was a 20-ft pile. The instrumentation for both piles is shown in Figure 4-34. The string potentiometers and strain gauges were identical in both specimens, but the LED configuration was different to account for the difference in the pile specimen length.

Load was applied cyclically to UH12FS, and the load reported by the two combined load cells was monitored. Figure 3-35 illustrates the load protocol used for the testing of the UH12FS. Loading was paused at the peak of each cycle before unloading throughout the test to inspect for microcracking and document the damage using photographs. Microcracking on the pile surface was only visible by rubbing acetone on the pile surface. The acetone quickly evaporates from the pile surface, but leaves traces inside the microcracking, resulting in a highlighted microcrack. The pile was unloaded and reloaded after 30 kips. At 40 kips, the first flexural microcracking was observed in the constant moment region between the load application rollers. After this point, three cycles were performed at each load level, 55 kips and 70 kips. Shear microcracks were observed outside of the constant moment region on each side of midspan at 70 kips. Following that, one cycle of 80 kips was performed, followed by loading until failure at 95.5 kips. The pile failed in compression, with UHPC crushing at the specimen's top surface. The load dropped by 20% at the point of failure, with one tension crack localizing near midspan and one localized shear crack positioned outside of the constant moment region. Figure 3-36 shows the crack progression. The pile specimen was further subjected to increased displacement, but the applied force continued to decrease. The load on the

pile specimen was unloaded and then reloaded to 67 percent of its peak force before the test was completed.

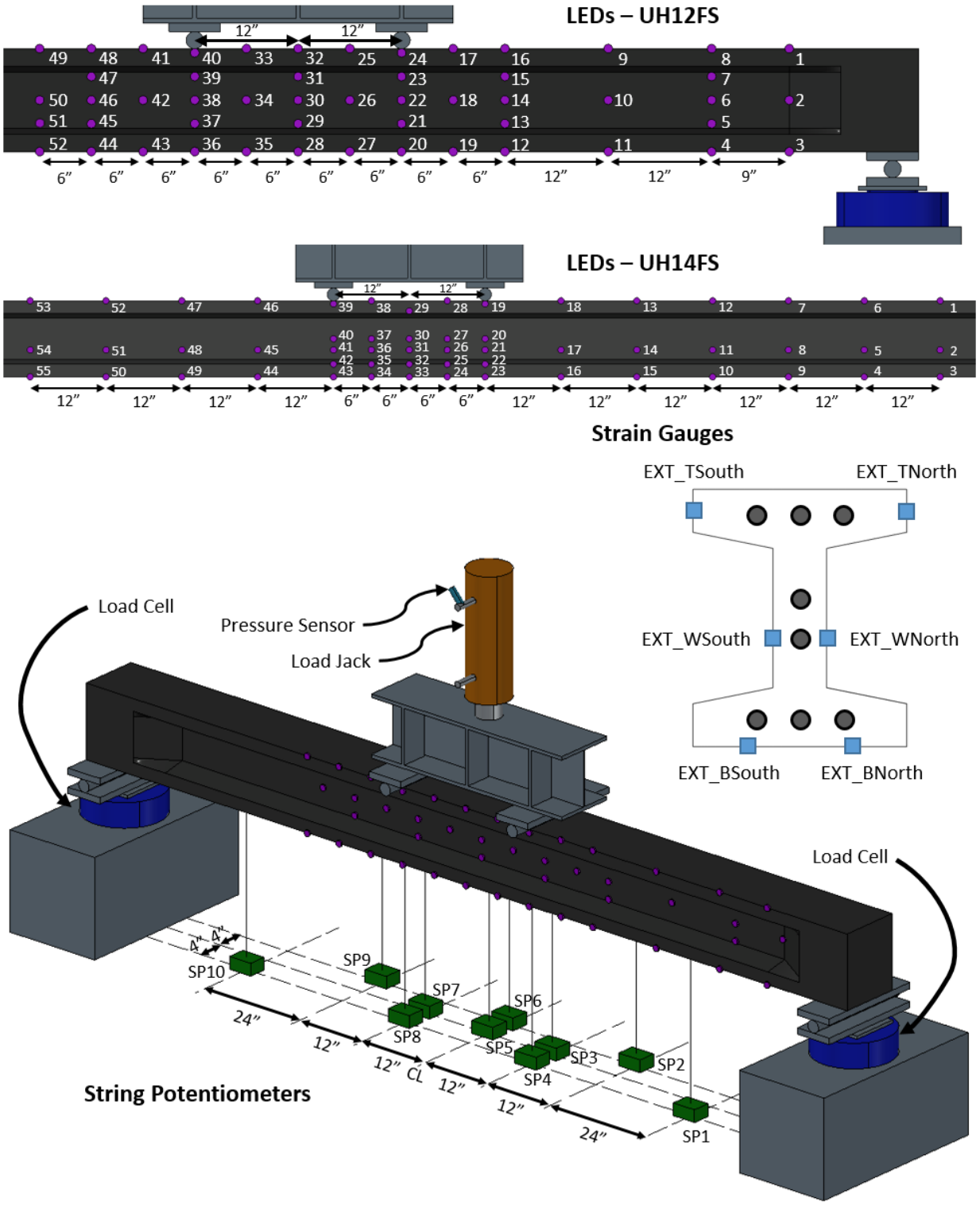


**Figure 3-34 Instrumentation and setup for strong-axis flexure**

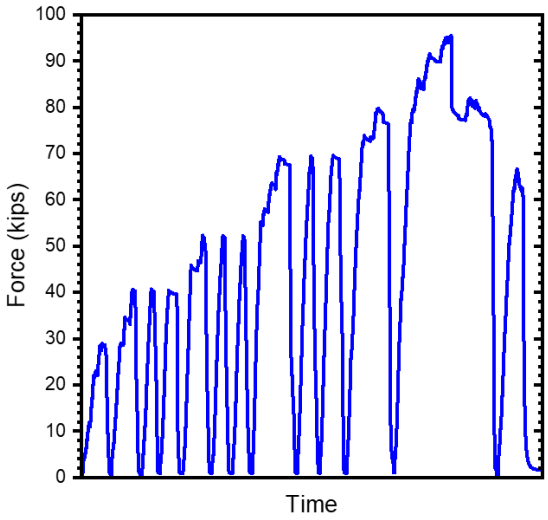


**Figure 3-35 Load protocol for UH12FS**

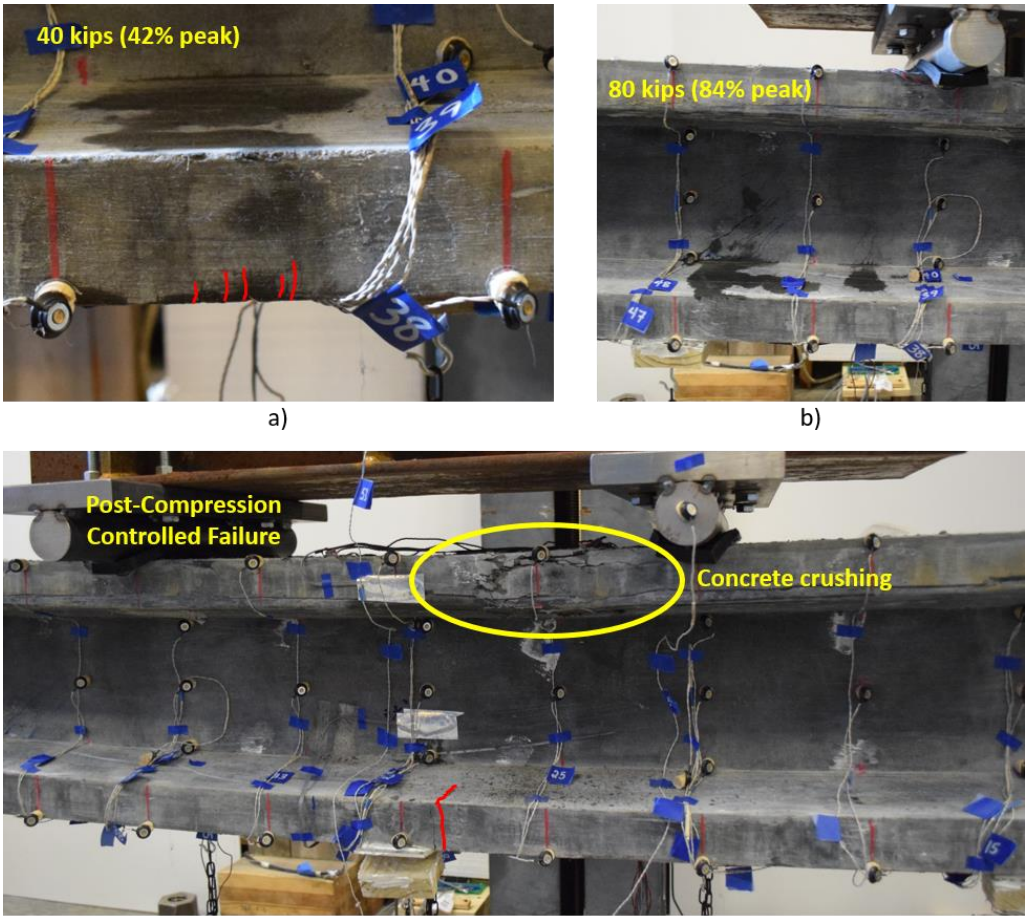


a) b)

c)

**Figure 3-36 Crack progression for UH12FS: a) first observed flexural microcracking, b) shear cracking outside of constant moment region, c) UHPC crushing and localized tension crack at failure.**

UH14FS testing proceeded in a similar manner as UH12FS, with a series of cyclic loading. Three cycles were applied every 10 kips beginning at 45 kips and continuing until failure. Flexural microcracks were observed for the first time at 35 kips on the bottom flange at midspan. Flexural shear microcracks were observed outside the constant moment region at 65 kips. Some concrete spalling on top of the pile was observed after 85 kips of load. The top surface of this pile had air voids, and thin layers of UHPC atop some of these bubbles began to pop. The pile eventually experienced compression-controlled failure at load of 90.6 kips. Concrete crushing was widespread, with one localized tension crack situated at midspan, as shown in Figure 3-38.

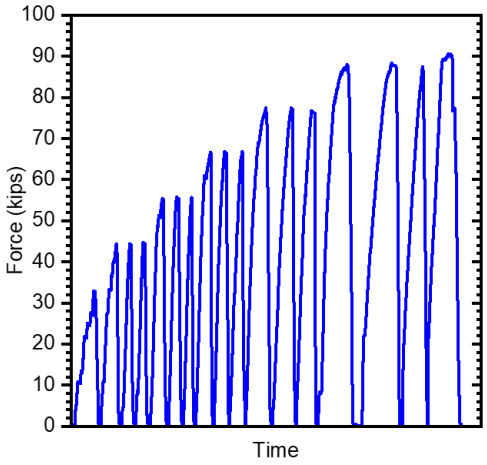


**Figure 3-37 Load protocol used for laboratory testing of UH14FS**

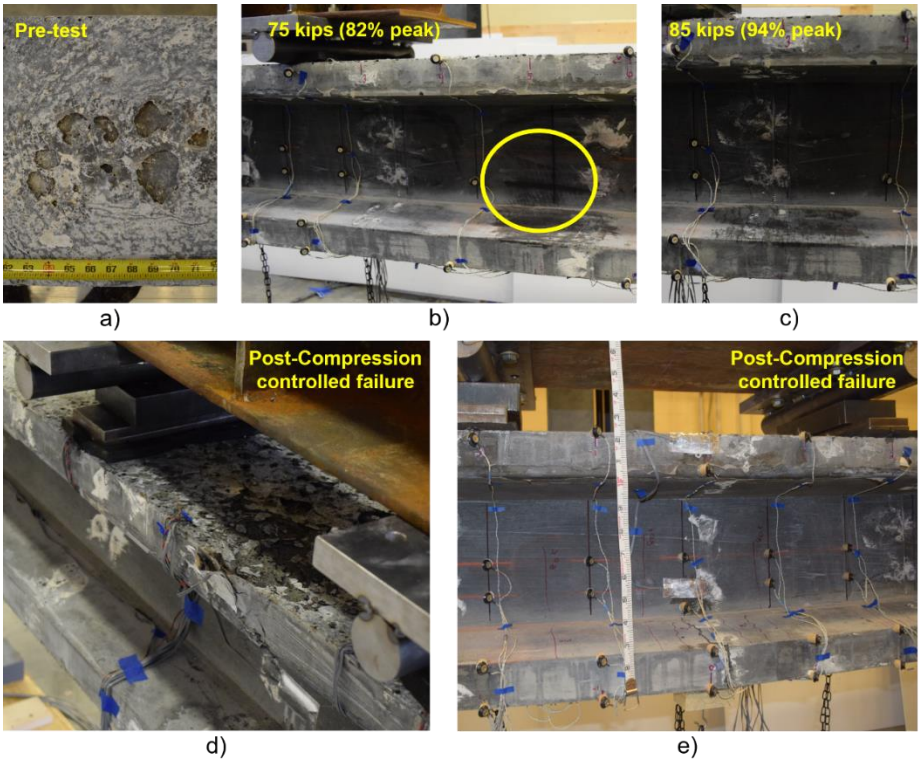


**Figure 3-38 Crack progression of UH14FS a) voids on the top surface pre-test, b) shear microcracks, c) flexural microcracks, d) concrete crushing, e) localized tension crack.**

### 3.5.1.2 Weak-axis Flexure

In each pile size, two piles were tested in weak-axis bending. Both UH12FW and UH14FW were 12-foot piles. Figure 3-39 depicts the instrumentation setups used by both piles. For both tests, LEDs, string potentiometers, load cells, pressure sensors, and internal and external strain gauges were used. The load protocol shown in Figure 3-40 was used to apply load cyclically to the UH12FW. At the peak of each cycle, the pile was inspected for microcracking, as with previous testing. The first flexural microcracks were observed at midspan on the bottom surface of the flange at 17 kips. These initial cracks did not extend up the pile's sides. The flexural microcracks grew and crept up the pile's side as more load was applied. Figure 3-41a depicts a dense field of flexural microcracking in the constant moment region as a result of this. Cycles were performed at loads of 20, 30, and 37 kips. Popping noises were consistently heard after 37 kips, until the pile finally failed in a compression-controlled manner at 42 kips. Figure 3-41b depicts concrete crushing from the top of the pile down to the web, as well as a tension crack located at midspan at the time of failure. The load dropped to 24 kips, or 57 percent of the peak load, after the pile ruptured. After unloading and reloading the pile to 23 kips, the applied force no longer increased. The pile was unloaded and reloaded one last time to 21 kips, 50% of the ultimate capacity, before the test was completed.

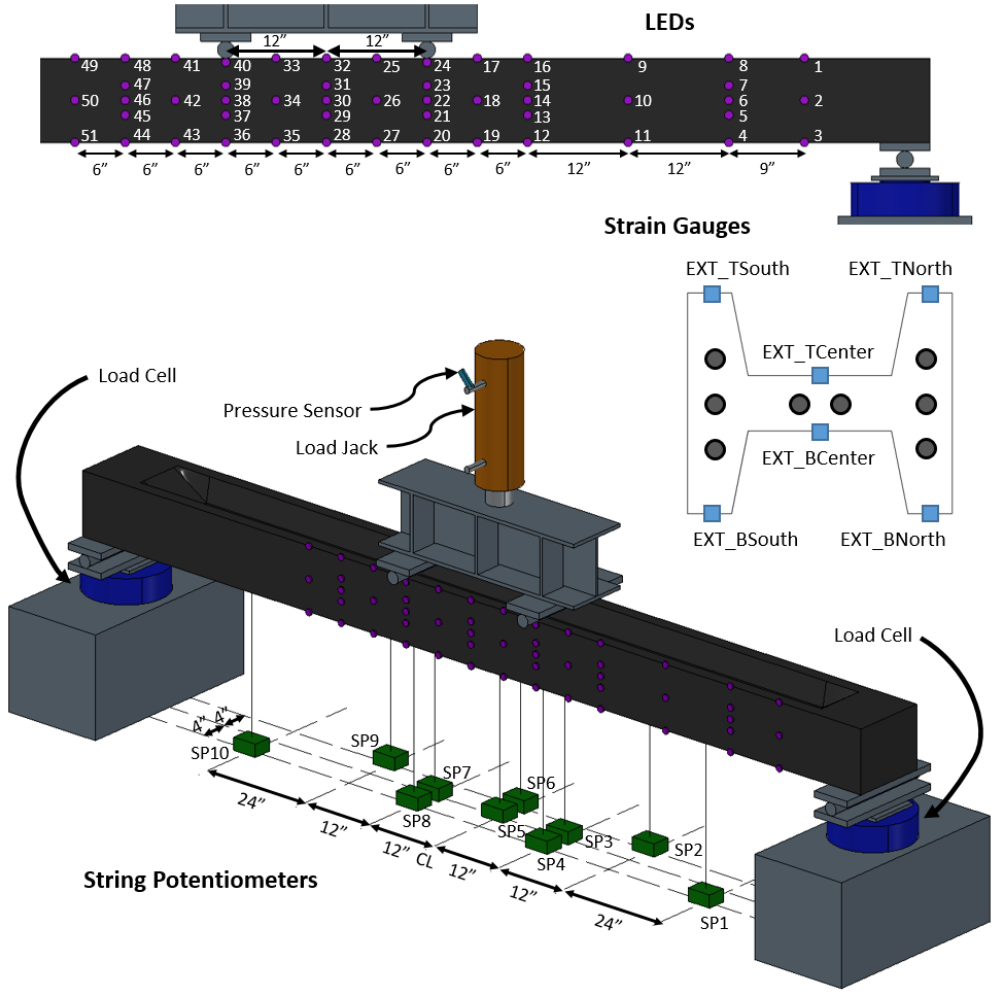


**Figure 3-39 Schematic of instrumentation used for Weak-axis flexure test**

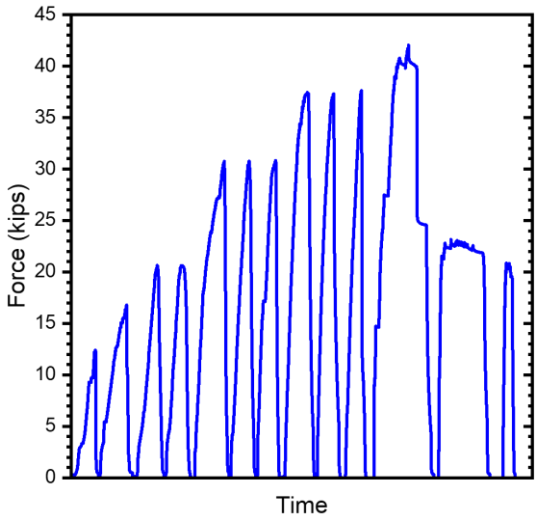


**Figure 3-40 Load protocol used for testing of UH12FW**

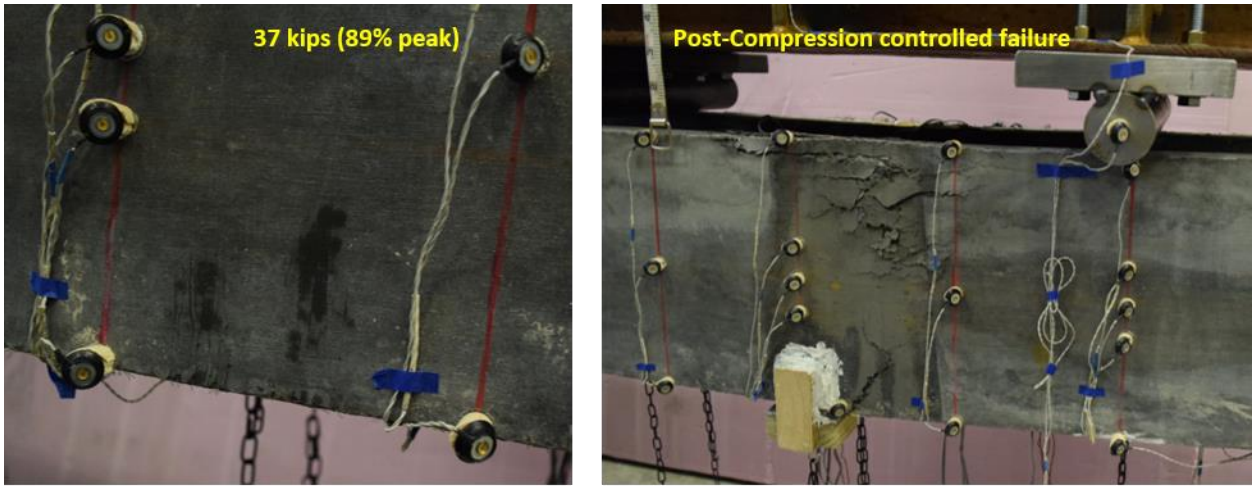


**Figure 3-41 UH12FW crack progression: a) flexural microcracks, b) UHPC rupture and localized tension crack at failure**

UH14FW testing went similarly. Flexural microcracking was observed on the bottom of the pile beginning at 30 kips and extending about 1 inch up the side. Following this load level, three cycles for all loads were performed, including 45 kips, 60 kips, 70 kips, and 80 kips. The length and density of the cracks increased throughout these cycles, as shown in Figure 3-43a. UH14FW, like the other flexural testing piles, eventually failed in compression-controlled failure at 93 kips, but this pile failed under one of the rollers and just outside of the constant moment-region, as shown in Figure 3-43c. A small tension crack less than 2.5 in. long localized at failure on the back bottom flange (Figure 3-43b), but no tension cracks localized on the front bottom flange.

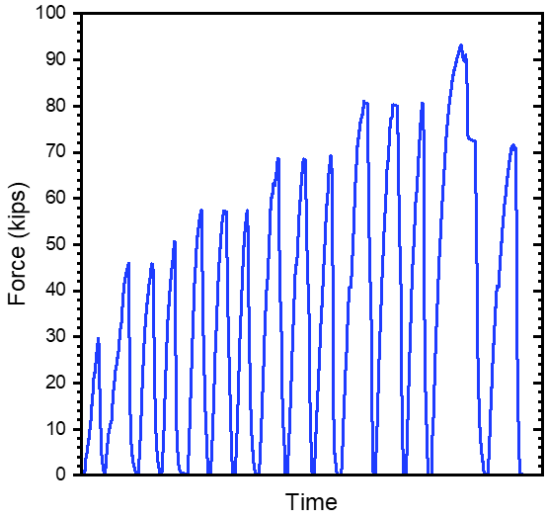


**Figure 3-42 Load protocol for UH14FW**

### 3.5.2 Shear Testing

Flexural testing caused relatively minor damage to the piles, which was mostly limited to the midspan region. As a result, all flexural piles were reused for testing under shear loading. These tests were named after the pile they were performed on, followed by V1 or V2 to indicate whether it was the first or second shear test on that pile. For example, the second shear test done using UH12FW would be called UH12FW_V2. A total of seven shear tests were performed, but the setup for the first test, UH14FS_V1, was unique and will be discussed separately.

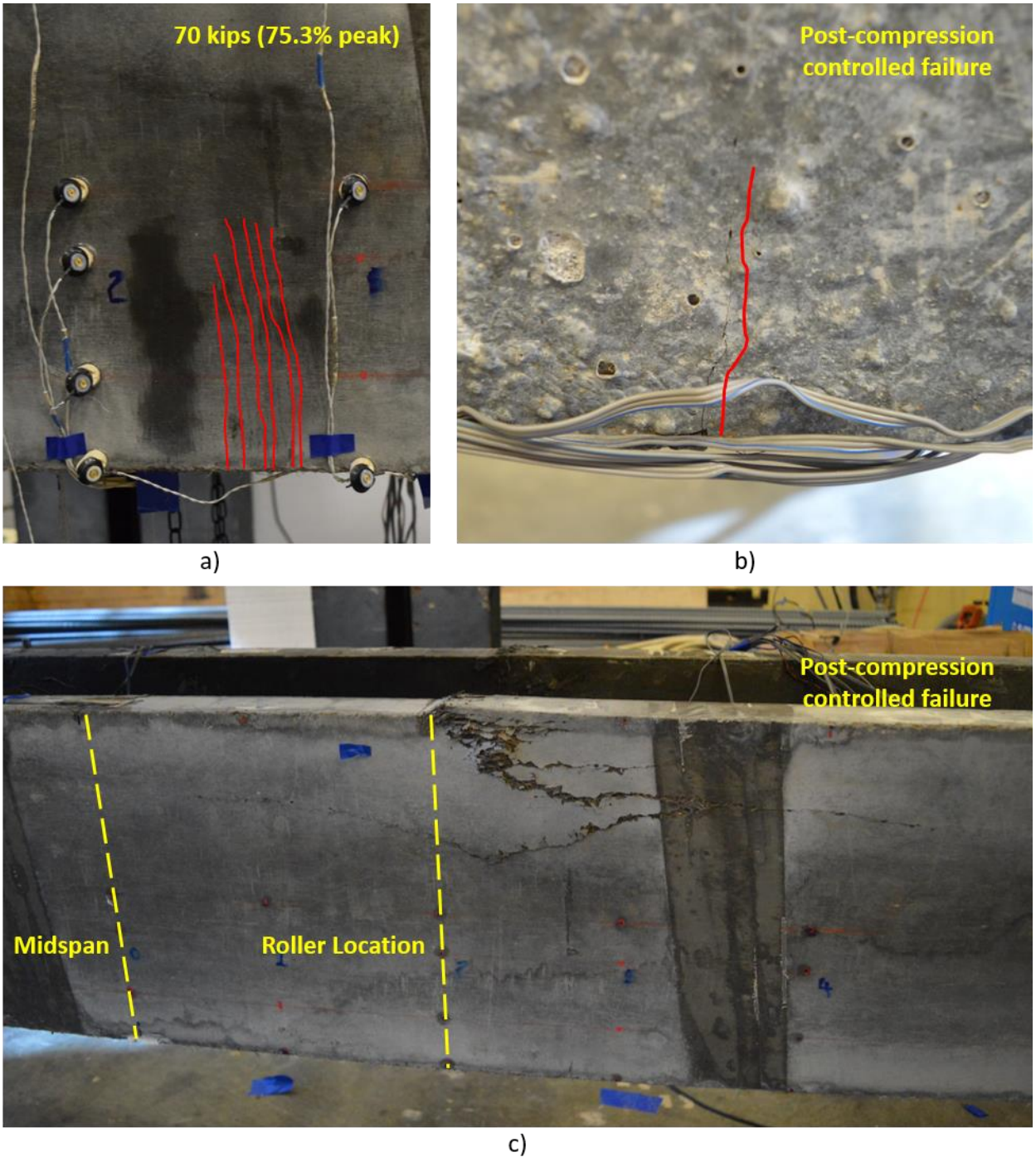


**Figure 3-43 UH14FW crack progression: a) flexural microcracks at 70 kips, b) small, localized tension crack post-failure, c) UHPC crushing post-failure.**

The 20-foot pile, UH14FS, was tested first because it had the longest undamaged spans. The test setup for subsequent shear tests evolved as a result of the testing of this first pile. The goal of UH14FS_V1 was to test the spans on the interior of the pile rather than the block-end. To that end, the setup was designed to support the pile in three places, with the middle support just past the flexural testing damage. According to elastic structural analysis, a tie-down force on one end was

required to induce higher shear forces at the pile interior support, as shown in Figure 3-44a. The first iteration of the test setup, labeled UH14FS_V1.1 (Figure 3-44b), used a 200 kip capacity load jack at the load application point with a load beam on top. Because the load beam was tied to the floor, when the jack was pumped up on it, it was held in place and the reciprocal force pushed downward on the pile. A beam was placed across the width of the pile on the tie-down end, and nuts were tightened with wrenches to post-tension the pile-end to a force of 6 kips. The amount of tie-down force was measured using a load cell at this support. The problem with this setup became apparent on test day, when the single load-jack provided little stability to the system. With increasing loads, the load beam began to twist out of plane. The next configuration, UH14FS_V1.2, addressed the instability by directly placing the load beam on the pile and then applying the load more evenly with two load jacks, as shown in Figure 3-44c. The tie-down end remained the same. However, the pile's shear capacity exceeded pretest predictions, and the applied load approached the section yield capacity of the steel load beam. As a result, the test was stopped, and a new higher capacity steel load beam was fabricated and used to complete the testing. The tie-down shear test setup with high-capacity load beam was finalized as UH14FS_V1.3, as illustrated in Figure 3-44d.

Shear testing instrumentation was generally similar to flexural testing instrumentation. Load cells were placed under each support to measure support reactions, and pressure sensors were attached to each load jack to measure applied force. LEDs attached to the specimen's face tracked displacement along the span. The UH14FS_V1 did not use any string potentiometers, but all other shear tests used two string potentiometers at the specimen's center to measure displacement at the load application point. Because the shear capacity of UH14FS_V1 had already outperformed expectations, the final test used fewer LEDs to ensure that the LEDs were not damaged in a potentially brittle shear failure. Figure 3-48 depicts the LED configuration for UH14FS_V1.3.

Loading for the UH14FS occurred in three stages, as shown in Figure 3-45. Apart from a few small flexural microcracks, no microcracking was observed during the first test, UH14FS_V1.1. The pile was loaded to 127 kips before the test was terminated due to out-of-plane tilting of the load beam. The second test, UH14FS_V1.2, was more eventful, with shear microcracks appearing as early as 140 kips total load. The length and density of the shear microcracks increased as the test progressed, and they were present on both sides of the load. Under the load, there was also flexural microcracking. The load approached the flexural capacity of the steel load beam, so the test was terminated at 220 kips.

The pile was tested to failure with a stronger load beam in the final test, UH14FS_V1.3. The previous peak of 220 kips was surpassed, and shear cracking increased throughout the test. More flexural microcracks were present and densely spaced under the load application point, as shown in Figure 3-46b. After 250 kips, the pile began to crackle, and the load began to increase more slowly. Eventually, the moment on the pile began to approach the pile's flexural capacity as determined by previous testing. The pile suddenly failed in flexural-shear around a load of 270 kips, with a crack originating from the top flange where the load was applied, through the web, and down to the interior support. After the failure, the load dropped to 35 kips, or 13% of peak capacity. According to the time-lapse photos in Figure 3-46c and d, the crack started in the web and then extended through the rest of the pile. Although a crack that begins in the web would normally be classified as web shear, this pile was classified as flexural shear because it had also reached its moment capacity. The moment capacity observed in flexural testing was 400 k-ft, and the moment at the point of failure in UH14FS_V1.3 was 416.6 k-ft. The different crack pattern presentations observed in true web shear failures seen in subsequent shear tests also supported classification of this failure as flexural-shear failure.

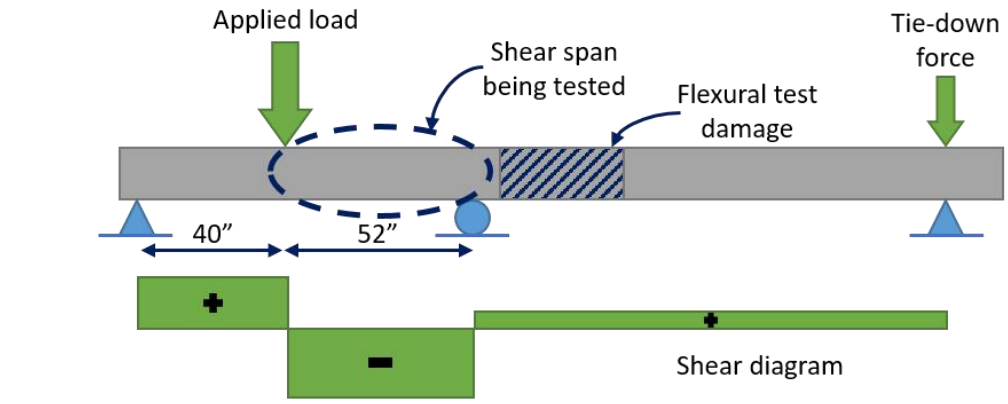


a)

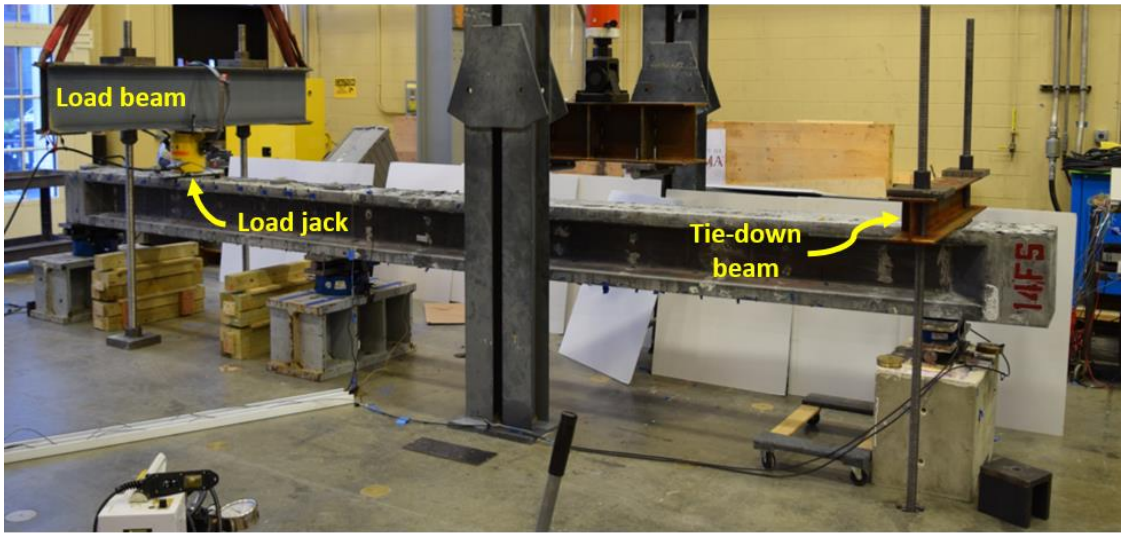


b)

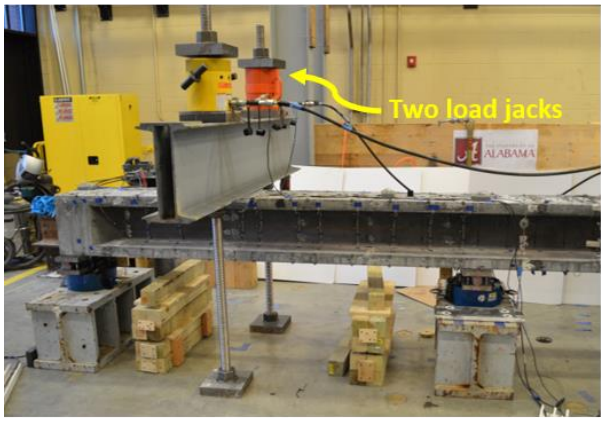


c)

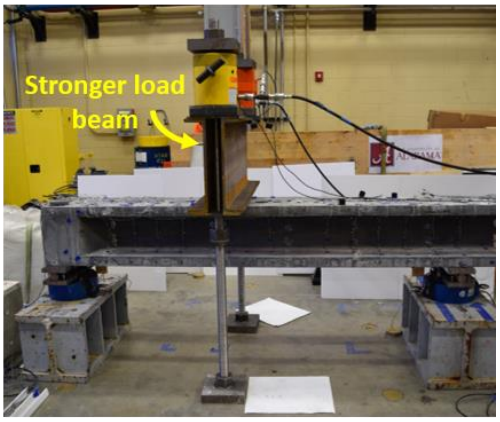


d)

**Figure 3-44 UH14FS_V1 shear test setup evolution: a) schematic of test, b) UH14FS_V1.1 configuration with one load jack, c) UH14FS_V1.2 configuration with two load jacks for even loading, d) UH14FS_V1.3 configuration with stronger load beam**

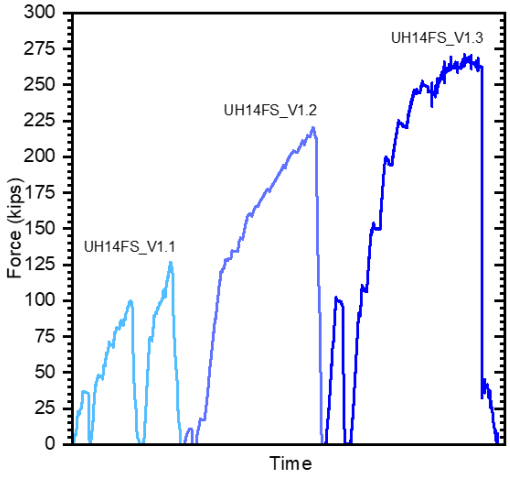


**Figure 3-45 Load progression from the testing of Pile UH14FS_V1**

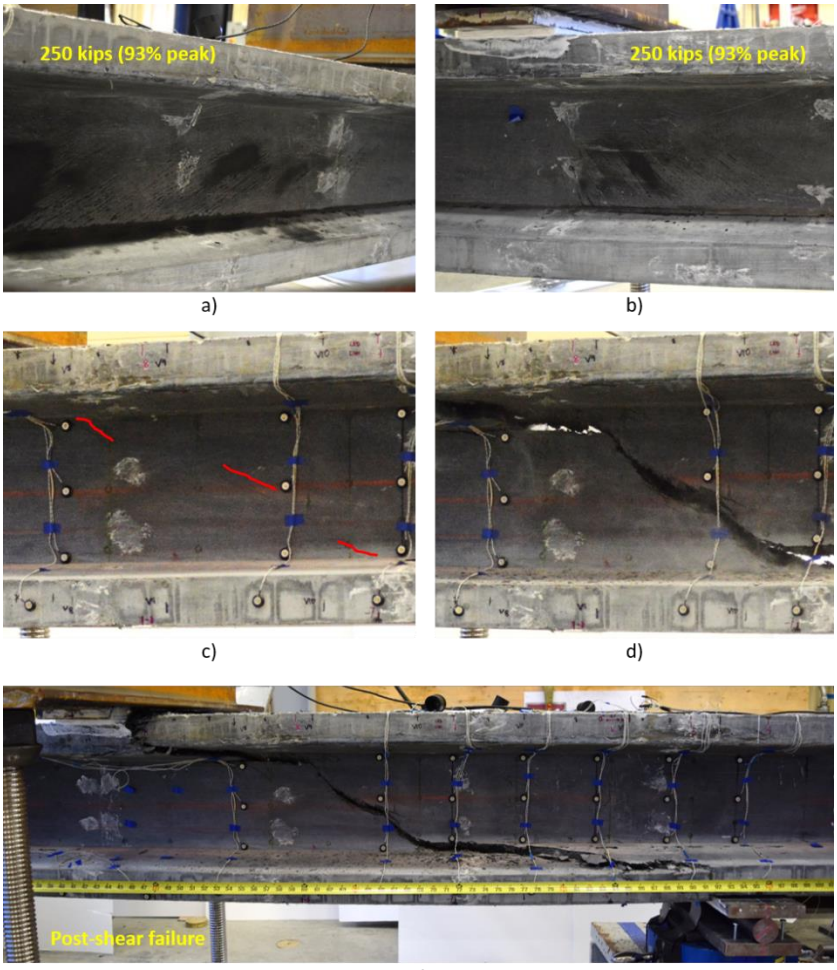


**Figure 3-46 Crack progression of UH14FS_V1.3: a) shear cracking on 52-in. span, b) flexure and shear cracking on 40-in. span, c) localized shear crack forming just before failure, d) same location immediately after failure, e) full shear failure**

The tie-down setup was not used for the remaining shear tests. Instead, each pile was supported in three places, and when a load was applied to one side, the pile was allowed to pick up from the third support. The plates beneath the pile at the third support were removed as soon as possible during the test to ensure that there was no contact between the pile and the third support, and thus zero load transfer to that support. The self-weight of the overhanging pile was transferred to the middle support, resulting in a simply supported configuration. Figure 446a depicts a schematic of this configuration with a shear diagram. Table 6 shows the shear lengths, $L_A$ and $L_B$, for all shear tests. With this notation, $L_A$ will always be on the side closest to the pile's end, and $L_B$ will always be on the side closest to the middle support.

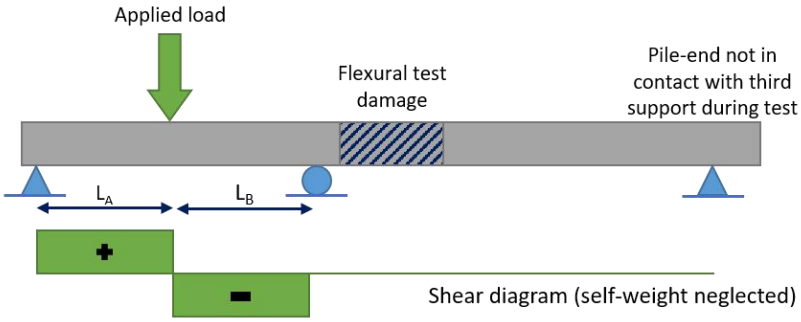


a)

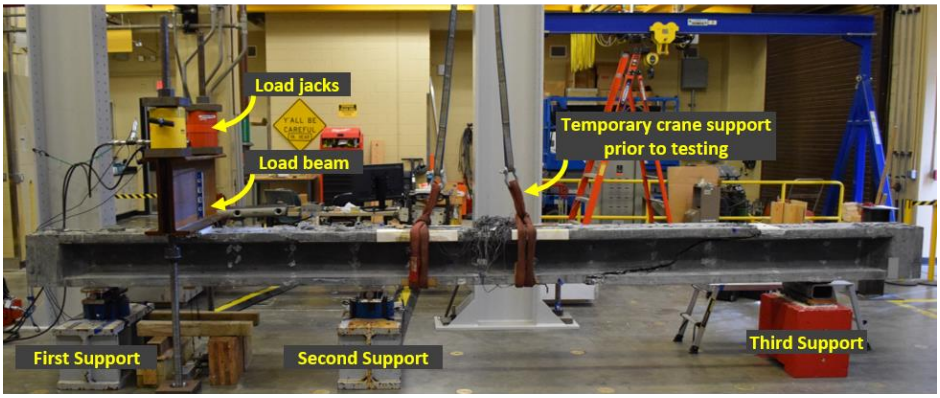


b)

**Figure 3-47 General shear test setup for all piles except UH14FS_V1: a) schematic and shear diagram, b) photo of test setup**

**Table 3-6 Shear spans for UH12 and UH14 shear testing**

| Pile Test | $L_A$ (in.) | $L_B$ (in.) | Peak Load (kips) | Applied moment vs. measured flexural moment capacity ($M_v/M_u$) | Cracking Angle (degrees) |
|---|---|---|---|---|---|
| UH14FS_V1 | 40 | 52 | 270 | 1.04 | 34 |
| UH14FS_V2 | 24 | 48 | 270 | 0.82 | 35 |
| UH14FW_V1 | 24 | 33 | 316 | 0.81 | 29 |
| UH12FS_V1 | 24 | 30 | 184 | 0.83 | 28 |
| UH12FS_V2 | 28.5 | 28.5 | 178 | 0.86 | 29 |
| UH12FW_V1 | 24 | 30 | 184 | 0.83 | 30 |
| UH12FW_V2 | 24 | 30 | 174 | 0.78 | 27 |

As previously stated, pressure sensors on each load jack, load cells under each support, two string potentiometers under the load application point, and LEDs on one specimen face were used for the remaining shear tests. Figure 3-48 depicts the LED configuration for all shear tests, while Figure 3-49 depicts the force-displacement relationships.

UH14FS_V2, the second shear test, examined the other end of the 20-foot pile. Loading was done in a monotonic manner, pausing at 20-kip intervals to inspect for microcracking. Shear microcracks were first observed on the shorter span at 80 kips of load ($L_A$). The microcracks on the $L_A$ span had grown denser and longer at 180 kips, and shear cracking had also been observed on the other shear span ($L_B$). The slope of the force-displacement curve changed as a result, as shown in Figure 3-49. At higher loads, flexural microcracking was also observed near the midspan. The load peaked at 270 kips, and a 35-degree web-shear crack was localized. Two longitudinal cracks formed along the top of the pile, at each web-flange interface, just prior to this localized shear crack (Figure 3-50b). The load jacks were pushed further until the web crack widened and the load dropped to 205 kips. Following that, the load was released.

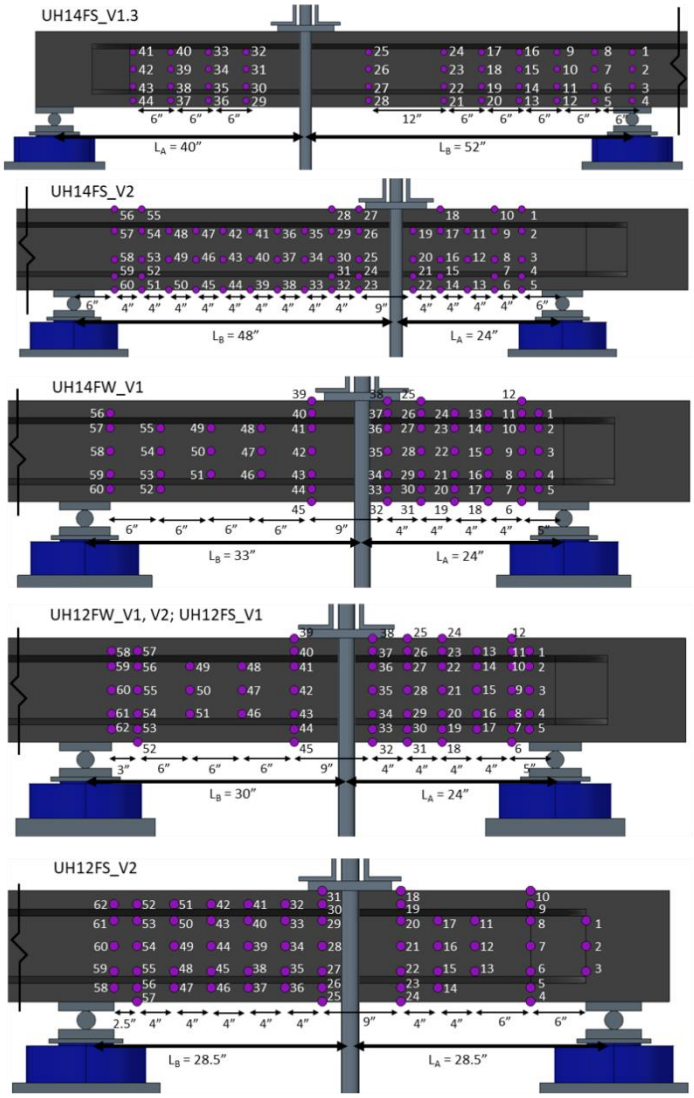


**Figure 3-48 LED setup for all UH12 and UH14 shear tests**

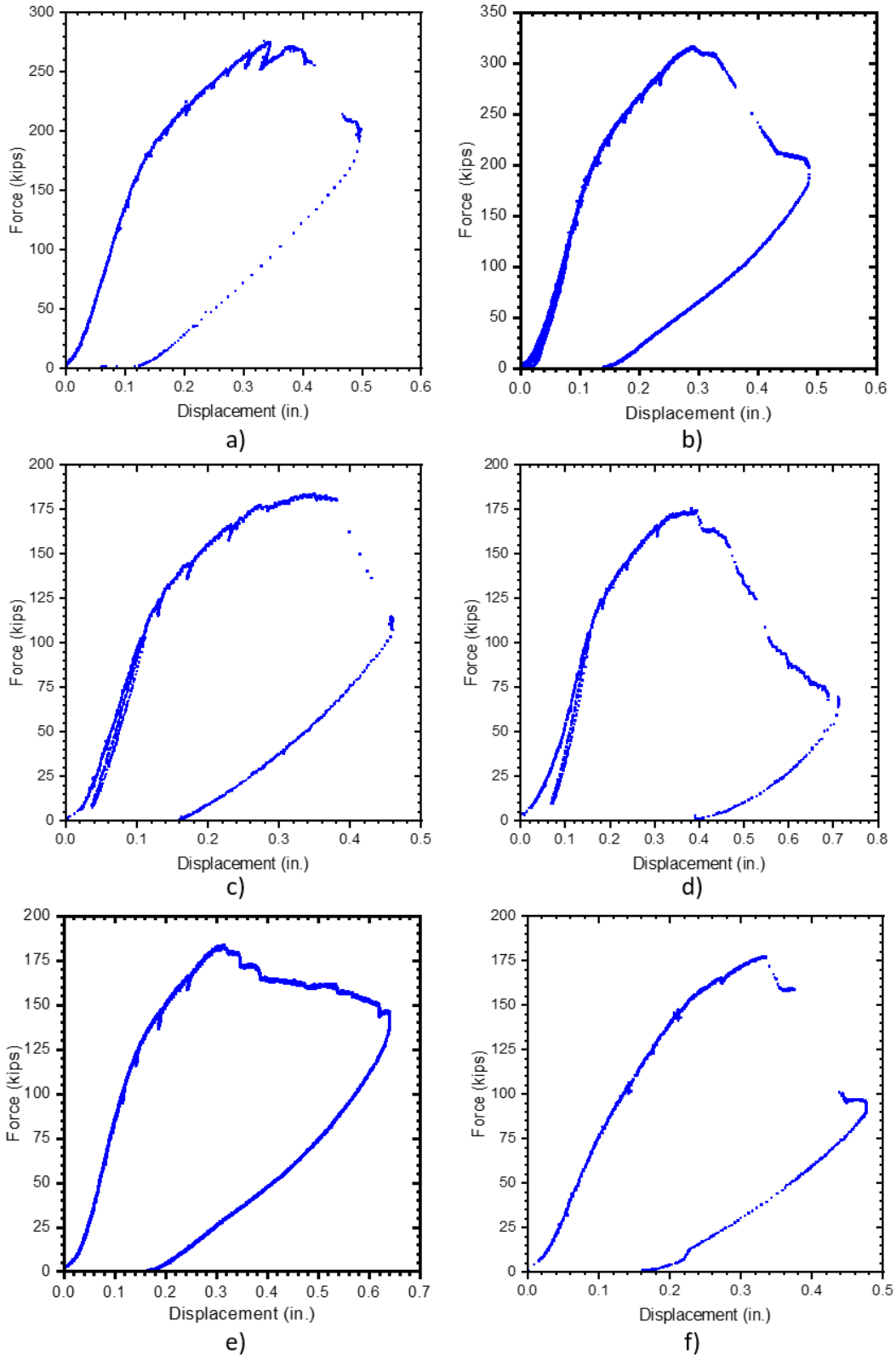


**Figure 3-49 Force-displacement for a) UH14FS_V2, b) UH14FW_V1, c) UH12FW_V1, d) UH12FW_V2, e) UH12FS_V1, f) UH12FS_V2**

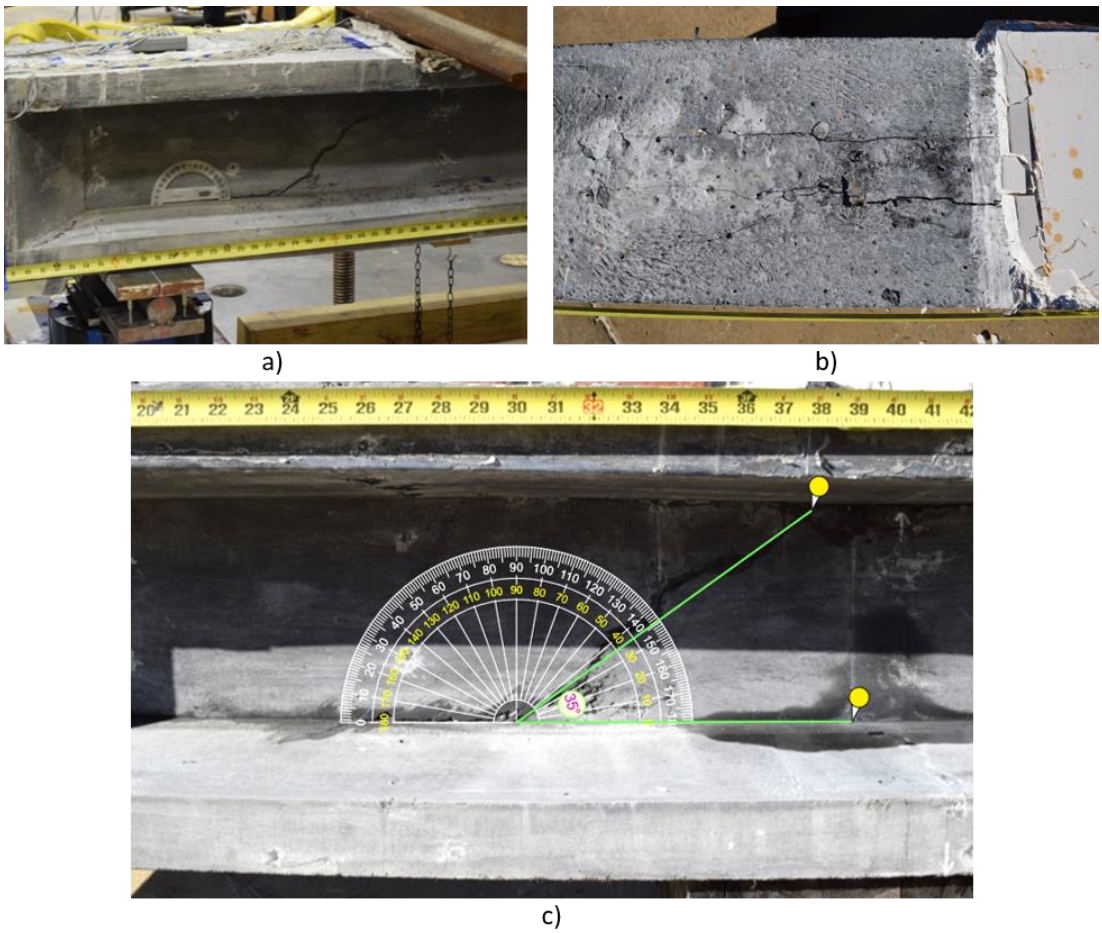


**Figure 3-50 UH14FS_V2 crack patterns a) localized shear crack, b) longitudinal cracks on top flange, c) shear cracking angle**

The flexural damage on UH14FW was not as concentrated to the midspan as on the other piles because it failed just under one of the load application rollers. Because there was not enough room on this pile for two shear tests, only one test was performed. UH14FW_V began in the same manner as all shear testing, but at 120 kips, out-of-plane tilting of the load beam was observed. To mitigate this, the pile was unloaded, and the load beam was re-centered on the pile. Shear microcracking was first observed on the $L_A$ span at 120 kips and on the $L_B$ side at 180 kips. The slope of the force-displacement curve also began to change around 180 kips, as shown in Figure 3-49. Flexural microcracks, as shown in Figure 3-51a, were common at loads of 200 kips. As the load increased past 280 kips, some out-of-plane tilting of the load beam was observed again. Loading continued because the pile was expected to fail shortly thereafter, based on the UH14FS_V2 test with the same LA shear span. The peak load eventually occurred at 316 kips, which was higher than expected, and a web-shear crack localized at an angle of 29 degrees. The load was then reduced to 200 kips. After the pile was unloaded, longitudinal cracks on the top flange were discovered, as shown in Figure 3-51b.

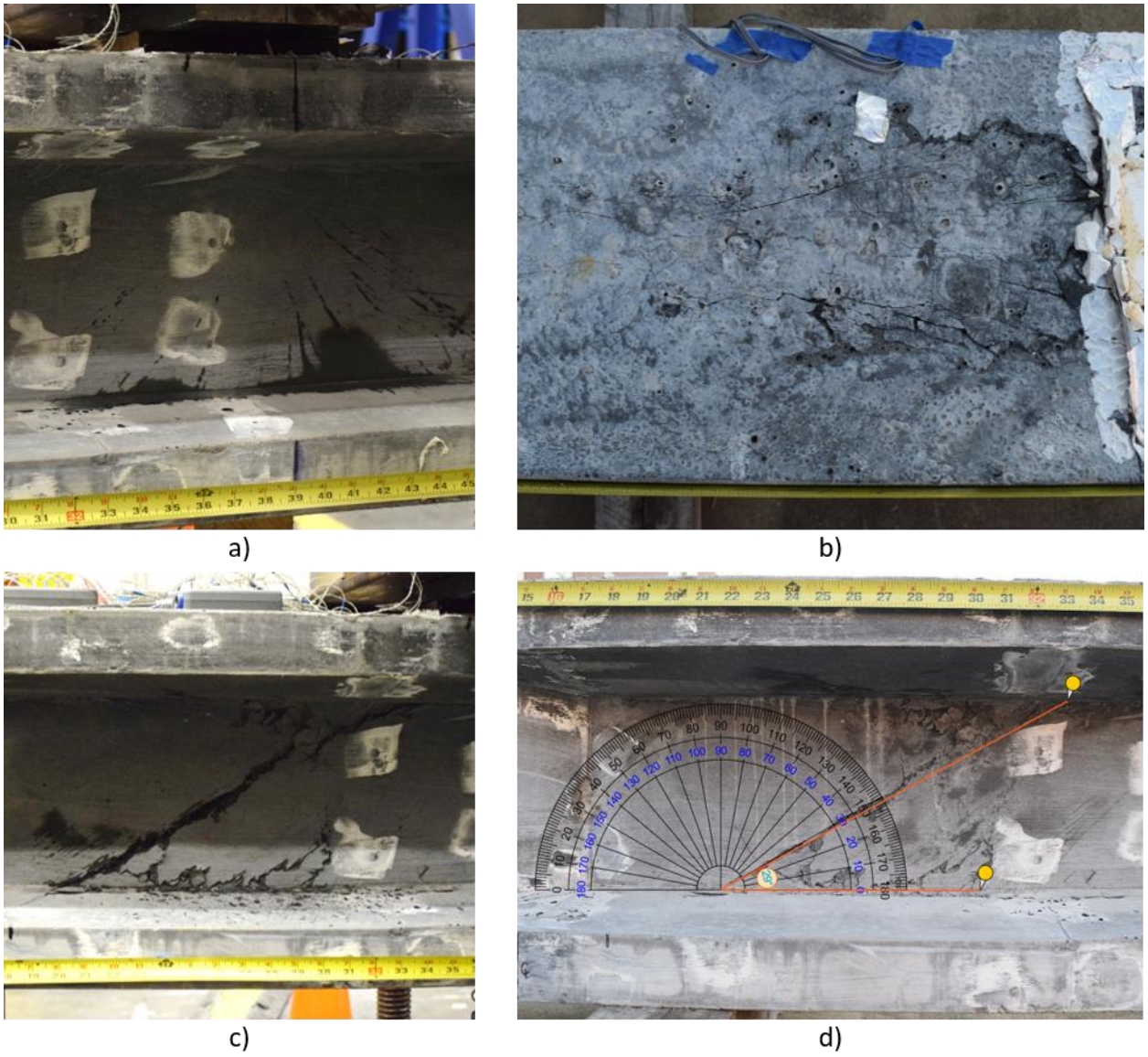


**Figure 3-51 UH14FW_V1 crack patterns: a) flexural cracking at 280 kips, b) longitudinal top flange cracking, c) localized shear crack, d) shear cracking angle**

The pile size and shear span lengths were the same in the next three shear tests, UH12FW_V1, UH12FW_V2, and UH12FS_V1. The behavior observed in these tests all proceeded in a similar manner and will thus be summarized together. Shear microcracking was first observed on the $L_A$ shear span for each pile between 80 and 100 kips. Each pile eventually failed due to web-shear, which occurs when a shear crack forms in the web of each pile. UH12FW_V1, UH12FW_V2, and UH12FS_V1 had peak forces of 184, 174, and 184 kips, respectively. Figure 3-49c, d, and e depict the force-displacement behavior of these piles. Although the UH12FW_V1 test was terminated shortly after the force drop associated with crack localization, the other two piles were allowed to fail in order to observe the secondary behavior. This resulted in the formation of a secondary shear crack in UH12FW_V2, as well as another drop in load at approximately 125 kips.

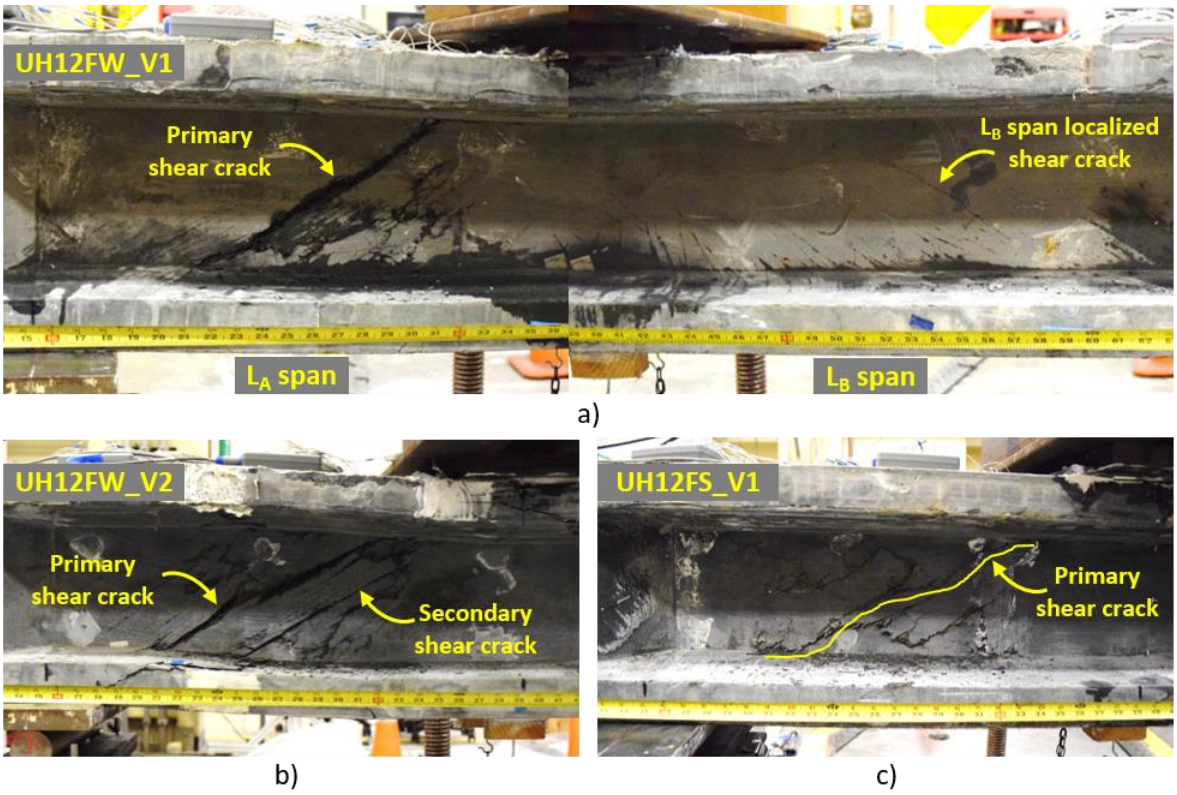


**Figure 3-52 Shear crack at failure in a) UH12FW_V1, b) UH12FW_V2, and c) UH12FS_V1**

After a small load drop caused by the primary shear crack localization, there was no discernible drop in load as the pile was pushed further. However, as displacement increased, the load gradually decreased, and the cracks became more severe. Figure 3-52 depicts the failure cracks for each of these three piles, with the primary localized crack depicted for each. There were longitudinal cracks on the top flanges at the web-flange interface in all three tests.

UH12FS_V2 used equal shear spans, but the pile itself was shifted so that some of the block-end was past the first support and included in $L_A$. Because the block-end has a larger cross-section and consequently, larger capacity, the expected failure span for this test was $L_B$. Loading began similarly to the previous piles, but at 140 kips, the load beam was found to be tilting out of plane. On one side of the top flange, a longitudinal crack formed. Previous tests found these cracks forming at both web-flange interfaces, but only one formed in this case due to the load beam tilting. After that, the pile was unloaded, and the load beam was repositioned. An additional 4-in. by 7-in. by 2-in. thick plate was placed beneath the load beam, with the 7-in. dimension running the length of the pile, so that the load beam would distribute the load evenly across the web of the pile rather than continuing to load the cracked flange. The load peaked at 178 kips, at which point a web-shear crack appeared on the $L_B$ span.

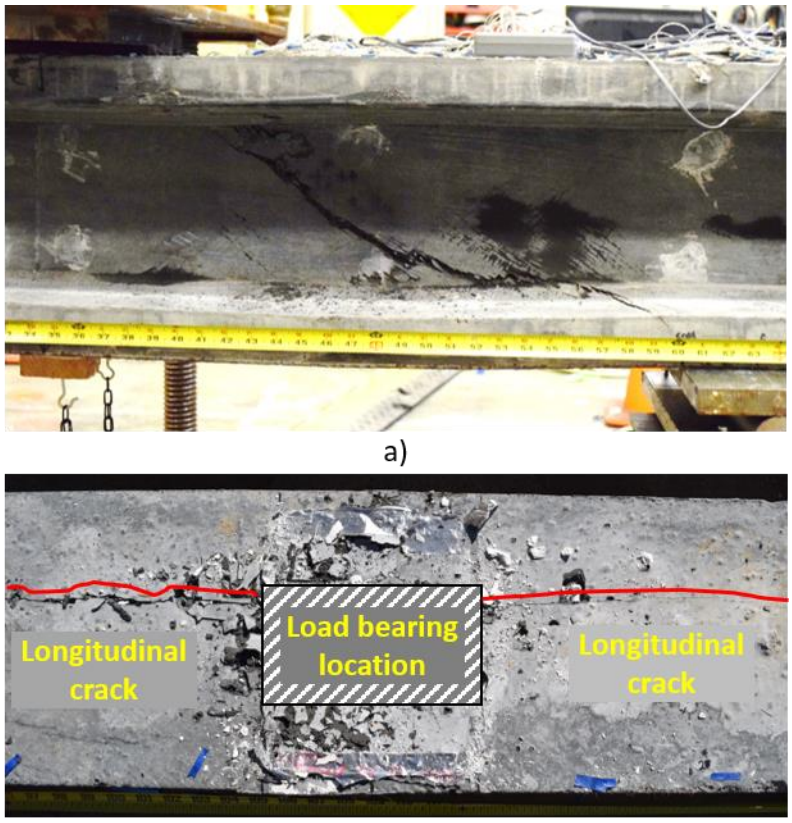


**Figure 3-53 UH12FS_V2 shear cracking: a) web-shear crack, b) longitudinal crack from tilting load beam**

## 3.6 Results and Discussion

### 3.6.1 Verification of Material Properties

Although the testing of material characteristics is detailed in Section 3.4, some of these properties can be verified by experimental results or compared to current code provisions. Prestressing strand transfer length, modulus of elasticity, prestressing losses due to elastic shortening, and effective prestressing at the time of flexural testing will be verified.

#### 3.6.1.1 Prestressing Strand Transfer Length

The strain gauge readings during detensioning were used to verify the transfer length of the 0.6-in. diameter prestressing strand. Strain gauges placed on the strands at the expected transfer length were compared to strain gauges placed at midspan. If the results from these two locations are similar, it means that the prestressing strand force is fully effective at the transfer length. If the strain gauge readings at the pile ends show a smaller drop from detensioning than at the midspan, the prestressing force has not fully transferred. Figure 3-54 depicts these strains; there is a small difference between the end-pile gauges and the gauges at midspan, and the drop from detensioning is the same for both, indicating that the prestressing force fully transfers over 15-in.

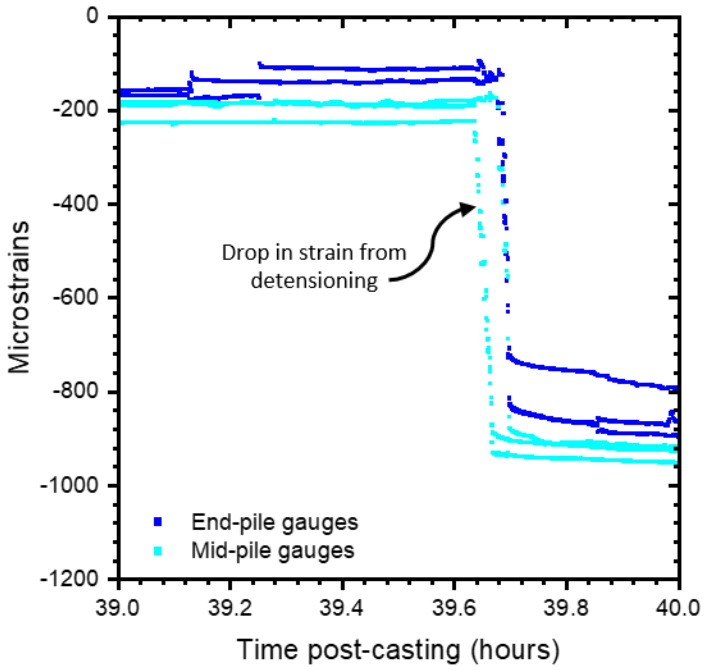


**Figure 3-54 Loss in strains during detensioning**

### 3.6.1.2 Modulus of Elasticity

The modulus of elasticity values discovered through experimental testing can be compared to the AASHTO (2017) calculation based on concrete compressive strength. The compressive strength at release was 13.9 ksi and the compressive strength when the full-strength modulus was measured was 23.4 ksi. The modulus at release and 28 days was 6052 ksi, and 6974 ksi respectively. The differences between measured to the calculated based on the code amount to 1.6 percent and 1.4 percent respectively. This suggests that the AASHTO equation for predicting the modulus of elasticity of UHPC is applicable to the UHPC used for these piles.

$$E_c = 2500(f_c)^{0.33} \quad \textbf{3-3}$$

### 3.6.1.3 Losses and Effective Prestressing

Effective prestressing is classified as the prestressing force imparted after losses. In general, prestressing losses are classified into two types: short-term and long-term. AASHTO and PCI, two of the major prestressing design guidelines, classify elastic shortening as a short-term loss and creep, shrinkage, and strand relaxation as long-term losses. PCI also includes autogenous shrinkage as a short-term loss.

The loss of prestressing that occurs during detensioning is referred to as elastic shortening. When prestressing strands are pulled to their initial stress and then released, a compressive stress is applied to the concrete member. In turn, the concrete member shortens elastically. As a result, the prestressing strands are stretched over a shorter length, and some of their prestressing is lost. Equation 3-4 shows the first principles calculations of elastic shortening losses, where the stress on concrete due to prestressing, $f_{cgp}$, is proportionately transformed to a stress loss in prestressing via the modular ratio. This method of calculating elastic shortening losses is used by both AASHTO and PCI.

$$\Delta f_{pES} = \frac{E_{ps}}{E_{ci}} * f_{cgp} \quad \textbf{3-4}$$

$$f_{cgp} = f_{pi} * \frac{A_{ps}}{A_t} \quad \textbf{3-5}$$

Using this method, the predicted elastic shortening losses for the UH12s and UH14s are 22.4 and 23.3 ksi, respectively. The strain gauge readings from detensioning were used to double-check these values. These losses are depicted in Figure 3-54 and Table 3-7. The average loss for UH12s and UH14s is 22.9 ksi and 22.0 ksi, respectively. This results in a 2.2 percent difference for the UH12s and a 5.9 percent difference for the UH14s. The predicted values in both cases are reasonably close to the results obtained during specimen fabrication.

The remainder of PCI short-term losses are due to autogenous shrinkage, or the chemical shrinkage that occurs during the hydration process. As concrete shrinks, it shortens, and the shortened concrete member allows for the loss of some prestressing, similar to the principle behind elastic shortening.

**Table 3-7 Stress loss for UH12 and UH14 internal strain gauges during detensioning**

| Gauge Name | Detensioning stress loss (ksi) | Gauge Name | Detensioning stress loss (ksi) |
|---|---|---|---|
| UH12AS_C1B | 22.7 | UH12FS_C5M | 26.7 |
| UH12AS_S2B | 20.6 | UH12FS_S4B | 20.5 |
| UH12AS_C2T | 24.6 | UH14AS_C1B | 21.8 |
| UH12AS_S4B | 21.1 | UH14FW_C4T | 18.9 |
| UH12AS_C6T | 22.9 | UH14FW_C5M | 23.3 |
| UH12FW_C4T | 24.5 | UH14FW_S4B | 21.9 |
| UH12FW_S4B | 21.0 | UH14FS_S4B | 25.3 |
| UH12FS_C4T | 24.5 | UH14FS_S1B | 20.8 |

To calculate short-term prestressing losses, PCI recommends using 300 microstrains for autogenous shrinkage of UHPC. PCI also suggests multiplying the shrinkage strain by a transform section coefficient, $K_{id}$, calculated through Equation 3-7.

$$\Delta f_{pshi} = \epsilon_{shi} E_{ps} K_{id} \quad \textbf{3-6}$$

$$K_{id} = \frac{1}{1 + \left(\frac{E_{ps}}{E_{ci}}\right) * \left(\frac{A_{ps}}{A_g}\right) * \left(1 + \left(\frac{A_g e_{pg}^2}{I_g}\right)\right) * \left(1 + 0.7\psi_{b(if)}\right)} \quad \textbf{3-7}$$

where: $\epsilon_{shi}$ = 300 microstrains for UHPC

The main factor to consider for this provision is the assumption of 300 microstrains for autogenous shrinkage prior to detensioning. The shrinkage testing discussed in Section 4.4.5 found 80 microstrains of shrinkage strain after two days, but there are no "day zero" readings that can be taken with the ASTM standard test. The shrinkage strains from casting to detensioning, on the other hand, could be examined. Two outliers, UH12AS_C1B and UH14FW_C4T, were excluded from the averages. Over the first two days before detensioning, there was an average of 170 microstrains of autogenous shrinkage, shown in Table 3-8. This is 57 percent of the value recommended by PCI, indicating that PCI is conservative on this issue. Although this is a safe practice, more research is needed with other UHPCs to confirm whether or not this recommendation is overly conservative.

**Table 3-8 Autogenous stress loss of UH12 and UH14 internal strain gauges before detensioning**

| Gauge Name | Autogenous shrinkage loss (με) | Gauge Name | Autogenous shrinkage loss (με) |
|---|---|---|---|
| UH12AS_C1B | 0 | UH12FS_C5M | 98 |
| UH12AS_S2B | 165 | UH12FS_S4B | 207 |
| UH12AS_C2T | 132 | UH14AS_C1B | 128 |
| UH12AS_S4B | 305 | UH14FW_C4T | 544 |
| UH12AS_C6T | 280 | UH14FW_C5M | 62 |
| UH12FW_C4T | 177 | UH14FW_S4B | 164 |
| UH12FW_S4B | 103 | UH14FS_S4B | 213 |
| UH12FS_C4T | 112 | UH14FS_S1B | 240 |

AASHTO and PCI long-term losses necessitate more detailed calculations. Because PCI generally defers to AASHTO, both codes provide the same overall equations, though the humidity factors for creep and shrinkage differ. AASHTO divides long-term losses into two time periods: "between transfer and deck-placement" and "after deck-placement." The time span between transfer and deck-placement is the shortest in terms of long-term losses, whereas after deck-placement proceeds until time infinity. Because the piles were tested within a few months of casting, equations for between transfer and deck-placement with a time period of 150 days were used for these piles. The time period from transfer to deck-placement can vary from weeks to months depending on the production flow at a particular precast plant, so this was deemed a reasonable time period for comparison for these piles.

$$\Delta f_{pT} = \Delta f_{pES} + \Delta f_{pLT} \quad \textbf{3-8}$$

$$\Delta f_{LT} = \Delta f_{pSR} + \Delta f_{pCR} + \Delta f_{pR1} \quad \textbf{3-9}$$

$$\Delta f_{pSR} = \epsilon_{b(id)} E_p K_{(id)} \quad \textbf{3-10}$$

$$\Delta f_{pCR} = \frac{E_{ps}}{E_{ci}} f_{cgp} \psi_{b(id)} K_{(id)} \quad \textbf{3-11}$$

$\Delta f_{pR1} = 1.2\ ksi$ for low-lax strands **3-12**

$$\epsilon_{bid} = k_s k_{hs} k_f k_{td}(t_d, t_i) K_4 * 0.6 \times 10^{-3} \quad \textbf{3-13}$$

$$K_{id} = \frac{1}{1 + \left(\frac{E_{ps}}{E_{ci}}\right) * \left(\frac{A_{ps}}{A_g}\right) * \left(1 + \left(\frac{A_g e_{pg}^2}{I_g}\right)\right) * \left(1 + 0.7\psi_{b(if)}\right)} \quad \textbf{3-14}$$

where: $K_3$ = By physical testing, otherwise 1.0

$K_4$ = By physical testing, otherwise 1.0

$k_s$ = 1.0 for UHPC

$k_{hs}$ = $1.5 - 1.0 * H$ per AASHTO, 1.0 per PCI

$k_{hc}$ = $1.12 - 0.24 * H$ per AASHTO, 1.0 per PCI

$k_f$ = $\frac{18}{1.5 * f'_{ci} - 3}$

$k_l$ = $t_i$ is less than 7 days, 1.0

$k_{td}$ = $\frac{t - t_i}{\left(\frac{300}{30 + f'_{ci}}\right) + 0.8(t - t_i)^{0.98}}$

The total losses predicted by AASHTO and PCI for the UH12s and UH14s were calculated. AASHTO predicts 64.5 ksi losses for UH12s and 65 ksi losses for UH14s, while PCI predicts 77.8 ksi losses for UH12s and 78.3 ksi losses for UH14s. This equates to effective prestressing values of 138 and 137.5 per AASHTO, and 124.7 and 124.2 ksi for PCI, respectively.

The effective prestressing was estimated using the flexural testing results to validate these findings. When UHPC begins to crack, its tensile behavior changes. This is reflected by a change in the slope of the stress vs. strain curve, as well as a change in the slope of the bottom strain vs. force curve. The piles begin with a compressive strain due to prestressing, so the experimental strain must be the tensile cracking limit strain plus the compressive effective prestressing strain combined to reach the cracking limit. The effective prestressing can then be calculated using material properties and section geometry.

$$\epsilon_{b,exp} - \epsilon_{t,cr} = \epsilon_{pe} \quad \textbf{3-15}$$

$$\epsilon_{t,cr} = \frac{f_{t,cr}}{E_c} \quad \textbf{3-16}$$

$$f_{pe} = \frac{\left(\left(\epsilon_{b,exp} - \epsilon_{t,cr}\right) * E_c * A_{transform}\right)}{A_{ps}} \quad \textbf{3-17}$$

where: All strains are positive in tension, negative in compression

This method is dependent on being able to identify the point at which the slope of the bottom strain vs. force changes, and this point was very obvious in several flexural tests. The curves for each

pile are depicted in Figure 3-55. The point where the slope changes is easily discernible for the 14-in. piles. The problem occurs with the UH12s. For UH12FS, the change in slope was very gradual, so to find a strain value within a reasonable range, tangent lines were drawn along the curve to pinpoint where the slope changes. Furthermore, UH12FW did not have any curves that could be used for this exercise. The effective prestressing was approximated as an average of 172 ksi for all piles using the three 14-in. pile curves and the one 12-in. pile curve from UH12FS. In subsequent sections, this value will be used for section analysis.

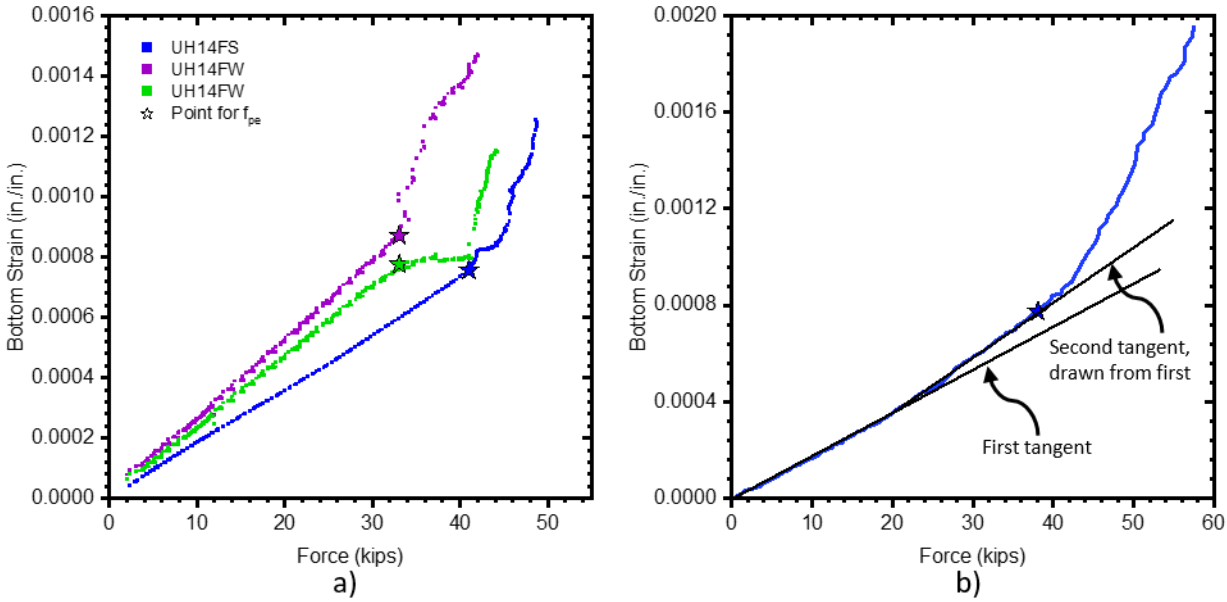


**Figure 3-55 Bottom strain vs. force used to calculate $f_{pe}$ for a) UH14s and b) UH12s**

172 ksi of effective prestressing corresponds to 30.5 ksi of losses. This is less than half of the smallest predicted losses, indicating that the current code provisions for intermediate losses are extremely conservative for these piles. This could be due to the smaller section geometry of these piles, the symmetric prestressing strand layout, or simply the fact that the current code provisions are inapplicable to UHPC piles. However, more research is needed to confirm these findings.

### 3.6.2 Flexural Testing Results

Flexural testing analysis was designed to compare experimental results to analytical models. The models were built using the first principles techniques described in Section 0 and calibrated using UHPC material properties and effective prestressing. Throughout the analysis, three tensile behaviors were considered: average, upper-bound, and lower-bound tensile stress-strain. The main elements of flexural testing investigated are moment-curvature and force-displacement.

For each flexural test, the experimental moment-curvature was calculated by creating a strain profile along the depth of the pile section at midspan. This could be accomplished using a variety of instruments, including external surface strain gauges, internal and external strain gauges, and paired LEDs. Strain gauges performed better than LEDs on the UH12s and 14s. Figure 3-56 depicts the experimental outcomes for each flexural test. Three different tensile curves' analytical moment-curvatures are also included. The experimental and theoretical moment-curvatures match perfectly in all cases.

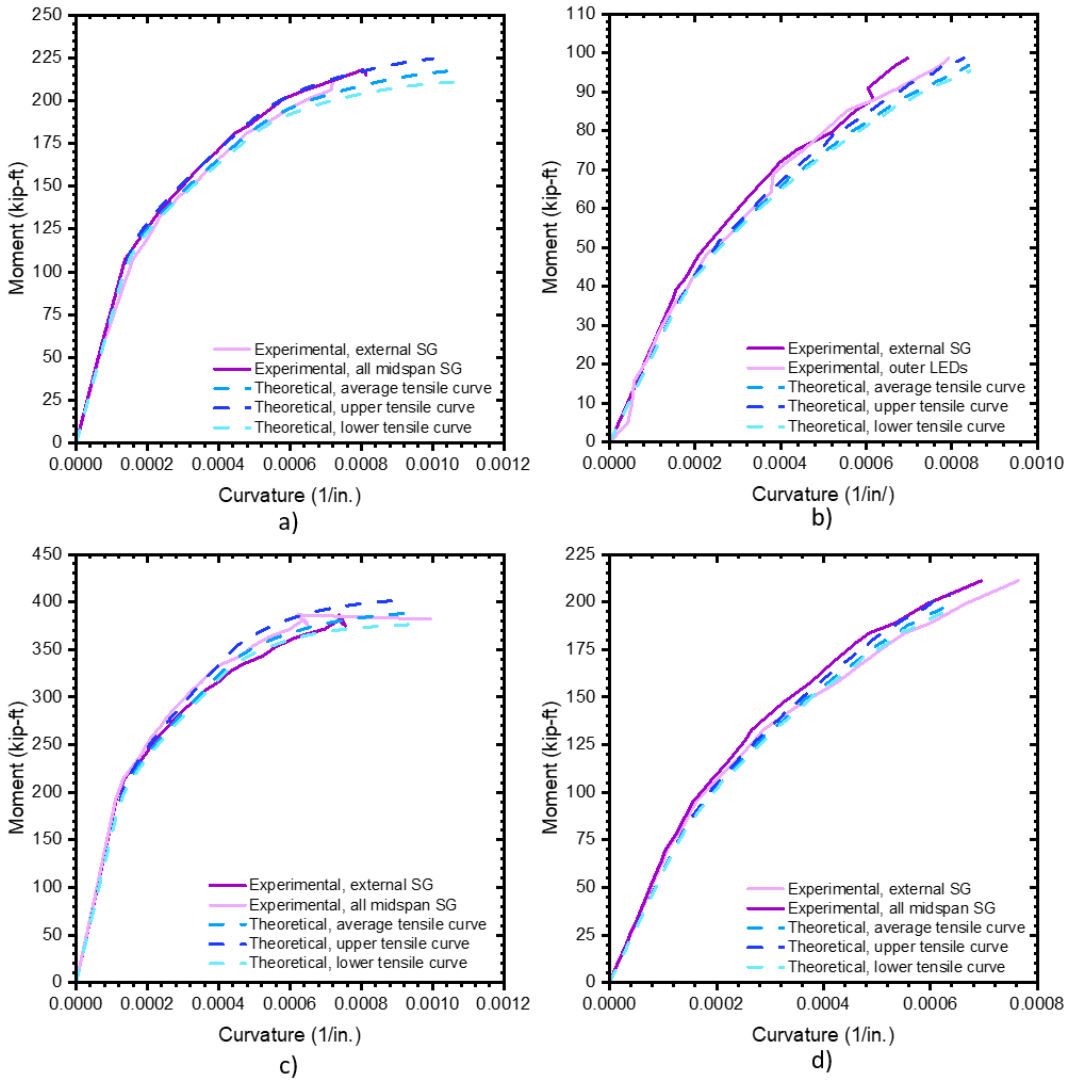


**Figure 3-56 Experimental and analytical moment-curvature comparisons for a) UH12FS, b) UH12FW, c) UH14FS, and d) UH14FW**

Force-strain was also investigated to validate the moment-curvature results. Any set of strain profiles can return the same curvature, which can be especially deceptive in piles that start with a non-zero compressive strain from the prestressing. The analytical moment-curvature top and bottom strains were compared to the experimental top and bottom strains measured with external surface strain gauges. Figure 3-57 depicts the results of each test. The experimental and analytical curves match well in most cases, especially in the elastic region. EXT_BSouth for UH12FW was one of the exceptions, as shown in Figure 3-57f. The strains did not increase as quickly for this strain gauge after about 23 kips of load. This is most likely due to the formation of a microcrack near the strain gauge. The local stresses under the strain gauge would no longer increase at the same rate once the microcrack formed, as some of the energy would be dissipated into the crack formation. Despite this flaw, the rest of the curves match reasonably well and corroborate the moment-curvature results.

Two experimental and two analytical curves were generated for force-displacement analysis. The first experimental curve is the direct force-displacement curve measured at midspan by the load

cells and string potentiometers. The subsequent force-displacement curves were calculated using various moment-curvatures, including the experimental moment curvature and the moment-curvatures generated by the average and upper tensile behavior. The moment-area method was used in these calculations in each case, with Equations 3-18 through 3-23 and symbols as shown in Figure 3-58. Because of the symmetric loading, this method can be used at any point along the length of the pile. For different loading scenarios, the equations would need to be modified.

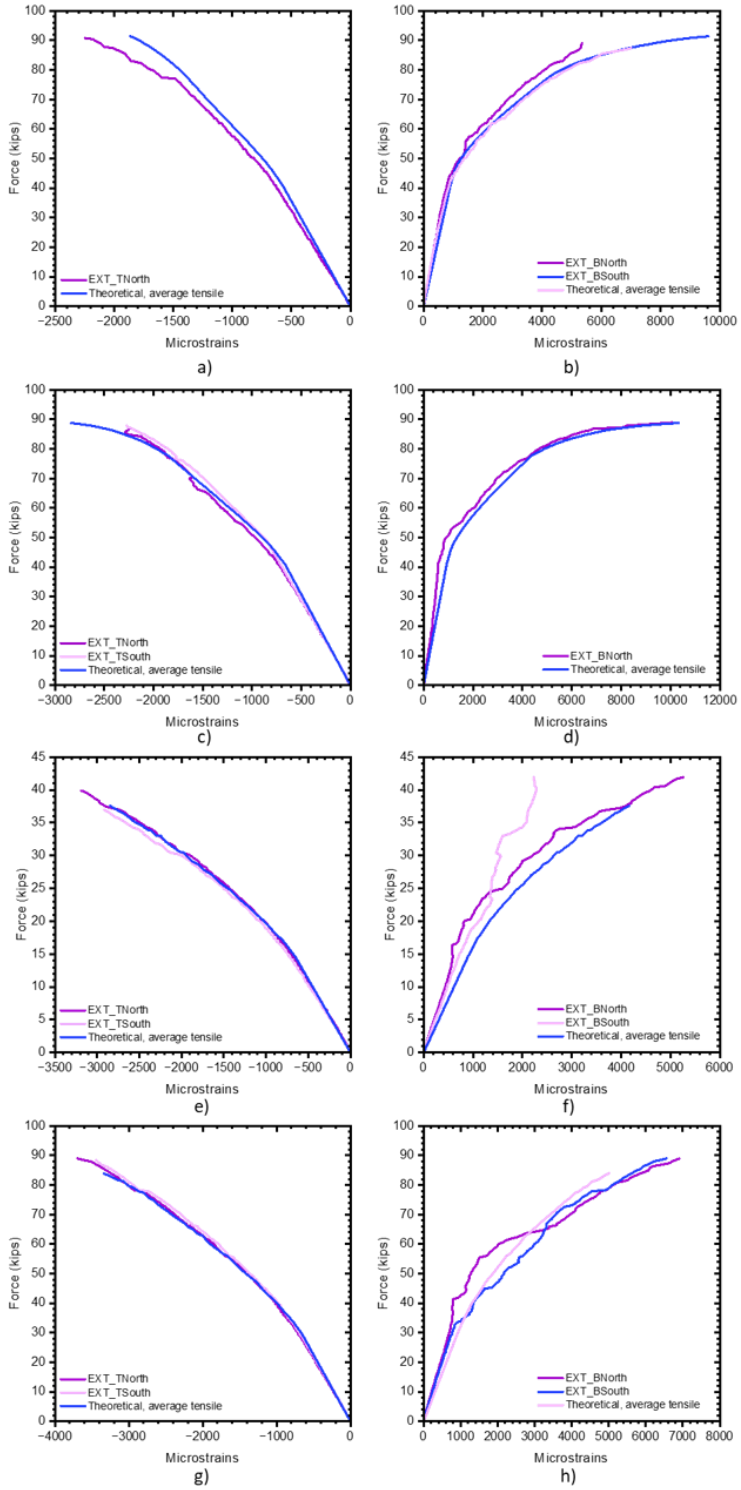


**Figure 3-57 Force vs. strain for a) top of UH12FS, b) bottom of UH12FS, c) top of UH14FS, d) bottom of UH14FS, e) top of UH12FW, f) bottom of UH12FW, g) top of UH14FW, h) bottom of UH14FW**

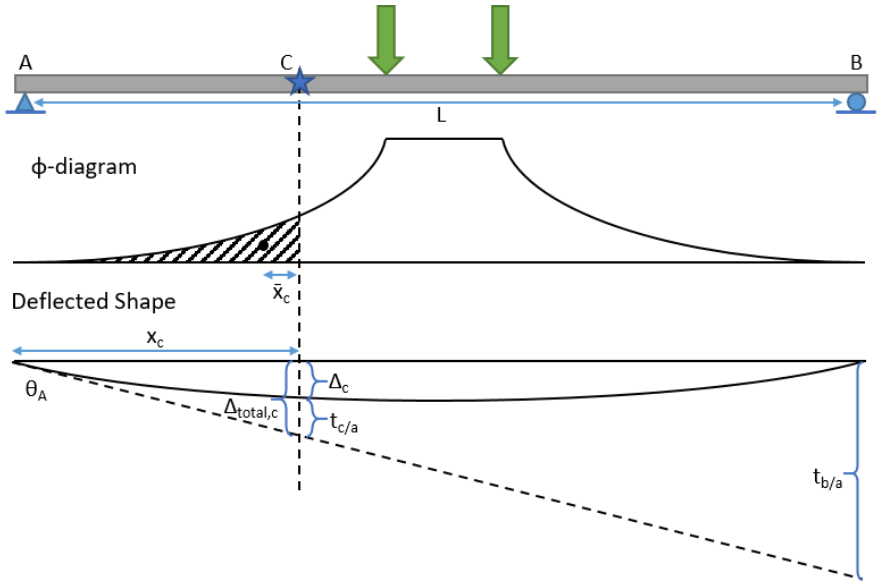


**Figure 3-58 Moment-area method for calculating flexural deflections for symmetric four-point bending.**

$$\Delta_{total,c} = \Delta_c + t_{c/a} \quad \textbf{3-18}$$

$$\Delta_{total,c} = \theta_A * x_c \quad \textbf{3-19}$$

$$\theta_A = \frac{t_{b/a}}{L} = \frac{1}{2}\int_0^L \phi \, dx \quad \textbf{3-20}$$

$$\Delta_{total,c} = \frac{x_c}{2}\int_0^L \phi \, dx \quad \textbf{3-21}$$

$$t_{c/a} = \bar{x}_c \int_0^x \phi \, dx \quad \textbf{3-22}$$

$$\Delta_c = \frac{x_c}{2}\int_0^L \phi \, dx - \bar{x}_c \int_0^x \phi \, dx \quad \textbf{3-23}$$

The force-displacement curves all match well in general, shown in Figure 3-59. By definition, the curves calculated from the experimental moment-curvature and the experimental value should show similar results; however, these two curves show the most discrepancies. This could be due to a variety of factors. First, the force-displacement back-calculation utilizes the experimental moment-curvature, which was previously approximated by determining the curvature of a line of best fit strain profile from experimental data. When data is approximated in this way and then compared to the original experimental data, some degradation is to be expected. Furthermore, as previously stated, the moment-area method for calculating displacements only accounts for flexural displacement. In reality, there is a non-zero amount of shear displacement as well. The expected elastic shear deformation at midspan is calculated using Equation 3-24. With the proper geometric properties and a Poisson's ratio of 0.2 (the upper range for UHPC), the worst-case scenario for UH14FS is 0.04-in. shear displacement. This would cause the back-calculated force-displacements to shift slightly to the right, but not sufficiently to match the string potentiometer readings.

$$\Delta_v = \gamma_v L = \frac{VL}{AG} = \frac{2VL(1+\nu)}{AE} \quad \textbf{3-24}$$

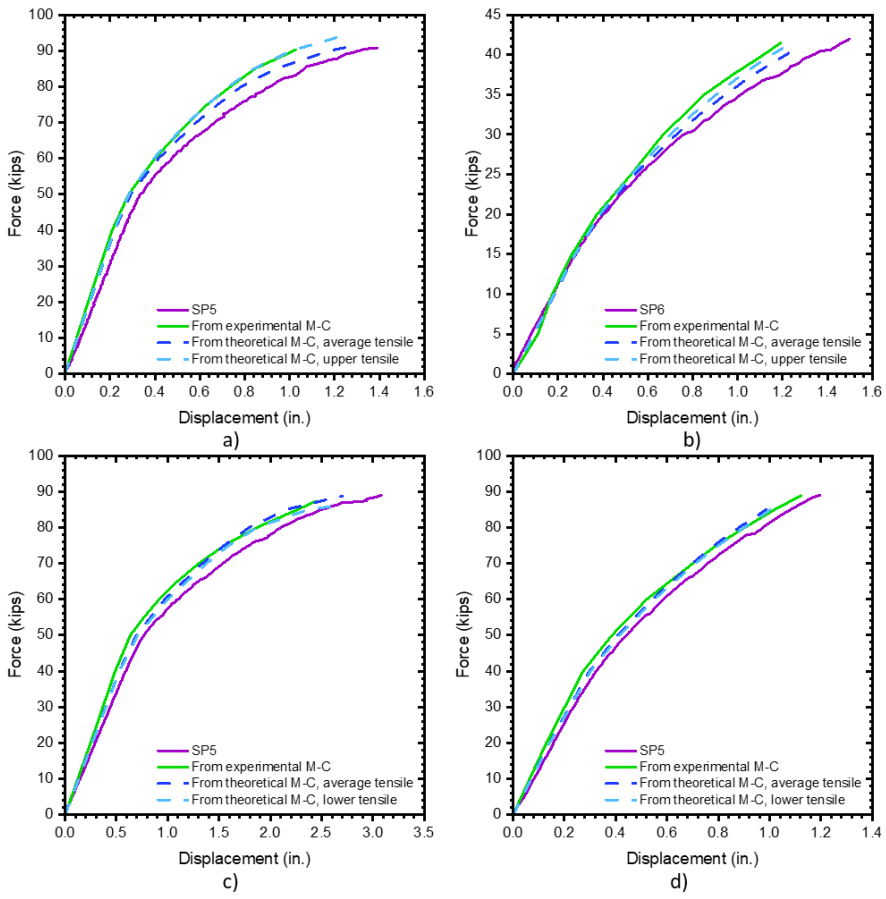


**Figure 3-59 Force-displacement curves for a) UH12FS, b) UH12FW, c) UH14FS, and d) UH14FW**

### 3.6.3 Shear Testing Results

Shear testing had two goals: first, to analyze the accuracy of current shear codes for UHPC and their applicability for these piles, and second, to determine whether transverse reinforcement was required. The AASHTO (2017) and PCI (2021) codes for UHPC were chosen for comparison. These prestressed UHPC piles are designed to be used as an alternative to steel pile sections in bridge foundations. AASHTO's LRFD design manual is the most widely used bridge design code in the United States, and PCI is a prevalent prestressed concrete design guide. Both codes use the same general equation, Equation 3-25, in which the section shear capacity is a combination of contributions from UHPC ($V_{UHPC}$), transverse reinforcement ($V_S$), and prestressing force components in the shear force direction ($V_P$). Because there is no transverse reinforcement in these piles and the prestressing strands are all straight, the UHPC is the only contributor to the sectional shear capacity. Although applying load can cause some draping of the prestressing strands and generate some $V_P$, this is a secondary effect that is generally ignored in design equations such as these. The equation for calculating the VUHPC, as described by AASHTO Equation 3-26 and PCI Equation 3-27, is similar to the process for normal concrete. The effective shear area and shear cracking angle are multiplied by the tensile strength of concrete. The tensile strength of normal concrete is simplified as a ratio of the compressive strength, but for UHPC, an actual tensile strength can be used.

The first distinction between the AASHTO and PCI codes is in the definition of tensile strength. AASHTO utilizes the localization stress, whereas PCI bases their equation on French

recommendations for UHPC fiber contribution, utilising the post-cracking residual strength. PCI recommends a value of 0.75 ksi for this value to be conservative and account for fiber orientation, size, and shape factors, as long as the UHPC meets certain material criteria. These properties include 17.4 ksi compressive strength, 1.5 ksi first cracking flexural strength, and 2.0 ksi ultimate flexural strength.

$$V_n = V_{UHPC} + V_S + V_P \quad \textbf{3-25}$$

$$V_{UHPC,AASHTO} = \min\left(0.25 f_c' b_v d_v \; and \; f_{t,loc} b_v d_v \cot(\theta_v)\right) \quad \textbf{3-26}$$

$$V_{UHPC,PCI} = \left(\frac{4}{3} f_{rr}\right) b_v d_v \cot(\theta_v) \quad \textbf{3-27}$$

$$\epsilon_s = \frac{\left(\frac{M_u}{d_v}\right) + 0.5N_u + \left|V_u - V_p\right| - A_{ps} f_{po} - f_{t,cr} A_{ct}}{E_{ps} A_{ps}} > 0.0 \; and < \epsilon_{t,cr} \quad \textbf{3-28}$$

$$\epsilon_s = \frac{\left(\frac{M_u}{d_v}\right) + 0.5N_u + \left|V_u - V_p\right| - A_{ps} f_{po}}{E_{ps} A_{ps} + E_c A_{ct}} \quad \textbf{3-29}$$

$$\epsilon_{t,loc} = \frac{\epsilon_s}{2}\left(1 + \cot^2\left(\theta_{A,Gen}\right)\right) + \frac{2 f_{t,loc}}{E_c} \cot^4(\theta_{A,Gen}) \quad \textbf{3-30}$$

$$\theta_{PCI} = 29 + 3500\epsilon_s \quad \textbf{3-31}$$

The effective shear area for each code is defined the same way, as the area formed by the effective web width and effective shear depth. The final element of the $V_{UHPC}$ equations, the shear cracking angle, is calculated for each code using different methods for AASHTO and PCI.

AASHTO allows for two methods to find theta: a general approach, and a table approach. Both begin with finding the net longitudinal strain at the centroid of the tensile reinforcement, or $\varepsilon_s$. Two equations are given to find $\varepsilon_s$ based on the load demand at the section being evaluated, Equations 3-28 and 3-29. The second equation is only to be used if the first returns a negative strain or a positive strain that is less than the cracking strain. With the heavy prestressing on these small cross-sections, the second equation typically dominates. For the first method of finding theta, once the net longitudinal strain is found, theta is calculated through an iterative set of equations. Because these piles do not use transverse reinforcement, only one equation is required to find theta, Equation 3-30. The second AASHTO method finds theta through a table of values based on $\varepsilon_s$ and the localization strain of the UHPC. For the purposes of analysis in this chapter, the shear cracking angle found using AASHTO's general approach will be called $\theta_{A,Gen}$ and the angle found using the table method will be referred to as $\theta_{A,Tab}$.

PCI determines the shear cracking angle with a similar approach. It begins by finding the net longitudinal strain, using the same equations as AASHTO but discounting any additional axial load placed on the section. These piles did not feature additional axial loads, so this did not affect the results. The net longitudinal strain is then directly used in Equation 3-31 to find the cracking angle, which will be referred to as $\theta_{PCI}$. PCI bounds their cracking angle between 27.6 and 50 degrees.

For each shear test performed on the UH12x71 and UH14x105 piles, these calculations were performed to compare both the shear cracking angles and overall shear capacity predicted by AASHTO and PCI to the values observed during experimental testing. All methods require the sectional demand to calculate the longitudinal strain. Although the critical section is often defined as a distance $d_v$ from the support, (the effective shear depth) the localized shear crack did not always occur at this location in experimental testing. To determine which section to examine, the angle for

AASHTO's general approach, $\theta_{A,Gen}$, was calculated at four locations: $d_v$, the beginning of the localized shear crack, the midpoint of the localized shear crack, and the end-point of the localized shear crack. The start and endpoints were defined as the point where the primary localized shear crack began angling into the web and the point where the localized shear crack met the top flange, respectively. The mid-point was defined as halfway between the start and end, with an example shown in Figure 3-60. Results from this study, shown in Table 3-9, indicate that the shear cracking angle varied by less than a degree for each specimen, which would result in a maximum of a 5% difference in ultimate shear capacity. Because the location did not prove to have a large effect on the capacity calculations for these piles, the mid-crack location was used for the rest of the calculations. During experimental testing, the web-shear cracks often first localized near the mid-point of the web, and the moment demand at this point is close to the average between the crack-start and crack-end, making it a suitable point to examine.

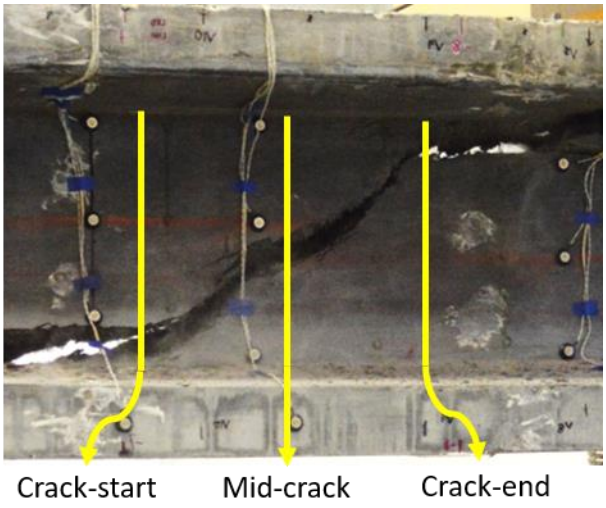


**Figure 3-60 Shear crack angle calculation points**

For each shear test, the three shear cracking angles were calculated according to AASHTO and PCI specifications and compared to the angles observed during lab testing, with results shown in Table 3-10. AASHTO's general approach was found to be the most conservative, but across the board, the experimental angles were larger than those calculated, corresponding to a lower predicted shear capacity. UH12FS_V2 was the only exception, where the angle was the same as that calculated by AASHTO's table method and PCI's general approach.

More important than the angle, however, is the expected shear capacity for each section. This was found using the code equations, but with the various angles already calculated for each code. For AASHTO, the shear capacity was calculated with $\theta_{A,Gen}$, $\theta_{A,Tab}$, and the experimental angle, $\theta_{Exp}$. For PCI, the shear capacity was calculated with $\theta_{PCI}$ and $\theta_{Exp}$. All of these values, shown in Table 3-11, are conservative compared to the experimental shear capacities.

Table 3-12 provides the unity ratio of the experimental shear capacity by the nominal code capacities, $V_{exp}/V_n$, every value is greater than 1.00, meaning the code predictions are conservative. Between the two codes, AASHTO better predicts the capacities of each pile compared to PCI. This is unsurprising considering PCI restricts the tensile contribution of UHPC to a flat 0.75 ksi, whereas AASHTO allows the use of the UHPC localization stress. In the case of these piles, PCI only predicts

half of the experimental pile capacity, whereas AASHTO predicts roughly 75% of the experimental strengths observed.

Ultimately, the concern lies with the borderline cases. The 14-in. piles which failed in web-shear, UH14FS_V2 and UH14FW_V1, failed at similar shear loads and well out-performed the code expectations, with the smallest unity values over 1.6. UH14FS_V1 failed in web-shear, at a lower capacity, with unity values as small as 1.22. This indicates that for the 14-in. piles, as long as the flexural capacity is not reached, web-shear will be the primary failure mode, even when up to 82% of the flexural moment capacity is applied (Table 3-6). The code equations are very conservative for the web-shear failure mode.

For the 12-in. piles, the code equations are closer to the experimental values, while still conservative. No flexural-shear failures occurred for these piles, despite applying up to 86% of the flexural moment capacities (Table 3-6), indicating that this failure mode is unlikely to happen for these piles with heavy prestressing in this loading configuration.

**Table 3-9 Effect of shear section location on AASHTO shear crack angle calculations.**

| | UH14FS_V1 | UH14FS_V2 | UH14FW_V1 | UH12FW_V1 | UH12FW_V2 | UH12FS_V1 | UH12FS_V2 |
|---|---|---|---|---|---|---|---|
| $M_{u@dv}$ (k-ft) | 8.10 | 199.51 | 196.90 | 92.60 | 87.38 | 92.29 | 79.29 |
| $\theta_{A,Gen}$ (degrees) | 24.65 | 25.78 | 25.76 | 25.5 | 25.4 | 25.48 | 25.3 |
| $M_{u@CrackStart}$ (k-ft) | 117.98 | 117.36 | 46.33 | 60.27 | 24.39 | 34.34 | 59.31 |
| $\theta_{A,Gen}$ (degrees) | 25.16 | 25.38 | 25.05 | 25.23 | 24.9 | 25.02 | 25.13 |
| $M_{u@MidCrack}$ (k-ft) | 179.96 | 195.47 | 146.77 | 103.37 | 69.06 | 77.27 | 110.82 |
| $\theta_{A,Gen}$ (degrees) | 25.45 | 25.75 | 25.52 | 25.58 | 25.25 | 25.37 | 25.55 |
| $M_{u@CrackEnd}$ (k-ft) | 242.00 | 273.77 | 246.47 | 146.48 | 113.83 | 120.23 | 161.99 |
| $\theta_{A,Gen}$ (degrees) | 25.75 | 26.15 | 26 | 25.94 | 25.62 | 25.71 | 25.97 |

**Table 3-10 Shear cracking angles calculated through different methods.**

| | | UH14FS_V1 | UH14FS_V2 | UH14FW_V1 | UH12FW_V1 | UH12FW_V2 | UH12FS_V1 | UH12FS_V2 |
|---|---|---|---|---|---|---|---|---|
| AASHTO | $\theta_{A,Gen}$ | 25.45 | 25.75 | 25.52 | 25.58 | 25.25 | 25.37 | 25.55 |
| | $\theta_{A,Table}$ | 27.49 | 27.76 | 27.55 | 27.60 | 27.32 | 27.42 | 27.57 |
| PCI | $\theta_{PCI}$ | 27.81 | 28.32 | 27.92 | 28.01 | 27.60 | 27.65 | 27.95 |
| Experimental | $\theta_{Exp}$ | 34 | 35 | 29 | 28 | 29 | 30 | 27 |

**Table 3-11 Pile shear capacities through different code calculations**

| | Angle | UH14FS_V1 | UH14FS_V2 | UH14FW_V1 | UH12FW_V1 | UH12FW_V2 | UH12FS_V1 | UH12FS_V2 |
|---|---|---|---|---|---|---|---|---|
| AASHTO | $\theta_{A,Gen}$ | 112.5 | 111.0 | 112.2 | 78.6 | 79.8 | 79.3 | 78.7 |
| | $\theta_{A,Table}$ | 102.9 | 101.7 | 102.6 | 72.0 | 72.8 | 72.5 | 72.0 |
| | $\theta_{Exp}$ | 79.4 | 76.5 | 96.6 | 70.8 | 67.9 | 65.2 | 73.8 |
| PCI | $\theta_{PCI}$ | 72.5 | 71.0 | 72.2 | 50.5 | 51.4 | 51.3 | 50.6 |
| | $\theta_{Exp}$ | 56.7 | 54.6 | 69.0 | 50.5 | 48.5 | 46.5 | 52.7 |
| Experimental | -- | 137.8 | 184 | 182.6 | 102.3 | 96.5 | 101.9 | 89.4 |

**Table 3-12 Unity tables for shear code capacities vs. experimental capacities ($V_{exp}/V_n$)**

| | ANGLE | UH14FS_V1 | UH14FS_V2 | UH14FW_V1 | UH12FW_V1 | UH12FW_V2 | UH12FS_V1 | UH12FS_V2 |
|---|---|---|---|---|---|---|---|---|
| AASHTO | $\theta_{A,Gen}$ | 1.22 | 1.66 | 1.63 | 1.30 | 1.21 | 1.28 | 1.14 |
| | $\theta_{A,Table}$ | 1.34 | 1.81 | 1.78 | 1.42 | 1.33 | 1.40 | 1.24 |
| | $\theta_{Exp}$ | 1.74 | 2.41 | 1.89 | 1.45 | 1.42 | 1.56 | 1.21 |
| PCI | $\theta_{PCI}$ | 1.90 | 2.59 | 2.53 | 2.02 | 1.88 | 1.99 | 1.77 |
| | $\theta_{Exp}$ | 2.43 | 3.37 | 2.65 | 2.02 | 1.99 | 2.19 | 1.69 |
| Experimental | -- | 1.00 | 1.00 | 1.00 | 1.00 | 1.00 | 1.00 | 1.00 |

# 4 DEVELOPMENT AND STRUCTURAL CHARACTERIZATION OF A 16 in. UHPC PILE ALTERNATIVE TO PRESTRESSED NORMAL CONCRETE PILES

## 4.1 Introduction

Due to their greater durability, increased load-bearing capacity, and resistance to harsh coastal conditions, Ultra-High-Performance Concrete (UHPC) piles offer a compelling alternative to conventional square normal concrete piles in maritime situations. A material with high compressive strength and impermeability is produced by the distinctive composition of UHPC, which is defined by an optimum combination of cementitious materials, fine aggregates, fibers, and water-reducing admixtures. UHPC's impermeability shields against the entry of chloride ions and other corrosive agents in the corrosive and erosive maritime environment, thereby reducing the risk of reinforcing corrosion that frequently afflicts traditional concrete piles. When compared to their square concrete equivalents, UHPC piles have the potential to have a much longer service life due to their increased resilience.

Owing to its exceptional compressive and flexural strengths, UHPC piles have a greater load-bearing capacity, which is one of their main advantages. These characteristics make UHPC piles a superior option for marine constructions subject to dynamic forces from waves, currents, and tides because they enable them to endure greater vertical and lateral loads. Due to its high ductility and energy-absorbing qualities, UHPC performs better during extreme occurrences like earthquakes or hurricanes, making it a safe and dependable choice for marine infrastructure projects. When compared to regular concrete square prestressed piles, UHPC's inherent toughness can offer much better capacities while enabling section optimization to reduce pile weight. Construction sequences may be more effective if pile weight is lower.

This chapter's goal is to provide a design and experimental testing description of a UHPC substitute for the typical concrete prestressed piles typically employed in maritime conditions. The experimental methodologies for material testing, flexural testing, and shear testing will be discussed after a description of the section design and pile production. The outcomes of these tests will then be examined, and conclusions will be made.

## 4.2 Section Design

A UHPC pile's development process began with the definition of some design objectives. The primary goal was to create a replacement for the 16-in. square standard concrete precast, prestressed pile. This pile is used frequently by several DOTs, especially where marine conditions are prevalent. The ideal UHPC pile would have an optimized shape to save weight without compromising strength while yet maintaining the same overall dimensions to allow for the use of the same driving equipment. An alternate pile should take advantage of the inherent tensile capabilities of UHPC. These piles would also need to be compatible with the current construction techniques used in precast plants and, ideally, not require any additional shear reinforcing to keep pile costs down. To aid with section design, previous literature was consulted. Researchers at Iowa State developed a 10-in. UHPC H-pile. (T. Vande Voort, 2008) Although replacing the HP10x57 steel pile—rather than a concrete pile—was the main objective of their UHPC section, the whole design procedure served as inspiration.

### 4.2.1 Design Parameters

Three major elements were considered for section design: material properties, section shape, and strand properties, including size, cover, and spacing. The minimal design properties advised by AASHTO's UHPC guidelines were used to determine the material properties for the concrete stress-strain curves. This comprised a localization stress of 0.75 ksi in tension and an ultimate compressive strength of 17.5 ksi. The ultimate strains in compression and tension came from prior UHPC testing carried out in the Large-Scale Structures Lab at the University of Alabama, not from any recommended guidelines. The suggested AASHTO equation for UHPC was used to calculate an approximate modulus of elasticity. Figure 4-1 depicts the bilinear compressive curve and trilinear tension curve that are employed in design. Equations provided by the Precast Concrete Institute (PCI) for 270 ksi prestressing strand were used to predict the stress-strain behavior of the prestressing strand. Figure 3-2 and Equations 3-1 and 3-2 and describe the stress-strain behavior of prestressing strand.

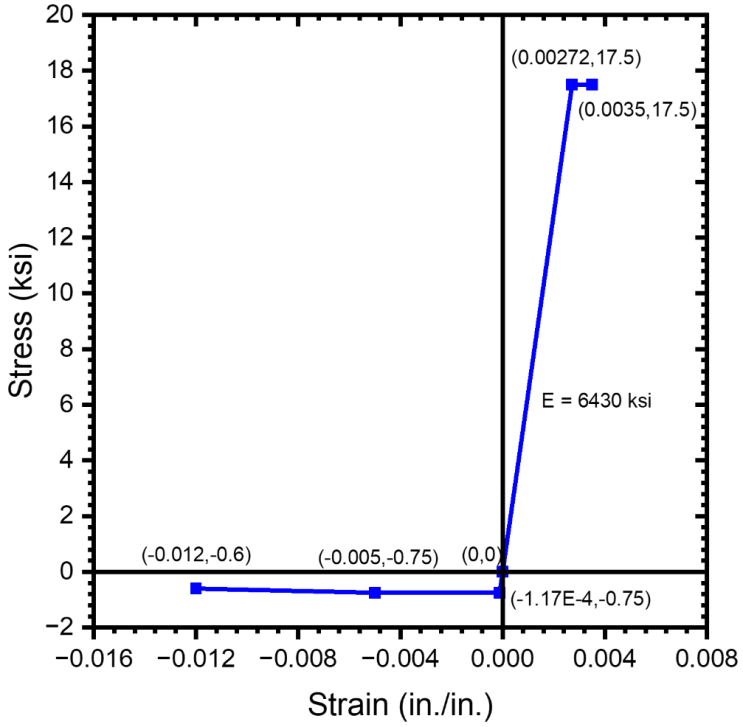


**Figure 4-1 Design UHPC material properties used for the design of 16 in. UHPC pile alternative (positive for compression)**

Once the design material specifications for UHPC and the prestressing strand were determined, the section shape was determined. In a solid piece, the compressive capabilities of UHPC would be ineffective. Because of UHPC's strong compressive strength, huge cross-sectional areas seen in traditional concrete piles are unneeded, despite the fact that end-bearing piles gain capacity with larger cross-sectional areas. Furthermore, using a solid cross-section would increase the cost while delivering no benefit because UHPC has a higher material cost than normal concrete. Hollow portions were also considered, although these require more precise formwork and complicated demolding techniques.

Based on the unsuitability of solid and hollow sections, and based on previous research, the H-section was considered. An H-shape is significantly easier to produce and construct, and will still

attain adequate flexural and shear capacities, without sacrificing material cost. However, an H-shape with straight edges, or where the flanges have a constant thickness across the entire section width, would be more difficult to demold, and would not allow for air to escape on the upper surface of the bottom flanges. Thus, a tapered H-shape was chosen, where the flanges would gradually increase in thickness along the width to the web. This would prevent stress concentrations where the flanges meet the web, as well as allow a more natural path for air in the bottom flanges to escape during casting.

The strand details, including size, cover, and spacing, was the final aspect to consider. For this pile, 0.6-in. strands were chosen to maximize the amount of prestressing that could be applied to the area. When no external force is applied, there is increased compressive stress with more prestressing. When tensile tensions are formed in the pile head during the driving operation, this is advantageous. More prestressing would allow the piles to be driven with greater force without tensile cracking. Previous research has indicated that less cover is required for UHPC sections compared to normal concrete (T. Vande Voort, 2008). To continue to optimize the cross-sectional area, the minimum amount of cover, 1.0-in., was used. The typical strand spacing of 2-in., or multiples of 2-in. was used both horizontally and vertically.

### 4.2.2 Final Section Details and Predicted Capacities

Figure 4-2 depicts the completed 16-in. pile cross section. This pile section was named using the same convention as HP steel sections. The name begins with UH, which stands for UHPC H-pile, and is followed by 16, which is the nominal section depth, and 151, which is the weight in pounds per linear foot. As a result, the full name is UH16x151. The section measures 16 inches wide by 16.75-in. deep and has fourteen 0.6-in. prestressing strands. On these strands, the initial prestressing was 202.5 ksi, or 75% of the strand strength. For these sections, no transverse reinforcement was specified, and only the UHPC contribution was incorporated for section shear strength. Table 4-1 compares the characteristics of the UH16x151 section to those of its standard concrete counterpart. The UH16x151 is 43% lighter than the 16-in. pile and provides five times the initial prestressing.

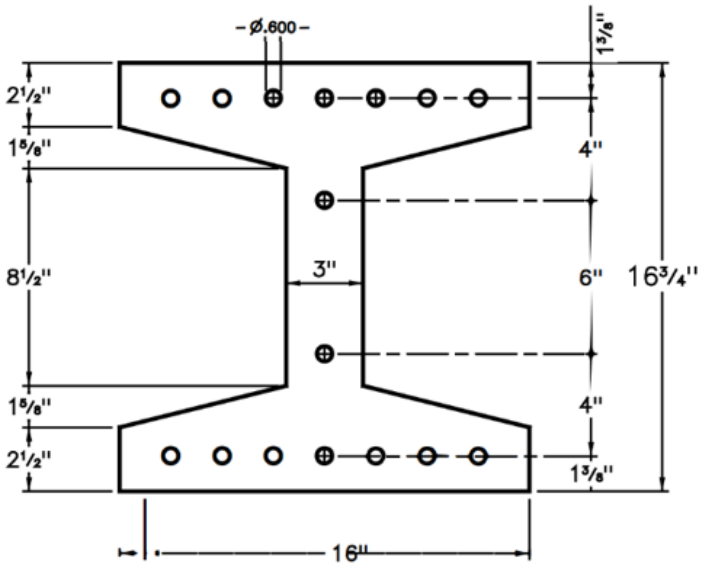


**Figure 4-2 UH16x151 final section details**

Using the previously described design material properties, a spreadsheet was created to determine both the moment-axial interaction and the moment-curvature behavior of the UH16x151 section. The tensile properties of UHPC were accounted for using first-principles prestressed concrete section analysis. This analysis is discussed in greater depth in Chapter 4. Twelve different scenarios for moment-axial interaction were investigated, ranging from pure flexure with zero axial stress to pure compression with zero applied moment. According to AASHTO LRFD guidelines, phi-factors were used to reduce capacity for safety considerations. These interaction diagrams for strong and weak-axis bending were compared to the interaction diagrams created for typical ALDOT 16-in. normal concrete piles with (8)-0.5-in. prestressing strands. For instances with no additional axial load, the moment-curvature was examined. The expected failure mode in both strong-axis and weak-axis bending was compressive failure and concrete crushing in the extreme compressive fibers. As illustrated in Figure 4-3 and Figure 4-4, UH16x151 has substantially larger capabilities in both the strong-axis and weak-axis bending orientations.

**Table 4-1 Properties of 16-in. normal concrete (NC) square pile and UH16x151**

| Property | 16-in. square NC pile | UH16x151 |
|---|---|---|
| Weight (lb/ft) | 267 | 151 |
| Cross-sectional area ($in^2$) | 256 | 136 |
| Initial prestressing on section (ksi) | 0.97 | 5.16 |

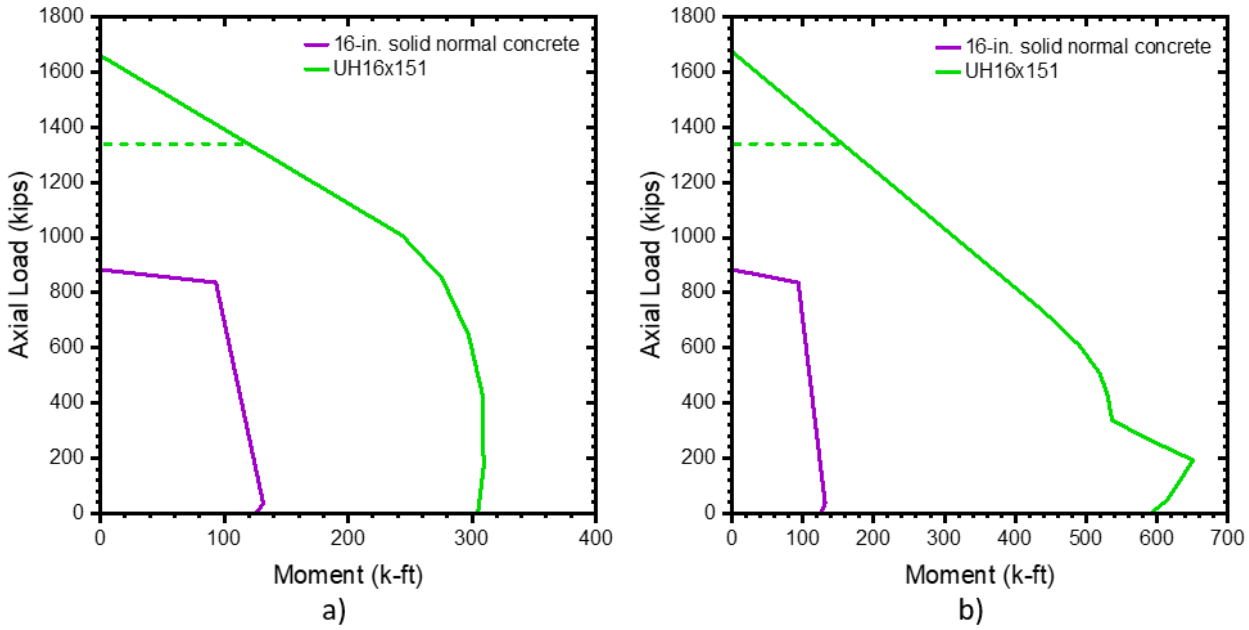


**Figure 4-3 Axial-moment interaction diagrams for a) strong-axis flexure and b) weak-axis flexure**

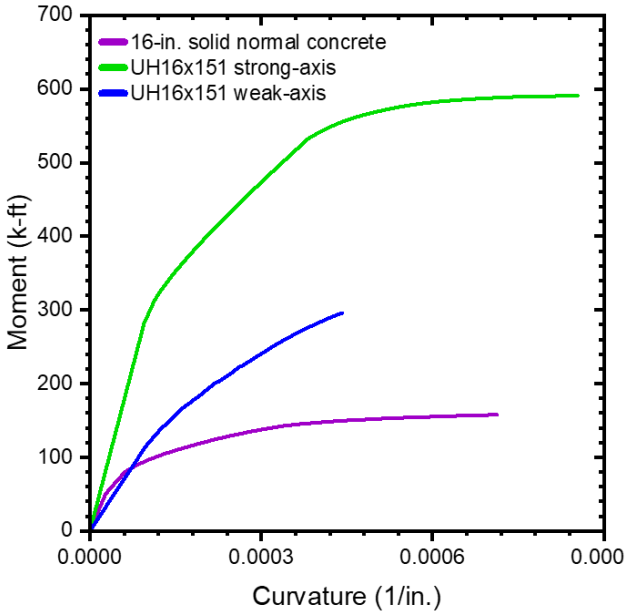


**Figure 4-4 Moment-curvature for UH16x151 without external axial load**

## 4.3 Pile Fabrication

Five full-scale UH16x151 piles were developed and precast by a manufacturer in Tampa, Florida, and afterwards tested at the University of Alabama's Large-Scale Structures Lab in Tuscaloosa, Alabama, USA. One pile was used for strong-axis flexural testing, another for weak-axis flexural testing, and three shorter piles were used to monitor losses and undertake future shear testing. The longer piles were 24-ft and 16-ft long, while the shorter piles were 6-ft long. Initially, the 24-foot pile was labeled UH16-24, while the 16-foot pile was labeled UH16-16. During the experimental phase, their names were modified to UH16FS (Flexural, Strong-axis testing) and UH16FW (Flexural, Weak-axis testing), respectively. UH16-6.1, UH16-6.2, and UH16-6.3 were the names of the three shorter piles. The longer piles were designed with one end tapering into a solid square block section, and the other end retaining the H-section shape. This was intended to evaluate the difference in behavior between the block-end and the free-end in shear testing. Figure 4-6 shows a 3D mockup of all experimental piles.

The casting of the UH16s was done on October 26th, 2022, at the Standard Precast®'s production facility in Tampa. A member of the University of Alabama study team flew to Tampa two days before pouring to outfit each pile with internal instrumentation, including foil and embedded strain gauges. While the piles were in Tampa, these gauges fulfilled a variety of functions. They were first used to confirm the transfer length of the prestressing strands at the ends of the larger piles, ensuring that the entire effective prestressing force had been transferred to the UHPC pile section. Second, they captured the change in concrete stresses prior to prestressing strand detensioning, which allowed for an assessment of current provisions for losses in UHPC. The gauges were also used to detect the strain change in the prestressing strands during detensioning, allowing the researchers to calculate elastic shortening losses. Sufficient instrumentation was necessary for later experimental testing to record the full response of the piles during flexural and shear lab testing.

An instrumentation plan was developed to achieve these goals. The majority of the strain gauges were centered at the midspan and its adjacent area, including gauges set along the section depth at the top-strand, bottom-strand, and lower-web strand levels. The bulk of gauges used to collect

strains on the UHPC section were embedded concrete gauges, however a foil gauge was also placed at midspan to measure the PT strand strain. In addition, foil gauges were placed at each end of the lengthier piles, equal to the expected transfer length of 15-in. As shown in Table 4-2, all gauges were labeled after the type of material monitored (S for strand, C for concrete), the position in feet along the length of the pile, and the strand level in the pile's depth (T for top, M for middle, and B for bottom). A gauge measuring strains in concrete, for example, located 11 feet from the pile end on the top strand level would be designated as C11T. Instead of a precise location in feet, the gauges set at the predicted transfer length of the strands were labeled Lt. Figure 4-5 and Figure 4-6 provide schematics of the exact gauge locations for each pile, as well as photographs of the various types of equipment utilized in the piles.

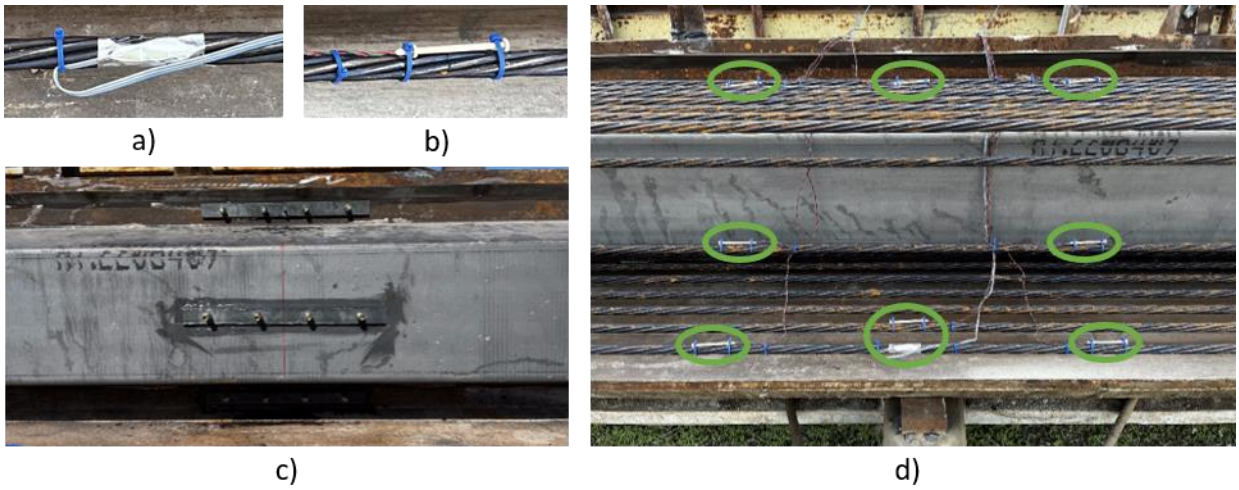


**Figure 4-5 Sample internal pile instrumentation for UH16s: a) foil gauge on strand b) concrete gauge on strand c) DEMEC template on side forms d) midspan strain gauge samples**

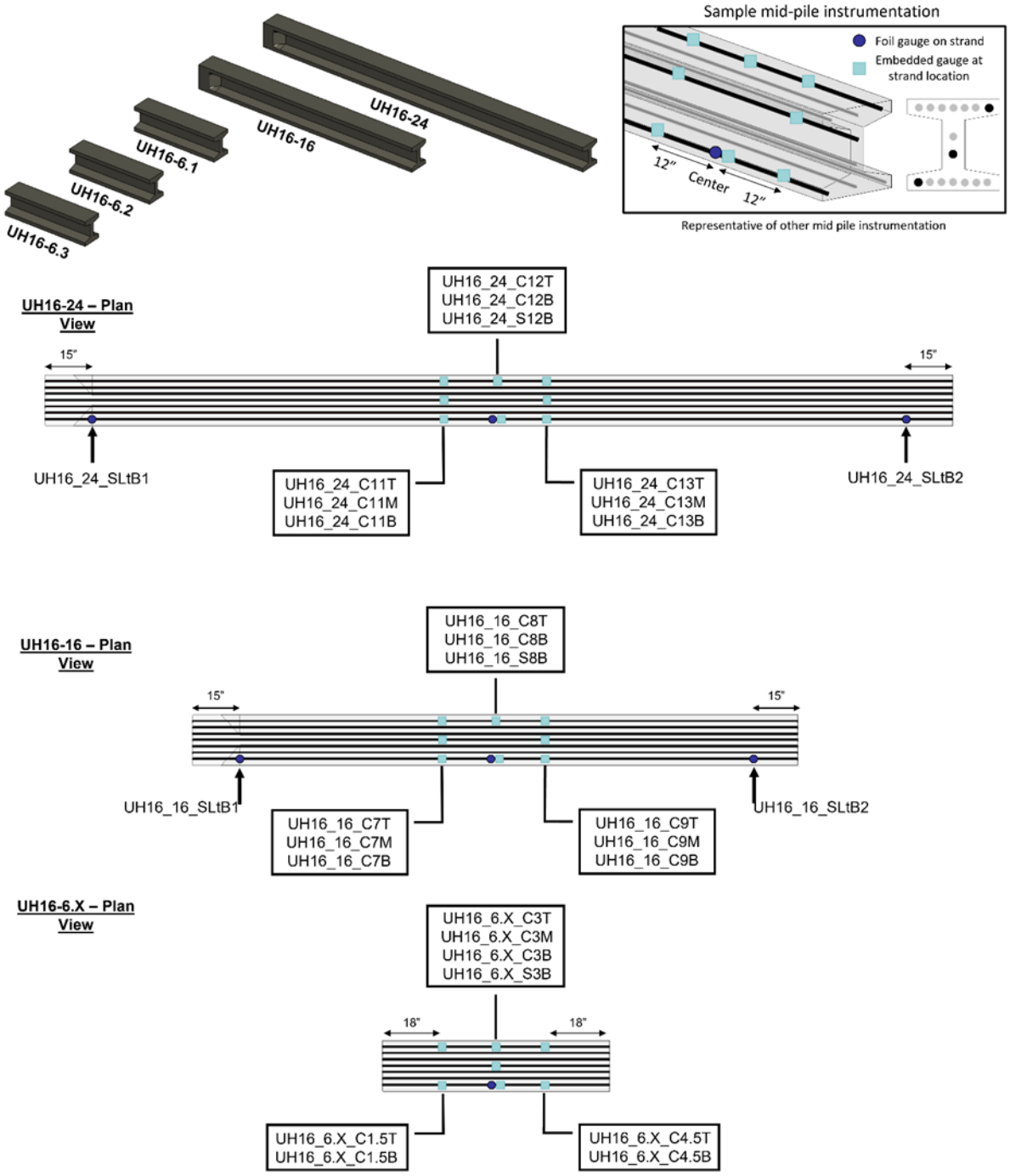


**Figure 4-6 Schematic of piles and internal instrumentation locations**

**Table 4-2 16-in. pile internal strain gauge names**

| Pile UH16_24 Gauge Name | Pile UH16_16 Gauge Name | Pile UH16_6.1 Gauge Name | Pile UH16_6.2 Gauge Name | Pile UH16_6.3 Gauge Name |
|---|---|---|---|---|
| SLtB1 | SLtB1 | C1.5T | C1.5T | C1.5T |
| C11T | C7T | C1.5B | C1.5B | C1.5B |
| C11M | C7M | C3T | C3T | C3T |
| C11B | C7B | C3M | C3M | C3M |
| C12T | C8T | C3B | C3B | C3B |
| C12B | C8B | S3B | S3B | S3B |
| S12B | S8B | C4.5T | C4.5T | C4.5T |
| C13T | C9T | C4.5B | C4.5B | C4.5B |
| C13M | C9M | | | |
| C13B | C9B | | | |
| SLtB2 | SLtB2 | | | |

The shorter piles also included threaded inserts cast into them for DEMEC gauge readings, which were used to capture shrinkage following casting and detensioning. DEMEC is an abbreviation for Demountable Mechanical Strain Gauge, which is a non-electronic method of measuring strains over time. The DEMEC gauge is a dial gauge with conical points on the ends attached to an invar bar. These conical points are aligned with tiny discs that have corresponding indentations. On each short pile, six DEMEC insert templates were inserted, one at the front and rear of the top flange, one at the front and back of the web, and one at the front and back of the bottom flange, all at midspan. Figure 4-7 depicts photos of the DEMEC gauge, template, and screw area.

Figure 4-5 depicts three of these templates joined to the side forms. As a precaution, each location received two sets of inserts, so that if any were broken during the casting process, measurements could still be obtained with the remaining screws. These inserts are discussed in the fabrication section of this chapter, but the long-term results will be studied in future research.


**Figure 4-7 a) DEMEC gauge b) DEMEC template with threaded inserts c) screws with inlaid DEMEC disks and threaded inserts**

In terms of fabrication, steel side formworks were built for casting in the strong-axis orientation, with wooden header boards used to arrange the 16 prestressing strands. After installing one steel side-form on the prestressing bed, all strands were pulled through the twelve header boards and stressed to 202.5 ksi, or 75% of their ultimate strength. Before joining the opposite side-form and closing the section, all internal instrumentation was applied, with embedded concrete gauges lightly zip-tied to the strands and 1-mm foil steel gauges glued to the stressed PT strands. Because the foil gauges were short enough in length, they could be positioned so that they sat evenly in the direction of the prestressing on a single wire without significant curvature. The flat DEMEC template pieces were secured to the side forms on the shorter piles with high-strength double-sided tape, and the edges were sealed with silicone caulk to prevent UHPC from leaking to the exterior of the inserts during casting and removal during demolding.

After taking initial gauge readings, the other side forms were fastened to the prestressing bed. To make side form removal easier after casting, 3/4-in. tapered edges were created by placing wooden triangular pieces along the length of each pile at the corners, as shown in Figure 4-8a. The space between each set of header boards between two separate piles was filled with sand to prevent the boards from kicking out during casting and leaking UHPC. All gaps in the forms were also filled with silicone caulk. Three vibrators were welded to the prestressing bed next to the pile formwork at this time for use during casting.

Aside from the pile formworks, formworks for ten direct tension and eight four-point bending specimens were built to characterize the tensile strength of the UHPC. Cylinders measuring 4-in. by 8-in. (4x8) and 3-in. by 6-in. (3x6) were cast. Because the precast facility in Tampa lacked the equipment to test 3x6 cylinders, 4x8 cylinders were evaluated for compressive strength during detensioning. All subsequent strength tests were carried out with 3x6 cylinders.

On pour day, about two hours before UHPC mixing commenced, another set of initial readings of all internal gauges were collected to get a baseline reading on the same day as casting. The UHPC cast and poured for this project was the precast company's in-house mix. To pour the needed volume, two batches of 1.6 cubic yards of UHPC were required, and both batches were mixed in sequence and placed into the same Tuckerbilt concrete transporter. After that, the Tuckerbilt transporter was driven about 0.5 mile to the prestressing bed. The piles were cast in the following order along the bed length: UH16-16, UH16-24, the three shorter piles, and an additional 84-foot pile

requested by the precast maker but not shipped to the lab in Alabama. Placement began with putting UHPC into the formwork and allowing it to flow. When UHPC filled the dumping location, the Tuckerbilt truck moved a few feet to resume pouring (Figure 4-8d). During casting, the prestressing bed was vibrated for approximately 10 seconds at a time. After finishing the pile surfaces with spiky rollers (Figure 4-8e), they were immediately covered with a heavy tarp. Material testing specimens were cast back at the batch factory at the same time, with UHPC straight from the mixer.


**Figure 4-8 Fabrication of UH16s: a) wooden header boards, b) metal sideforms with PT strands, c) concrete batch plant, d) Tuckerbilt truck pouring UHPC, e) finished 6-ft pile, f) pile surface finishing.**

Internal strain gauges readings were recorded for three hours, starting one hour after casting, and continuing throughout the day. On October 28th, two days after UHPC pouring, the compressive strength was checked and found to be 12.6 ksi, which was sufficient for detensioning. The side forms and steel DEMEC templates were removed, and the screws with inlaid DEMEC inserts were replaced, then the first DEMEC readings were taken. Detensioning the strands in the order depicted in Figure 4-9 was accomplished using two blowtorches, one at each end of the prestressing bed. After the ends of the beds were freed, the following set of strands inward were released, and so on

until all strand connections between piles were severed. Internal strain was monitored throughout the entire detensioning process.

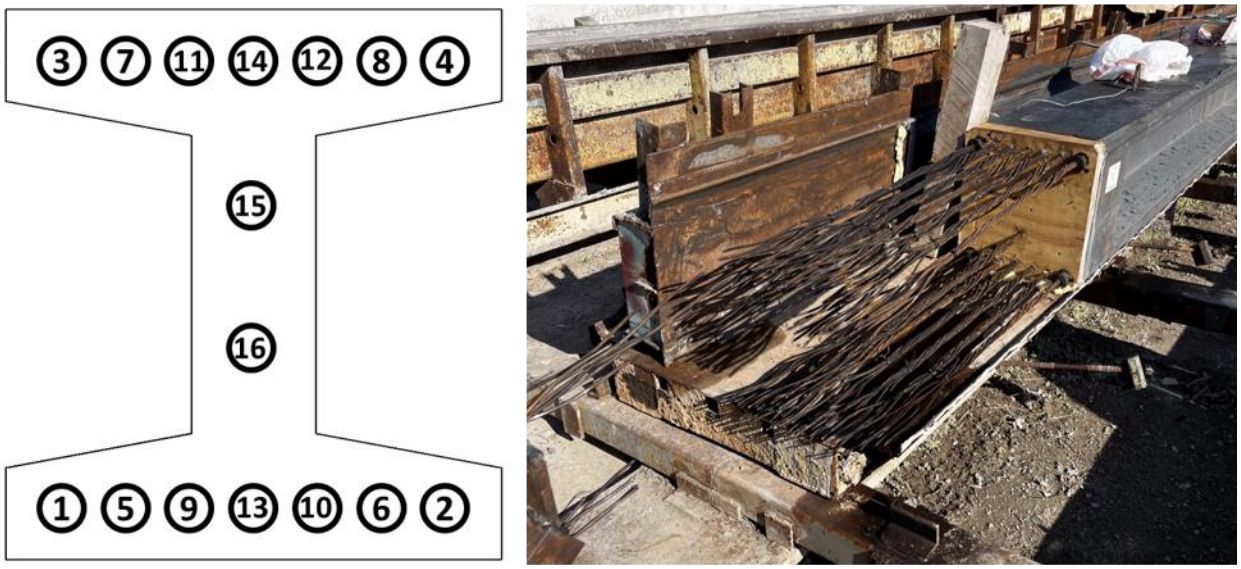


**Figure 4-9 Pile detensioning pattern and cut strands.**

After the strands were cut, a second set of DEMEC gauge readings were taken, and the strain gauge monitoring equipment was removed. The piles were subsequently carried to Tuscaloosa, Alabama on a flatbed trailer, together with the material testing specimens, and delivered to the Large-Scale Structures Lab.

## 4.4 Material Properties

### 4.4.1 Compressive Strength

The compressive strength of concrete was determined using procedures consistent with ASTM C39 (2021), with changes for UHPC in accordance with ASTM C1856 (2017). Compressive strength tests were carried out on a regular basis throughout the first 28 days after casting, as well as prior to large-scale flexural testing. Three cylinders were tested for each series of tests, and an average was taken. Figure 4-10 depicts the increase in compressive strength over time as well as a tested cylinder. Compressive strengths of 18.7 ksi were measured three months after casting during flexural testing.

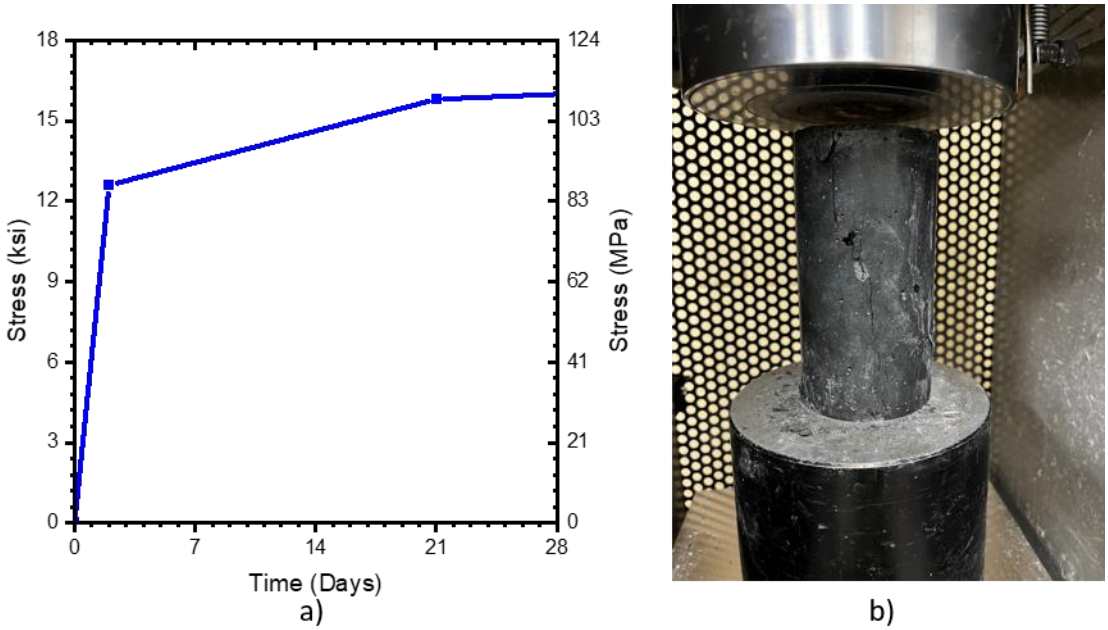


**Figure 4-10 Compressive strength a) graph over time b) testing photo**

### 4.4.2 Modulus of Elasticity

Two modulus of elasticity values are important for characterizing and assessing the UHPC. The first is $E_{ci}$, or the modulus of elasticity upon release. Researchers were unable to directly measure $E_{ci}$ at two days after strands were released due to equipment limitations at the precast factory where the piles were built. $E_{ci}$, on the other hand, is calculated backwards using strain gauge measurements and is described in 4.6.1.2.

The modulus at full strength, $E_c$, is the second important modulus of elasticity. $E_c$ was measured experimentally using ASTM C469 (2022) criteria with adjustments stated in ASTM C1856 (2017). A 400-kip load cell was used to measure force, and two strain gauges were mounted on opposing sides of each of three cylinders to measure strains. A typical Forney machine was used to control the load application. Figure 4-11 depicts a photo of the test setup.

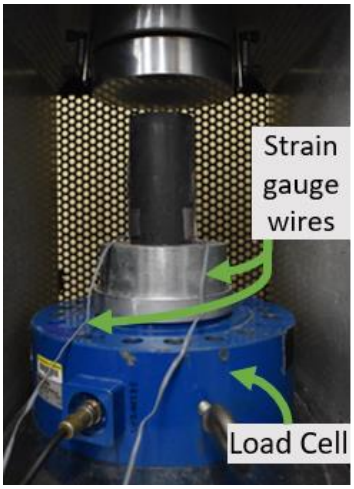


**Figure 4-11 Test setup for modulus of elasticity**

$E_c$ was initially determined using the ASTM C469 technique, providing an average value of 5850 ksi. This figure appeared to be low for a concrete with a compressive strength of 18.7 ksi. A closer examination of the stress-strain curves indicated a gentler slope at the low stress and strain values required for ASTM $E_c$ computation. This difference could be related to inaccurate load control at tensions less than 1000 psi.

To overcome this issue, the modulus was computed for each cycle by fitting a linear curve to the stress-strain data between 1500 psi and 40% of the ultimate stress. Figure 4-12 depicts these lines for each cylinder and load cycle executed. As demonstrated in Table 4-3, the goodness-of-fit for these lines, indicated by the r-squared value (ranging from 0 to 1), was consistently strong, with values ranging from 0.998 to 1.000 in all cases. When the modulus determined by the front strain gauge and the back strain gauge diverged by more than 1000 ksi, that cycle was excluded from the average modulus value. This was true for cylinder 1 cycle 1 as well as cylinder 3 cycles 1 and 2. The average $E_c$ was found to be 6350 ksi using this revised approach. This figure was confirmed to be consistent with current standard code equations for calculating $E_c$, as detailed in Section 4.6.1.2.

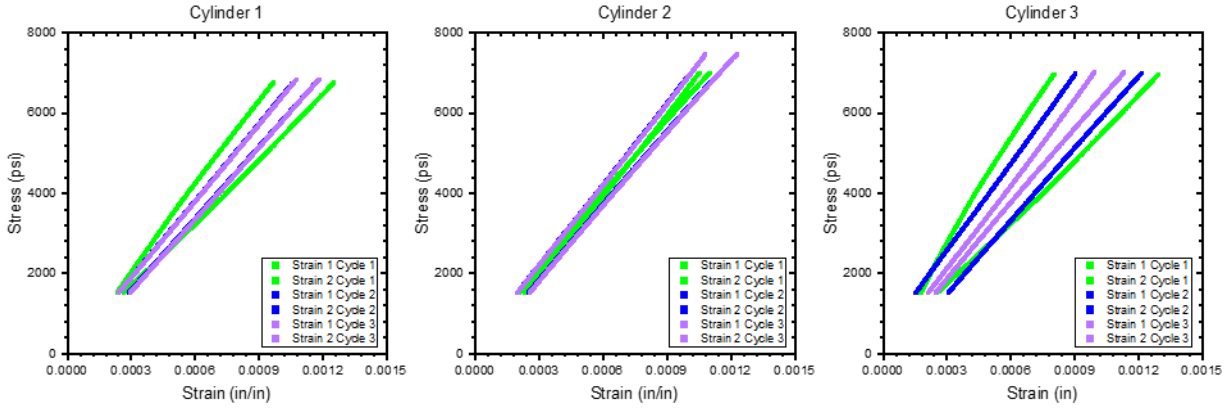


**Figure 4-12 Modulus of elasticity stress-strain curves used for fitting.**

**Table 4-3 Modulus of elasticity curve fitting results.**

| | | E1 (ksi) | E1 $r^2$ | E2 (ksi) | E2 $r^2$ |
|---|---|---|---|---|---|
| Cylinder 1 | Cycle 1** | 5292 | 1.000 | 7129 | 0.999 |
| | Cycle 2 | 5951 | 1.000 | 6377 | 1.000 |
| | Cycle 3 | 5972 | 1.000 | 6344 | 1.000 |
| Cylinder 2 | Cycle 1 | 6698 | 1.000 | 6130 | 1.000 |
| | Cycle 2 | 6717 | 1.000 | 6141 | 1.000 |
| | Cycle 3 | 6686 | 1.000 | 6160 | 1.000 |
| Cylinder 3 | Cycle 1** | 5220 | 0.998 | 8668 | 1.000 |
| | Cycle 2** | 6034 | 1.000 | 7229 | 1.000 |
| | Cycle 3 | 6226 | 1.000 | 6960 | 0.999 |

**Data not included in average due to large difference in E1 and E2

### 4.4.3 Tensile Strength

The tensile strength of the UHPC was measured using two methods. The first approach, currently accepted by AASHTO, was the Direct Tension Test. The second method was the Four-Point Bending Test, which measures tensile strength indirectly through strains caused in flexure. Following the completion of both types of tests, specimens were saw-cut on each side of the crack location and the number of fibers counted in an attempt to correlate with tensile strength and localization strain. Finally, idealized analytical curves with an average, upper-bound, and lower-bound curves were built from experimental data.

#### 4.4.3.1 Direct Tension Tests

The prisms evaluated for Direct Tension Testing (DT) have 2-in. by 2-in. cross-sections and a 17-in. length. Tension testing was carried out in accordance with AASHTO T397, which specifies a fixed-end, uniaxial, displacement-controlled test. While grasping specimen ends at a given pressure, the MTS machine captures load and overall platen displacement. Tapered aluminum plates were attached to parallel faces at the ends of each specimen with a high-strength epoxy prior to testing. Figure 4-13 depicts the test setup and loading direction.

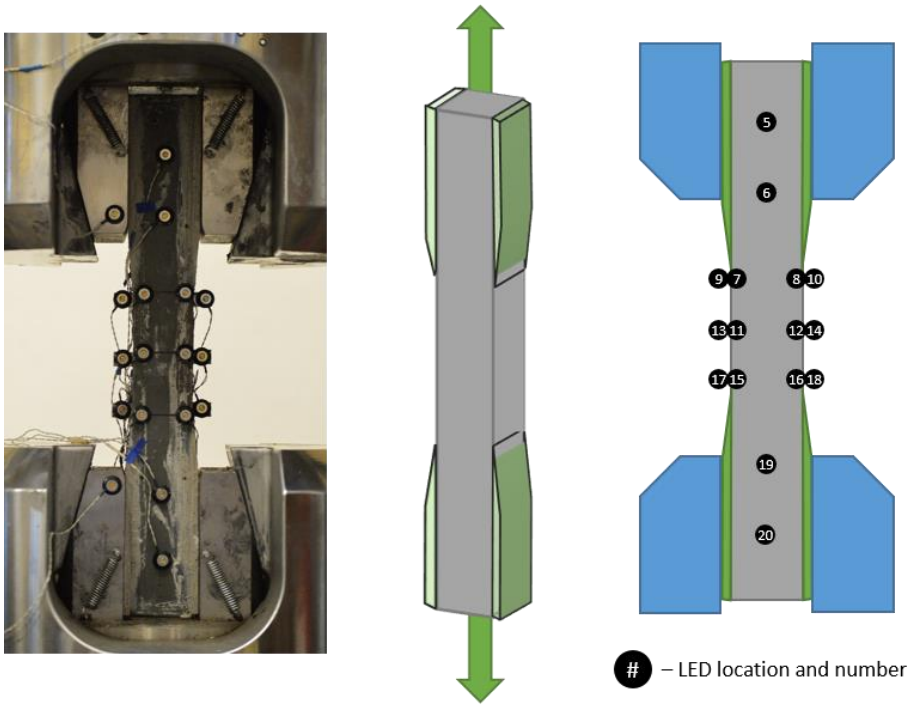


**Figure 4-13 Direct tension a) setup photo b) schematic and instrumentation**

On each end, each specimen was gripped to a pressure ranging from 2.03 to 3.62 ksi. A particular gripping approach was used because tensile or compressive forces can be generated while grasping the specimens. First, the bottom of the specimen was fully gripped. The platen was then adjusted in 0.01-mm increments as gripping pressure was slowly applied to the top of the specimen to reduce the amount of force read by the MTS. This procedure was critical in verifying that no stresses exceeded the elastic limit of UHPC before the test began.

Instead of using a system of extensometers to detect strains in direct tension specimens, as shown in Figure 4-13, a series of LED 3D displacement trackers were mounted to each specimen. These LEDs were later used to calculate the strains on the specimen during the test. Displacement-controlled loading was applied at a rate of 0.0001 in./s until localization, when the rate was increased to 0.001 in./s. The test was halted when the isolated crack had developed to at least 1/16-in., corresponding to a strain of roughly 0.015. In general, localized cracks developed on these specimens at the gauge length between the two gripping plates or just above the gauge length at the extreme end of the gripping plates in the transition zone. Figure 4-14 depicts a snapshot of all cracked specimens, whereas Figure 4-15 depicts a schematic with highlighted cracks.


**Figure 4-14 Direct tension specimens after testing**

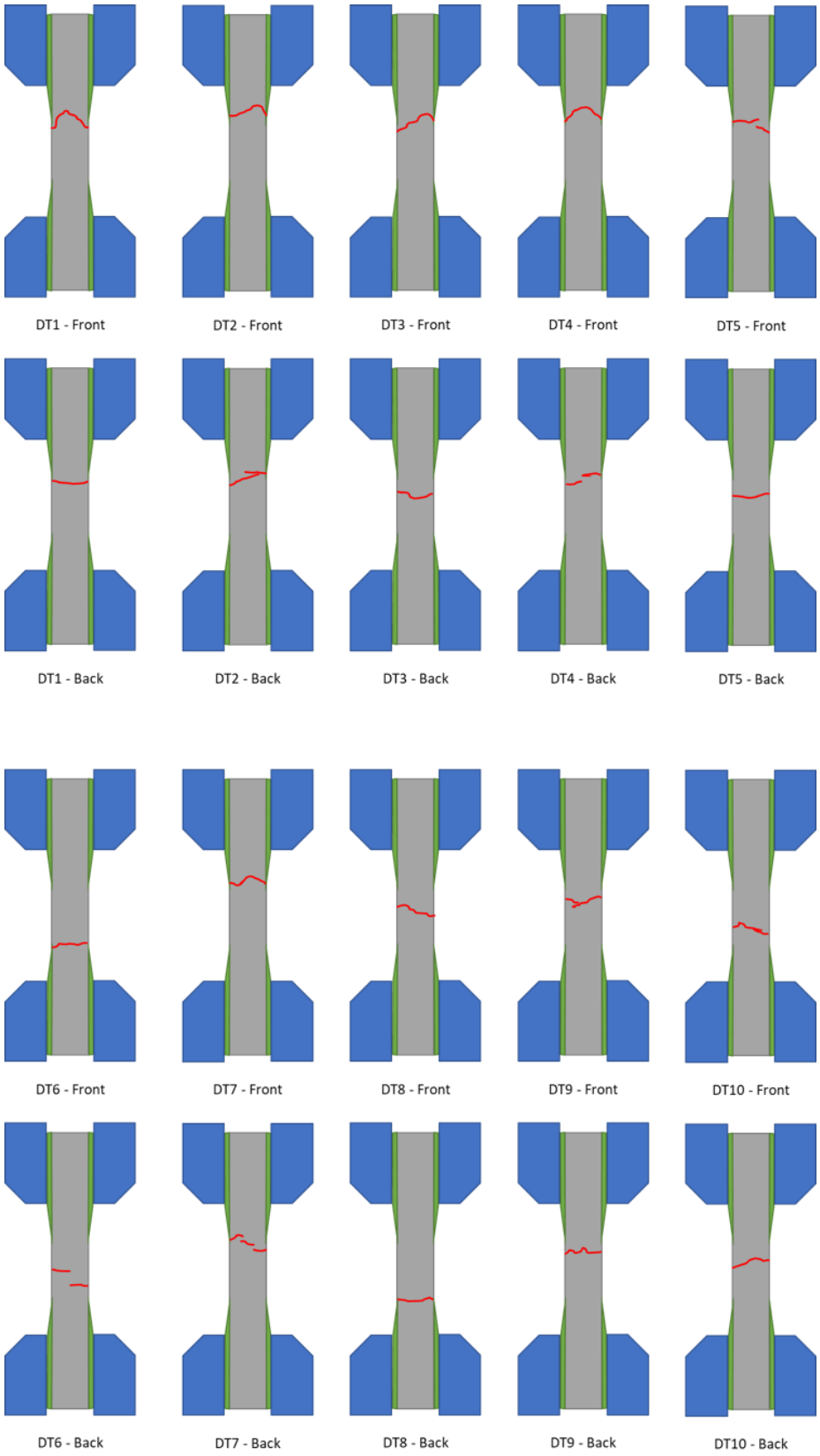


**Figure 4-15 Direct tension test crack schematic for each specimen**

Each test's force and displacement data were converted into stress-strain data, producing a stress-strain curve for each specimen. The force and average cross-sectional area of each specimen were used to determine stress. Strain was estimated by averaging the strains of all four corners using the LEDs at the ends of the gauge lengths, specifically LEDs 7 and 15, 8 and 16, 9 and 17, and 10 and 18. Figure 4-16 depicts all of the generated stress-strain curves. The localization point, where the stress began to fall regularly after peaking, was determined for each curve. The localization strains in these specimens ranged from 1000 to 4000 microstrains. One curve, DT2, took 8000 microstrains to localize, which was twice as long as any other specimen.

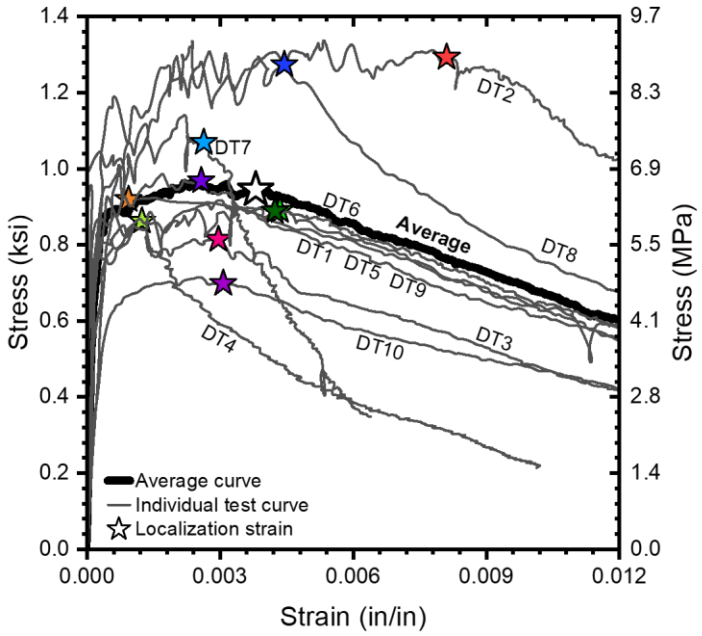


**Figure 4-16 Direct tension stress-strain curves for each specimen**

#### 4.4.3.2 Four-point Bending Tests

Four-Point Bending (4PB) prisms have 4-in. by 4-in. cross-sections and a 14-in. length. Each beam was simply supported on rollers, and compression was applied to two rollers four inches apart on the top of the beam, as shown in Figure 4-17. These beams were evidently cast on a sloped surface upon inspection, since there was a rise in depth along the length of each beam, up to 0.25-in. over 14-in.

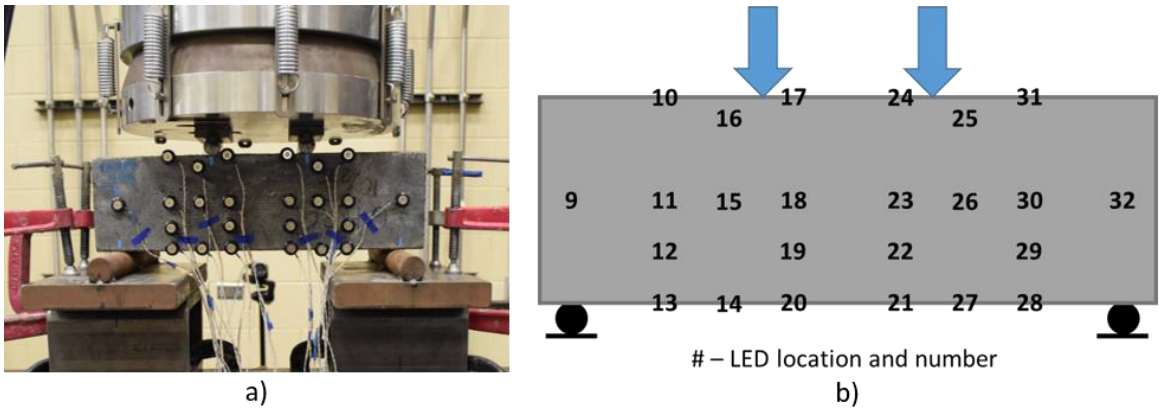


**Figure 4-17 Four-point bending a) test photo and b) instrumentation schematic.**

The MTS machine that was utilized for testing evaluated both the applied load and the overall platen displacement. Each specimen was fitted with a set of LED 3D displacement trackers, and the measurements were used to create a strain profile for each specimen throughout testing. During the test, the strain profiles were used to compute the curvature of the beam, and the force and span data were utilized to calculate the moment delivered to the system. All strains in the system in between the two load application points should be flexural, due to the constant moment zone between the two loading sites. Following that, a moment-curvature for each specimen's material test can be developed to match the moment-curvature measured by experimental moments and stresses.

Four of the eight four-point bending beams failed in shear, with localized cracks forming outside of the load application rollers, as illustrated in pictures in Figure 4-18 and schematic form in Figure 4-19. This could be due to the sloped beam shape or the fact that the span to depth ratio of these beams was 1, resulting in strut action. The crack patterns of 4PB2, 5, and 6 are very reminiscent of strut action. 4PB1, 3, 4, and 8 failed in flexure, resulting in localized cracks in the constant moment area. Moment-curvatures could be fit for these materials that failed in flexure, but the strain values were substantially larger than predicted, with localization strains around 8000 microstrains, outside of normal ranges for UHPC. As a result, the strains were deemed unreliable, but some information could still be gathered from the stresses achieved. The cracking stress of the specimens that failed in flexure was 0.75 ksi on average, and the peak tensile strength was 1.20 ksi on average. Figure 4-20 depicts the stress-strain curves for these specimens. In general, the cracking stresses and peak tensile stresses fall within the range of direct tension testing results and can assist validate such results.

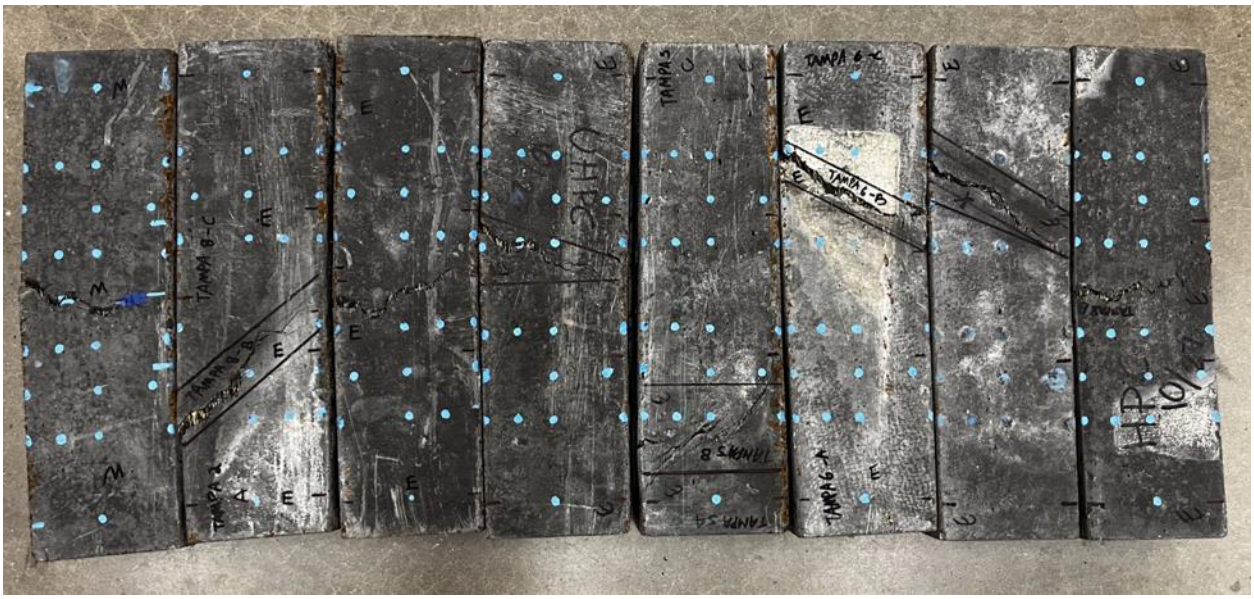

**Figure 4-18 Four-point bending specimens after testing**

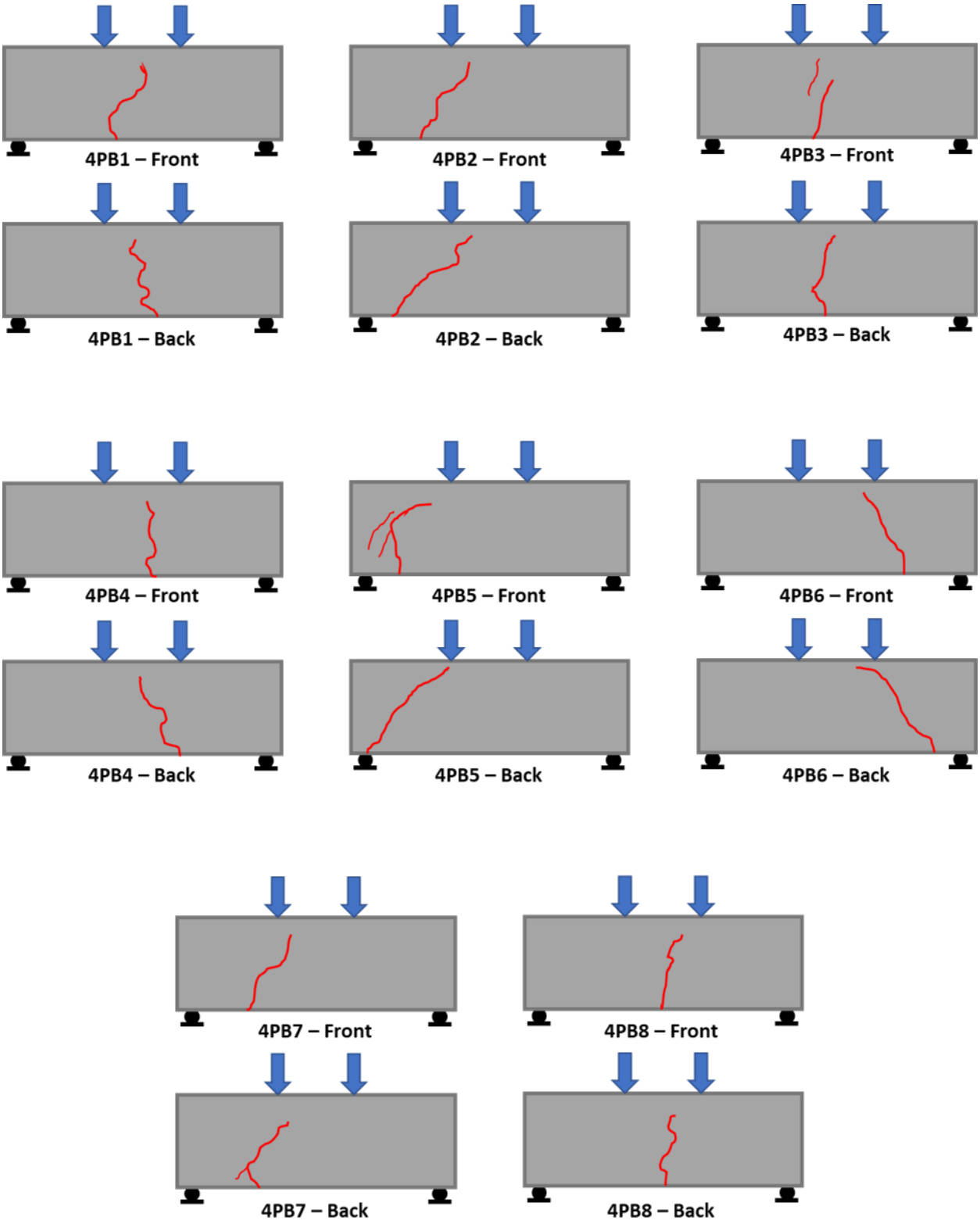


**Figure 4-19 Four-point bending test crack schematic for each specimen**

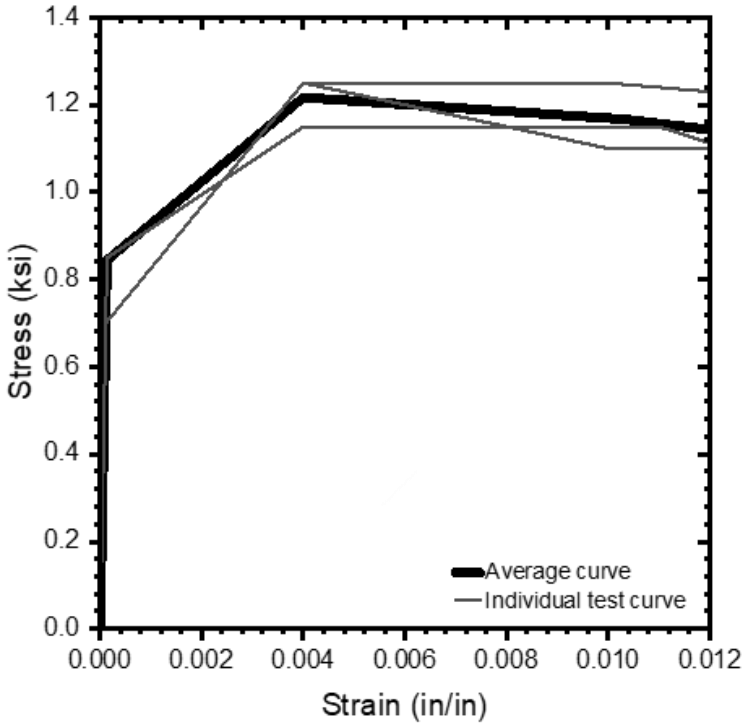


**Figure 4-20 Four-point bending stress-strain curves for viable specimens**

#### 4.4.3.3 Fiber Counts and Tensile Properties

Following the completion of material testing, specimens were cut next to the localized cracks on each side. Because of the angle and path of the tension cracks, six of the 10 specimens had straight 90-degree cuts through the specimen. The remaining specimens, DT1, 3, 8, and 10, were cut at an angle, in line with their slanted cracks. The cut sections were photographed, and a calibrated MATLAB code was used to count the number of fibers in each cross-section. Figure 4-21 depicts the MATLAB fiber counts picture outputs for each specimen. These images show the variation in fiber distribution quality. DT9 features a big circular area with no fibers, but DT7 appears to have a well-distributed fiber network. After MATLAB image processing, the number of fibers in specimens with angled cuts was lowered by multiplying by the sine of the cut angle to account for the variation in cross-sectional area. Table 4-4 shows the average fiber count, peak stress, and localization strains for each specimen.

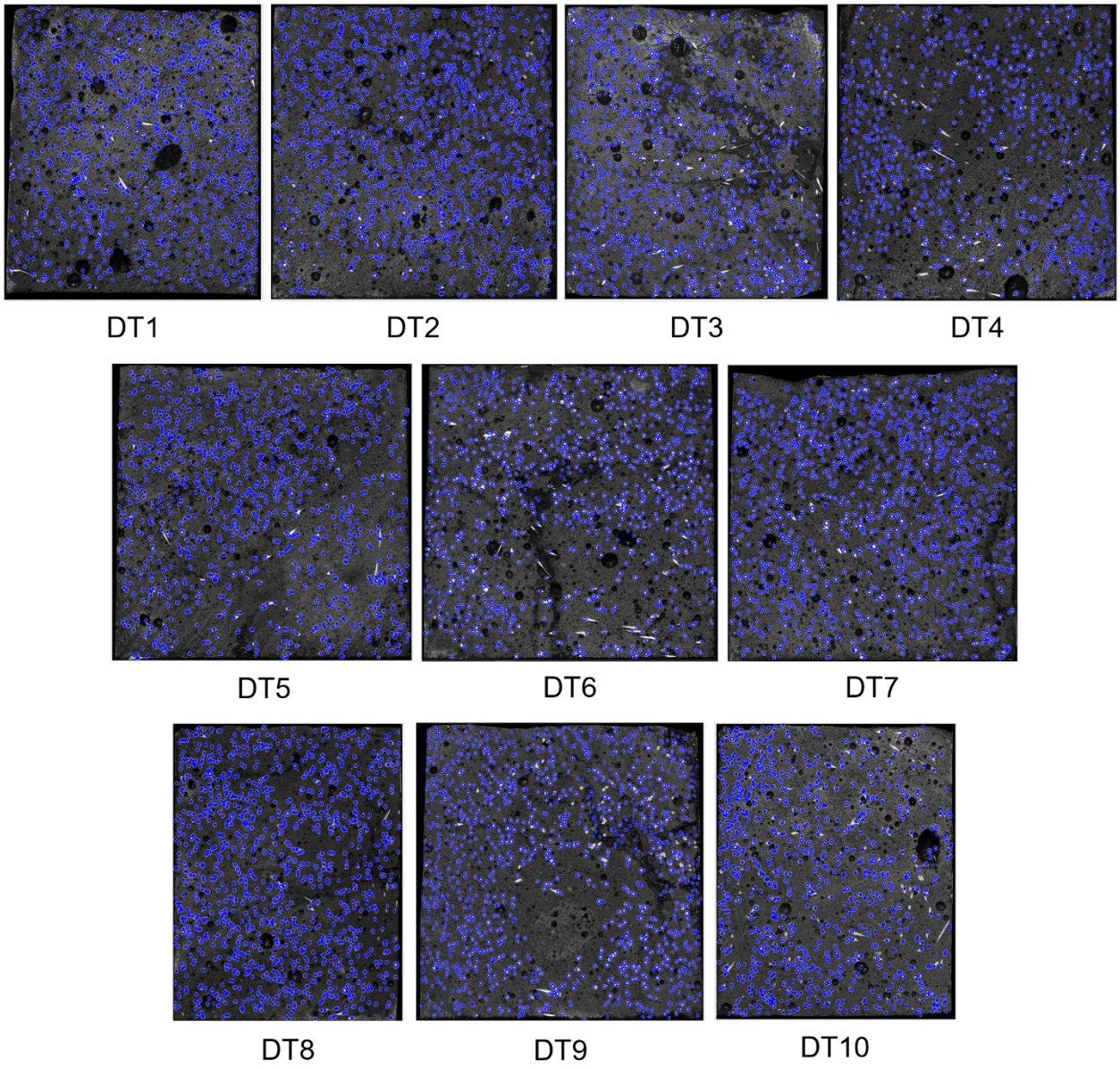


**Figure 4-21 MATLAB fiber count images for each UH16 direct tension specimen**

In Figure 4-22c, the fiber count was plotted against the peak tensile stress and localization strain. For these samples, there does not appear to be a significant relationship between fiber count and localization strain; nonetheless, Figure 4-22a and b demonstrate a general positive correlation between fiber count and peak stress. When all specimens are included in this correlation, DT 2 and 8 stand out as distinct outliers, having achieved larger stresses than all other specimens. When this outlier is included, the $r^2$ value is 0.435, but when these two data points are deleted, the $r^2$ becomes 0.860.

**Table 4-4 Fiber counts, peak stress, and localization strains of direct tension specimens**

| Specimen Name | Fiber Count | Peak Stress (ksi) | Localization Strain (microstrains) |
|---|---|---|---|
| DT1 | 1026 | 1.05 | 963 |
| DT2 | 1262 | 1.34 | 8100 |
| DT3 | 893 | 0.89 | 2960 |
| DT4 | 965 | 0.87 | 1270 |
| DT5 | 1001 | 0.90 | 4350 |
| DT6 | 956 | 0.92 | 4230 |
| DT7 | 1221 | 1.15 | 2630 |
| DT8 | 926 | 1.34 | 4450 |
| DT9 | 1128 | 0.99 | 2570 |
| DT10 | 735 | 0.72 | 3070 |

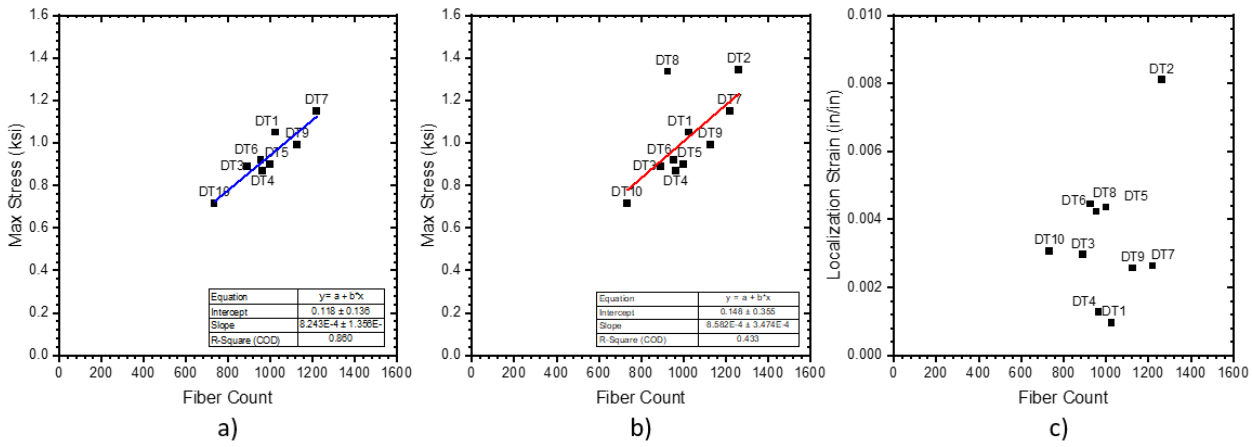


**Figure 4-22 Fiber count for vs. a) peak stress, excluding outliers, b) peak stress, including outliers, and c) localization strain**

#### 4.4.3.4 Idealized Curves for Section Analysis

Because the four-point bending data was inconclusive when it came to strain, they were deemed unreliable for use in analysis. Furthermore, because the direct tension test is currently the sole AASHTO-accepted method for measuring the tensile strength of UHPC, the results of this test were chosen for finalizing three material curves for use in analysis: average, upper-bound, and lower-bound. The average curve was discovered by averaging all direct tension stress-strain curves. Because it showed the highest tension curve, the stress-strain curve of specimen DT8 was chosen as the upper-bound. The peak stress of DT2 was the same as that of DT8, but the localization strain was substantially greater than that of any other direct tension specimen, 800 microstrains compared

to the average 400 microstrains, and hence it was not chosen as the typical upper bound. The lower-bound curve DT10 was chosen because it had the lowest peak stress value and a reasonable localization strain of 320 microstrains. Each curve has four sections: the elastic region, the post-cracking to peak stress region, the peak stress to localization region, and the localization to ultimate region. Table 4-5 shows the stress and strain values for each curve. Figure 4-23 depicts the idealistic curves in comparison to their experimental counterparts.

**Table 4-5 Idealized tensile stress-strain curves used in analysis**

| | Average | | Upper Bound | | Lower Bound | |
|---|---|---|---|---|---|---|
| | Strain (με) | Stress (ksi) | Strain (με) | Stress (ksi) | Strain (με) | Stress (ksi) |
| Zero | 0 | 0 | 0 | 0 | 0 | 0 |
| Cracking | 510 | 0.89 | 550 | 1.19 | 320 | 0.62 |
| Peak | 2400 | 0.97 | 2380 | 1.34 | 2500 | 0.71 |
| Localization | 3900 | 0.97 | 4400 | 1.34 | 3100 | 0.71 |
| Ultimate | 13000 | 0.56 | 13000 | 0.64 | 13000 | 0.40 |

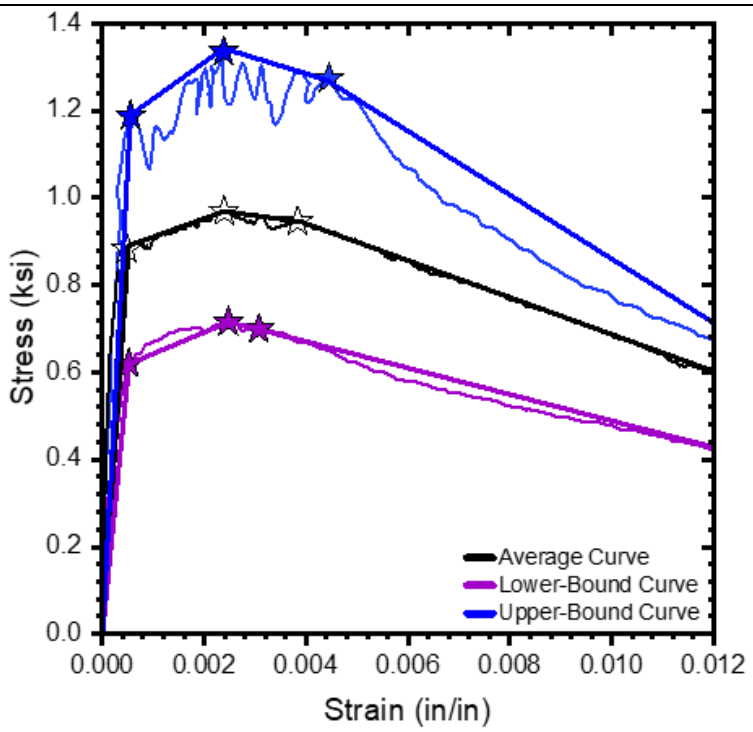


**Figure 4-23 Idealized tensile stress-strain curves compared to experimental curves.**

## 4.5 Experimental Testing and Observations

Four large-scale experimental tests were conducted: two flexural tests and two shear tests. The piles were named according to their size and testing purpose, with the 24-ft pile named UH16FS (Flexural, Strong-axis testing) and the 16-ft pile named UH16FW (Flexural, Weak-axis testing). UH16FW did not sustain widespread damage during flexural testing and was subsequently chosen for retesting in shear. Two shear tests were conducted, one on each end, UH16V1 and UH16V2.

### 4.5.1 Flexural Testing

#### 4.5.1.1 Test Setup and Instrumentation

Each flexural testing pile was supported at each end by a roller and a pin, with a load jack positioned in the middle to apply force. An electric pump was used to apply force to a spreader beam, distributing the load to rollers 16-in. from each side of the midspan, resulting in a four-point bending loading configuration. A variety of instrumentation was used during testing to collect comprehensive data, including string potentiometers, pressure sensors, load cells, 3D LED displacement tracking sensors (LEDs), and exterior surface strain gauges. Furthermore, the internal strain gauges used during fabrication were constantly monitored.

To measure displacement, eight string potentiometers were placed along the pile's length. A pressure sensor was connected to the double-acting load jack's input, providing data on the applied pressure to determine the applied force. To validate the force readings received from the pressure sensor, a load cell was put beneath the load jack. LEDs were placed on the pile's front face to collect 3D displacement data throughout testing. During the testing procedure, this data would be utilized to determine flexural and shear strains along the pile. External and internal strain gauges were deliberately installed at specific locations to directly measure strains in the steel and concrete. Figure 4-24 shows the test setup and instrumentation labels for the strong-axis flexure test, UH16FS, and Figure 4-25 shows the corresponding instrumentation labels for the weak-axis flexure test, UH16FW.

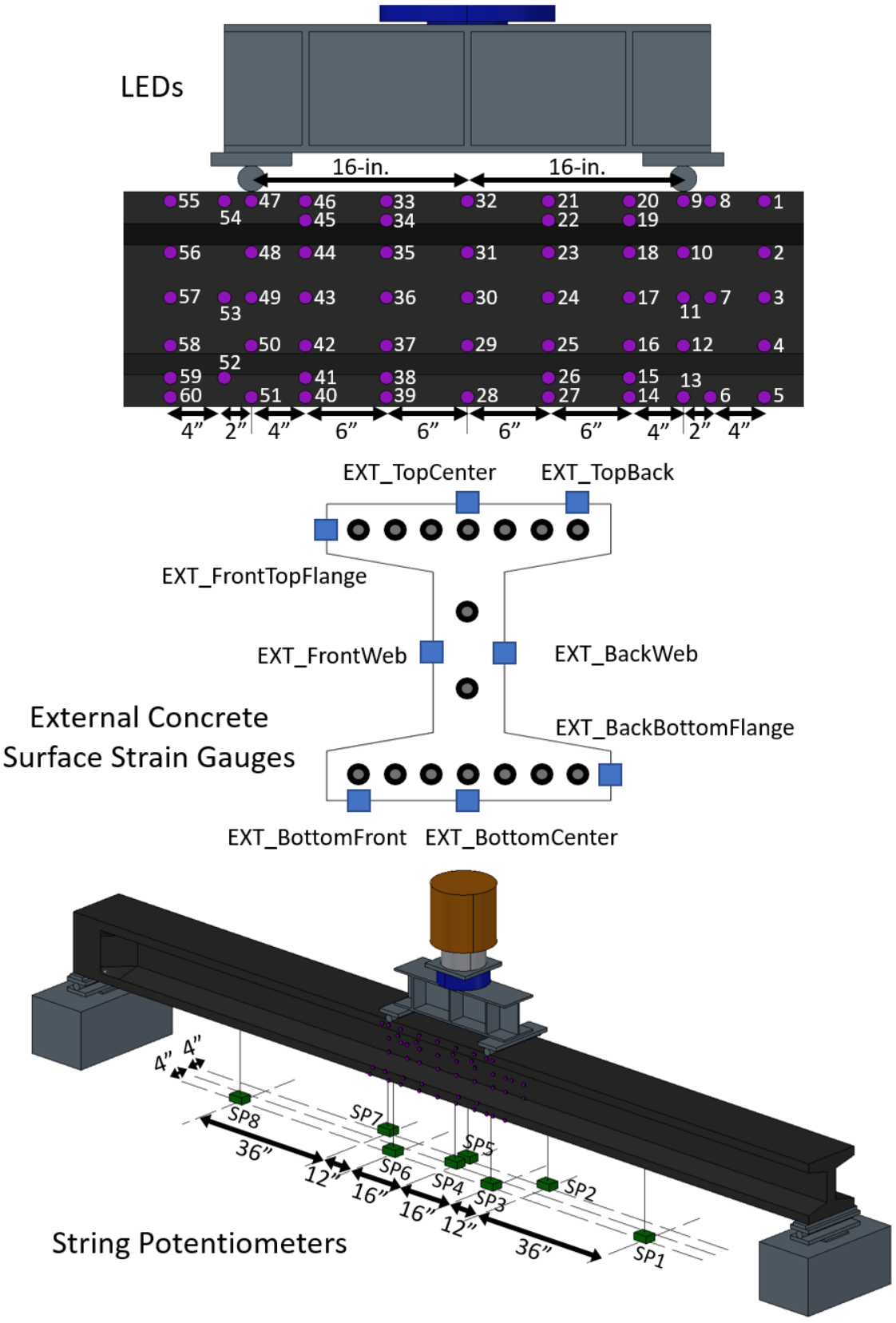


**Figure 4-24 UH16FS test setup and instrumentation**

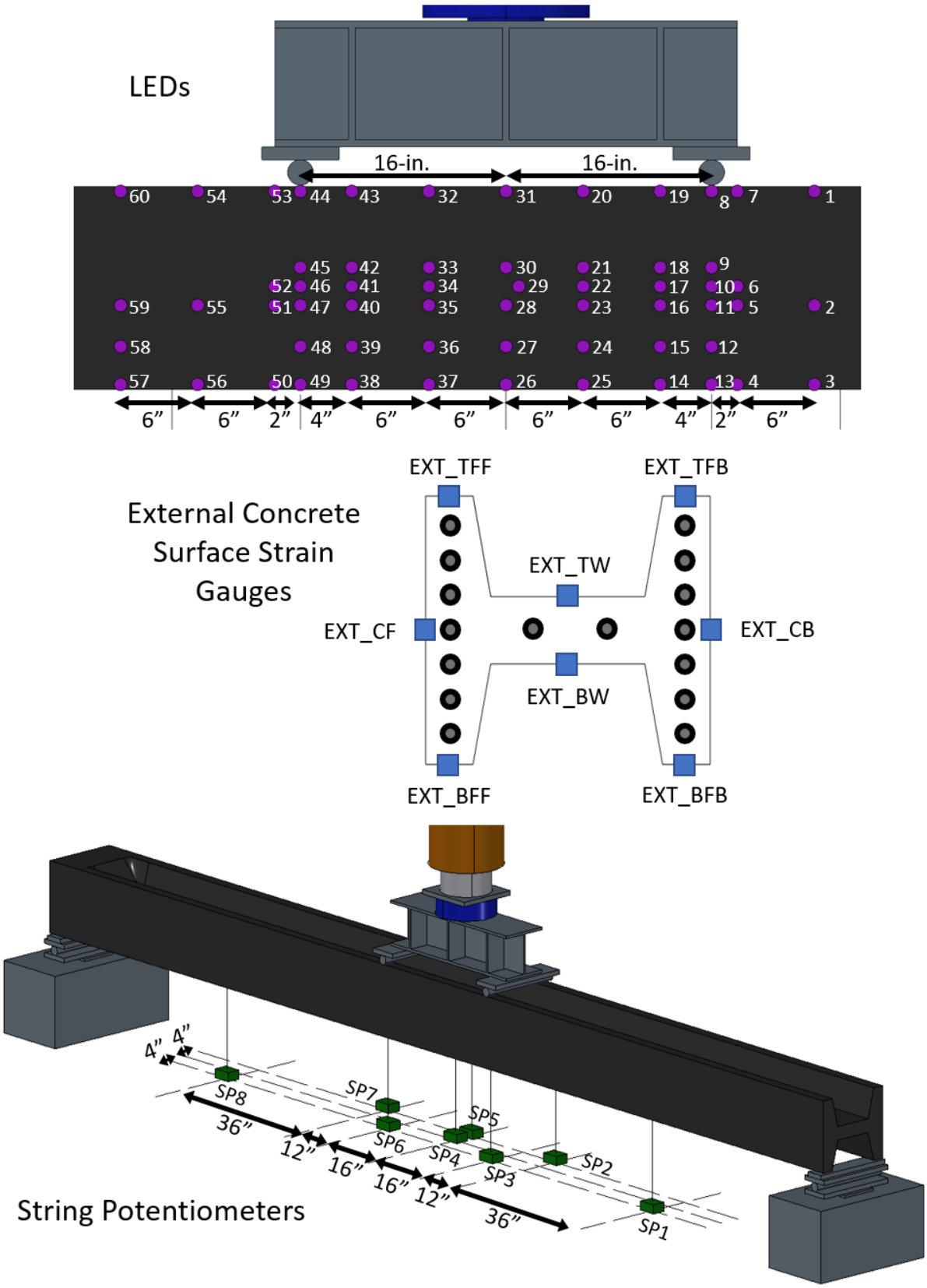


**Figure 4-25 UH16FW test setup and instrumentation**

#### 4.5.1.2 Strong-axis Flexure

The load cell was used to monitor the loading of the UH16FS strong-axis flexural test specimen. Load application was stopped after every 15 kips (66.7 kN) load increase to check the pile for cracks. Except at 60 kips (267 kN) and 90 kips (400 kN), where three load cycles were done, load was applied monotonically. The load protocol and testing cycles are depicted in Figure 4-26. Acetone was applied to the pile during testing to look for microcracks. The first flexural microcracks were observed at 45 kips (200 kN) on the pile's bottom flange at midspan. These microcracks were between 0.5 and 0.75 inches long when first observed. Flexural microcracks increased in length but did not localize as the test progressed, despite being present throughout the constant moment region. The flexural microcracks had stretched past mid-height at 110 kips (489 kN), as seen in Figure 4-27c.

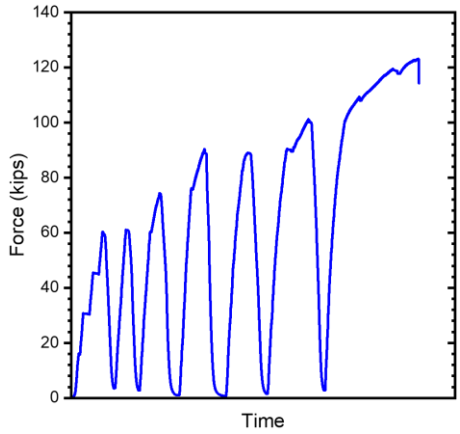


**Figure 4-26 UH16FS load protocol**

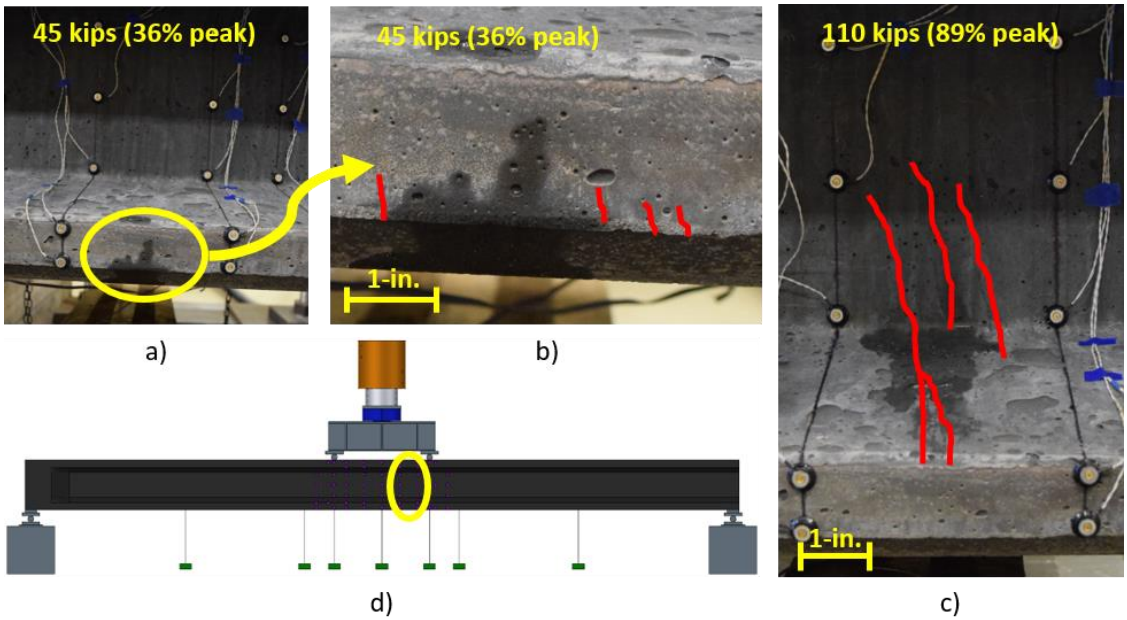


**Figure 4-27 Flexural crack progressing during UH16FS testing: a) flexural cracks at 45 kips, b) zoomed and highlighted cracking at 45 kips, c) flexural cracking at 110 kips, d) schematic of photographed location.**

Shear microcracks were initially noticed in the web outside of the constant moment region on the right side at 90 kips (400 kN). Figure 4-28a depicts cracks that were 4 to 5 in. long and spaced about 2 in. apart. It is anticipated that these cracks existed prior to 90 kips of stress based on the length, number, and spacing of shear cracks, although the region outside of the loading span was not inspected until that time. There were no shear microcracks seen on the left side of the constant moment region at this load. The shear cracks had spread significantly from 110 kips (489 kN) to 1-in. spacing. Small popping noises were consistently heard after 110 kips of load while load application proceeded. At 123 kips (548 kN) of load and 3.4 in. (8.6 cm) displacement at midspan, the pile failed suddenly, experiencing a flexural-shear failure. A large flexural-shear crack localized from just outside the right roller, traveled diagonally through the web, and proceeded along the web-bottom flange interface until it reached the outer pin support (Figure 4-28c).

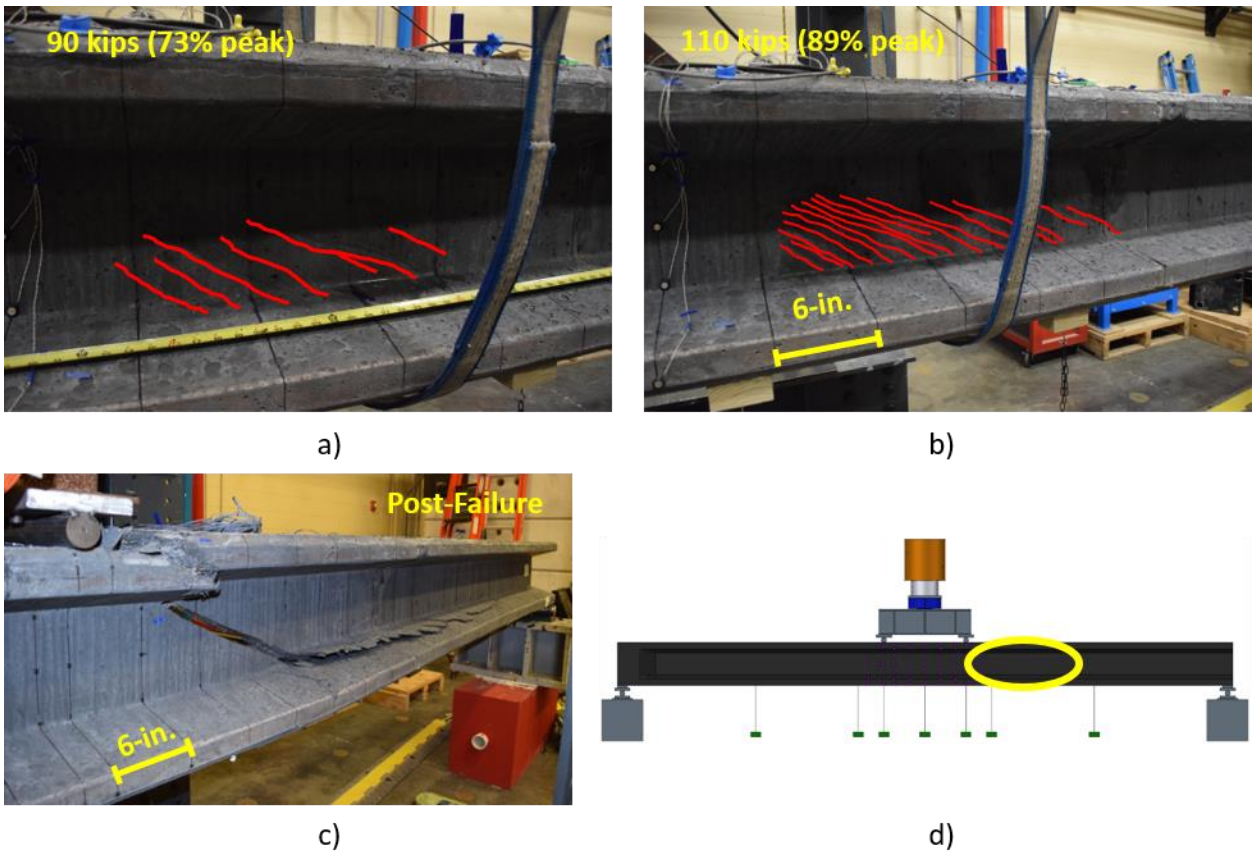


**Figure 4-28 Shear crack progression during UH16FS testing: a) shear cracks at 90 kips, b) shear cracks at 110 kips, c) flexural-shear crack at failure, d) schematic of photographed location.**

#### 4.5.1.3 Weak-axis Flexure

The load procedure for the weak-axis flexure specimen was identical to that of the UH16FS. Loading was halted every 15 kips to inspect UH16FW for cracks with acetone (66.7 kN). Aside from three cycles at 45 kips (200 kN) with the load protocol indicated in Figure 4-29, load application was monotonic.

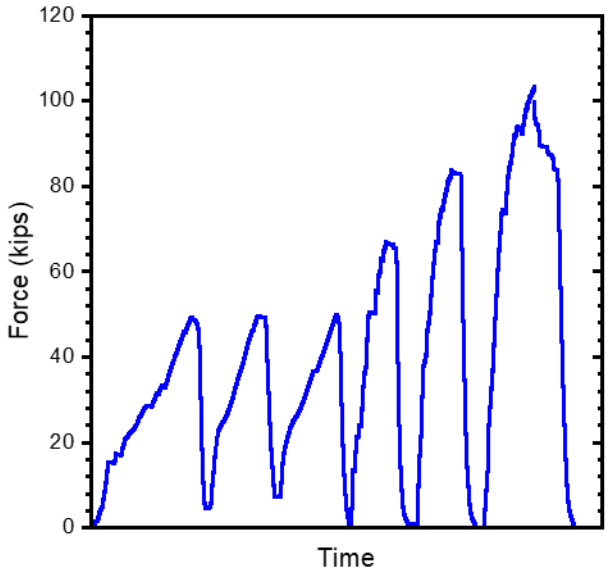


**Figure 4-29 Load protocol for UH16FW**

Only microcracks were observed before failure, as in strong-axis testing, with the first flexural microcracks observed at 30 kips (123 kN) load. Figure 4-30a depicts the initial length of these cracks, which was approximately 1-in. (2.5-cm). Throughout the UH16FW testing, no shear microcracks were discovered. The frequency of small popping noises increased as load rose over 75 kips (334 kN), but no substantial decline in load was observed. Flexural microcracks were common at this time in the constant bending moment zone between the load application location and the surrounding 2-ft (61-cm), as shown in Figure 4-30c. At 103 kips (459 kN) stress and 1.4-in. (3.6-cm) midspan displacement, compression-controlled failure occurred. There were no tension flexural cracks localized upon specimen failure, although concrete crushing on the pile's top flanges was observed and documented in Figure 4-30d. The pile was not pushed any farther once the load had reduced after peaking in order to preserve the specimen for future shear testing.

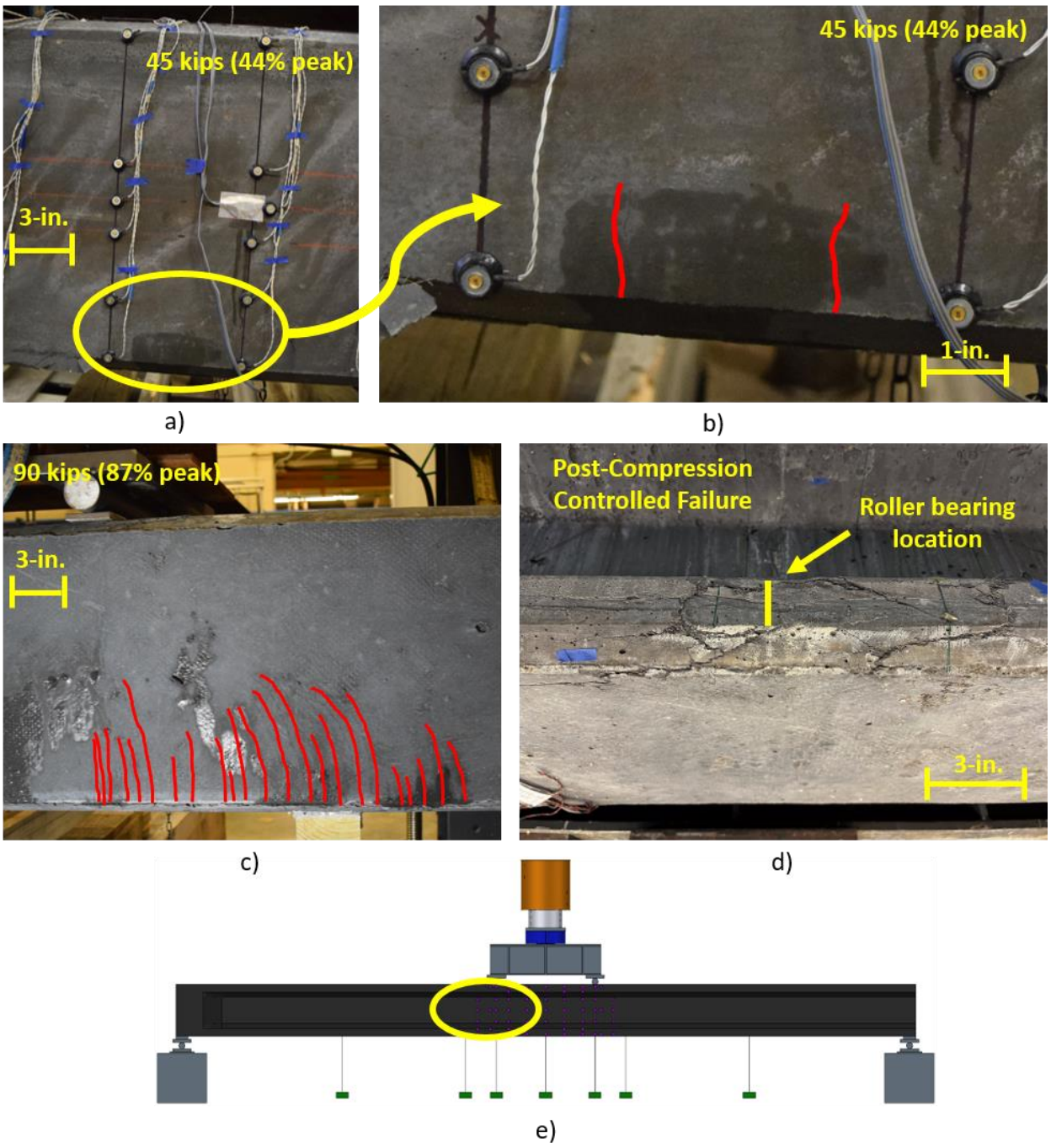


**Figure 4-30 Crack progression during UH16FW testing: a) flexural cracking at 45 kips, b) highlighted flexural cracks at 45 kips, c) flexural cracking outside of constant moment region at 90 kips, d) concrete crushing after removal of load beam, e) schematic of photographed locations**

### 4.5.2 Shear Testing

Two shear tests were performed: one on each side of the midspan, outside of the weak-axis flexural testing damage region. The first test, dubbed UH16FW_V1, was performed on the pile's block-end side, designed to fail in the interior span, and the second test was performed on the opposite end, with the "free-end," or the end with the H-shape. This test was designated as UH16FW_V2. Figure 4-31 depicts the configurations and load spans, which will be explored in further detail.

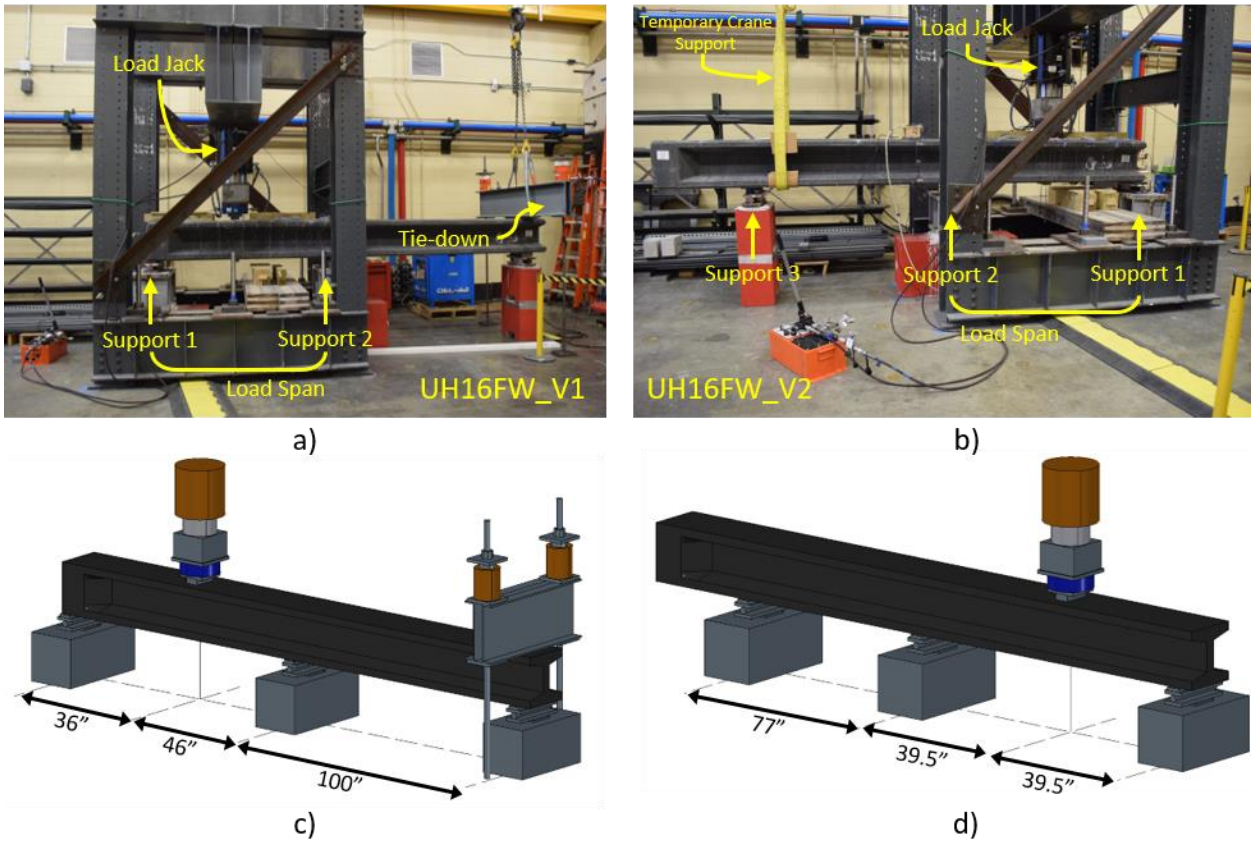


**Figure 4-31 Shear test setups for UH16FW_V1 (a and c) and UH16FW_V2 (b and d)**

#### 4.5.2.1 UH16FW_V1

The purpose of UH16FW V1 was to determine the shear capacity of an interior span of pile sections by supporting at three locations and loading between two supports: one support at either end and the other support slightly outside of the flexural testing damaged region. Because the UHPC block at the end of the pile has a significantly higher shear capacity than the H-section, the intention was to induce higher stresses in the region of the pile between the load and the middle support. Based on statics analysis and the available undamaged span lengths, a tie-down force was required on the span not being tested. This tie-down would ensure that the pile worked as a continuous beam rather than lifting up and becoming simply supported, allowing the force to be distributed in such a way that the intended failure mechanism would be facilitated.

After the pile had been positioned and secured to its supports, a steel beam was placed perpendicular across it and loaded with 50 kips of tie-down force. To quantify the amount of uplift

force operating on the steel beam, a pressure sensor was mounted to the tie-down jacks and monitored throughout testing.

With the exception of the additional pressure sensors on the tie-down jacks, the instrumentation was comparable to flexural testing specimens but reduced due to shorter spans. The force was measured using a pressure sensor and a load cell. At the projected crack position, three external surface strain gauges were mounted in a rosette pattern, with the location chosen based on previous testing and the crack angle observed in UH16FS. Internal strain gauges such as C11T, C11M, C11B, and SLtB1 were monitored during the loading span. Two string potentiometers recorded displacement under the load, while LEDs measured displacement across the specimen's front face. Figure 4-32 shows the names and locations of external instruments.

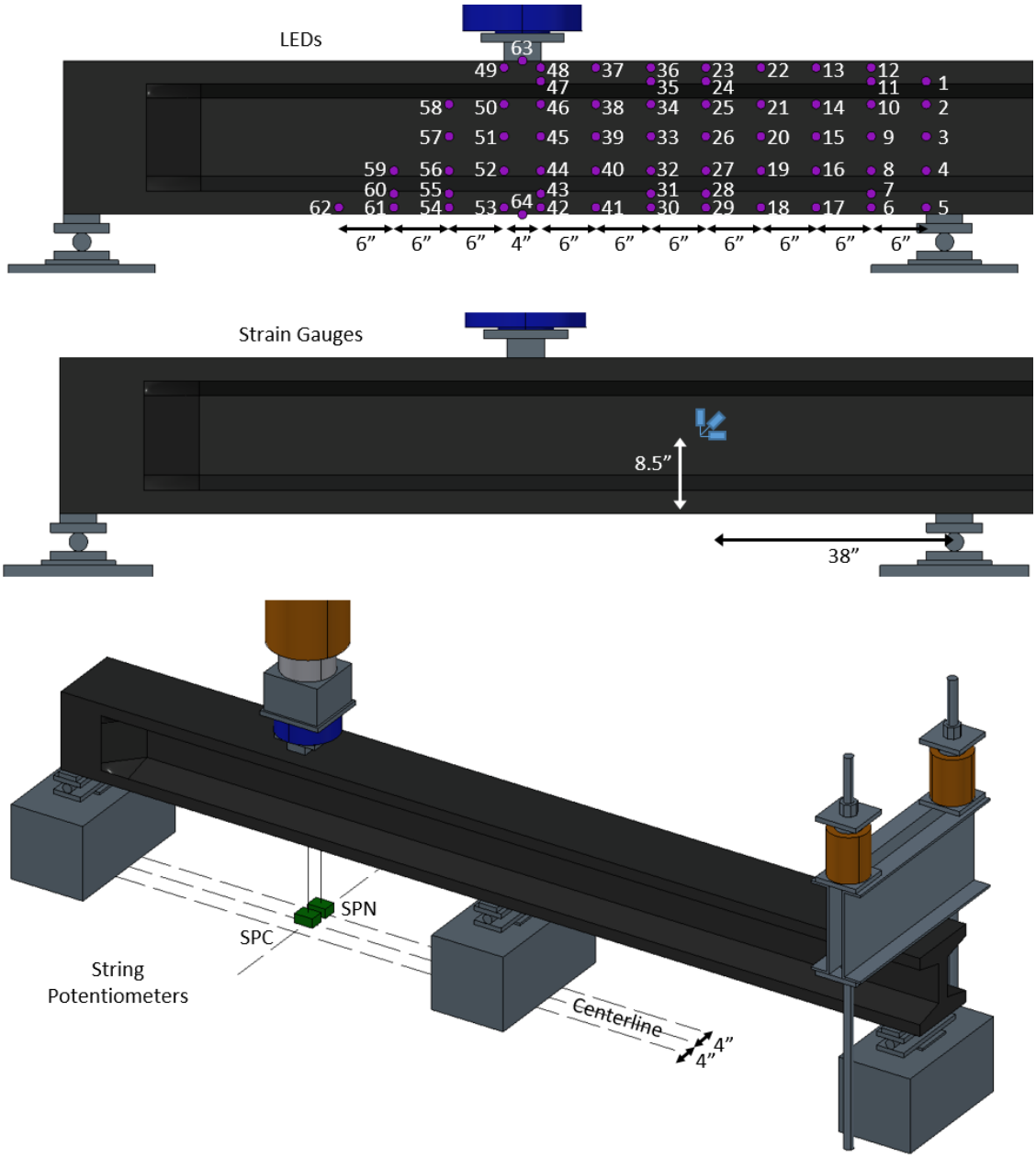


**Figure 4-32 Instrumentation and labels for UH16FW_V1**

The load was manually applied with a hydraulic pump and stopped every 15-20 kips beginning at 30 kips to check for microcrack progression. Figure 4-33 depicts the force-displacement curve for the test. The first microcracks were found at 125 kips of load, extending horizontally roughly 26 in. from the block end. Horizontal cracks indicate strand sliding and bond failure. These horizontal cracks did not expand or grow more severe later in the test, indicating that they formed during detensioning and were accentuated by the additional load from shear testing.

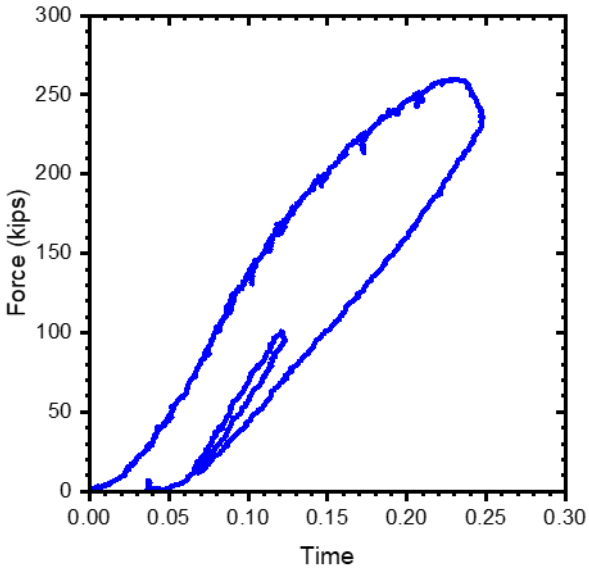


**Figure 4-33 UH16FW_V1 force-displacement**

Small popping noises could be heard as loading progressed after 125 kips. With acetone, significant shear microcracks were seen on the interior span web at 145 kips. Shear microcracks were found on both load spans once 160 kips of load was reached, and popping noises became more frequent. At 250 kips, several minor shear cracks were evident with the naked eye on the inner span. This span's shear cracks were numerous and densely spaced. There were no shear cracks on the block-end span. During testing, the maximum load reached was 259 kips, following which the load continued to fall with additional pumping. The pile was unloaded at 235 kips to preserve the specimen for the second shear test. The pile was reloaded to 100 kips to determine residual strength before being unloaded for the last time.

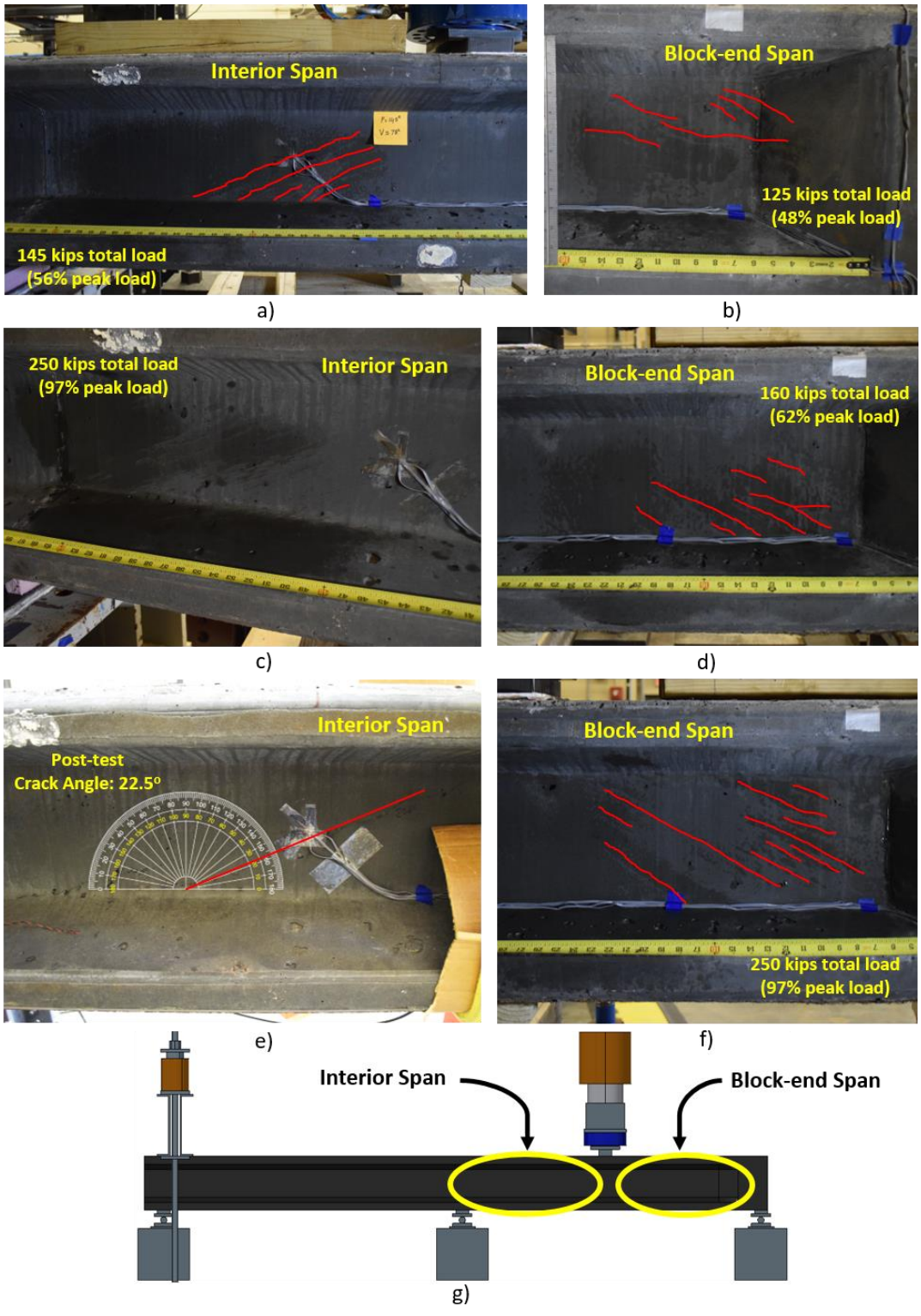


**Figure 4-34 Crack progression of UH16FW_V1 a) interior span cracking at 145 kips, b) block-end span cracking at 125 kips, c) interior span cracking at 250 kips, d) block-end span cracking at 160 kips, e) interior span crack angle, f) block-end span cracking at 250 kips, g) schematic of photographed locations**

#### 4.5.2.2 UH16FW_V2

The free-end shear test, UH16FW_V2, was designed to assess the shear capacity of the pile's end, when prestressing is not fully effective before the transfer length. This test was set up similarly to UH16FW_V1, with three supports employed, but no tie-down was used. This alters the force distribution because, with sufficiently applied force, the pile's end lifts, and the pile acts simply supported. The same equipment was used, but with a modified LED configuration and LVDTs installed on multiple PT strand ends to measure any bond slip during the test. Figure 4-35 depicts all instrumentation locations and labels.

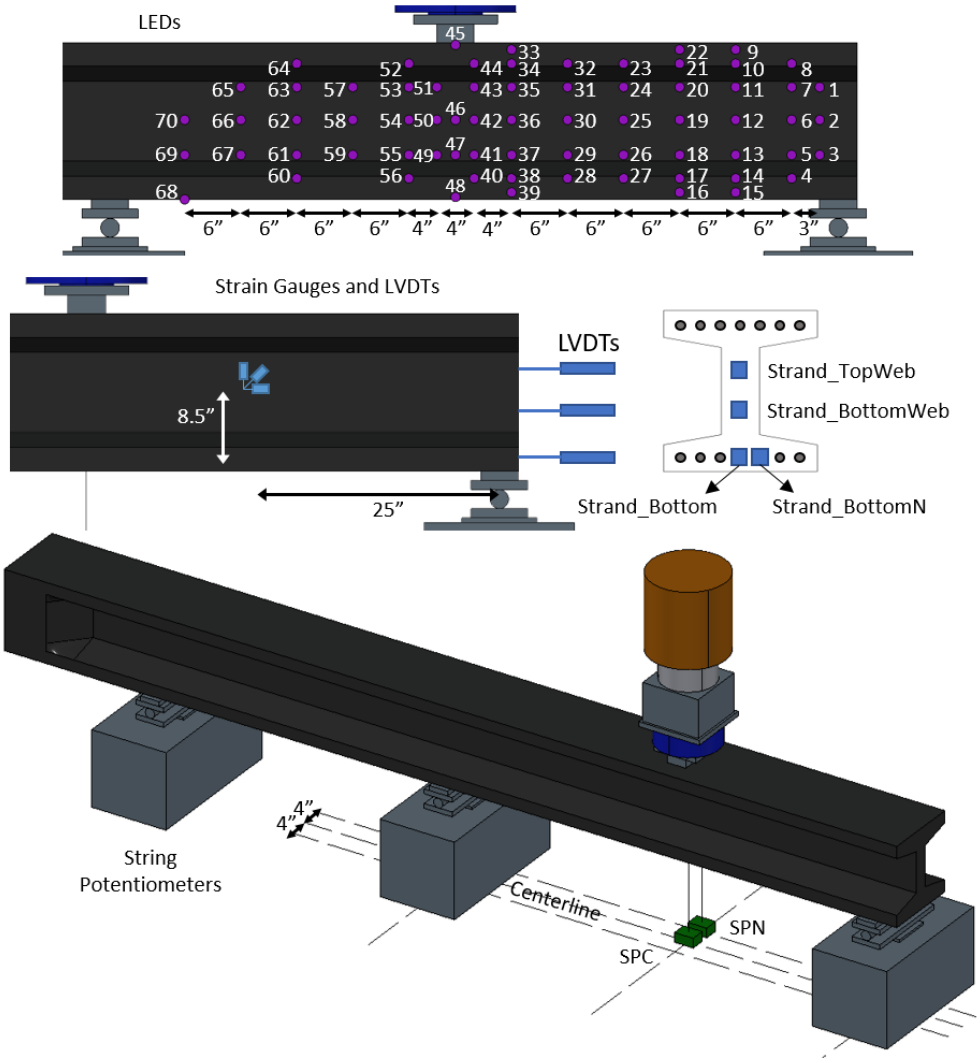


**Figure 4-35 Instrumentation and labels for UH16FW_V2**

Acetone was added to the pile prior to testing to look for pre-existing cracks, particularly in the endzone. For the first 12-in. of pile length, some endzone cracking associated with detensioning was discovered on the upper web. The detensioning cracks were not a concern prior to testing because their direction was in the opposite direction of any anticipated shear cracking from the planned test.

Load was applied manually with a hydraulic pump, similar with UH16FW_V1, with the force-displacement for the test given in Figure 4-36. The pile was inspected for microcracks every 30 kips

for the first 90 kips of load, and then every 15 kips thereafter. At 90 kips, shear microcracks were observed for the first time on the end span web. Longitudinal microcracks were observed at the PT locations on the bottom flange after 135 kips of load. A shear crack was also seen on the web of the end span. The cracks grew in size as the loading increased. The shear cracks in the web extended down into the bottom flange at 200 kips. The load eventually peaked at 211 kips, at which point a strand debonded, major shear cracks appeared, and the load dropped by 9 percent. With further load application, loud popping noises occurred as more strands debonded, and the load dropped by another 25%. The localized shear crack in the web had a 21-degree angle.

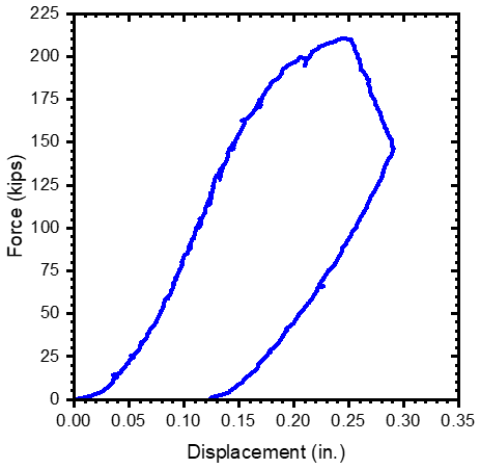


**Figure 4-36 Measured force-displacement response of UH16FW_V2**

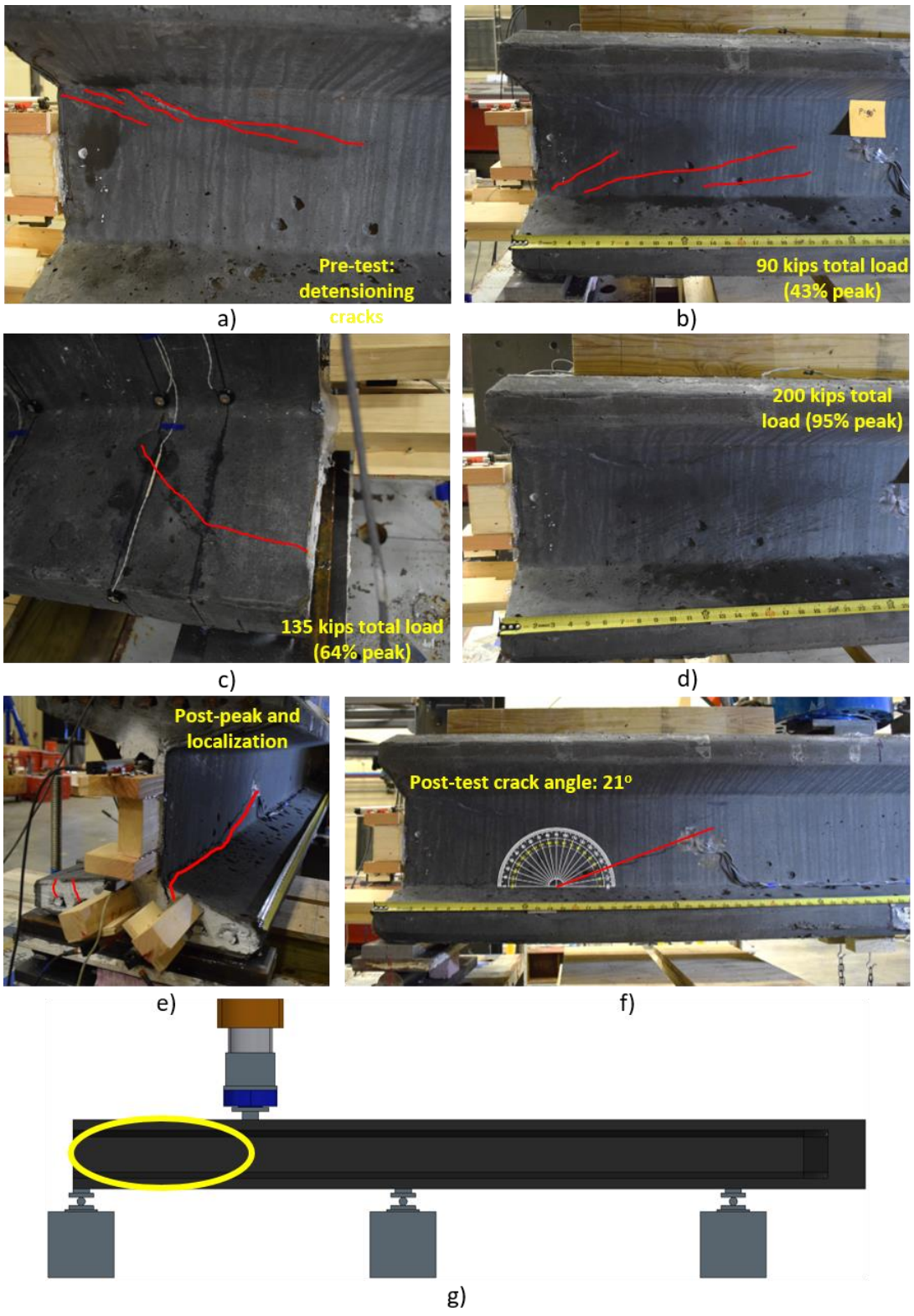


**Figure 4-37 UH16FW_V2 crack progression: a) pre-test detensioning cracks, b) first observed shear cracking, c) longitudinal cracks from strands, d) widespread shear microcracking, e) crack localization, f) post-test crack angle, g) schematic of photographed location**

## 4.6 Results and Discussion

### 4.6.1 Verification of Material Properties

Aside from the material properties tested and detailed in Section 4.4, there were other material properties that needed to be verified through analysis. These parameters included the prestressing strand transfer length, modulus of elasticity during detensioning, and effective prestressing following losses during full-scale flexure and shear testing. These characteristics are crucial for calibrating predictive models and outcomes for flexure and shear testing.

#### 4.6.1.1 Prestressing Strand Transfer Length

The prestressing strand transfer length was validated using strain gauge measurements. Strain gauges at the pile's ends, at the expected transfer length, were compared to strain gauges in the pile's core. As seen in Figure 4-38 the readings were quite similar, showing that 15-in., or $24d_b$, was appropriate for the 0.6-in. prestressing strands. The current AASHTO requirement for transfer length is $24d_b$, although PCI suggests $20d_b$. This testing cannot remark on transfer lengths of $20d_b$, however the more conservative figure of $24d_b$ proved sufficient in this example.

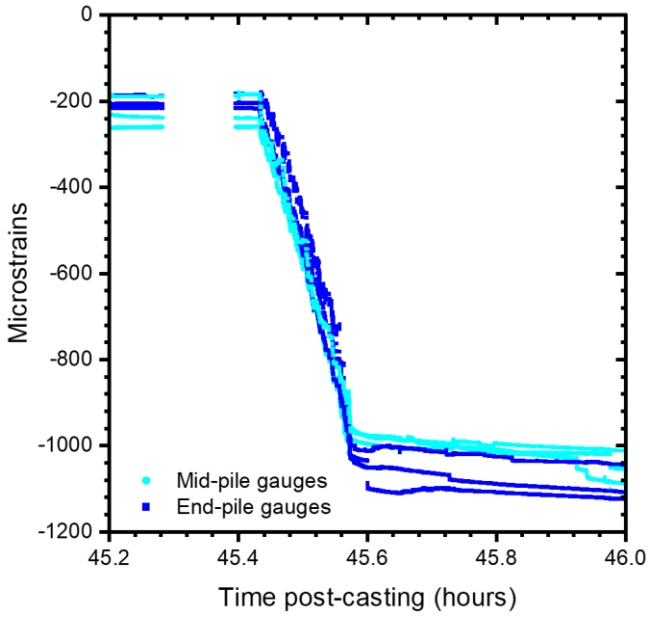


**Figure 4-38 Loss in strains during detensioning**

#### 4.6.1.2 Modulus of Elasticity

The modulus of elasticity, as previously stated in Section 4.4.2, is divided into two relevant numbers: beginning and full-strength, denoted by $E_{ci}$ and $E_c$, respectively. $E_c$ was measured by testing, but $E_{ci}$ could not be measured empirically due to jobsite limitations. However, $E_{ci}$ can be back-calculated. Through Equation 4-1, the loss of strain during detensioning can be connected to the initial modulus of elasticity.

$$\epsilon_{DT} = \frac{f_{pi} * A_{ps}}{E_{ci} * A_t} = \frac{f_{pi} * A_{ps}}{E_{ci} * \left( A_g + A_{ps} \left( \frac{E_{ps}}{E_{ci}} - 1 \right) \right)} \quad \textbf{4-1}$$

$E_{ci}$ was calculated using the measured loss in stresses to be 5385 ksi. This result can be compared to Equation 4-2, the AASHTO equation for approximating modulus of elasticity based on

compressive strength. The AASHTO anticipated value is 5768 ksi, a difference of 6.6 percent. The full-strength modulus of elasticity, $E_c$, was determined by testing to be 6350 ksi. AASHTO anticipates a value of 6536 ksi at maximum strength, a 2.8 percent difference. The AASHTO equation may predict the modulus of elasticity with considerable accuracy at both early and full development.

$$E_c = 2500(f_c)^{0.33} \quad \textbf{4-2}$$

#### 4.6.1.3 Losses and Effective Prestressing

When discussing the concepts of effective prestressing and associated losses, there are two types of losses to consider: short-term and long-term. Both the AASHTO and PCI codes include elastic shortening in short-term losses, with the PCI recommendations additionally include an additional term for short-term autogenous shrinkage—chemical shrinkage of concrete during the hydration process. Long-term, both AASHTO and PCI concur that shrinkage, creep, and relaxation losses influence successful prestressing within a segment.

The AASHTO method of quantifying prestressing losses is outlined through the following equations, beginning with Equation 4-3, the general equation combining elastic shortening, relaxation, shrinkage, and creep losses. It is critical to note that for the sake of assessing "long-term" losses for these piles, a timeframe of 90 days was used—the average time from casting to the start of flexural and shear testing. Given the relatively short lifespan of UHPC members, the long-term equations used were designed for the period "between the time of transfer and deck placement," or from $t_i$ to $t_d$, in accordance with AASHTO LRFD 5.9.3.4, with revisions made by the AASHTO T-10 committee for UHPC. The period between transfer and deck placement can range from a week to several months depending on the production and job flow, so this was deemed more appropriate than using the equations for time infinity.

$$\Delta f_{pT} = \Delta f_{pES} + \Delta f_{pLT} \quad \textbf{4-3}$$

$$\Delta f_{pES} = \frac{E_{ps}}{E_{ci}} * f_{cgp} \quad \textbf{4-4}$$

$$\Delta f_{LT} = \Delta f_{pSR} + \Delta f_{pCR} + \Delta f_{pR1} \quad \textbf{4-5}$$

$$\Delta f_{pSR} = \epsilon_{b(id)} E_p K_{(id)} \quad \textbf{4-6}$$

$$\Delta f_{pCR} = \frac{E_{ps}}{E_{ci}} f_{cgp} \psi_{b(id)} K_{(id)} \quad \textbf{4-7}$$

$$\Delta f_{pR1} = 1.2\ ksi \text{ for low-lax strands} \quad \textbf{4-8}$$

$$\epsilon_{bid} = k_s k_{hs} k_f k_{td}(t_d, t_i) K_4 * 0.6 \times 10^{-3} \quad \textbf{4-9}$$

$$K_{id} = \frac{1}{1 + \left(\frac{E_{ps}}{E_{ci}}\right) * \left(\frac{A_{ps}}{A_g}\right) * \left(1 + \left(\frac{A_g e_{pg}^2}{I_g}\right)\right) * \left(1 + 0.7\psi_{b(if)}\right)} \quad \textbf{4-10}$$

where: $K_3$ = By physical testing, otherwise 1.0

$K_4$ = By physical testing, otherwise 1.0

$k_s$ = 1.0 for UHPC

$k_{hs}$ = $1.5 - 1.0 * H$ per AASHTO, 1.0 per PCI

$k_{hc}$ = $1.12 - 0.24 * H$ per AASHTO, 1.0 per PCI

$k_f$ = $\frac{18}{1.5 * f'_{ci} - 3}$

$k_l$ = $t_i$ is less than 7 days, 1.0

$k_{td}$ = $\frac{t - t_i}{\left(\frac{300}{30 + f'_{ci}}\right) + 0.8(t - t_i)^{0.98}}$

The PCI technique employs the same equations and vocabulary as AASHTO, with the exception of a change to Equation 4-3 and one new equation. Furthermore, PCI recommends that the humidity factors for creep and shrinkage remain 1, with no humidity-based reductions.

$$\Delta f_{pT} = \Delta f_{pES} + \Delta f_{pshi} + \Delta f_{pLT} \quad \textbf{4-11}$$

$$\Delta f_{pshi} = \epsilon_{shi} E_{ps} K_{(id)} \quad \textbf{4-12}$$

where: $\epsilon_{shi}$ = 300 microstrains for UHPC

The material properties and section geometry of the piles were used to determine the prestressing losses. Short-term losses were expected to reach 24.7 ksi and 32.2 ksi, respectively, according to AASHTO and PCI recommendations. Total losses are expected to reach 71.1 ksi and 84.7 ksi within the first 90 days, according to AASHTO and PCI, respectively. Given that the initial stress applied to the strands was 202.5 ksi, these results suggest that the effective prestressing on the pile sections during testing was 131.4 ksi according to AASHTO and 117.8 ksi according to PCI.

The strain gauge measurements obtained during detensioning were used to validate the AASHTO and PCI projected short-term losses. The strain loss during detensioning is depicted in Figure 4-38. The strain loss experienced by each internal strain gauge is shown in Table 4-6. An average of 863 microstrains translates to a stress decrease of 23.7 ksi. For this data, the standard deviation is 2.0 ksi. There is a 4% variation between projected and observed values when compared to AASHTO.

**Table 4-6 Stress loss for each internal strain gauge during detensioning**

| Gauge Name | Detensioning stress loss (ksi) | Gauge Name | Detensioning stress loss (ksi) |
|---|---|---|---|
| UH16_24_C11T | 20.4 | UH16_6.3_C4.5T | 22.2 |
| UH16_24_C11M | 22.3 | UH16_6.3_C4.5B | 23.2 |
| UH16_24_C11B | 22.4 | UH16_6.2_C1.5T | 22.3 |
| UH16_24_C12T | 24.4 | UH16_6.2_C1.5B | 22.4 |

| | | | |
|---|---|---|---|
| UH16_24_C12B | 22.8 | UH16_6.2_C3T | 23.2 |
| UH16_24_C13T | 24.5 | UH16_6.2_C3M | 23.3 |
| UH16_24_C13M | 22.6 | UH16_6.2_C4.5T | 29.4 |
| UH16_24_C13B | 23.7 | UH16_6.2_C4.5B | 24.3 |
| UH16_16_C7M | 20.1 | UH16_6.1_C1.5T | 25.4 |
| UH16_16_C7B | 21.6 | UH16_6.1_C1.5B | 23.8 |
| UH16_16_C8T | 20.9 | UH16_6.1_C3T | 29.3 |
| UH16_16_C8B | 22.3 | UH16_6.1_C3M | 24.6 |
| UH16_16_S8B | 23.3 | UH16_6.1_S3M | 25.1 |
| UH16_16_C9T | 21.5 | UH16_6.1_C3B | 25.4 |
| UH16_16_C9M | 22.2 | UH16_6.1_C4.5T | 24.3 |
| UH16_16_C9B | 23.0 | UH16_6.1_C4.5B | 24.6 |
| UH16_6.3_C3T | 26.0 | UH16_24_SLtB1 | 23.9 |
| UH16_6.3_C3M | 25.9 | UH16_24_SLtB2 | 25.9 |
| UH16_6.3_S3M | 22.7 | UH16_16_SLtB1 | 25.6 |
| UH16_6.3_C3B | 22.6 | | |

Strain gauge values prior to detensioning were compared to the PCI predicted value. During the casting process and the two hours before the first set of measurements, each gauge was subjected to a tensile strain. Tensile strain levels ranged from 130 to 450 microstrains. The broad range could be due to gauge location discrepancies. During this monitoring period, the tensile strain rose throughout the early hydration phase. The next day, the strain gauge readings had stabilized, and some strain had been lost. This pattern remained consistent across all gauges until detensioning. The average strain lost due to shrinkage from casting to detensioning was 206 microstrains, which corresponded to 5.9 ksi. When combined with the measured elastic shortening losses, this leads to a total initial loss of 29.6 ksi, an 8% divergence from the projected value. The 206 microstrains recorded are much lower than the 300 microstrains advised by PCI, although more research is needed to confirm these findings.

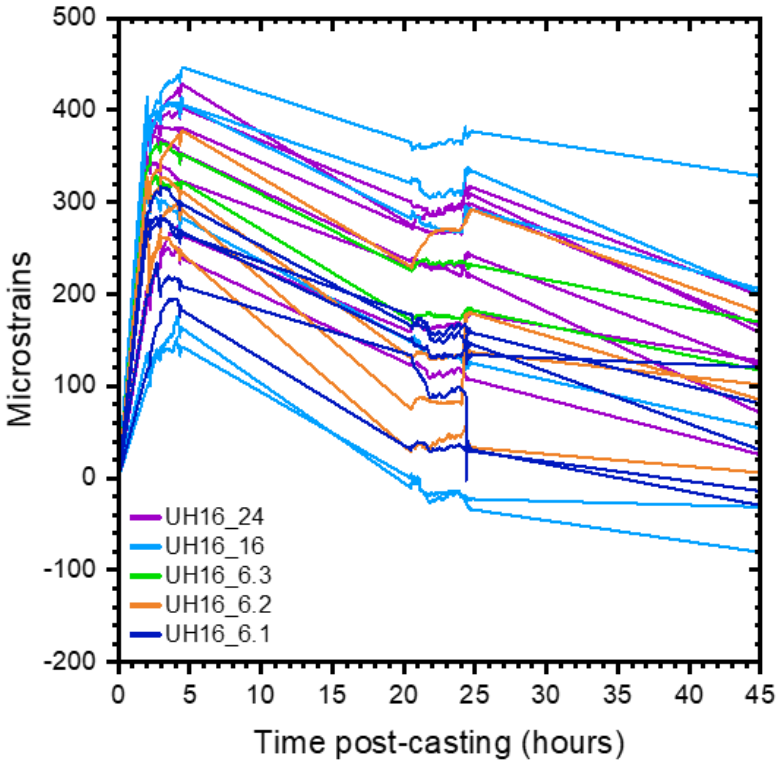


**Figure 4-39 Strain gauge readings from casting to detensioning**

Long-term losses are more difficult to quantify and separate from creep and shrinkage losses to obtain a value for effective prestressing during flexural testing. The original prestressing strain, however, can be approximated during flexural testing by studying the bottom external strain gauge values. When strain vs. force is shown for these gauges, the strain should remain elastic and grow at a consistent slope until cracking occurs. When cracking occurs, the total strain at the pile's bottom should be a combination of prestressing strain and UHPC cracking strain. After this point, the slope of the strain vs. force curve will change. This strain, along with the known material parameters, can be utilized to back-calculate the effective prestressing on the pile at the time of testing using Equations 4-13, 4-14, and 4-15. This procedure was also used piles tests performed in the same lab, described in 3.6.1, and was found to be consistent.

$$\epsilon_{b,exp} - \epsilon_{t,cr} = \epsilon_{pe} \quad \textbf{4-13}$$

$$\epsilon_{t,cr} = \frac{f_{t,cr}}{E_c} \quad \textbf{4-14}$$

$$f_{pe} = \frac{\left(\left(\epsilon_{b,exp} - \epsilon_{t,cr}\right) * E_c * A_{transform}\right)}{A_{ps}} \quad \textbf{4-15}$$

where: All strains are positive in tension, negative in compression

The location of slope change strain was reasonably obvious for UH16FS. However, when cracking occurs in UH16FW, the strains at the bottom of the pile either drop or plateau rather than increase. Until this time, the strain gauge readings had been linear and within an expected range, therefore this is most likely due to a microcrack growing exactly adjacent to the strain gauge. The slope shift for this pile was discovered by comparing an internal concrete gauge at a higher depth to

the external bottom gauge. When this internal concrete gauge began to change slope, that is when the concrete at that location reached this total cracking strain. The strain at the bottom of the pile can be estimated by extending the slope of the external gauge till this point. That extrapolated strain was utilized to calculate effective prestressing, yielding results similar to UH16FS. Despite the wide range, successful prestressing has little effect on the moment-curvature behavior of these sections. Figure 4-40 depicts the moment curvature curves for UH16FS with variable effective prestressing values. Although decreasing effective prestressing increases possible curvatures, the ultimate moment capacity remains constant.

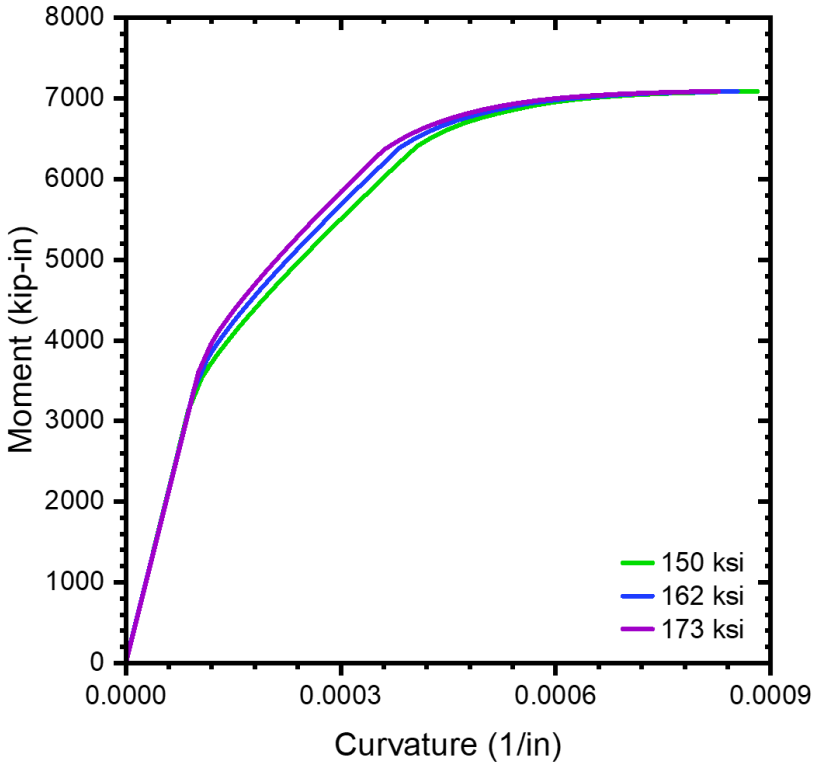


**Figure 4-40 Moment curvature comparison for different effective prestressing levels**

UH16FS returned 779 microstrains, while UH16FW returned 741 and 696 microstrains, respectively. These strains correspond to respective effective prestressing stresses of 173, 163, and 150 ksi. The finalized effective prestressing of 162 ksi was chosen for analysis in the following section. This effective prestressing amounts to a total reduction of 40.5 ksi. As previously stated, AASHTO predicts overall losses of 71.1 ksi while PCI predicts total losses of 84.7 ksi after 90 days. This suggests that the long-term losses for the time between transfer and deck placement are conservative. More research is needed to validate these findings and separate the creep and shrinkage effects.

### 4.6.2 Flexural Testing

The flexural testing findings were analyzed using two key elements: moment-curvature and force-displacement. The goal for both aspects was to compare experimental values to an analytical model derived from first principles analysis. This ensures that the design equations are suitable for predicting the behavior of these piles.

The external LED instrumentation was used to determine the experimental moment-curvature for UH16FS (strong-axis flexure). The horizontal positions of two LEDs set at the same section depth can be utilized to calculate the strain between those LEDs at a given load. The strain profile of paired LEDs down the depth of the pile was used to calculate curvature. From the experimental LED data, two alternative moment-curvature curves were calculated: one based on the inner LEDs, closer to midspan, and one based on the outer LEDs, the LEDs placed beneath the rollers at the borders of the constant moment-region. Figure 4-41 shows these LED pairs as well as the moment-curvature curves for UH16FS. The theoretical moment-curvature is compared to the experimental moment-curvatures generated from using the different material tensile profiles generated in Section 4.4.3.4.

Overall, the experimental and theoretical moment-curvatures are very close. Despite not falling within the material property constraints, the experimental curves are closest to the top bound tensile curve. This implies that the UHPC in UH16FS performed better in tensile tests than material testing would indicate. The failure mode is another piece of information that may be learned from the moment-curvature graph. UH16FS failed in flexure-shear, with a large diagonal crack originating beyond the constant moment area. The moment-curvature curves, on the other hand, indicate that the pile had reached its flexural capacity, and that load growth had hit a plateau. As a result, the flexural and shear capacities were almost certainly surpassed at the same time, resulting in the flexural-shear failure. This is supported by shear testing in Chapter 4, which revealed comparable failure mechanisms and crack patterns in specimens that exceeded their moment capabilities.

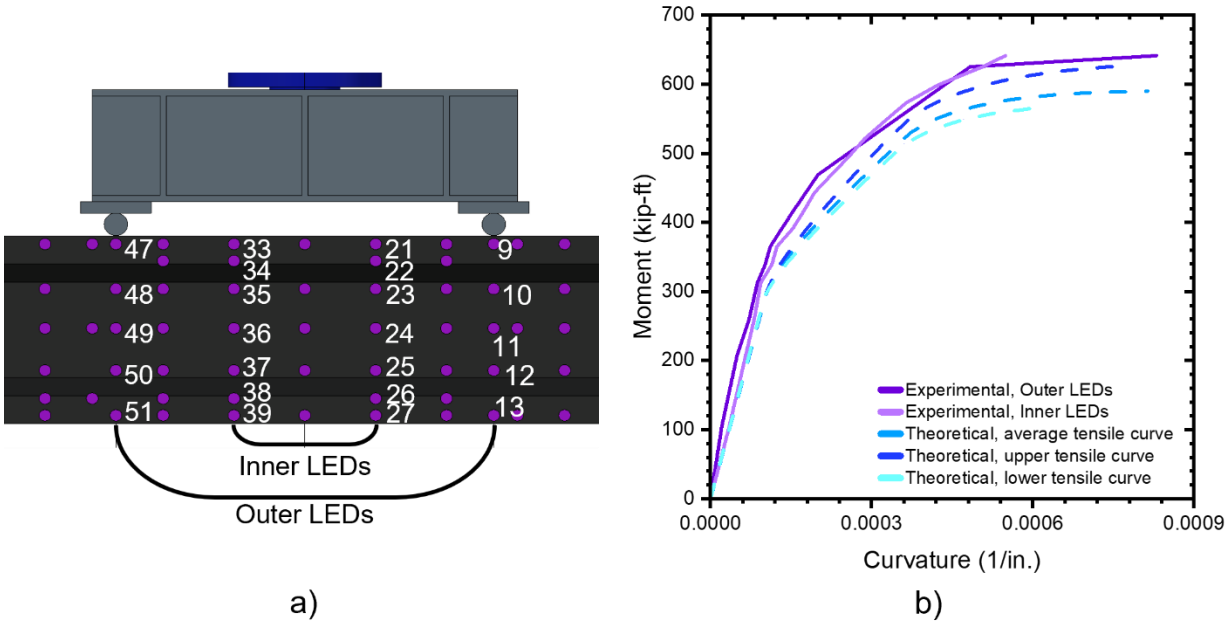


**Figure 4-41 Moment-curvature for UH16FS a) LED pairs for strain profiles, b) experimental and theoretical graphs**

Despite the positive results of moment-curvature, comparing simply curvature can be problematic. Moment-curvature can be deceiving since prestressed members begin with an initial level of strain from prestressing. Any set of strain profiles set at the same slope could result in the same curvature. To address this, the top and bottom strains calculated by the moment-curvature spreadsheets were compared to the top and bottom strains measured by external foil gauges attached to the piles. These curves for the top and bottom fibers of UH16FS are depicted in Figure 4-42, and they agree well in general, especially in the elastic region. Local strain and microcracking

can explain some of the discrepancy between predicted and experimental strains in the inelastic zone. A microcrack likely formed under the strain gauge EXT_BottomC at 65 kips, causing the abrupt increase in strain. However, when stress increased, additional microcracks began to dominate, and the behavior returned to normal, following the expected trend. Nonetheless, these force-strains support the accuracy of the analytical modeling based on first principles section analysis.

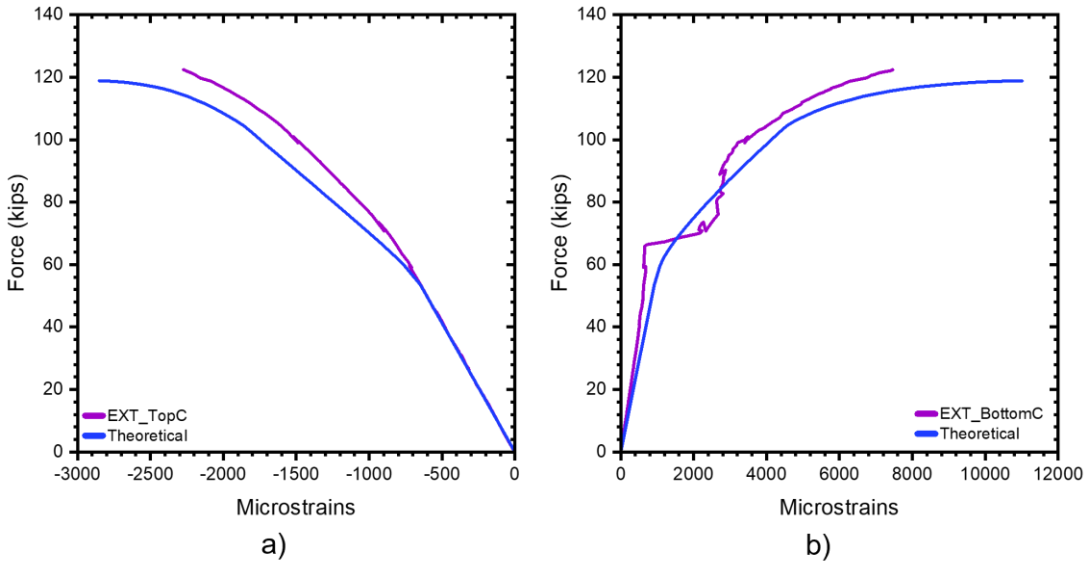


**Figure 4-42 Force vs. strain for UH16FS a) top strains, b) bottom strains**

The same procedures were used to generate moment-curvature and force-strain curves for UH16FW. Instead of employing inner and outer sets of LEDs, all internal and external strain gauges were used at midspan to create another strain profile. Again, the theoretical and experimental curves correspond well, particularly in the elastic range, as illustrated in Figure 4-43. Figure 4-44 plots force vs. strain, and the top strains match the theoretical strains fairly closely. However, due to an issue with the bottom surface strain gauges during testing, the strains are only shown for the first 32 kips.

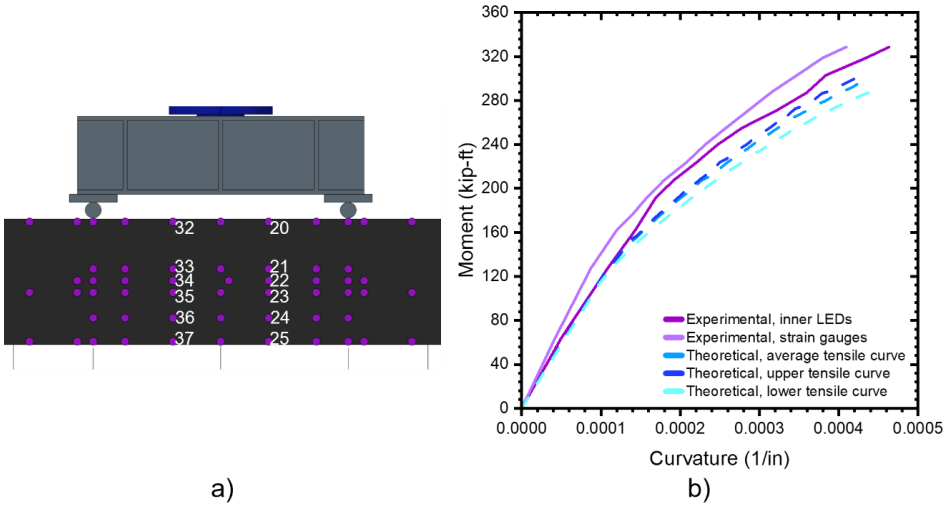


**Figure 4-43 Moment-curvature for UH16FW a) LED pairs for strain profiles, b) experimental and theoretical graphs**

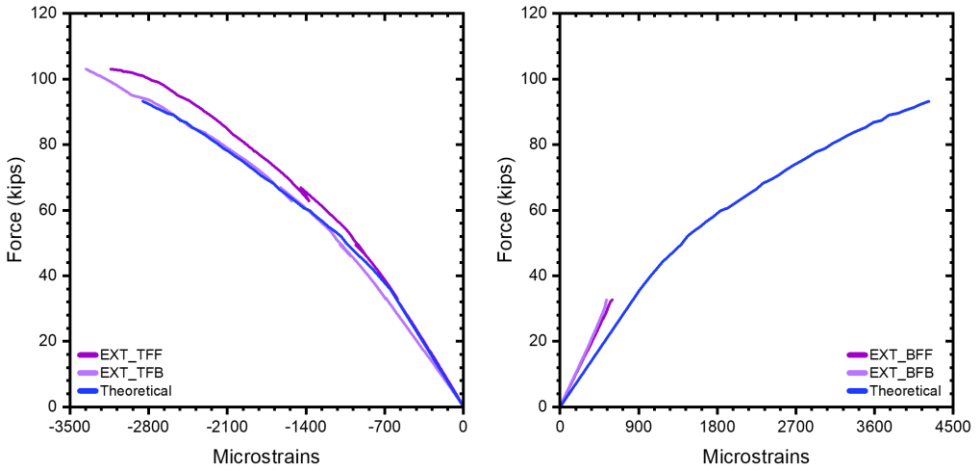


**Figure 4-44 Force vs. strain for UH16FW a) top strains, b) bottom strains**

The force-displacement relationship was the final key factor in interpreting the flexural testing data. Using the moment-area method described in Section 3.6.2, two force-displacement curves were generated from the moment-curvatures for each pile. The first was based on the experimental moment-curvature discovered using LEDs, while the second was based on the theoretical moment-curvature obtained by using the upper-bound of tensile behavior. Because the upper bound was the best approximation of behavior in both piles, it was chosen over the average or lower bound.

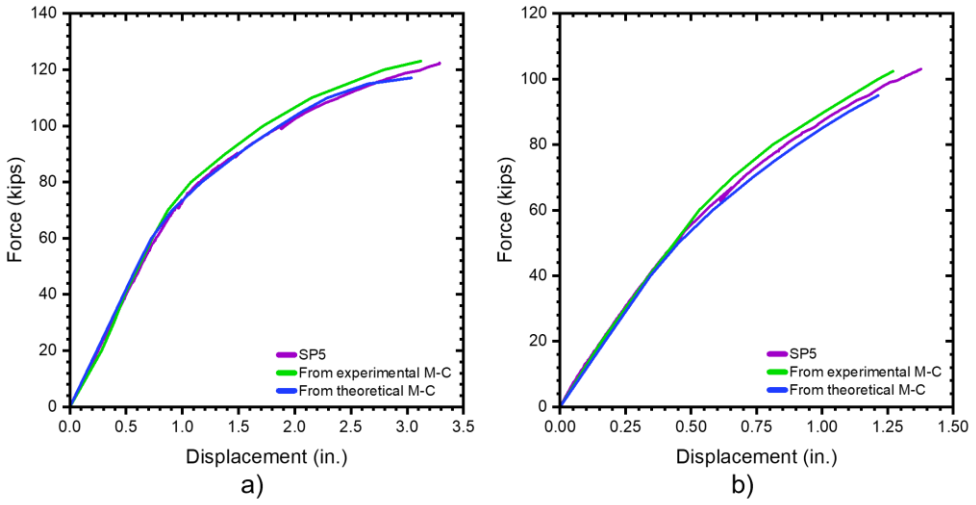


**Figure 4-45 Force-displacement for a) UH16FS, b) UH16FW**

$$\Delta_v = \gamma_v L = \frac{VL}{AG} = \frac{2VL(1+\nu)}{AE} \qquad \textbf{4-16}$$

The back-calculated force-displacement values for both piles corresponded well with the string potentiometer experimental readings, as shown in Figure 4-45. In both cases, the string potentiometer curve differs from the experimental moment-curvature curve. This could be explained by the method used to calculate moment-curvature. Fitting a strain profile to strains at various levels yielded the moment-curvature. This procedure is subject to some variability. Furthermore, back-calculating force-displacement accounts only for flexural displacement, but there could have been some shear displacement as well. Unfortunately, because the majority of the instrumentation was centered at the midspan to capture flexural behavior, shear displacement was not captured.

Equation 4-16 can be used to compute the elastic shear displacement at midspan to yield the theoretical shear displacement. At peak load, this results in 0.024 and 0.014 in. for the UH16FS and UH16FW, respectively. This would slightly shift each experimental force-displacement curve to the right, bringing it closer to the string potentiometer curves, but not by much.

### 4.6.3 Shear Testing

Shear testing was done primarily to assess the applicability of current shear codes and to see if UHPC had enough tensile strength to prevent the need for extra mild steel shear reinforcement. The AASHTO LRFD code, which has been changed for compatibility with UHPC, and the PCI UHPC recommendations will both be examined. Equation 4-17, which multiplies the effective shear area by the UHPC localization stress and the shear cracking angle, is the basic shear capacity equation for UHPC without transverse reinforcement.

There are two methods approved by AASHTO for estimating the shear cracking angle. Both involve calculations based on the net longitudinal tensile strain in the section at the centroid of the tensile reinforcement, $\varepsilon_s$, or the tensile localization strain. Equation 4-18 or Equation 4-19 are used to compute the net longitudinal tensile strain, which is based on the specimen's amount of loading at a specific section. Equation 4-19 usually takes precedence for these pile sections because of the heavy prestressing force.

The "general approach" is the name given to the first shear cracking angle calculation method detailed in AASHTO. This method is iterative and uses a set of equations to get the shear cracking angle. Equation 4-20 makes it easy to calculate the shear angle, designated $\theta_{A,Gen}$ for the purposes of this investigation, in the absence of any mild steel transverse reinforcement or external axial stress. The second approach makes use of a table that calculates the shear cracking angle from the longitudinal strain at a section, $\varepsilon_s$, and the UHPC localization strain. The label "$\theta_{A,\,Table}$" will indicate the shear angle found with this method.

$$V_{UHPC} = \min\left(0.25 f_c' b_v d_v \; and \; f_{t,loc} b_v d_v \cot(\theta_v)\right) \quad \textbf{4-17}$$

$$\epsilon_s = \frac{\left(\frac{M_u}{d_v}\right) + \left|V_u - V_p\right| - A_{ps} f_{po} - f_{t,cr} A_{ct}}{E_{ps} A_{ps}} > 0.0 \; and < \epsilon_{t,cr} \quad \textbf{4-18}$$

$$\epsilon_s = \frac{\left(\frac{M_u}{d_v}\right) + \left|V_u - V_p\right| - A_{ps} f_{po}}{E_{ps} A_{ps} + E_c A_{ct}} \quad \textbf{4-19}$$

$$\epsilon_{t,loc} = \frac{\epsilon_s}{2}\left(1 + \cot^2\left(\theta_{A,Gen}\right)\right) + \frac{2 f_{t,loc}}{E_c} \cot^4\left(\theta_{A,Gen}\right) \quad \textbf{4-20}$$

The PCI code was also considered for comparing ultimate shear capacity, outlined in Equations 4-21 through 4-25. The fundamental equation for PCI is fairly similar to that of AASHTO, except it substitutes a flat value of 0.75 ksi for the residual tensile strength of UHPC in place of the tensile stress at localization. This figure, which conservatively integrates conversion factors for ultimate flexural strength to post-cracking tensile strength, unfavorable fiber orientation factors, size effects, and shape effects, is derived from the correlation of flexural tensile capabilities. The PCI calculations are the same as those employed by AASHTO with the exception of the usage of the residual tensile strength, $f_{rr}$. Given that $4/3 f_{rr}$ is equal to 1 and the tensile localization stress utilized in AASHTO's equation is 0.97 ksi in the case of this UHPC, the findings obtained from PCI's equation match those of AASHTO.

Similar to AASHTO, PCI requires the calculations of the shear cracking angle, but it offers a less complex calculation using Equation 4-23. For analysis, we'll refer to this angle as $\theta_{PCI}$. Equations 4-24 and 4-25 are used to determine the longitudinal strain, the same value used in AASHTO equations. The longitudinal strain for PCI, however, has a lower bound of -400 microstrains.

$$V_n = \min\left(0.18 f_c' b_v d_v + V_p \ \ and \ V_{cf} + V_s + V_p\right) \quad \textbf{4-21}$$

$$V_{cf} = \left(\frac{4}{3} f_{rr}\right) b_v d_v \cot\left(\theta_v\right) \quad \textbf{4-22}$$

$$\theta_v = 29 + 3500\epsilon_s \quad \textbf{4-23}$$

$$\epsilon_s = \frac{\left(\frac{M_u}{d_v}\right) + (V_u - V_p) - P_e}{E_{ps} A_{ps}} \geq 0.0 \ and \leq 0.006 \quad \textbf{4-24}$$

$$\epsilon_s = \frac{\left(\frac{M_u}{d_v}\right) + (V_u - V_p) - P_e}{E_{ps} A_{ps} + E_c A_{ct}} \leq 0.0 \ and \geq -0.0004 \quad \textbf{4-25}$$

where $f_{rr}$ = 0.75 ksi

The section along the pile length studied, the shear cracking angle, and the shear capacity were the three aspects of these equations that were of interest. The longitudinal strain, which affects the cracking angle and shear capacity, is determined by the section along the pile length that will be subject to analysis. The "critical section," which is the standard section to inspect, is defined as one unit of shear depth from the support, or dv. However, the moment varies greatly from one support to the next, and the shear crack was not always confined at dv. Because of this, three locations aside from the critical section were examined. The start of the localized crack, defined as the point where the fracture angles up into the web, the end of the localized crack, defined as the point where the angled crack meets the top-flange interface, and the middle point between the two. In the case of UH16FW_V2, where bond failure was present, the localized crack did not reach the top-flange interface and only reached the middle of the pile's height. In this test, the mid-crack was taken as the point at which the localized crack reached mid-height rather than the end-crack, which was not calculated. For each shear section location, Table 4-7 displays the various AASHTO general approach shear cracking angles. The shear angle shifts less than one degree, resulting in a maximum shear capacity change of 4.5%. This suggests that the shear angle and capacity for the spans at which these piles were tested are not significantly impacted by the changing section location. The shear cracking angles at mid-crack were chosen for use in subsequent calculations. This location represents the typical crack location based on prior testing, including UH16FW V1, where the shear crack localized in the middle of the web, and the prior shear testing carried out and described in Chapter3.

The three previously described shear cracking angles were computed for each shear test, as indicated in Table 4-8. When the angle was calculated according to PCI guidelines, the lower strain limit was attained for each pile. After that, an additional angle, $\theta_{PCI,2}$, was calculated while ignoring the lower limit. Overall, the projected shear cracking angles are greater than those found during testing, implying that all of the calculated methods are conservative.

**Table 4-7 Effect of shear section location on AASHTO shear crack angle calculations**

| | UH16FW_V1 | UH16FW_V2 |
|---|---|---|
| $M_{u@dv}$ (k-ft) | 32.53 | 129.03 |
| $\theta_{A,Gen}$ (degrees) | 24.94 | 25.19 |
| $M_{u@CrackStart}$ (k-ft) | 42.67 | 73.74 |
| $\theta_{A,Gen}$ (degrees) | 24.98 | 24.96 |
| $M_{u@MidCrack}$ (k-ft) | 148.75 | 169.69 |
| $\theta_{A,Gen}$ (degrees) | 25.44 | 25.37 |
| $M_{u@CrackEnd}$ (k-ft) | 254.32 | -- |
| $\theta_{A,Gen}$ (degrees) | 25.91 | -- |

Table 4-9 shows the expected shear capacity for each code based on the shear angles. The angle recorded during experimental testing was also used for each code. The unity values, which are the ratios of the experimental and predicted shear capacities, are also presented. The shear capacity obtained in experimental testing is typically greater than the capacity projected by both codes. The free-end test unity values, UH16FW_V2, are less conservative than UH16FW_V1, however failure occurred within the transfer length, and bond failure was seen in addition to shear cracking. This explains why the experimental shear angle has a reduced experimental capacity and an unconservative unity value.

**Table 4-8 Shear cracking angles calculated through different methods.**

| | | UH16FW_V1 | UH16FW_V2 |
|---|---|---|---|
| AASHTO Gen. Approach | $\theta_{A,Gen}$ | 25.44 | 25.37 |
| AASHTO Table Approach | $\theta_{A,Table}$ | 26.93 | 26.89 |
| PCI Gen. Approach | $\theta_{PCI}$ | 27.6 | 27.6 |
| PCI Gen. Approach, ignoring lower limit | $\theta_{PCI,2}$ | 25.95 | 25.75 |
| Experimental | $\theta_{Exp}$ | **22.5** | **21** |

**Table 4-9 Pile shear capacities and unity values for different code calculations**

| | | Capacity (kips) | | $V_{exp}/V_n$ | |
|---|---|---|---|---|---|
| | | UH16FW_V1 | UH16FW_V2 | UH16FW_V1 | UH16FW_V2 |
| AASHTO | $\theta_{A,Gen}$ | 94.6 | 94.9 | 1.40 | 1.09 |
| | $\theta_{A,Table}$ | 88.6 | 88.7 | 1.50 | 1.17 |
| | $\theta_{Exp}$ | 108.6 | 117.2 | 1.22 | 0.88 |
| PCI | $\theta_{PCI}$ | 86.1 | 86.1 | 1.54 | 1.20 |
| | $\theta_{PCI,2}$ | 92.4 | 93.3 | 1.44 | 1.11 |
| | $\theta_{Exp}$ | 108.6 | 117.2 | 1.22 | 0.88 |
| Experimental | -- | **132.8** | **103.5** | **1.00** | **1.00** |

# 5 DEVELOPMENT AND STRUCTURAL CHARACTERIZATION OF PLANNED UHPC PILE SPLICE

## 5.1 Introduction

Driven pile splices connect separate pile segments, turning them from independent parts into a cohesive foundation system. The significance of understanding and incorporating these splices into the overall design cannot be overstated. One primary reason for their indispensability lies in the inherent variability of field conditions and the often-unpredictable depths required for foundational support. Piles are typically fabricated in specific lengths, guided by precast plant prestressing bed lengths and maximum shipping lengths; however, the actual length needed in the field can vary due to site-specific factors such as soil composition, geotechnical considerations, or unforeseen obstacles. In such instances, driven pile splices come to the rescue, offering the flexibility and adaptability necessary to achieve the required depth and load-bearing capacity. Therefore, an exploration of driven pile splices is not merely a complementary aspect but a pivotal one in the comprehensive understanding of pile foundation systems, ensuring their viability and effectiveness in real-world applications. This chapter will discuss the design and large-scale testing of a splice companion to the 12-in. UHPC H-shaped pile section developed in Chapter 3.

## 5.2 Splice Design

There are numerous choices available for driven pile splices. In the case of steel piles, it is common practice to weld the ends of steel piles, occasionally using a "splicer plate"—another steel plate that spans the two piles. The piles are joined together into a single continuous piece by applying welds to the splicer plate's edges. The full bending and tensile strength of the unspliced pile can be achieved by accordingly designing the welds and splicer plates. For concrete piles, there are several options, with a mechanical splice being the most common. An anchor plate made of steel is cast into the pile’s end before steel wedges are inserted to span the two pile surfaces. This technique frequently makes use of proprietary systems that provide the full capacity of an unspliced pile. The dowel splice is another technique, which involves drilling or casting dowel bars into the pile’s end. Dowel bars are either grouted or epoxy-fixed into place after holes are drilled into the complementary pile's end.

The pile splice design was intended to build on previous work done at Iowa State (Garder, Aaleti, Zhong, & Sritharan, 2019), which is shown in Figure 5-1. The Iowa State design combined the principles of welded steel pile splices and mechanical concrete pile splices. A steel plate with the same H-shape as the pile was cast into the pile’s end, with steel angles extending along the length of the pile and shear studs for force transfer. For added moment capacity, two pieces of rebar were added to the web of the H-shaped plate. The two pile ends were then aligned and welded around the H-shape’s edges. The experimental testing of this splice was cut short due to weld failures at the angle-steel plate interface. The goal of this project was to create a splice that was more efficient and adaptable to larger pile sizes than the previous design.

The general goals of any pile splice are to sufficiently transfer loads experienced by the piles during installation and service life. Tension, compression, flexure, and shear are the primary loading types considered. During the driving process, tension forces are applied to driven piles, and these forces must be transferred from the steel splice to the UHPC via welds and shear studs. The H-shaped steel base plates absorb compressive stresses during driving and service, but due to the large steel area and high strength of steel and UHPC, these forces are not as influential for the

design. Flexural loading is transferred during service from the base steel plate to the steel angles via welds, and from the angles to the UHPC via shear studs. This also applies to shear loading. These were the critical components that had to be designed for the UHPC splice.

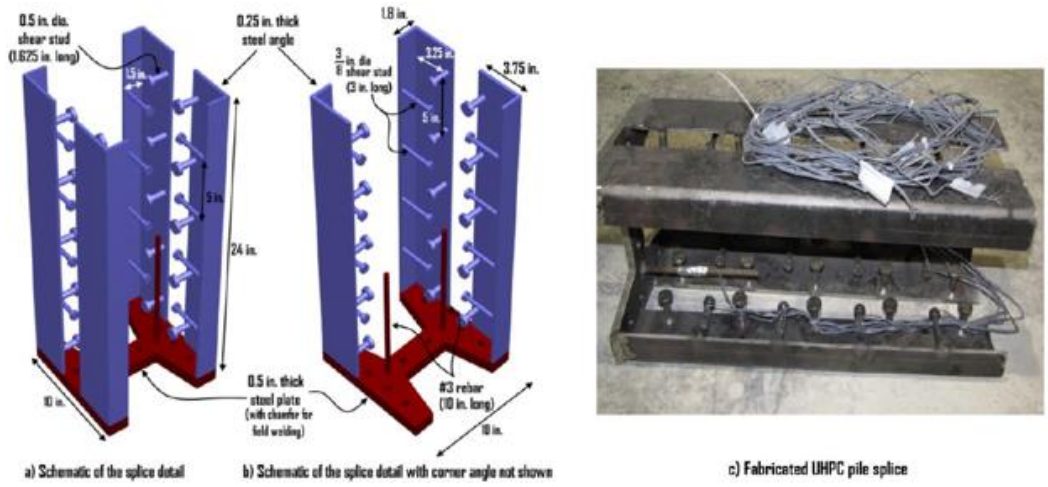


**Figure 5-1 Iowa State pile splice design (Garder, Aaleti, Zhong, & Sritharan, 2019)**

Because 12-in. steel piles are the most commonly used pile size in bridge abutments and foundations, the UH12x71 UHPC alternative was chosen for splice design. The details and design process of the unspliced cross-section are described in Section 3.2 and shown here in Figure 5-2. The splice would be designed for a strong-axis moment of 200 kip-ft, weak-axis moment of 90 kip-ft, and a tensile force corresponding to 1.25 ksi, or 82 kips. The embedded portion of the splice was designed first, with the capacity under each loading condition compared to the capacity of the unspliced pile. Shortly after starting this process, it became clear that using steel angles was not a cost-effective option for this pile section. There are no commercially available standard angles that would fit the flange depth and provide sufficient moment capacity. Either a larger angle must be purchased, and one leg cut along its length, or a custom built-up section must be fabricated. Both of these alternatives are time-consuming and costly. Instead of an angle at each corner, another option was to use a steel plate that spans the entire top and bottom flange. The moment couples shown in Figure 5-3 were used to calculate the thickness of this plate. The combined capacity of the moment couples from the steel plates and the rods should be greater than the pile's unspliced moment capacity. This calculation was performed in both strong and weak-axis bending, and a thickness of 0.5 in. was ultimately chosen, with two 100 ksi, #6 threaded rods in the web to aid in strong-axis flexural capacity. The welds between the H-shaped plate and the splice plates were designed to transfer the entire capacity.

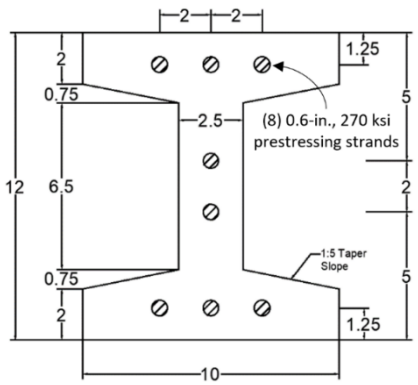


**Figure 5-2 UH12x71 pile section for splice design (dimensions in inches)**

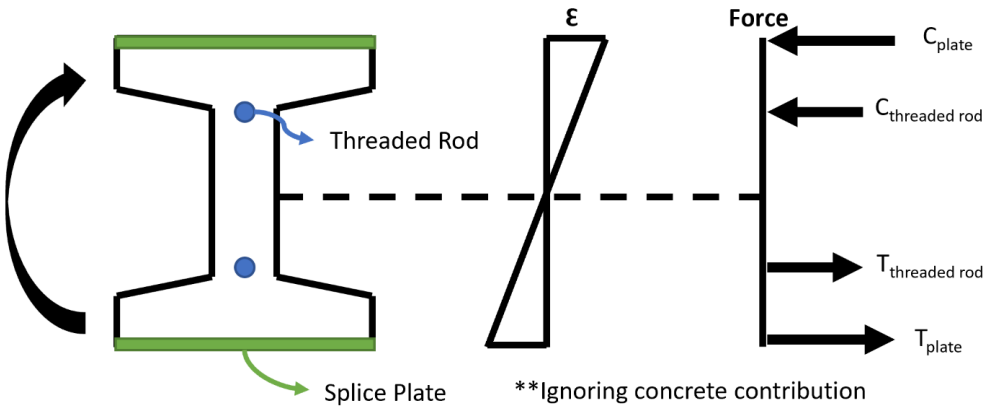


**Figure 5-3 Moment couples used for splice design.**

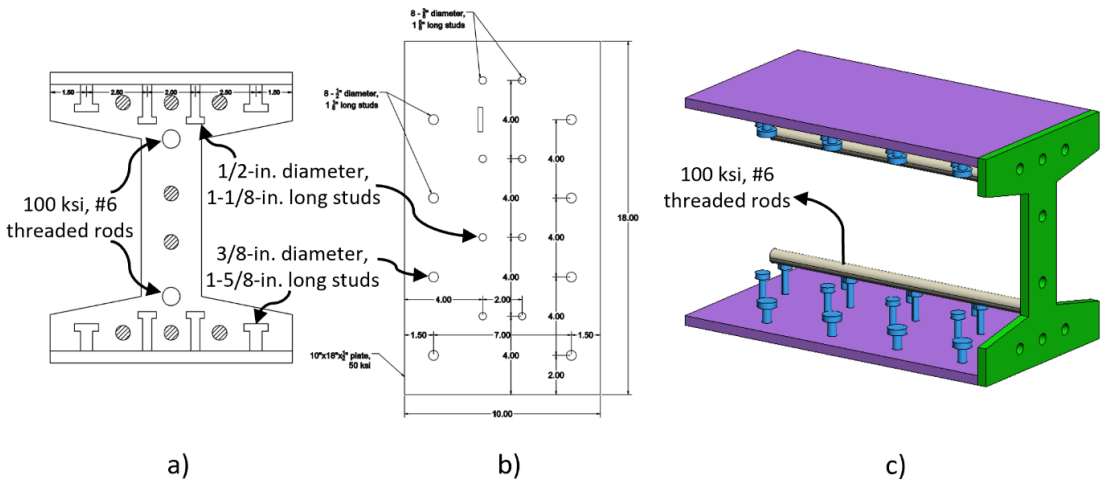


**Figure 5-4 Splice details a) cross-sectional view, b) plan view of splice plate with shear stud layout, c) 3D schematic of splice system**

The shear stud detailing was the final design element for the embedded portion of the splice. The stud dimensions were determined by the amount of space available in the pile flanges as well as the capacity requirements. The shear studs and prestressing strands both received at least one inch of concrete cover. The number of shear studs and the length of the splice plates were originally

designed to transfer 100% of the pile capacity. However, the number of studs and plate lengths were cost prohibitive. Furthermore, calculations were initially performed without any contribution from the UHPC pile. While this is true at the very end of the pile, the UHPC's contribution towards capacity will increase significantly over the transfer length. The splice plate length was decided to be 18 inches, or three inches longer than the anticipated transfer length. The pile should be able to withstand the loading on its own after the transfer length. Shear studs were placed so that the splice plate length had the smallest possible spacing. Finally, two types of shear studs were used: a 1/2-in. diameter stud and a 3/8-in. diameter stud. On the splice plates, eight of each stud type was provided, resulting in a total of 16 studs on each pile end. This number of studs alone provides 57 percent of the moment capacity. The shear studs' yield and ultimate strength were 49 and 61 ksi, respectively.

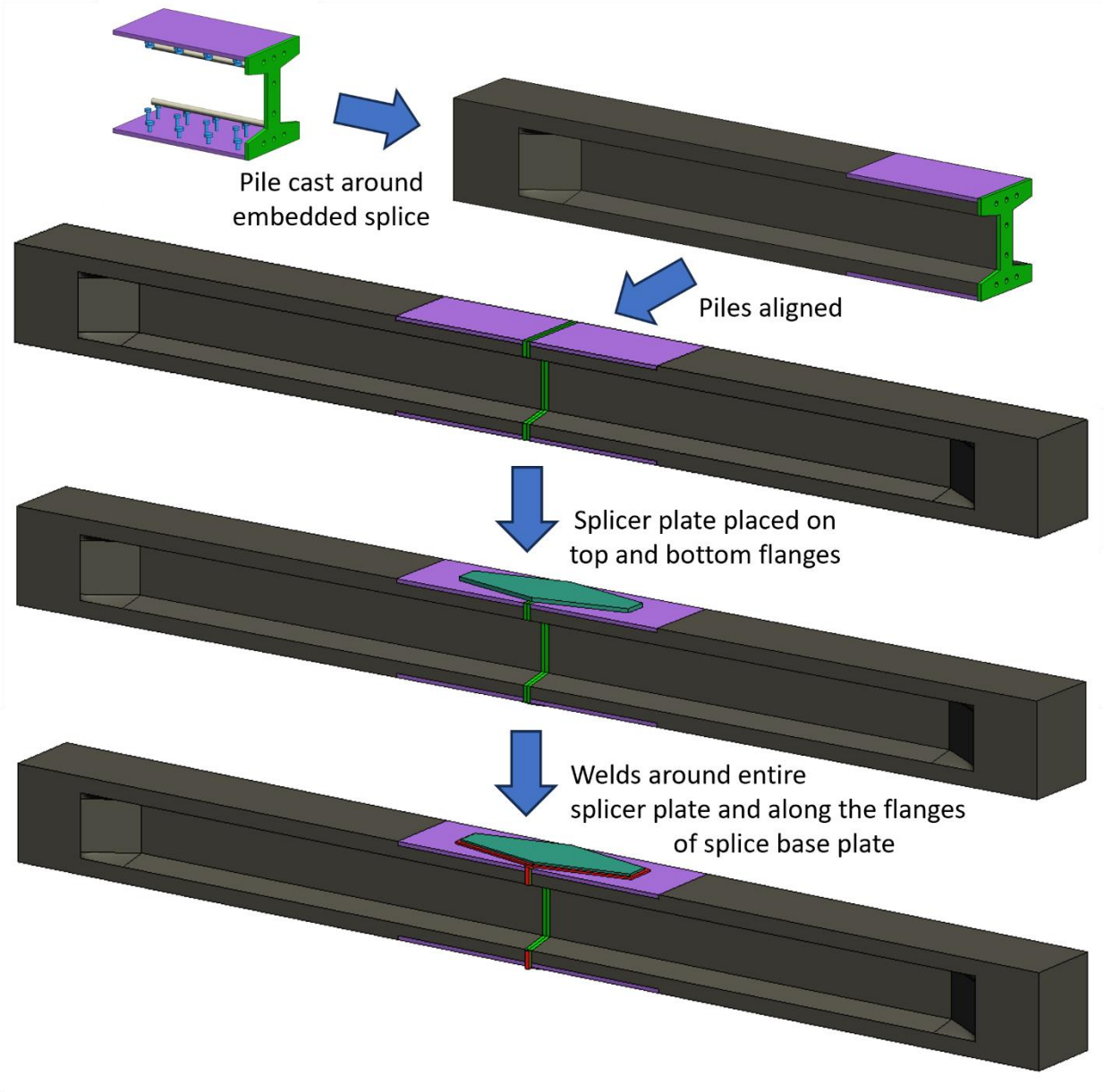


**Figure 5-5 Schematic of the splice assembly for UHPC Piles**

After finishing the embedded portion of the splice design, the emphasis shifted to how the piles would be joined together. The original plan called for aligning the piles and welding around the perimeter of the H-shaped base plates. Full or partial penetration butt welds would have been more than adequate to ensure full capacity. However, it was decided that in this case, a welded splice similar to that used for steel piles would be used. A diamond-shaped splicer plate with dimensions similar to those used in Alabama Department of Transportation projects would be welded around the perimeter of the piles' top and bottom flanges. When the splicer plates are first welded to the pile already in the ground, this system aids in alignment during pile driving. Figure 5-5 depicts the splice assembly process. Full-penetration butt welds were placed on the flanges in addition to 3/8-in. fillet welding around the perimeter of the diamond-shaped splicer plate. These additional welds provided the necessary strength to achieve full unspliced weak-axis flexural capacity.

## 5.3 Fabrication

The unspliced piles and spliced piles were cast at the same time, and the casting process for these piles is also described in Section 3.3. Details specific to spliced piles, such as splice internal instrumentation, will be covered in this section. Six full-scale 6.5-foot splice segments were cast in order to create three 13-foot spliced pile specimens. One pile would be tested for strong-axis flexure (UH12SS), one for weak-axis bending (UH12SW), and one for tension (UH12ST). For instrumentation purposes, the 6.5-foot segments were divided into "right" and "left" sections.

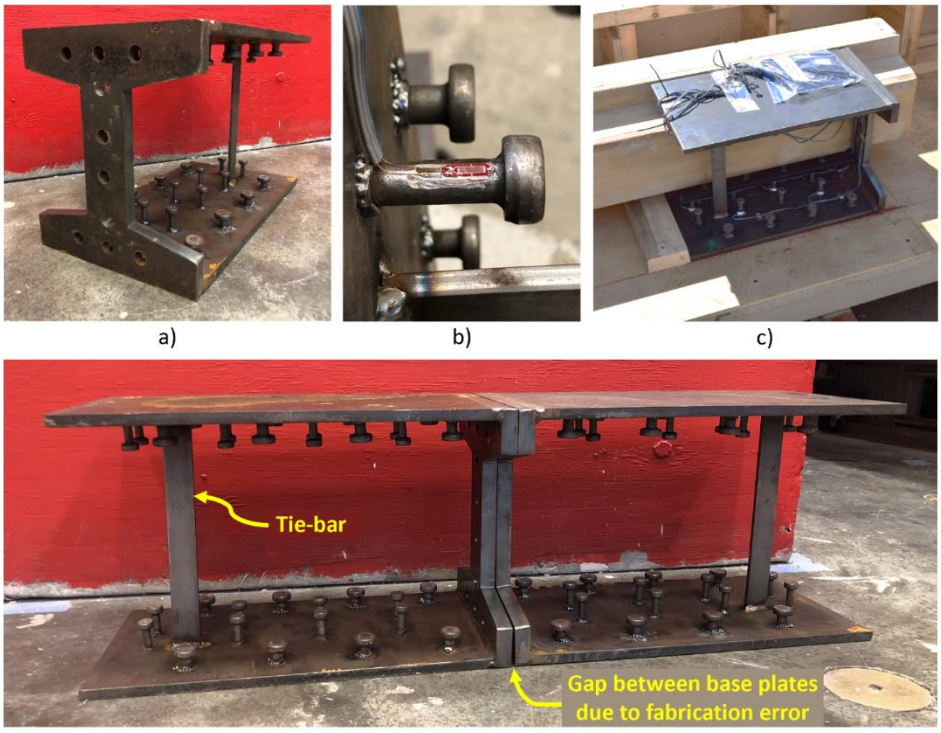


**Figure 5-6 a) Embedded splice assembly for one end, b) shear stud strain gauge, c) splice assembly in formwork, d) tie-bar and fabrication error gap between mated splice assemblies**

The embedded splice details were sent to a nearby fabrication shop for assembly. When the finished embedded splices were first received, it was discovered that the two splice stud plates were not parallel, sometimes by as much as 0.5-in. over 18-in. of length. Because this was unacceptable, they were returned to the shop and a tie-bar was added. Unfortunately, the tie-bar created a slight

curvature in the base plate. Figure 5-6 shows how the splice assemblies were paired for each pile based on which pairs minimized the gap. Following the completion of the assembly fabrication, foil gauges were installed on chosen shear studs. Because the shorter studs were not long enough to accommodate gauge placement, alternating long gauges were selected. The gauges were named after their parent pile, then a "R" for right or "L" for left, "T" for top or "B" for bottom, and a number. For example, the first strain gauge on the left side of the UH12ST's top stud plate would be labeled UH12ST_LT1. Figure 5-7 depicts this in schematic form. Figure 5-6b depicts a photograph of one strain gauge. Two burr holes were drilled in the top stud plate prior to transporting the splices to the precast plant for UHPC casting to allow trapped air to escape during casting.

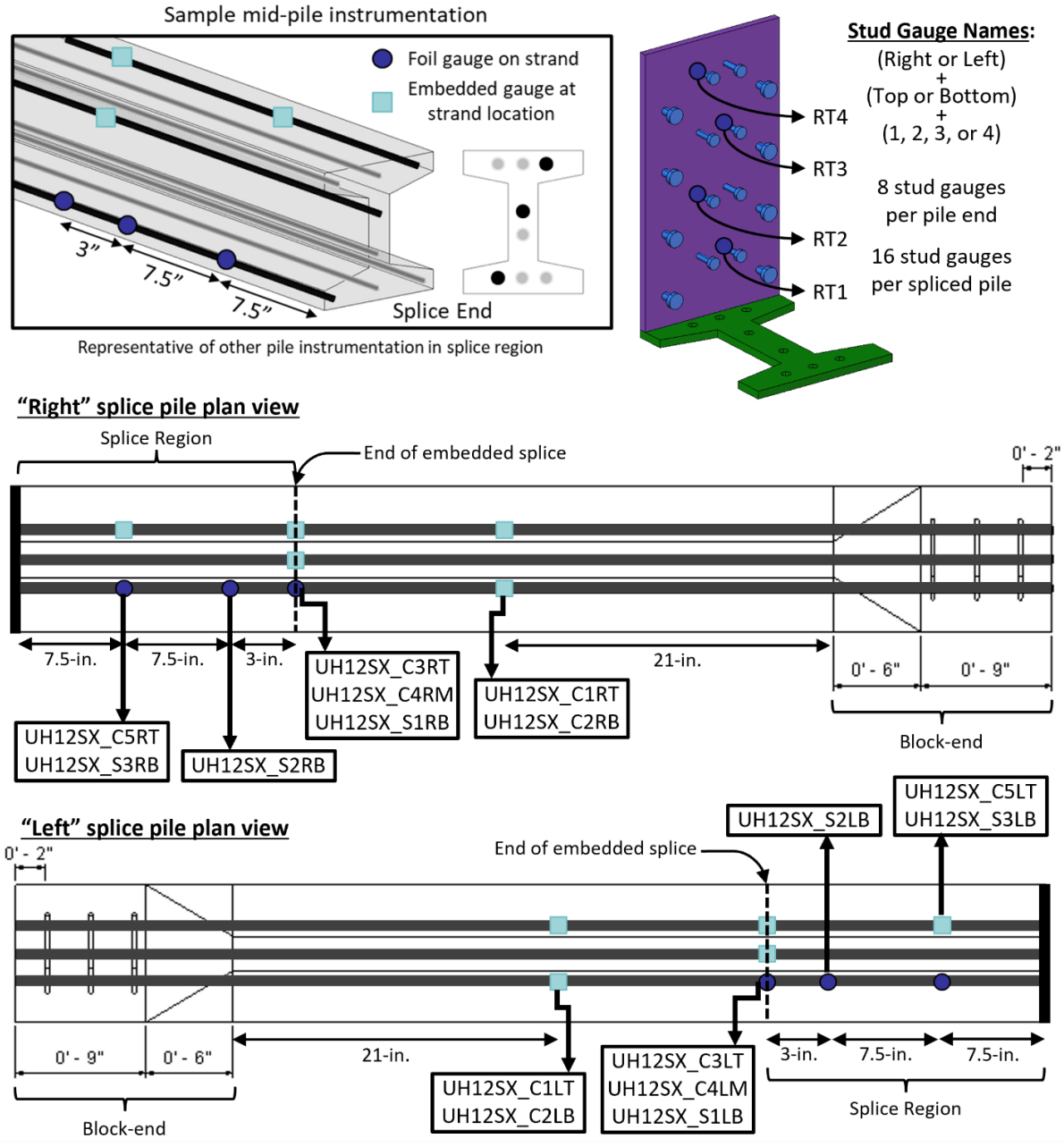


**Figure 5-7 Splice pile internal instrumentation**

At the precast plant, the remaining internal instrumentation was attached to the prestressing strands. As shown in Figure 5-7, the majority of gauges were placed in the splice region prior to the end of the embedded splice. A foil gauge was placed on the bottom strand at the anticipated transfer length of 15 in., and two gauges were placed at half that distance. Two embedded gauges and one foil gauge were installed at the end of the splice region to measure the concrete strains at the steel location. To understand the strains in the concrete in the non-spliced region, two additional embedded gauges were placed near midspan. All of these gauges were named after their parent pile, with "C" or "S" denoting concrete or steel strains, "L" or "R" denoting the left or right side of the splice, and "T," "M," or "B" denoting the strand level along the pile height.

At this stage of testing, each pile was also outfitted with three #3 stirrups spaced three inches apart to ensure no burst or endzone cracking in the pile block ends. In the H-shaped portion of the piles, no transverse reinforcement was used. The tension pile, UH12ST, was outfitted with additional testing hardware. Each block-end received four high-strength 1-in. threaded rods, with half of their lengths embedded in the pile formwork and the other half protruding. These would be used to anchor a steel section for testing purposes. Two 5/8-in. threaded rods with couplers on the end were placed in the formwork on the block ends for the same reason. Figure 5-8 depicts a cross-section of these additional items for UH12ST. These will be discussed in greater detail when Section 5.4.2 discusses the fabrication of the tension test specimen.

Overall, the casting of the spliced specimens went smoothly, but the stud plates made it difficult to determine when the formwork had filled with UHPC. The 12-in. burr holes were not visible when UHPC reached the top, and there was a small gap (less than 12-in.) at the end of the pile where the H-shaped steel plate met the top stud plate for two pile sections, UH12SWR and UH12SSL. This was later patched with the same UHPC but without fibers. This problem could have been mitigated in a number of ways. To begin, the burr holes could have been larger to make it easier to see when UHPC had filled the formworks. Second, the flow of the mix could have been improved. The splices were poured from a stiffer batch compared to the other two batches. More flow could have made it easier to fill out the forms. Finally, a more extreme option would be to cast these splices in a weak-axis orientation instead of the strong-axis orientation used for these piles. There would be a risk of voids forming on one side of the web, but it would ensure that the shear studs were completely covered, and the rest of the splice region was properly filled. A local fabricator successfully spliced the piles according to the specifications established by the researchers, following ALDOT standard construction specifications. For any of the three spliced piles, there were no issues with the splicer plate dimensions or the welds connecting the pile sections.

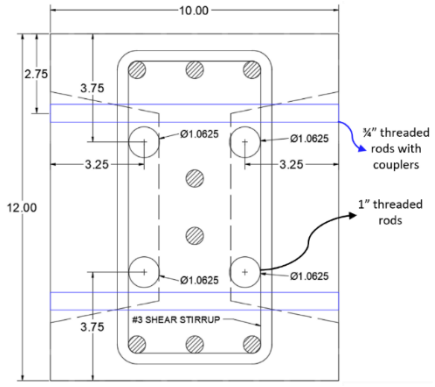


**Figure 5-8 UH12ST threaded rod and coupler locations**

### 5.3.1 Material Properties

The UHPC used for the spliced piles was the same as described in Chapter 4. The material properties and any pertinent analysis are discussed in Sections 3.4 and 3.6.1.

## 5.4 Experimental Testing and Observations

### 5.4.1 Flexural Testing

The two flexural test specimens, UH12SS and UH12SW, were designed to compare the spliced pile's capacity and behavior to the unspliced tests described in Chapter 4. Piles were simply supported at each end by a pin and a roller to achieve this. The load was applied to two rollers at midspan 24-in. apart using a 200-kip hydraulic jack spread across a spreader beam. For the spans of the spliced piles, the load protocols for each test were scaled from the unspliced equivalent. The instrumentation used for these tests was largely the same as that used for unspliced piles. Internal and external strain gauges measured concrete and steel strains, while non-contact LEDs and string potentiometers measured pile displacement. Figure 5-9 depicts the UH12SS instrumentation, while Figure 5-10 depicts the UH12SW instrumentation.

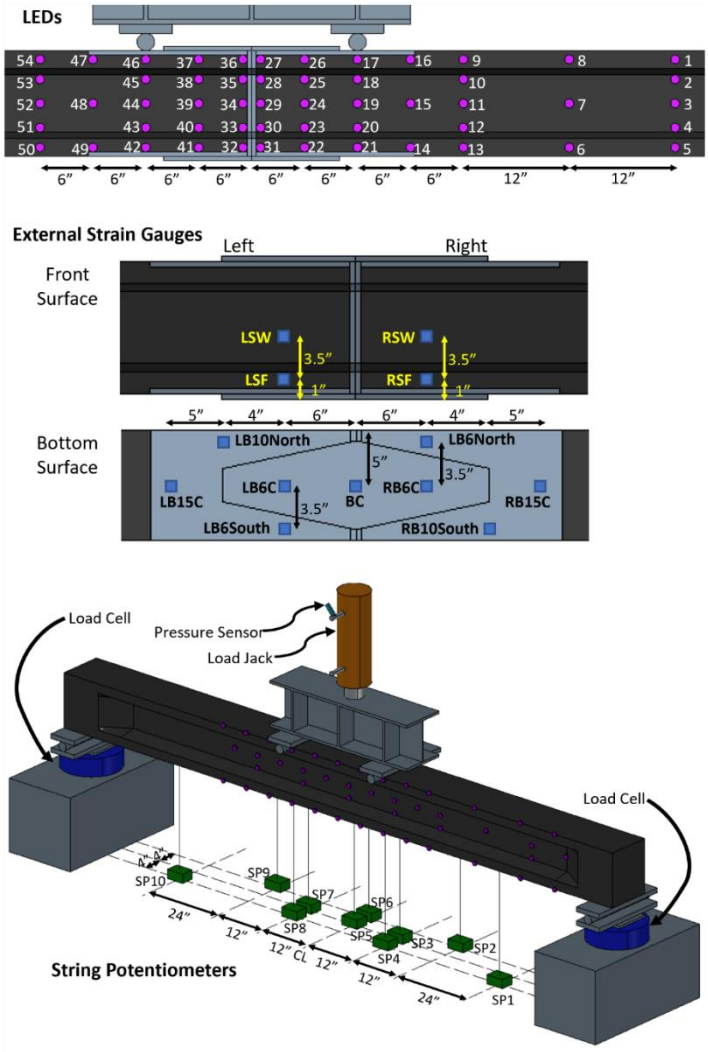


**Figure 5-9 UH12SS instrumentation**

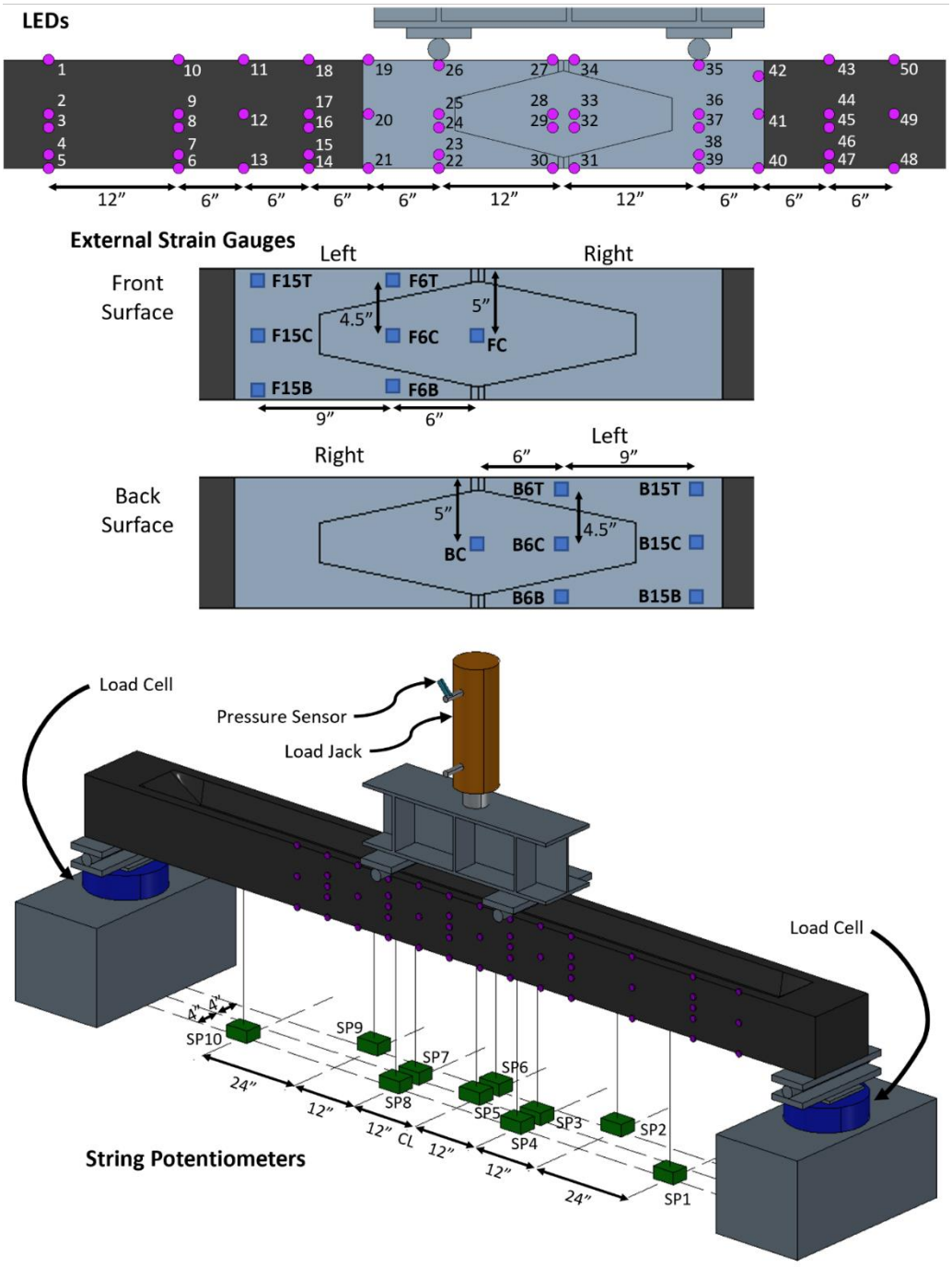


**Figure 5-10 UH12SW instrumentation**

Cyclic loading was applied to UH12SS, the strong-axis specimen. The plan for the test was to perform three cycles at each load level where the unspliced flexural test, UH12FS, was cycled. Cycles were performed at load levels of 35 kips, 44 kips and 54 kips, shown in Figure 5-11. Flexural microcracking was first observed in the bottom flange during 35 kips load cycle in the splice region, as shown in Figure 5-12a. During the third cycle of 44 kips, a localized crack was observed on the bottom flange, 15.5 in. from the splice joint on the pile's right side. A loud popping sound was heard from the pile at 51 kips of load, and subsequent loading of the pile did not increase the force. Slipping

of strand or a shear stud rupture could have caused this loud noise. There were U-shaped microcracks on the web, indicating local shear cracking originating from shear studs. Horizontal web cracks on the right side of the splice were observed at 54 kips, consistent with strand slip. The pile specimen made noises every time the load was released during these load cycles, most likely due to the movement of slipped web strand. At 56 kips, the load began to plateau, and inspection of the pile revealed a localized crack forming on the left side of the splice, about 15 inches from the splice joint. There was also a gap between the splice plate's end and the UHPC. The test was terminated at this point in order to preserve the pile for shear testing.

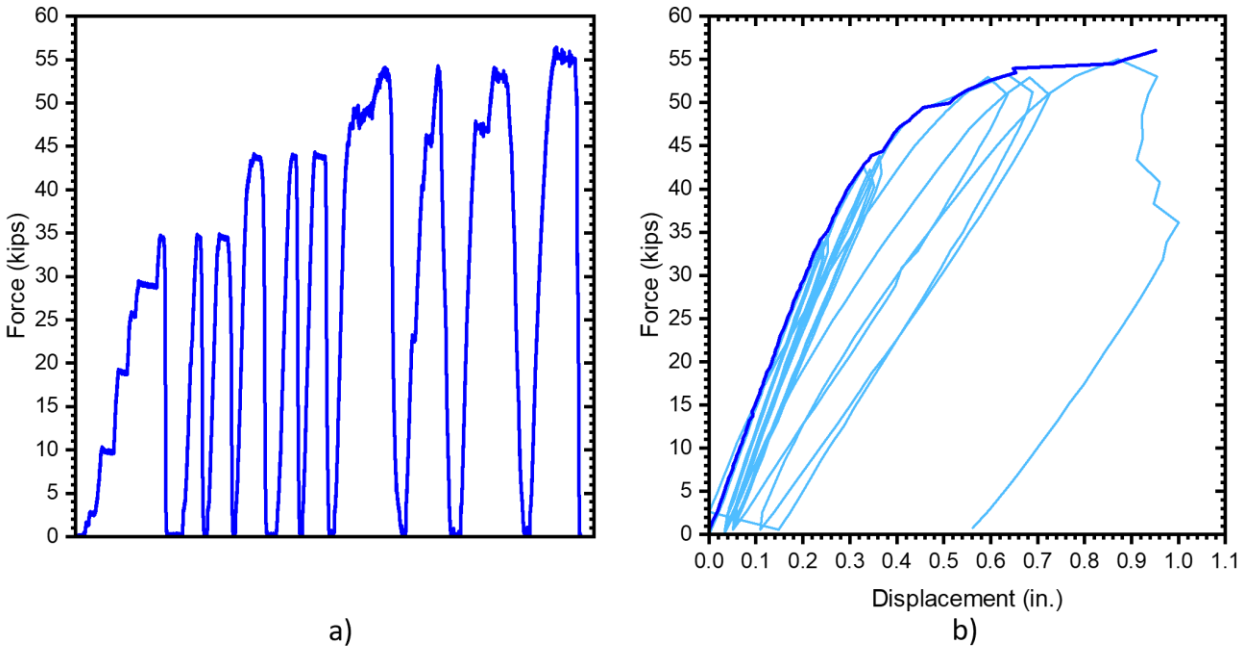


**Figure 5-11 UH12SS a) load protocol, b) force-displacement**

As shown in Figure 5-13a, UH12SW was loaded in a cyclic manner, with cycles performed at 15 kips, 18 kips, 27 kips, and 30 kips. The first flexural microcracks were observed just outside the splice region at 15 kips. Because of the splice's orientation, it was difficult to see any damage in the splice region. Microcracking was observed on the inside of the bottom flanges, as shown in Figure 5-14a and b, from 18 kips when inspecting beneath the pile. Concrete crushing was observed after 27 kips, just outside the splice plates on the pile's top. Except for the worsening concrete crushing, there was no significant damage to the rest of the pile at 30 kips. Three cycles of 30 kips were performed before stopping the test to preserve the pile for shear testing.

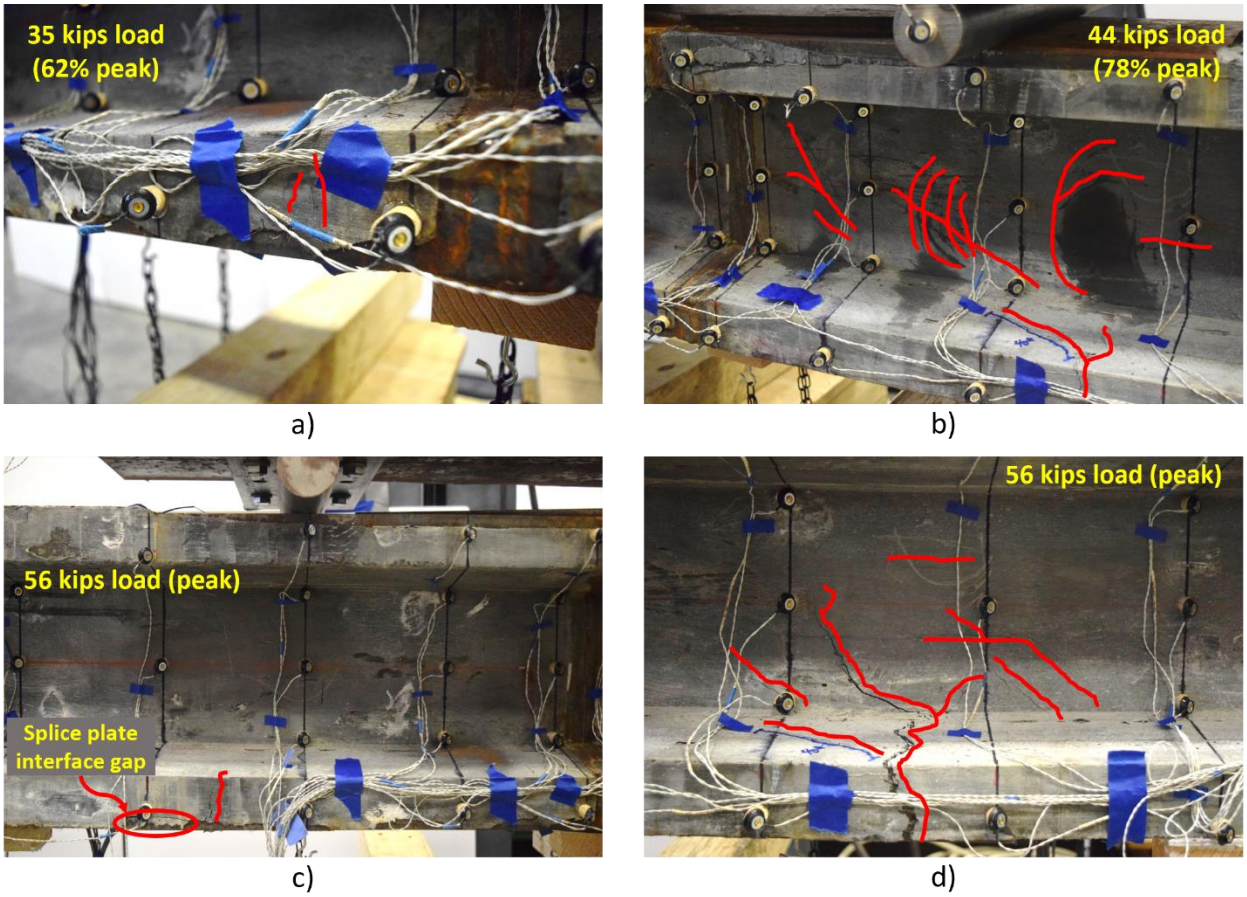


**Figure 5-12 UH12SS crack progression**

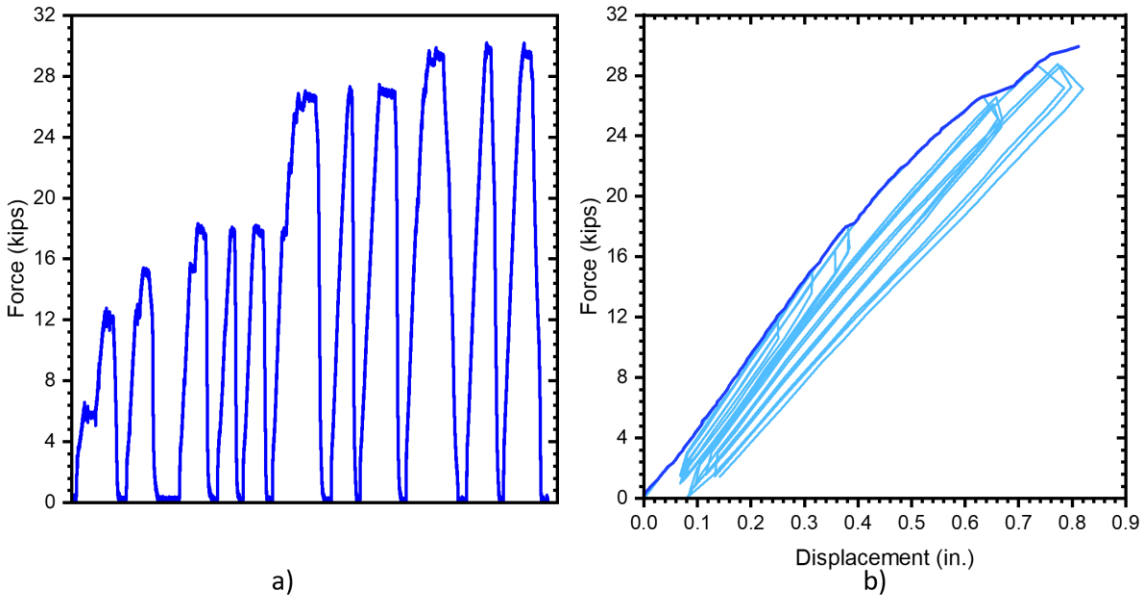


**Figure 5-13 UH12SW a) load protocol and b) force-displacement**

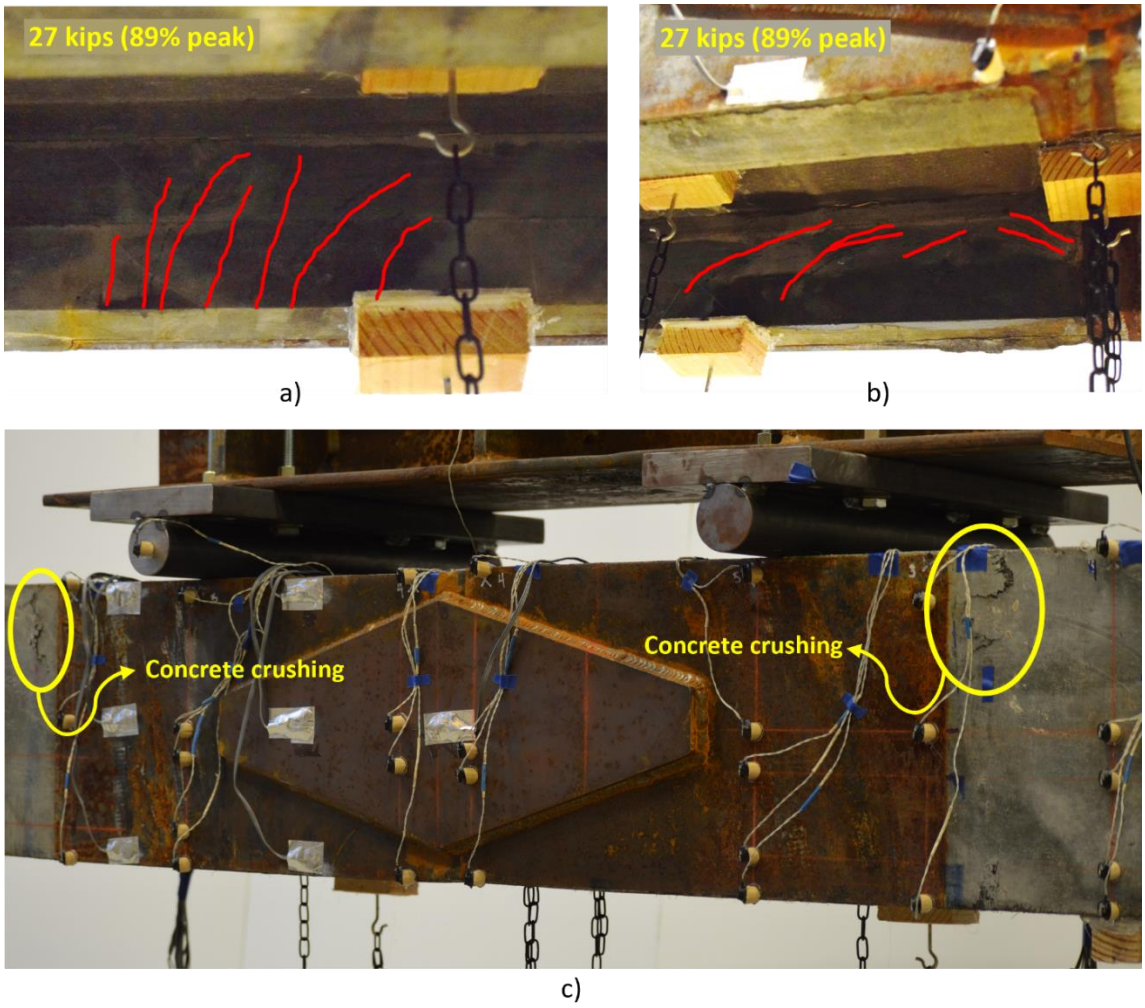


**Figure 5-14 UH12SW crack progression**

### 5.4.2 Tension Testing

#### 5.4.2.1 Test Setup Fabrication and Installation

The tension test specimen, UH12ST, necessitated a more complex setup. The purpose of this test was to determine the tensile strength of the spliced pile section. To that end, a system was devised in which each end of the pile was embedded in a concrete block. The concrete blocks would then be pushed by two 400-kip load jacks, applying tensile force to the pile splice, as shown in Figure 5-15a. The top and bottom concrete blocks were designed to withstand 200 kips of flexural shear and moment from each jack. Two 42-in. long HP12x53 sections were bolted to the pile ends using four 1-in. diameter, 100 ksi rods embedded during pile fabrication to ensure each end of the pile was properly anchored within the top and bottom blocks. In addition, four 5/8-in. rods were threaded in the transverse direction into the couplers cast into the pile ends. Figure 5-15b depicts the detailed drawings for the top and bottom blocks. The specimen's overall height was 15 feet, 9 inches, and it was designed to be tested vertically. PVC rods were embedded in the bottom block to secure the jack columns, and couplers were embedded in the top block to attach the load rams and ensure the system was self-reacting and secure during testing. Two 1-in. couplers were embedded in the bottom of the bottom block for added security, allowing the entire test to be bolted into the strong floor.

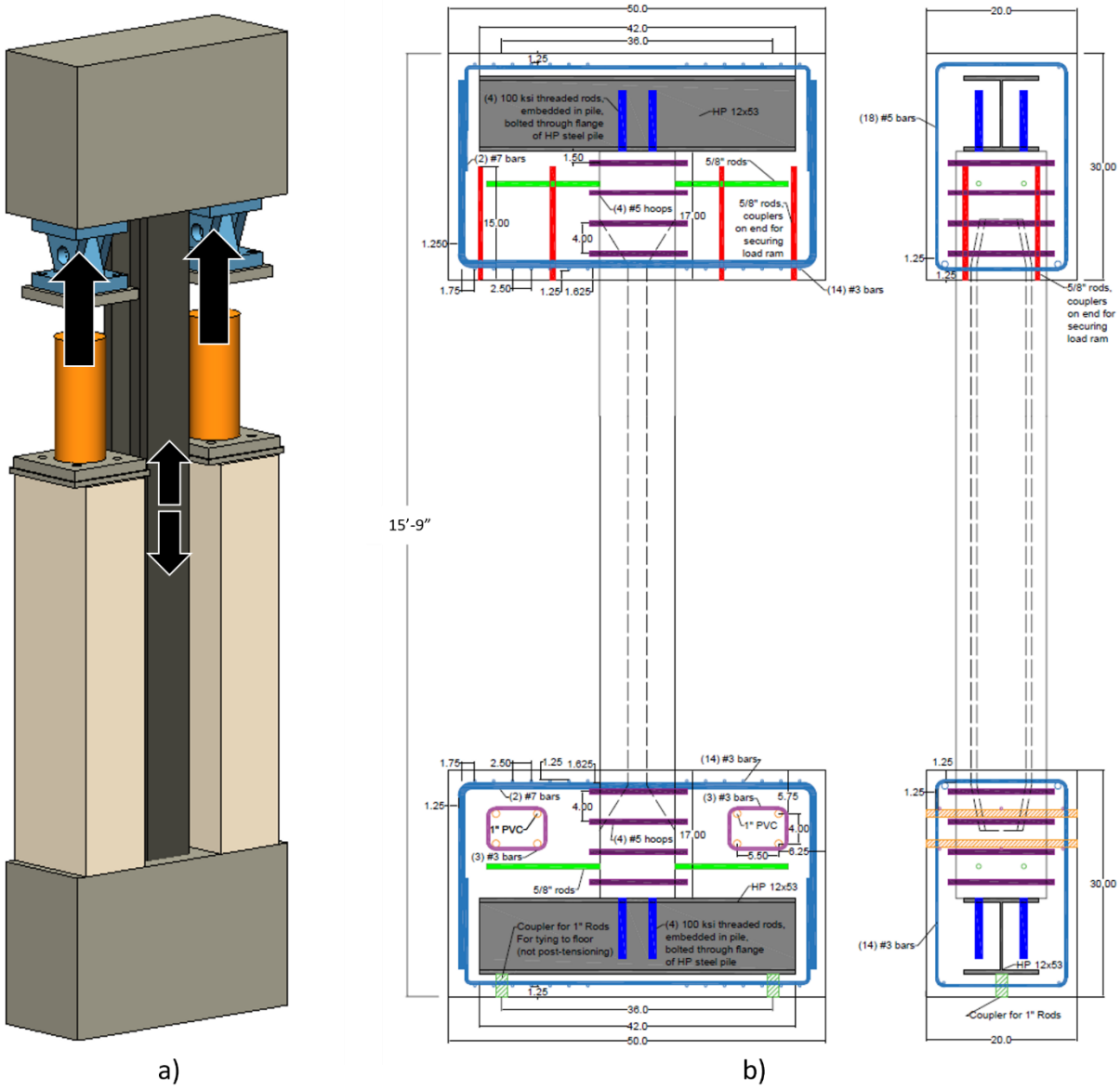


**Figure 5-15 UH12ST a) test schematic, b) detailed drawings for top and bottom concrete blocks (units in inches unless otherwise specified)**

The formwork for the top and bottom blocks, as well as the jack columns, were built in The University of Alabama's Large-Scale Structures Lab. The pile was laid horizontally at the appropriate height, and the top and bottom block formworks were constructed around the pile ends. Figure 5-16 depicts the formworks for each test setup element. Each set of formworks was cast with 5 ksi normal concrete and demolded one week later.

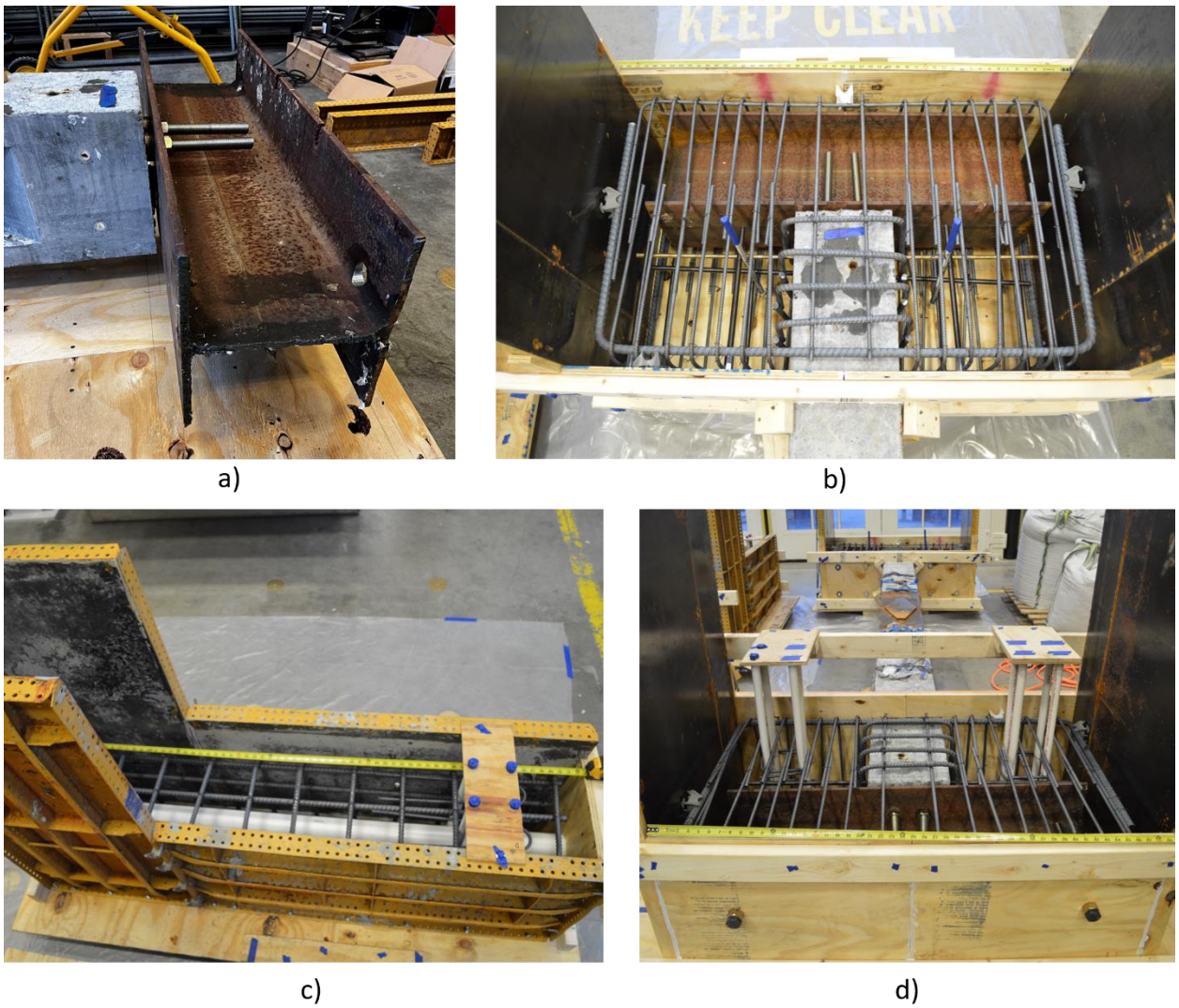


**Figure 5-16 Formworks for UH12ST: a) embedded HP12x53 attached to pile end, b) top block rebar and forms, c) jack column formwork, d) bottom block rebar and forms.**

The pile with embedded top and bottom blocks was stood vertically and anchored to the lab strong floor. The jack columns were bolted on each side of the bottom block with threaded rods running through the embedded PVC. The jacks were attached to the tops of the columns and pushed out with hinges to meet the top block. The top block was bolted to each jack, but the pressure in the jacks was monitored to ensure that no force was applied to the specimen during this process. Figure 5-17 depicts the fully assembled test setup.


**Figure 5-17 Completed test setup for UH12ST.**

#### 5.4.2.2 Instrumentation

On all four sides of the pile, UH12ST used a plethora of instrumentation. The four sides of the pile were labeled according to the cardinal directions, or north, south, east, and west, to describe instrumentation locations. Figure 5-18 depicts the pile schematics with the cardinal directions labeled. The applied force to the system was measured by four pressure sensors, two on each double-action load jack. Two string potentiometers measured the piston stroke of each jack, while the other two measured the elongation from the top of the concrete block to the floor. In addition to the internal strain gauges, ten external strain gauges were installed on the steel portion of the splice, five on the south side and five on the north side. To measure specimen displacement along the length of the pile, 48 LEDs were placed along its south face. Finally, 35 Linear Variable Differential Transformers (LVDTs) were installed on each of the pile's four sides. Four of these were placed at the joint opening, four at the end of the embedded splice plate, and three where the pile meets the top or bottom concrete block to measure pull out. The locations of all instrumentation are depicted in Figure 5-18, and the names of each LVDT are listed in Table 5-1.

**Table 5-1 LVDT names for UH12ST**

| Number | Name | Number | Name | Number | Name |
|---|---|---|---|---|---|
| 1 | N_12T | 13 | E_4BN | 25 | W_12T |
| 2 | N_EdgeT | 14 | E_12BS | 26 | W_12TS |
| 3 | N_EdgeB | 15 | E_12BN | 27 | W_4T |
| 4 | N_12B | 16 | E_32B | 28 | W_Joint_N |
| 5 | E_PO_T | 17 | E_PO_B | 29 | W_Joint_Web |
| 6 | E_32T | 18 | S_18T | 30 | W_Joint_S |
| 7 | E_12TS | 19 | S_EdgeT | 31 | W_4B |
| 8 | E_12TN | 20 | S_EdgeB | 32 | W_12BN |
| 9 | E_4TS | 21 | S_18B | 33 | W_12B |
| 10 | E_4TN | 22 | S_PO | 34 | W_12BS |
| 11 | E_Joint_Web | 23 | W_23T | 35 | W_23B |
| 12 | E_4BS | 24 | W_12TN | | |

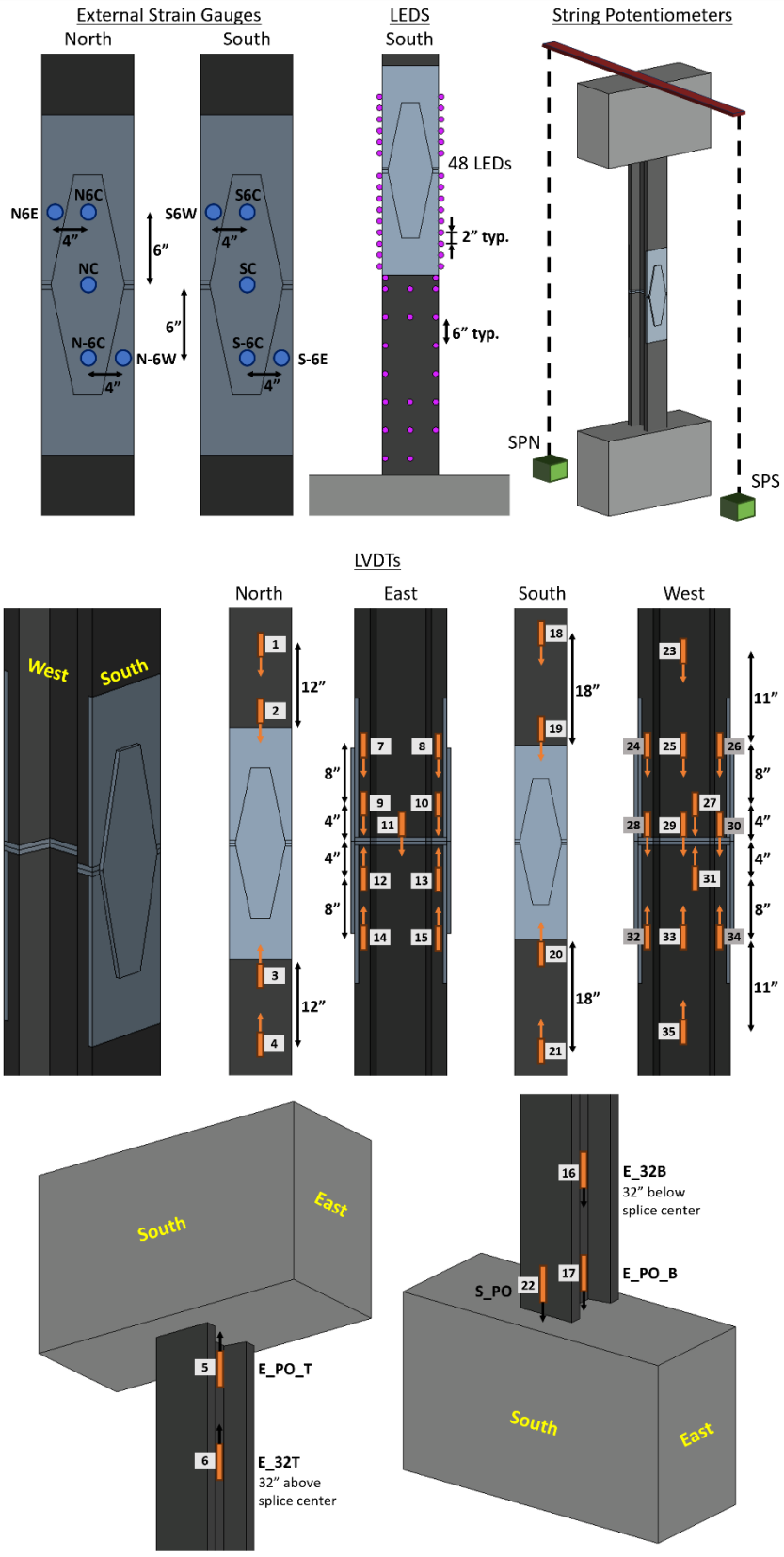


**Figure 5-18 Instrumentation schematic used for UH12ST testing**

#### 5.4.2.3 Test Observations

Loading of UH12ST was accomplished by manually pumping two hydraulic jacks in accordance with the protocol presented in Figure 5-19. At 20-kip load intervals, loading was paused to inspect for cracks. At 160 kips, three load cycles were performed. After 160 kips, cracking was observed on the top and bottom blocks, but the LVDTs detected no significant pullout. Loading continued despite the fact that these cracks were deemed superficial. Two 200-kips cycles were completed. The applied peak load was two cycles 256 kips. At this load, two-thirds of the full pile cracking capacity (with full prestressing and UHPC contributions) was achieved, and the cracking load of the UHPC alone was more than two and a half times higher. The crack on the top and bottom concrete blocks widened and so no further loading was applied for safety reasons. Two additional load cycles, one at 80 kips and one at 160 kips were applied to the pile specimen to examine any changes to its stiffness or behavior due to applied loading.

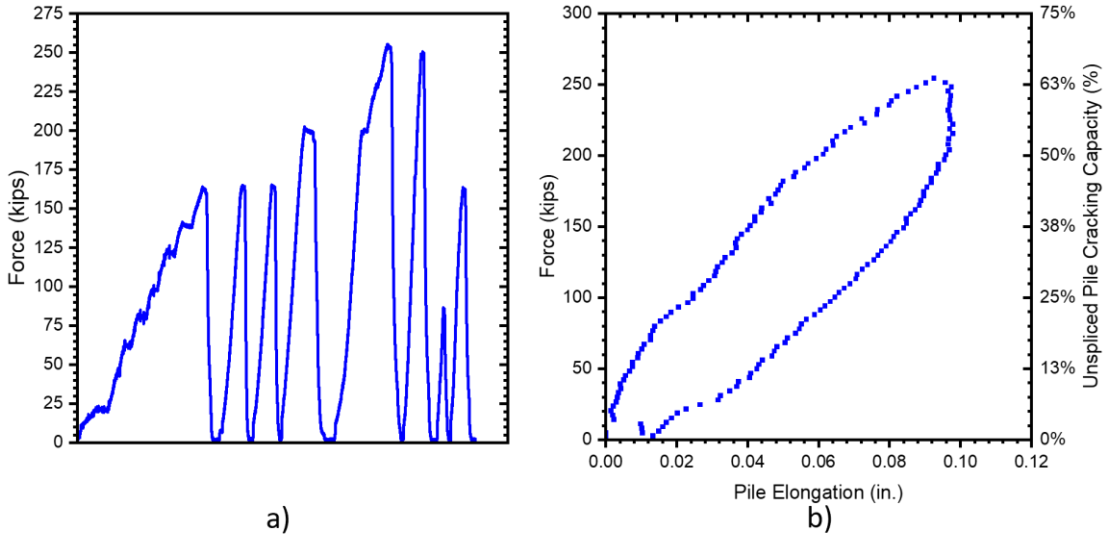


**Figure 5-19 UH12ST a) load protocol, b) force vs. pile elongation for peak load cycle**

During the test, no cracks were found on the flanges, and the web was difficult to inspect for microcracks. Following the release of the load, the web was inspected with acetone, and several longitudinal microcracks were discovered in the splice region of the web. Figure 5-20 shows these cracks. These cracks seemed to originate at web strands and the high-strength steel bar locations.


**Figure 5-20 Cracks observed on the web of UH12ST.**

### 5.4.3 Shear Testing

Shear testing was performed on the flexural splice piles. A total of five shear tests were carried out. Because the damage to UH12ST and UH12SW was minor, those piles were tested in shear twice, once on each side of midspan. Due to bond loss in the web strand on the right side, UH12SS was only tested once in shear, with the load applied on the left side of midspan. The shear tests were named after the original pile name, followed by V1 or V2 to indicate the pile's first or second shear test.

UH12ST_V1 and UH12ST_V2 were supported at three points: midspan, and just inside the tension testing concrete blocks. This was a continuous loading configuration, as shown in Figure 5-21, as opposed to the other shear tests that will be discussed, which were simply supported. The weight of the tension-tested concrete blocks was substantial, adding a significant amount of cantilevered force to the system.

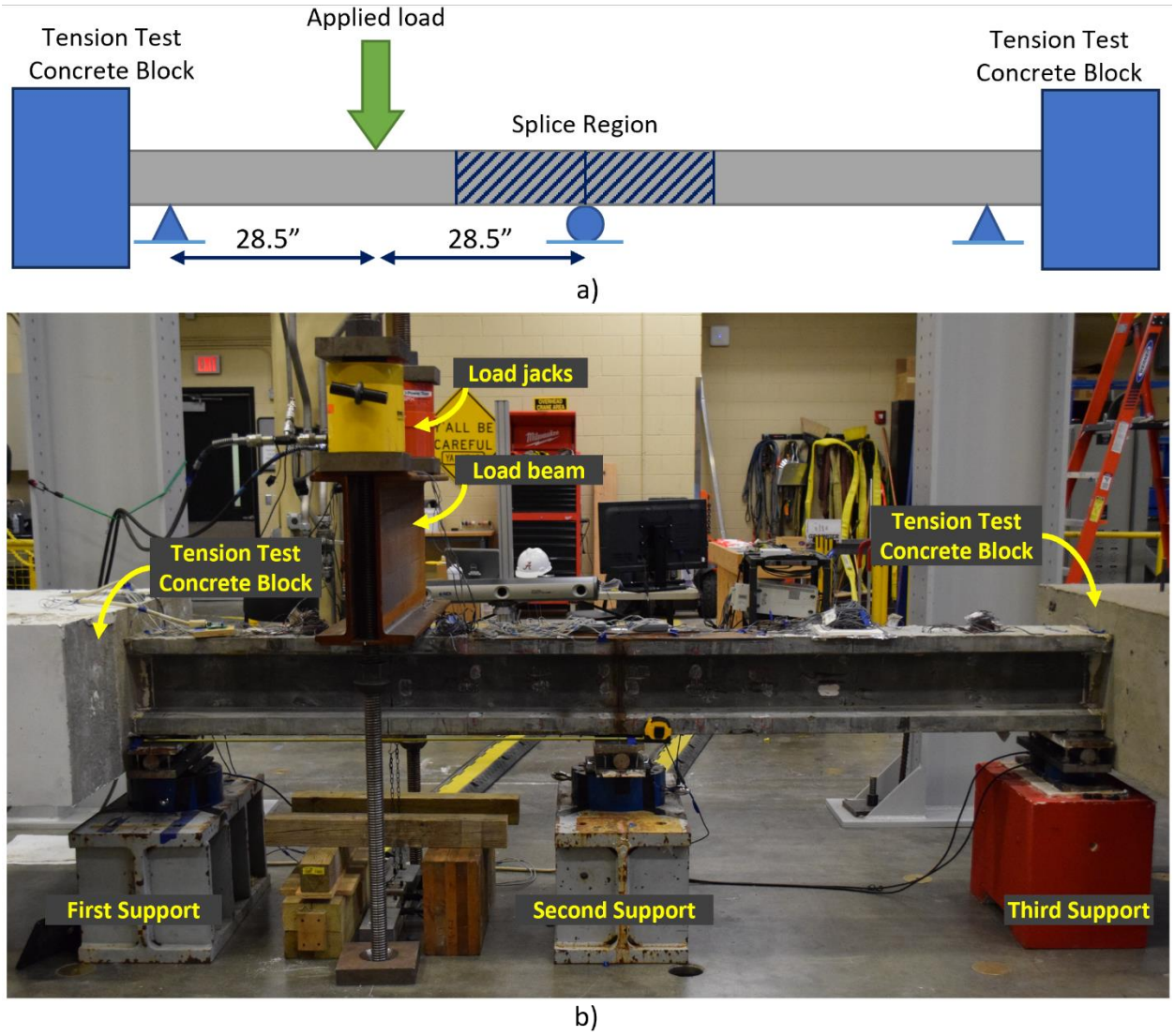


**Figure 5-21 UH12ST_V1 and UH12ST_V2 test setup**

During shear testing, a variety of instruments were used to record the pile behavior. Load cells were installed beneath each support to record the load transferred to that support. To measure the applied load, pressure sensors were attached to each load jack. Pile displacements were measured using two string potentiometers and LEDs placed along one face of the pile. Figure 5-22 depicts the LED configurations for all shear tests. During loading, internal strain gauges on the end of the pile being tested were monitored.

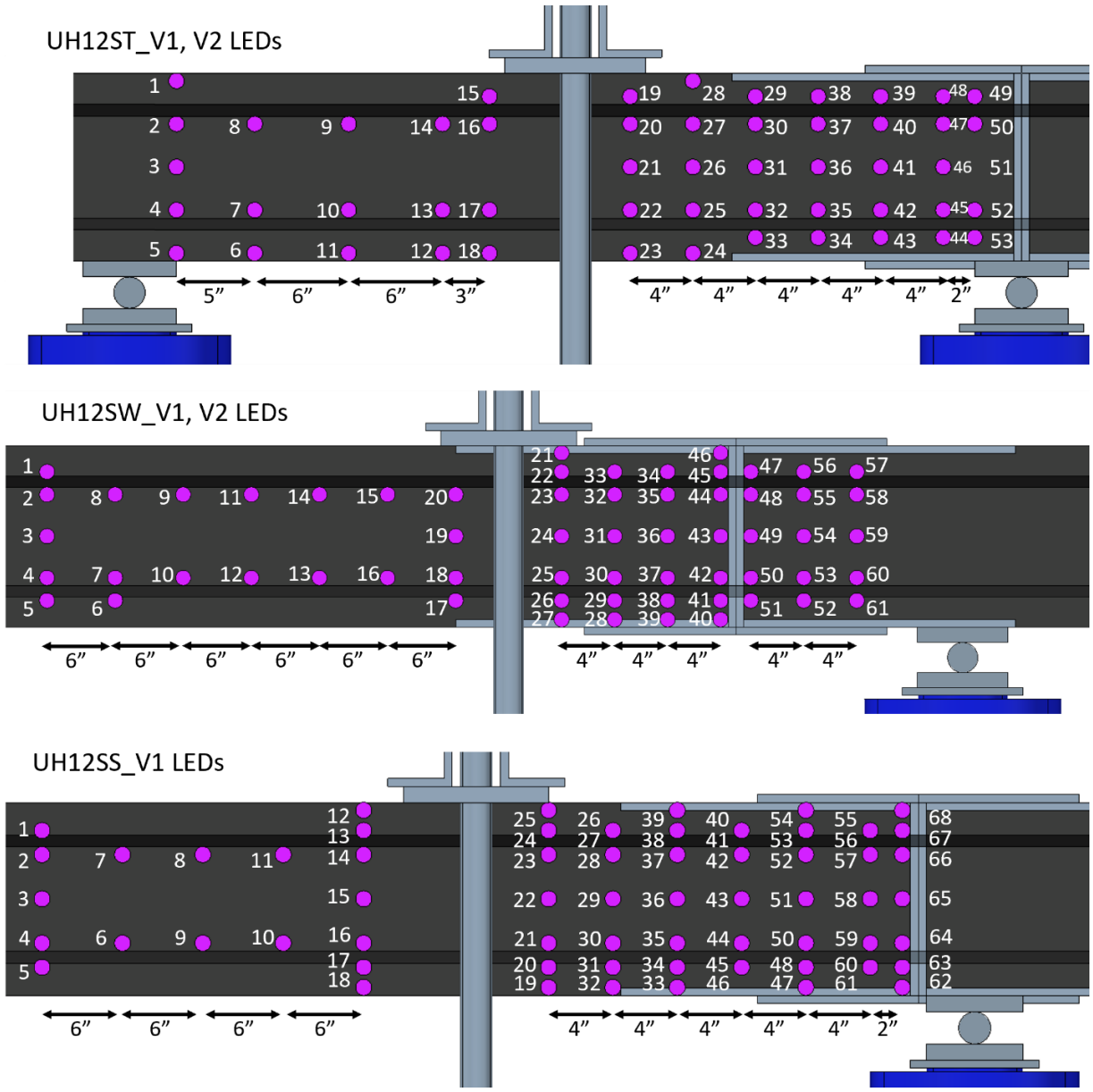


**Figure 5-22 Splice shear testing LED configurations**

UH12ST_V1 and UH12ST_V2 behaved similarly, and because they had the same shear spans, these tests will be summarized together. Figure 5-23 depicts the force-displacement relationships for each test. The load was applied monotonically, and every 20-kip load interval, the pile was inspected for possible formation of microcracks. No new microcracks were observed at 40 and 60 kips, but the length of longitudinal microcracks from tension testing increased. For both tests, shear microcracks were first observed at 80 kips at the end of splice plate. The shear cracks grew in length and number as the test progressed, becoming more densely spaced. The cracks became steeper closer to the load application point and were labeled as flexural cracks. At both web strand locations, the longitudinal cracks continued to lengthen along the splice length, indicating slippage of prestressing strands. The final failure load for UH12ST_V1 and UH12ST_V2 was 198.9 kips and 192.2 kips, respectively. Each specimen had a crack that starts at the bottom flange and angles up towards the load application point. This crack began 4-in. from the end of the splice plate in the case

of UH12ST_V1. One of the longitudinal cracks was also localized at the top web strand location. The main localized crack in UH12ST_V2 began 3-in. from the end of the splice plate, and multiple flexural-shear cracks in the web were also localized. Figure 5-24 presents the final crack patterns observed in both tests.

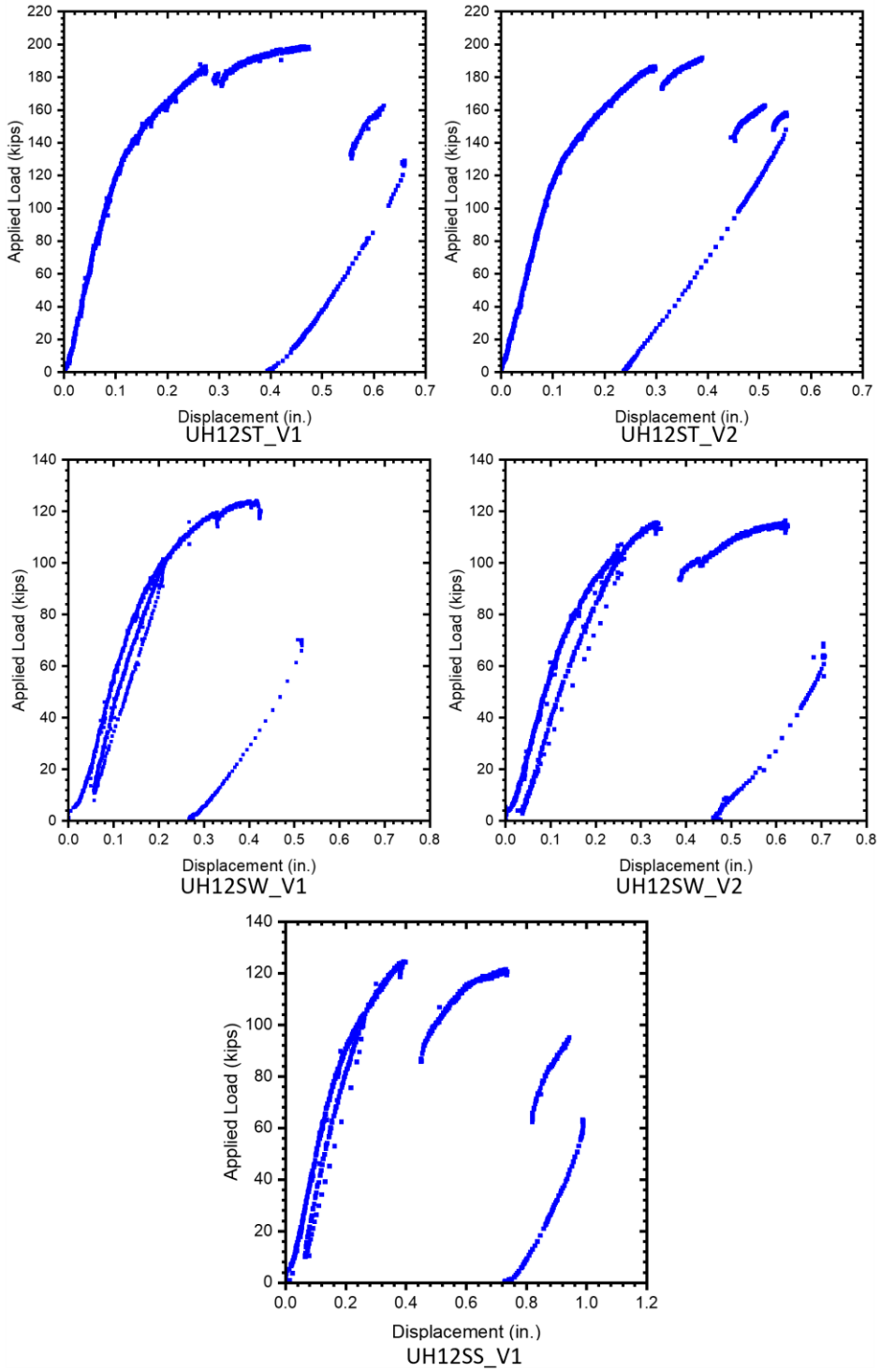


**Figure 5-23 Measured force-displacement responses of spliced shear tests**

UH12ST_V1

UH12ST_V2

UH12SW_V1

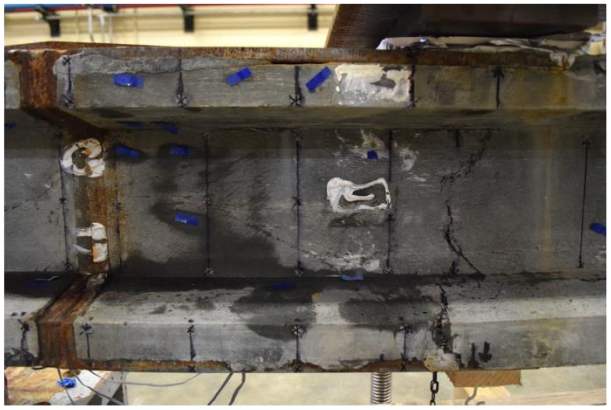

UH12SW_V2

UH12SW_V1

**Figure 5-24 Splice shear test crack patterns at failure**

Both shear tests on UH12SW had the same shear spans and behaved similarly. Because this pile lacked the large concrete blocks on the ends that UH12ST did, the loading configuration was slightly different, as illustrated in Figure 5-25. The pile was supported at both ends and on the opposite side of the splice joint. In this case, the third support was only used as a precaution, and before each test, it was ensured that the pile's end was not in contact with the support. As a result, the setup was simply supported, making analysis and load transfer simpler. The goal of these two tests was to apply shear force to the entire splice, including both sides of the joint.

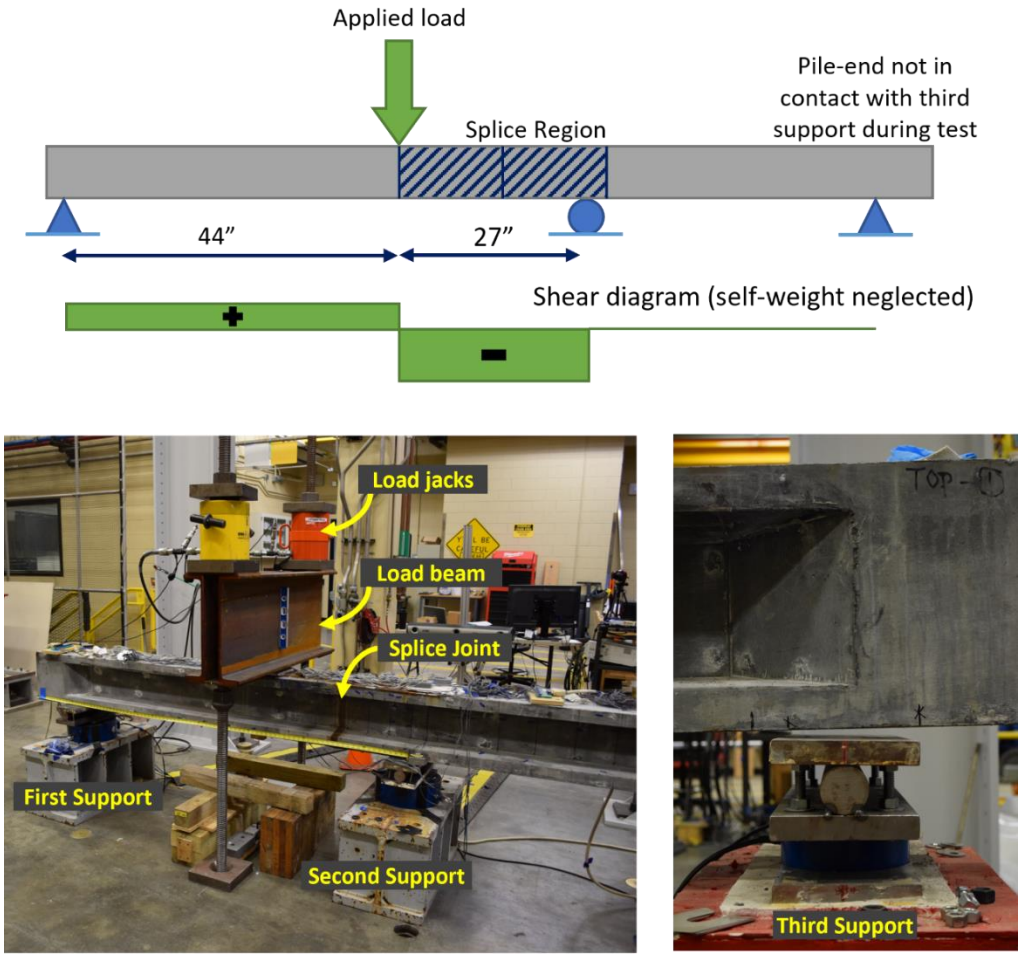


**Figure 5-25 Shear setup for UH12SW_V1 and UH12SW_V2**

The load was applied mostly monotonically, with one release and reload cycle at 100 kips. Minor shear microcracks were first observed on both sides of the splice joint at 60 kips. These microcracks were discovered after detensioning on the side of the splice joint closest to the second support. These detensioning microcracks were in the shear force direction, and the tensile stresses caused them to lengthen and open further. More shear microcracks formed as loading progressed, and the web of microcracking became more densely spaced on each side of the splice joint. Even when crossing the splice joint, the angle of the microcracks remained constant. From 80 kips of load, flexural microcracks were present. Both piles failed when a flexural crack developed directly beneath the load application point, approximately 15-in. from the splice joint in both tests, as shown in Figure 5-24. The peak load for the UH12SW_V1 and the UH12SW_V2 was 124.3 kips and 116.5 kips, respectively.

UH12SS_V1 used a simply supported configuration, similar to UH12SW_V1 and UH12SW_V2, but the right side of the splice was deemed unsuitable for further testing due to bond loss on the web strands during the strong-axis flexural test. As a result, the middle support was positioned just to the right of the splice joint, with the roller plate edge at midspan, as shown in Figure 5-26. Once again, the pile made no contact with the third support during the test.

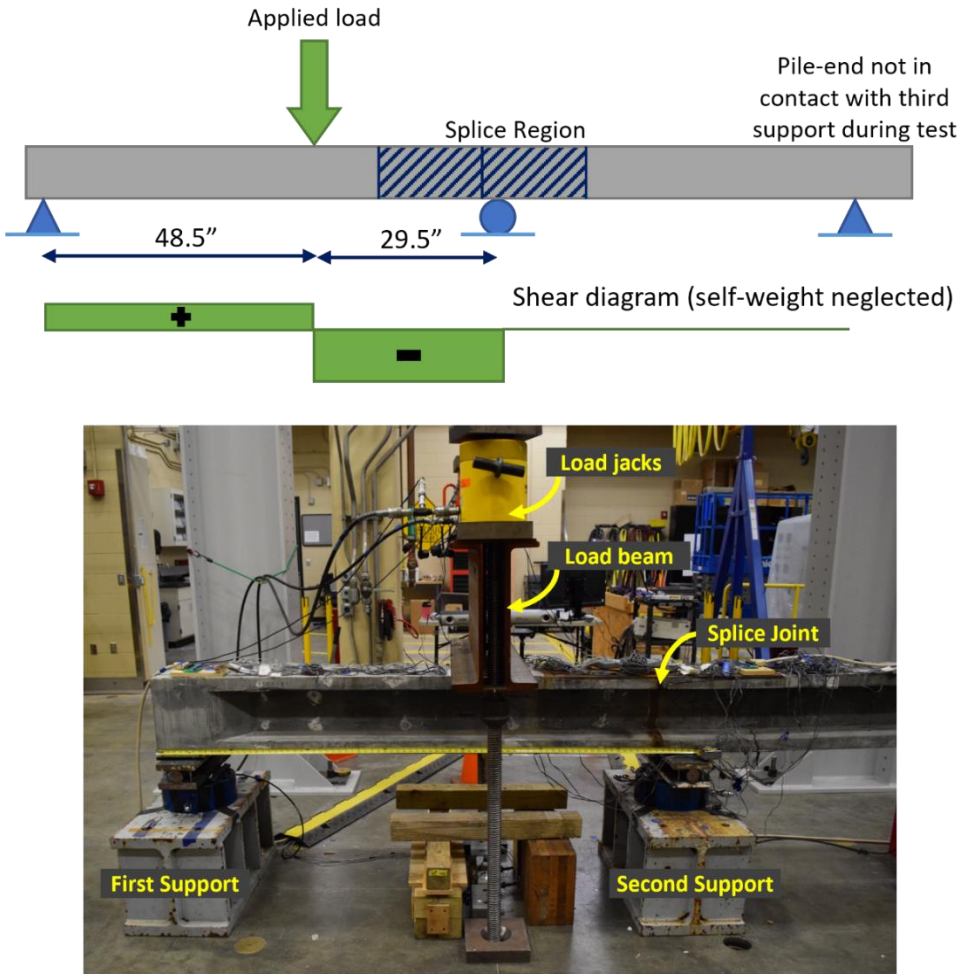


**Figure 5-26 UH12SS_V1 test setup**

The load was applied monotonically, as in previous shear tests, but one cycle was performed at 100 kips. At 60 kips, the first shear microcracks were observed, which grew with further loading. Longitudinal microcracks that were first seen in the previous flexural test reappeared at 80 kips. The load peaked at 124.6 kips, and there was a loud noise, followed by a 31% load drop, as shown in Figure 5-23. At this point, a shear crack developed, beginning at the bottom flange and angling towards the load application point until it reached about halfway up the pile web. Loading continued, and the force reached 121.4 kips before another loud noise and a 50% load drop occurred. The localized shear crack had progressed to the underside of the top flange by this point. When the pile was pushed again, the load peaked at 95 kips before dropping by 30%. Because there were no significant changes in the visible damage to the pile following this drop, it was assumed that the bond had been broken on one of the web strands or a shear stud had ruptured.

## 5.5 Results and Discussion

### 5.5.1 Flexural Testing

The splice flexural testing had a comparative goal: to achieve the capacity of the unspliced piles. The first step in the spliced testing was to compare the force-displacement behavior of unspliced and spliced equivalents. However, because the spans of the spliced piles were slightly different, comparing forces would be misleading, so the forces were converted to moments. The moment-

displacement comparisons for the strong and weak-axis flexure tests are shown in Figure 5-27. Both spliced piles behaved similarly to their unspliced counterparts in the elastic range. The behavior of both spliced piles began to deviate around 50% of the unspliced flexural capacity. The load began to plateau after this point in the case of UH12SS, the strong-axis flexural pile, before the test was terminated after the pile sustained significant damage on the right side of the splice. UH12SS had a maximum moment that was 68 percent that of its unspliced counterpart. The spliced pile was actually stiffer than the unspliced pile for the weak-axis pile. The damage sustained in that test was caused by the splice plate not bending at the same rate as the rest of the pile, resulting in concrete crushing at the top of the pile's splice plates. The weak-axis specimen could have been pushed further, but the test was cut short in order to save the pile for shear testing. However, UH12SW still was tested to 79 percent of its unspliced capacity.

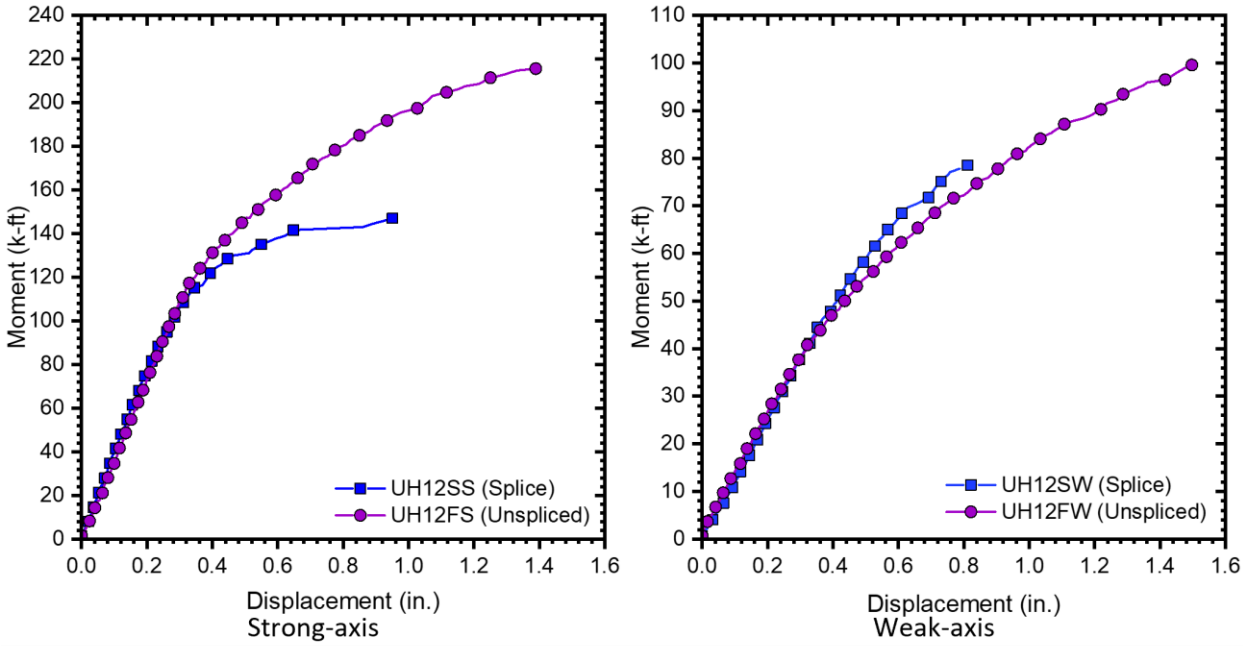


**Figure 5-27 Moment vs. displacement for the unspliced and spliced flexural tests**

Aside from moment and displacement capacities, the splice's behavior was investigated by examining the force vs. strains throughout the pile. The force vs. strain graphs for the strong-axis spliced pile are shown in Figure 5-28. Except for the strain gauges on the outermost shear studs, LB4 and RB4, the shear studs did not experience large strains. Both of these studs exceeded the yield strain, with RB4 rupturing near the end of the test. This is consistent with the large crack in the pile's bottom flange on the right side. Shear stud RB4 was 16-in. from the midspan, and the localized crack formed at 15.5-in. from the midspan.

External strain gauges installed on the pile's bottom provide information about the strong-axis splice behavior. Most strain gauges showed low-level tensile strains, as expected at the bottom of the pile, but the outermost external strain gauges, EXT_LB15C and EXT_RB15C, began to show decreasing strains after 40 kips of load. As the shear stud at the same location began to experience large tensile strains, the ends of the splice plate compressed. During the test, the splice plate ends also began to separate from the UHPC at this point.

The internal strain gauges were the final component of the strains studied for UH12SS. In C3RT, C4RM, and S3RB, the strains were greatest on the right side of the splice. The two concrete strain gauges were located at the top and bottom of the splice plate on a top and bottom web strand, respectively. S3RB is the steel gauge that is 7.5-in. from midspan. Aside from these three gauges, all of the strains were under 1000 microstrains. The strains in UH12SW were minor, which corresponds to the lack of damage observed. The strains in the shear studs and splice plates remained below yielding throughout the test. Internal strains were also minor, but S3RB demonstrated tensile strains curving to compression. The strains were still less than 1000 microstrains when the test was stopped, which is consistent with bond stress on the bottom strand. S3RB and C5RT were both at the same location on the pile, but one measured steel strains and the other measured concrete strains. The large difference between these two strain gauges suggests that some debonding occurred.

Overall, the flexural results indicate that the splice should have been longer and contained more shear studs to facilitate the development of higher strong-axis capacity and prevent the shear studs from rupturing in strong-axis flexure. The capacity may be adequate in the weak-axis, based on the strains observed in the system, and the lack of degradation in the moment-displacement curve up to 79% of the unspliced capacity.

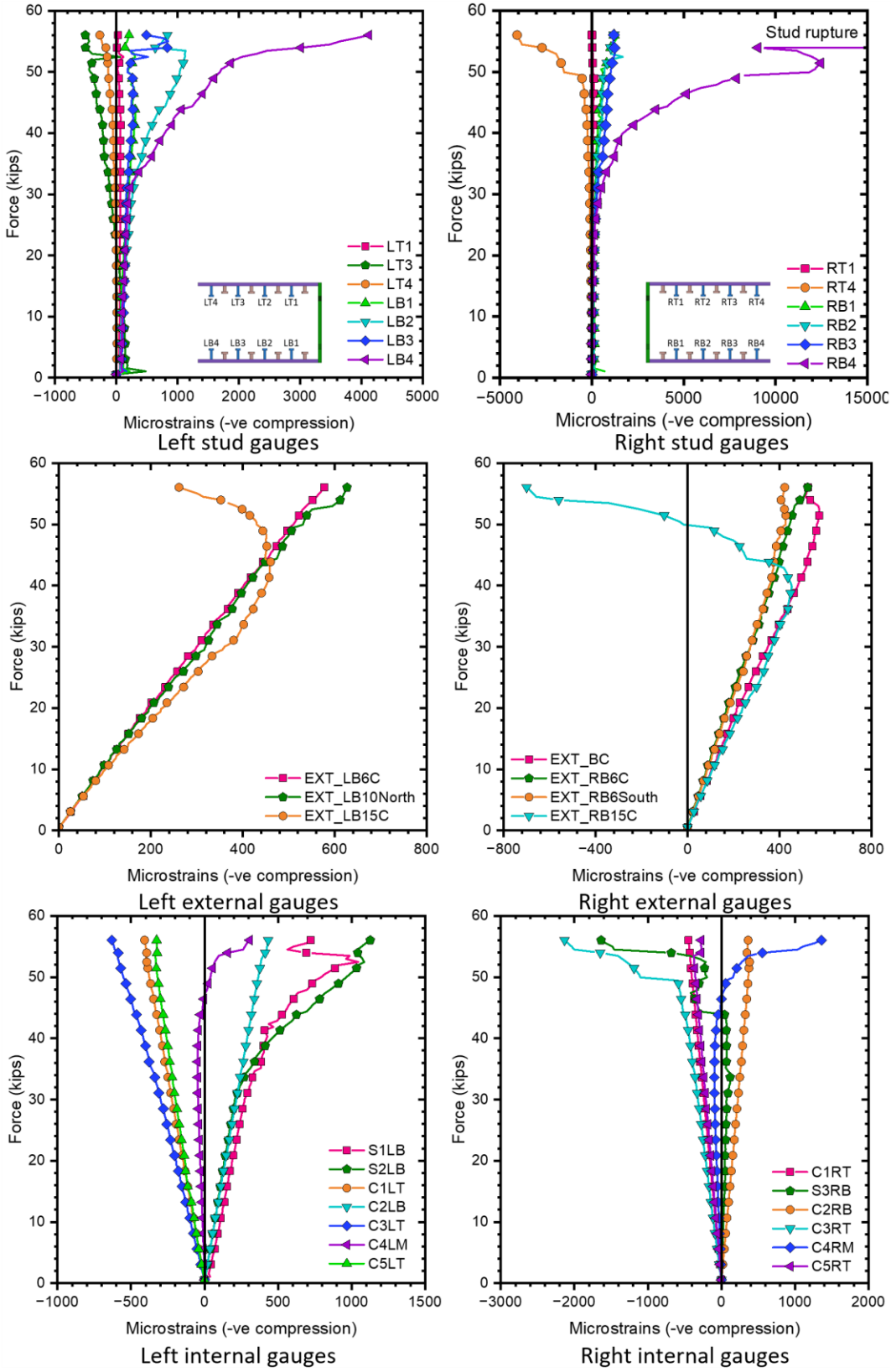


**Figure 5-28 Force vs. strain on the left and right side of the splice in UH12SS**

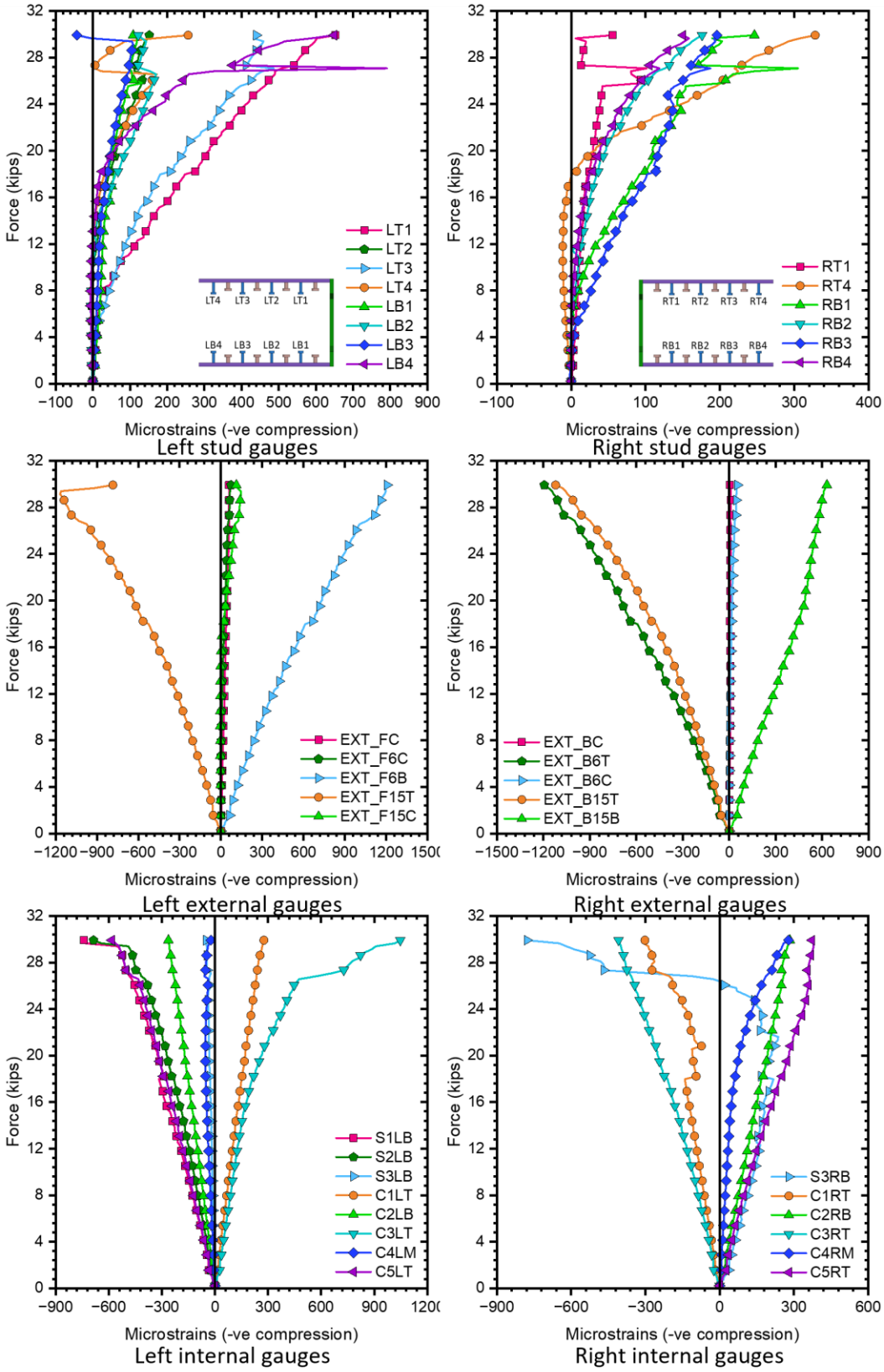


**Figure 5-29 Force vs. strain on the left and right side of the splice in UH12SW**

### 5.5.2 Tension Testing

UH12ST tested the splice to two-thirds of the unspliced pile cracking capacity in tension. Figure 5-19b shows the force vs. elongation for the test. Overall, there was not much damage observed in this experiment, but the strains in the system will help discern how well the splice fared during testing. Figure 5-30 shows the force vs. strain for the shear studs. In all cases, the strains were less than half of yield, indicating that the studs were transferring the load adequately.

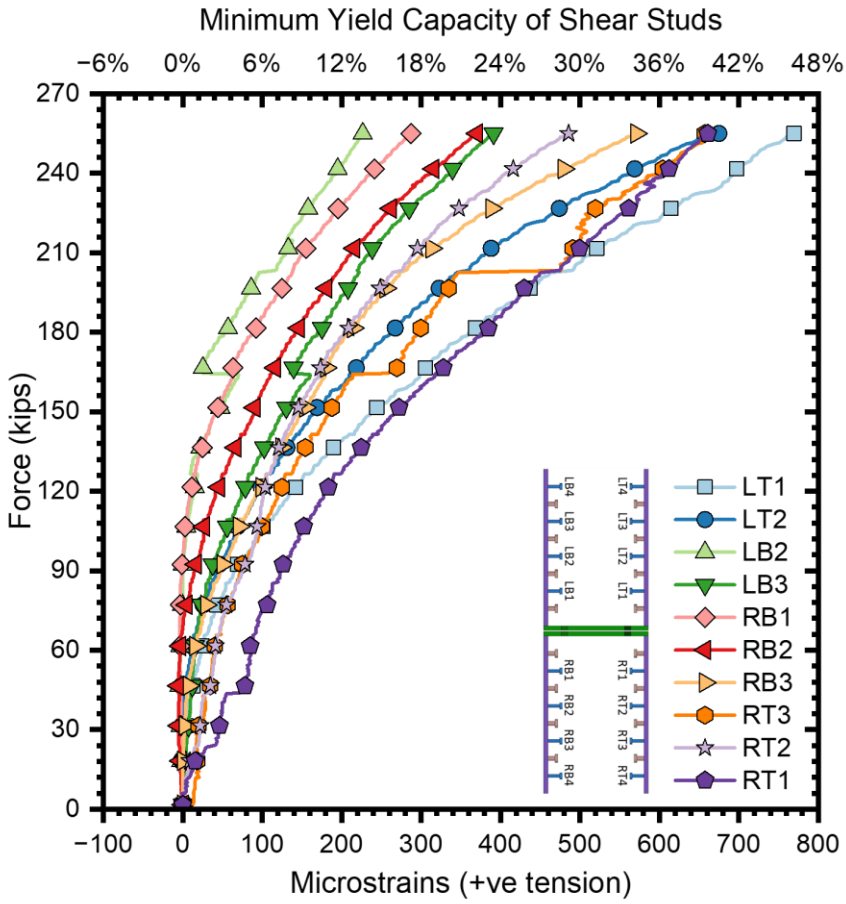


**Figure 5-30 UH12ST force vs. shear stud strain**

Through examining the other strain gauges, both the external gauges on the splice and the internal gauges along the pile length, no major anomalies were observed. Strains were minor, less than 500 microstrains, and were comparable whether the gauges were in the splice region or outside. This would suggest that the splice was transferring the load well.

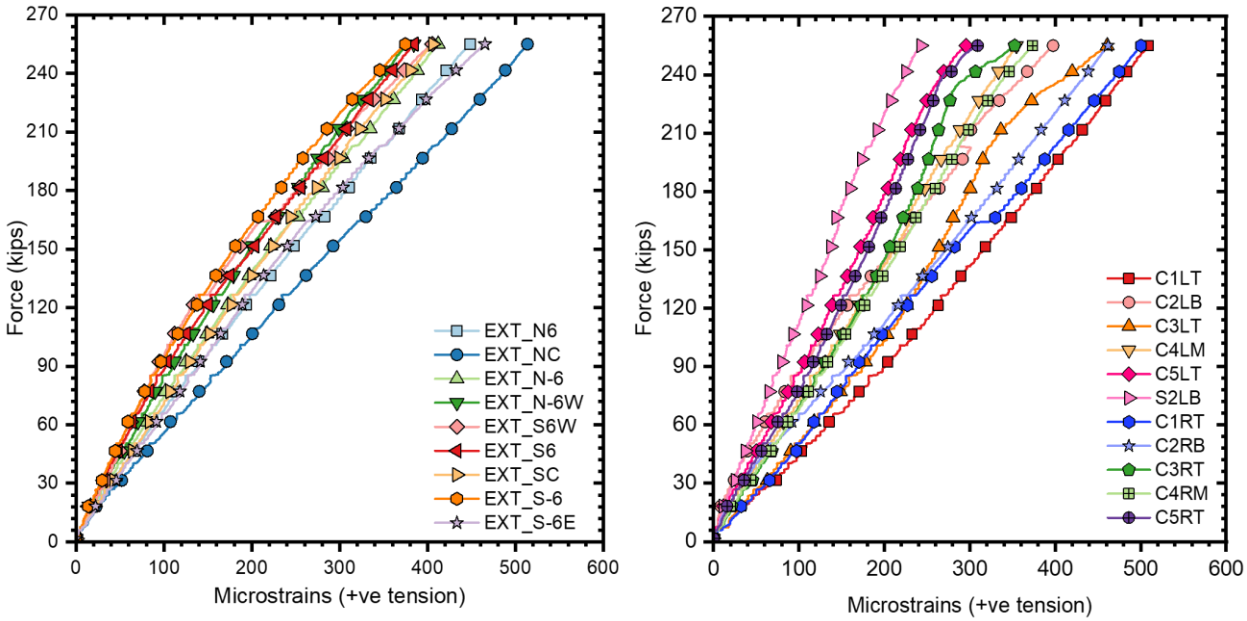


**Figure 5-31 UH12ST force vs. strain in external splice strain gauges (left) and internal strain gauges (right)**

### 5.5.3 Shear Testing

The results of the spliced shear testing are shown in Table 5-2. The peak shear force refers to the shear force experienced by the span where primary crack localization occurred, which was the splice side in all cases. The applied moment was also found for the middle of the crack location to determine how close to the spliced flexural capacity the piles were. In the case of the tests which failed in flexure, this was under the load application point. Finally, the localized shear crack angle for the three tests which failed in shear were found using photos taken during testing. For reference, the unspliced shear capacity of the UH12x71 measured during experimental testing averaged 97.5 kips with cracking angles ranging from 27 to 30 degrees. Further details on these tests can be found in Chapter 3.

Three of the five spliced shear tests failed in shear, while the remaining two tests failed in flexure. All of the piles resulted in localized cracking in the same region: between 15 and 17-in. from the splice joint. For the tests which failed in shear, the cracking angle varied from 35.5 degrees to 46 degrees. The UH12ST tests, which utilized a continuous span loading condition, attained higher peak shear forces compared to the remaining tests, which were simply-supported. This could be because the top and bottom steel plates allow the section to attain slightly larger capacities than an unspliced pile, along with the additional threaded rods in the web of UH12ST at the splice joint. The transform section, which converts a cross-section of multiple materials into an equivalent section of one material, uses the modular ratio to convert steel to concrete for analysis purposes. The modular ratio in this case is high, which would correspond to a larger transform section, which can attain higher capacities. The differences in capacity and shear cracking angle, despite the two tests using the same support and load application locations, could be explained by the strains that were already introduced to the system during tension testing. Although the results did not indicate these strains were large, they could still have an effect on later testing.

**Table 5-2 Spliced shear testing results summary**

| Pile Test | Failure Mode | Peak Shear Force (kips) | Applied moment at the middle of the localized crack (kip-ft) | Cracking Angle (degrees) |
|---|---|---|---|---|
| UH12ST_V1 | Shear | 115.9 | 107.1 | 35.5 |
| UH12ST_V2 | Shear | 111.9 | 103.6 | 46 |
| UH12SW_V1 | Flexure | 77.5 | 153.6 | -- |
| UH12SW_V2 | Flexure | 77.0 | 159.0 | -- |
| UH12SS_V1 | Shear | 78.2 | 76.5 | 44.5 |

UH12SW_V1 and UH12SW_V2 failed in flexure. The shear span tested had the splice joint nearly halfway between the load and the support. The shear forces were smaller than the unspliced capacity, but the moments experienced by the piles at failure, 153.6 k-ft and 159.0 k-ft, were higher than that achieved by the spliced strong-axis flexure test (UH12SS), 147.1 k-ft. These shear tests corroborate the flexural capacity found in UH12SS and indicate that UH12SS_V1 failed prematurely, likely from the strains already introduced during flexural testing. UH12SS_V1 used similar spans and support locations as UH12ST_V1 and UH12ST_V2, but in Section 5.5.1, results showed that some shear studs had reached their yielding capacity during testing. Reloading shear studs that had already yielded could have affected the behavior in the subsequent test.

## 5.6 Conclusions

The results from the splice study can be summarized into several conclusions:

- The embedded splice design was able to be fabricated in a standard precast plant. Some issues were encountered with being unable to tell when the forms had filled, but this can be remedied in future castings by either casting in a weak-axis orientation or by creating larger burr holes to allow entrapped air to escape.
- In strong-axis flexure, the pile failed before reaching the full unspliced capacity due to the rupture of a shear stud and bond loss of web strands. The pile reached 68% of the unspliced capacity, but a longer embedded splice with more shear studs would likely be able to reach higher capacities. The two shear tests which failed in flexure also failed at similar moments.
- In weak-axis flexure, the pile was tested to 79% of the unspliced capacity. The strains during this test were not overly large, but concrete crushing at the ends of the splice plates was observed. The moment-displacement behavior of the splice compared to the unspliced pile indicates that the splice was not approaching failure.
- Tension testing proceeded to two-thirds of the full pile cracking capacity with fully effective prestressing. No major damage was observed throughout the test, and the splice performed well, with all shear studs staying under 50% of minimum strain.
- Of the five shear tests conducted, three failed in shear and two failed in flexure. The capacities and cracking angles varied for these tests, some near and some below the average unspliced shear strength, but there were varying levels of strains already introduced into the system from previous testing. Despite this explanation, further study is still required to obtain conclusive results.

# 6 CONCLUSIONS

The research focused on development of 12-inch, 14-inch, and 16-inch prestressed precast, UHPC pile sections and extensive experimental testing was conducted to evaluate their material properties and structural performance. The UHPC piles were designed to match or exceed the load-bearing capacities of conventional piles while offering improved durability, especially in challenging environments like marine conditions. Material testing included compressive strength, tensile strength, modulus of elasticity, and shrinkage measurements. Prestressing bond tests were also performed to assess the bond between the prestressing strands and the UHPC mix.

Experimental structural tests on the UHPC piles involved flexural and shear testing, where large-scale specimens were subjected to four-point bending and shear loading to simulate real-world conditions. These tests provided insights into crack progression, stress distribution, and failure mechanisms. The results demonstrated that UHPC piles have excellent flexural and shear capacities, making them a viable alternative to steel H-piles. In addition to pile design, the research developed a splice system for the 12-inch UHPC piles, necessary for extending pile lengths in field conditions. The splice design was tested for flexure, tension, and shear, and it showed strong performance in transferring loads across spliced sections, proving its practical application for pile length extension. This chapter summarizes the conclusions found throughout this project and makes recommendations for future research:

## 6.1 UHPC H-Pile Development and Experimental Testing

- Three prestressed, precast UHPC H-pile sections, namely UH12x71, UH14x105, and UH16x151 were developed as viable alternatives to driven piles currently used in industry.
- All of these pile sections can be easily fabricated in a variety of precast plant conditions, with proprietary and nonproprietary UHPC mix designs.
- With embedded strain gauges, the strains in the piles during detensioning can be adequately captured to calculate elastic shortening losses.
- The transfer length for the prestressing strands was found to be around 15-in., or $24d_b$, is appropriate for design purposes irrespective of the UHPC mix designs used in the project.
- The short-term losses predicted by AASHTO UHPC specifications and PCI are appropriate for predicting elastic shortening losses, though the autogenous shrinkage strain recommended by PCI prior to detensioning is conservative for the UHPC used for these piles.
- Both AASHTO and PCI recommendations for calculating long-term losses are conservative for these piles. Experimental results show the total losses at the time of testing were less than half of those predicted by code equations.
- The flexural behavior of UH12x71 and UH14x105 can be accurately predicted using first-principles based analysis, such as strain compatibility approach, with using measured material properties. The accuracy of this approach was verified through experimental testing. These piles will generally fail due to compressive crushing in both bending directions.
- Shear failure is unlikely to occur before flexural failure in regions with fully effective prestressing, even without transverse reinforcement for these piles. The typical failure mode is web-shear, with flexural-shear failures difficult to achieve, even with more than 80% moment capacity applied under shear loading.
- The shear behavior of the pile differs in the end-region where the prestressing is not fully effective. Compared to shear testing in regions where prestressing has fully transferred,

lower capacities were achieved, and the failure mode was governed by bond failure. Current code equations were barely conservative for these cases.

- Current shear code provisions from AASHTO and PCI are conservative for regions with fully effective prestressing. AASHTO specifications provide a better measure of the pile behavior, after taking the tensile properties of UHPC into account.

## 6.2 UHPC H-Pile Embedded Splice Development and Experimental Testing

- The incorporated splice design is able to be manufactured in a typical precast plant. Some challenges with being unable to detect when the forms had filled were observed, however this can be avoided in future castings by casting in a weak-axis orientation or constructing larger burr holes to allow entrapped air to escape.
- The pile failed before reaching its full unspliced capacity due to a shear stud rupture and bond loss of web strands in strong-axis flexure. The pile reached 68% of its unspliced capacity, but a longer embedded splice with more shear studs may potentially reach higher capacities. Both shear tests that failed in flexure failed at comparable moment capacities.
- The pile was tested to 79 percent of its unspliced capacity in weak-axis flexure. Although the strains in this test were not severe, concrete crushing at the ends of the splice plates was observed. The splice's moment-displacement behavior relative to the unspliced pile implies that the splice was not nearing failure.
- Tension testing proceeded to two-thirds of the full pile cracking capacity with fully effective prestressing. No visible damage was observed throughout the test, and the splice performed well, with all shear studs staying under 50% of minimum strain.
- Of the five shear tests conducted, three failed in shear and two failed in flexure. The capacities and cracking angles varied for these tests, some near and some below the average unspliced shear strength, but there were varying levels of strains already introduced into the system from previous testing. Despite this explanation, further study is still required to obtain conclusive results.

## 6.3 Recommendations for Future Research

- Investigate the long-term losses in full-scale piles to understand the prestressing losses from creep and shrinkage, and to separate their contributions.
- Investigate the shear behavior in piles in regions with fully effective prestressing compared to free ends where the prestressing has not fully transferred. Only one free-end test was performed as part of this study.
- Evaluate the drivability of UHPC piles in different soil conditions in Alabama by driving UHPC H-piles in the field.
- Evaluate the impact of field splicing of UHPC H-piles on drivability by driving a spliced UHPC pile in the field.
- Conduct vertical and lateral load tests on UHPC piles in different soil conditions in Alabama to understand the geotechnical capacity of the UHPC H-piles and evaluate the applicability of current pile design methodology in accordance with Load and Resistance Factor Design (LRFD) for the design of UHPC H-piles.
- Investigate the adequacy and applicability of current pile-to-pile bend connection details for accommodating UHPC piles in real world application.

# 7 REFERENCES


- Aaleti, S., & Sritharan, S. (2019). Quantifying bonding characteristics between UHPC and normal-strength concrete for bridge deck application. *Journal of Bridge Engineering*, 24 no. 6.

- Aaleti, S., Petersen, B., & Sritharan, S. (2013). *Design guide for precast UHPC waffle deck panel system, including connections.* Washington DC: Federal Highway Administration.

- AASHTO. (2017). AASHTO LRFD bridge design specifications, 8th edition. Washington, D.C., USA: AASHTO.

- AASHTO. (2022). Standard Method of Test for Uniaxial Tensile Response of Ultra-High Performance Concrete. *T397-22*. Washington, D.C.: American Association of State Highway and Transportation Officials.

- Abokifa, M., & Moustafa, M. (2021). Mechanical characterization and material variability effects of emerging non-proprietary UHPC mixes for accelerated bridge construction field joints. *Construction and Building Materials*. doi:https://doi.org/10.1016/j.conbuildmat.2021.125064

- ARTBA. (2023). *ARTBA Bridge Report.* American Road and Transportation Builders Association.

- ASTM. (2022). C78. *Standard Test Method for Flexural Strength of Concrete*. West Consohocken, PA: ASTM.

- ASTM C1437. (2020). *Standard Test Method for Flow of Hydraulic Cement Mortar*. West Conshohocken, PA, USA: ASTM International.

- ASTM C157. (2017). *Standard Method for Length of Change of Hardened Hydraulic-Cement Mortar and Concrete*. West Conshohocken, PA, USA: ASTM International.

- ASTM C1856. (2017). *Standard Practice for Fabricating and Testing Specimens of Ultra-High Performance Concrete*. West Consohocken, PA, USA: ASTM International.

- ASTM C39. (2021). *Standard Method for Compressive Strength of Cylindrical Concrete Specimens*. West Consohocken, PA, USA: ASTM International.

- ASTM C469. (2022). *Standard Test Method for Static Modulus of Elasticity and Poisson's Ratio of Concrete in Compression*. West Consohocken, PA, USA: ASTM International.

- Bajaber, M., & Hakeem, I. (2021). UHPC evolution, development, and utilizaation in construction: a review. *Journal of Materials Research and Technology*, 1058-1074. doi:https://doi.org/10.1016/j.jmrt.2020.12.051

- Banta, T. E. (2005). *Horizontal shear transfer between ultra high performance concrete and lightweight concrete.* Blacksburg, VA, USA: Virginia Tech.

- Berry, M., Snidarich, R., & Wood, C. (2017). *Development of Non-Proprietary Ultra-High Performance Concrete.* Helena, MT.: Montana Department of Transportation. doi:http://dx.doi.org/10.13039/100009209

- Birkeland, P. W., & Birkeland, H. W. (1966). Connections in precast concrete construction. *Journal Proceedings*, Vol. 63 No. 3.

- Bridi Valentim, D. (2023). *Application of Ultra-High Performance Concrete in Prefabricated Bridge Element Connections for Accelerated Bridge Construction.* The University of Alabama ProQuest Dissertations Publishing.

- Carbonell Muñoz, M. A., Harris, D. K., Ahlborn, T. M., & Froster, a. D. (2014). Bond performance between ultrahigh-performance concrete and normal-strength concrete. *Journal of Materials in Civil Engineering*, 26, no. 8.

- Crane, C. K. (2010). *Shear and shear friction of ultra-high performance concrete bridge girders.* Atlanta, GA, USA: Georgia Institute of Technology.

- El Helou, R., & Graybeal, B. (2019). The Ultra Girder: A Design Concept for a 300-foot Single Span Prestressed UHPC Bridge Girder. *2nd International Interactive Symposium on Ultra-High Performance Concrete.* Albany, NY. doi:10.21838/uhpc.9707

- EN 1992-1-1. (2004). Eurocode 2-Design of Concrete Structures-Part 1: General Rules and Rules for Buildings. Brussels, Belgium: European Committee for Standardization.

- Federal Highway Administration (FHWA). (2013). *Development of Non-Proprietary Ultra-High Performance Concrete for Use in the Highway Bridge Sector: TechBrief.* Retrieved from https://rosap.ntl.bts.gov/view/dot/34789

- FHWA. (2021, December). *Deployments of UHPC in Highway Bridge Construction*. Retrieved from https://highways.dot.gov/research/structures/ultra-high-performance-concrete/deployments

- Garder, J., Aaleti, S., Zhong, L., & Sritharan, S. (2019). *Connection Details and Field Implementation of UHPC Piles - Phase II.*

- Graybeal, B. (2010). Behavior of Ultra-High Performance Concrete connections between precast bridge deck elements. *Proceedings of 2010 Concrete Bridge Conference: Achieving Safe, Smart & Sustainable Bridges* (pp. 1-13). Skokie, IL: National Concrete Bridge Council.

- Graybeal, B. (2014). *Design and construction of field-cast UHPC connections.* Federal Highway Administration, Washington, DC.

- Graybeal, B., & Baby, F. (2013). Development of a Direct Tension Test Method for UHPFRC. *ACI Materials Journal*.

- Hofbeck, J. A., Ibrahim, I. O., & Mattock, A. H. (1969). Shear transfer in reinforced concrete. *Journal Proceedings*, Vol. 66, No. 2.

- Huang, H., Gao, X., Li, L., & Wang, H. (2018). Improvement effect of steel fiber orientation control on mechanical performance of UHPC. *Construction and Building Materials*, 709-721. doi:https://doi.org/10.1016/j.conbuildmat.2018.08.146

- Hyzak, M., Galvan, M., Fisk, M., Smith, A., Johnson, D., Caldwell, D., & Miller, J. (2014). *Guidelines for the Use of Steel Piling for Bridge Foundations.* Texas Department of Transportation.

- Jang, H.-O., Lee, H.-S., Cho, K., & Kim, a. J. (2017). Experimental study on shear performance of plain construction joints integrated with ultra-high performance concrete (UHPC). *Construction and Building Materials, 152*, 16-23.

- Loh, P., Booya, E., and Gardonio, D. "Design and installation of UHPC H-Piles at the Lily River Detour Bridge, Highway 11, near Kapuskasing, Ontario, Canada," Canadian Society for Civil Engineering, 2021.

- Mast, R. F. (1968). Auxiliary reinforcement in concrete connections. *Journal of the Structural Division*, 94 (6), 1485-1504.

- Mattock, A. H., & Hawkins, a. N. (1972). Shear transfer in reinforced concrete. *PCI Journal*, 17.2, 55-75.

- Mohebbi, A., Saiidi, & Itani, A. (2018). Shake Table Studies and Analysis of a PT-UHPC Bridge Column with Pocket Connection. *Journal of Structural Engineering*. doi:https://doi.org/10.1061/(ASCE)ST.1943-541X.0001997

- Muzenski, S., Haber, Z. B., & Graybeal, B. (2022). Interface Shear of Ultra-High-Performance Concrete. *ACI Structural Journal*, 119, no. 1, 267-280.

- PCI. (2021). Implementation of Ultra-High Performance Concrete in Long-Span Precast Pretensioned Elements for Concrete Buildings and Bridges. Chicago, Illinois: Precast/Prestressed Concrete Institute.

- Russell, H. G., & Graybeal, B. A. (2013). *Ultra-high performace concrete: A state-of-the-art report for the bridge community.* McLean, VA, USA: Federal Highway Administration Office of Infrastructure Research and Development.

- Santos, P., & Júlio, E. N. (2014). Interface Shear Transfer on Composite Concrete Members. *ACI Structural Journal, 111*.

- Sarkar, J. (2010). *Characterization of the bond strength between ultra high performance concrete bridge deck overlays and concrete substrates.* Houghton, MI, USA: Michigan Technological University.

- Semendary, A. A., & Svecova, D. (2021). Bond Characterization and Interfacial Coefficients at Precast UHPC and Cast-in-Place UHPC Interface. *Journal of Materials in Civil Engineering*, 33, no. 7.

- Semendary, A., Walsh, K., & Steinberg, E. (2017). Early-age behavior of an adjacent prestressed concrete box-beam bridge containing UHPC shear keys with transverse dowels. *Journal of Bridge Engineering*. doi:https://doi.org/10.1061/(ASCE)BE.1943-5592.0001034

- Sen, R. &. (2007). Application of FRP composites for underwater piles repair. *Composites Part B: Engineering*, 751-758.

- Shahrokhinasab, E., & Garber, D. (2021). *Development of "ABC-UTC Non-Proprietary UHPC" Mix.* Accelerated Bridge Construction University Transportation Center.

- Sharma, S., Ronanki, V. S., Aaleti, S., & Okumus, a. P. (2021). Experimental Investigation of Surface Preparation on Normal and Ultrahigh-Performance Concrete Interface Behavior. *Journal of Bridge Engineering*, 26.4.

- T. Vande Voort, M. S. (2008). *Design and Performance Verification of UHPC Piles for Deep Foundations.* Ames, Iowa, USA: Center for Transportation Research and Education, Iowa State University.

- FDOT Transportation Innovation Initiative: UHPC−Design Innovations. Available online: http://www. fdot.gov/structures/innovation.shtm (accessed on 02 February 2024).

- Wang, J., Liu, J., Wang, Z., Liu, T., Liu, J., & Zhang, J. (2021). Cost-Effective UHPC for Accelerated Bridge Construction: Material Properties, Structural Elements, and Structural Applications. *Journal of Bridge Engineering*. doi:10.1061/(ASCE)BE.1943-5592.0001660